Analysis of Seismic Anisotropy in 3D Multi-component Seismic Data

Zhongping Qian

Thesis submitted in fulfilment of
the requirements for the degree of
Doctor of Philosophy

School of GeoSciences
University of Edinburgh
2009

Declaration

I declare that this thesis has been composed solely by myself and that it has not been submitted, either in whole or in part, in any previous application for a degree. Except where otherwise acknowledged, the work presented is entirely my own.

Zhongping Qian

January, 2009

Abstract

The importance of seismic anisotropy has been recognized by the oil industry since its first observation in hydrocarbon reservoirs in 1986, and the application of seismic anisotropy to solve geophysical problems has been keenly pursued since then. However, a lot of problems remain, which have limited the applications of the technology. Nowadays, more and more 3D multi-component seismic data with wide-azimuth are becoming available. These have provided more opportunities for the study of seismic anisotropy. My thesis has focused on the study of using seismic anisotropy in 3D multi-component seismic data to characterize subsurface fractures, improve converted wave imaging and detect fluid content in fractured reservoirs, all of which are important for fractured reservoir exploration and monitoring.

For the use of seismic anisotropy to characterize subsurface fracture systems, equivalent medium theories have established the link between seismic anisotropy and fracture properties. The numerical modelling in the thesis reveals that the amplitudes and interval travel-time of the radial component of PS converted waves can be used to derive fracture properties through elliptical fitting similar to P-waves. However, sufficient offset coverage is required for either the P- or PS-wave to reveal the features of elliptical variation with azimuth.

Compared with numerical modelling, seismic physical modelling provides additional insights into the azimuthal variation of P and PS-wave attributes and their links with fracture properties. Analysis of the seismic physical model data in the thesis shows that the ratio of the offset to the depth of a target layer (offset-depth ratio), is a key parameter controlling the choice of suitable attributes and methods for fracture analysis. Data with a small offset-depth ratio from 0.7 to 1.0 may be more suitable for amplitude analysis; whilst the use of travel time or velocity analysis requires a large offset-depth ratio above 1.0, which can help in reducing the effect of the acquisition footprint and structural imprint on the results.

Multi-component seismic data is often heavily contaminated with noise, which will limit its application potential in seismic anisotropy analysis. A new method to reduce noise in 3D multi-component seismic data has been developed and has proved to be very helpful in improving data quality. The method can automatically recognize and eliminate strong noise in 3D converted wave seismic data with little interference to useful reflection signals.

Component rotation is normally a routine procedure in 3D multi-component seismic analysis. However, this study shows that incorrect rotations may occur for certain acquisition geometry and can lead to errors in shear-wave splitting analysis. A quality control method has been developed to ensure this procedure is correctly carried out.

The presence of seismic anisotropy can affect the quality of seismic imaging, but the study has shown that the magnitude of the effects depends on the data type and target depth. The effects of VTI anisotropy (transverse isotropy with a vertical symmetry axis) on P-wave images are much weaker than those on PS-wave images. Anisotropic effects decrease with depth for the P- and PS-waves. The real data example shows that the overall image quality of PS-waves processed by pre-stack time migration has been improved when VTI anisotropy has been taken into account. The improvements are mainly in the upper part of the section.

Monitoring fluid distribution is an important task in producing reservoirs. A synthetic study based on a multi-scale rock-physics model shows that it is possible to use seismic anisotropy to derive viscosity information in a HTI medium (transverse isotropy with a horizontal symmetry axis). The numerical modelling demonstrates the effects of fluid viscosity on medium elastic properties and seismic reflectivity, as well as the possibility of using them to discriminate between oil and water saturation. Analysis of real data reveals that it is hard to use the P-wave to discriminate oil-water saturation. However, characteristic shear-wave splitting behaviour due to pore pressure changes demonstrates the potential for discriminating between oil and water saturation in fractured reservoirs.

Acknowledgements

Even five years ago, I didn't expect I would come to Edinburgh for a PhD project after so many years in the industry, but life is changing and now I have been in Edinburgh for nearly four years.

With great respect I would like to express my great gratitude to Prof. Xiang-Yang Li for his academic instruction, guidance, inspiration as well as enthusiastic supports that have accompanied me throughout the exciting time of my PhD research. I have benefited so much from him. I should say I was lucky enough to have met Mark Chapman, and I benefited so much from his knowledge in rock physics and so many academic suggestions. I would like to thank Dr. Enru Liu for his academic and living advices, even after he has left EAP for his adventures in the oil industry.

Special thanks go to Dr. Hengchang Dai for his very countless whole-range supports during my stay with Edinburgh Anisotropy Project (EAP). Without his help I couldn't get many things in the thesis done. I would like to thank my supervisor in the department Prof. Ian Main for his valuable academic supports and adviser Andrew Curtis for his good suggestions during the period.

I am so grateful to Dr. David Booth for having proof read every page of my first draft of the thesis and I was really moved by his serious attitude. He also has helped me so much in many other things. Special thanks go to Dr. Sonja Maultzsch for her enthusiastic help and valuable suggestions. I would like to give my big thanks to Dr. Christian Deplante and Dr. Bo Zhao for their academic advices.

I am thankful to all the sponsors of the EAP for funding this research project and providing the data sets in my study. I am thankful to all the members of the BGS computer support members, especially Brian Bainbridge, Steve Love and Jane Robertson for getting my old 'junk' running.

I was very happy to have so many lab mates, Barbel Traub, Lifeng Wang, Jinghua Zhang, Isabel Varela, Adam Wilson, Emeka Odebeatu, Anish Varghese, Aniekan Ekanem,

Yungui Xu, Cuntang Zhang, Tieqiang Zhang. I thank you all for the countless enjoyable days and so many laughs in the office. I would like to give my thanks to Alice Tonnellier for the nice field trips. It was with you that I found there was ‘desert’ in Scotland. I want to thank Steve Davison for the good KB time. I would like to thank all my friends in Edinburgh for giving me so many nice memories.

Finally, I would like to thank my wife Haizhen for her full supports and patience during my research. This thesis is a gift to my dear daughter Lishan and son Pengrui for the unforgettable happy time they have brought me.

To my family

Notations and conventions

Abbreviations

4C	conventional three components plus a hydrophone
ACCP	Asymptotic Common Conversion Point
AVD	Amplitude Variations with Direction
AVO	Amplitude Variations with Offset
CCP	Common Conversion Point
CIP	Common Image Point
CMP	Common Mid Point
DMO	Dip Move Out
HTI	Transverse Isotropy with a Horizontal axis of symmetry
MEMS	Micro Electro Mechanical System
NMO	Normal Move Out
OBC	Ocean Bottom Cable containing multi-component sensors
P-wave	comPressional seismic wave
PSTM	Pre Stack Time Migration
PS-wave	converted wave with down-going P-wave and up-going S-wave
R-	Radial
RMS	Root of Mean Square
S-wave	Shear wave
T-	Transverse
TI	Transverse Isotropy
VSP	Vertical Seismic Profile
VTI	Transverse Isotropy with a Vertical axis of symmetry

Symbols

qS1	fast quasi-shear-wave
qS2	slow quasi- shear-wave
qP	quasi-compressional wave
σ_{ij}	stress
c_{ijkl}	4th order elastic stiffness tensor
e_{kl}	strain tensor
λ	Lame's constants
μ	shear modulus
u_i	displacement vector
s_{ijkl}	elastic compliance constant
f_i	external body force component
x_j	cartesian coordinates
ρ	density
Γ	Christoffel matrix
n_i	direction cosine of propagation
U_k	polarization components
ω	angular frequency
t	travel time
δ_{ij}	Kronecker δ function
V_{phase}	phase velocity
V_{group}	group velocity (ray velocity)
α	P-wave velocity along symmetry axis
β	S-wave velocity along symmetry axis
V_{P}	P-wave velocity in an isotropic medium
V_{S}	S-wave velocity in an isotropic medium
V_{C2}	PS-wave NMO velocity in data for near offsets
V_{P2}	P-wave NMO velocity
V_{S2}	S-wave NMO velocity
ε	Thomsen parameter for P-wave anisotropy
γ	Thomsen parameter for S-wave anisotropy
δ	Thomsen parameter related to wave-front ellipticity
θ	angle between wave-front normal and symmetry axis

R	reflection coefficient
G	AVO gradient
ϕ	azimuthal angle
m_a	fluid mass in element α
κ	permeability
ς_g	grain size
η	fluid viscosity
p_a	pressures in element a
Φ_p	porosity
φ_c	crack density
γ	velocity ratio of P-wave to S-wave in isotropic a medium
γ_0	vertical velocity ratio of P-wave to S-wave
γ_2	NMO velocity ratio of P-wave to S-wave
γ_{eff}	effective velocity ratio of P-wave to S-wave
η_{eff}	effective anisotropic parameters for P-wave
ζ_{eff}	effective anisotropic parameters for S-wave
χ_{eff}	effective anisotropic parameters for PS-wave
ΔR_{pp}	P-wave seismic measurement in a HTI medium
ΔR_{ps}	PS-wave seismic measurement in a HTI medium

List of figures

Contents

Chapter 1

Introduction

In this chapter I introduce the general scope and rationale for the thesis, based on studying seismic anisotropy in fractured reservoirs with wide-azimuth multi-component seismic data. Especially, I describe the motivations, objectives, thesis structure and contents, as well as the data, tools and software used for the analyses.

1.1 Anisotropy in seismic data

Anisotropy is a very important concept in geophysical exploration. Seismic anisotropy is used to describe the directional dependence of seismic wave speed in subsurface media in the Earth. Crampin (1966, 1989) defines seismic anisotropy as the directional variation of seismic properties. In exploration geophysics, rocks are assumed to be isotropic, despite that most crustal rocks are found experimentally to be anisotropic. For example, the fine layering of a sedimentary basin may produce seismic anisotropic features if the individual layer thickness in the layer sequence is much smaller than the seismic wavelength (White and Sengbush, 1953, Backus, 1962). Aligned cracks may produce anisotropy because cracks tend to be preferentially aligned parallel to the direction of maximum compressive stress. There are many types of seismic anisotropy: transverse isotropy, orthorhombic anisotropy, monoclinic anisotropy, etc. (Sheriff and Geldart, 1995), directly analogous to the equivalent symmetry class in mineralogy. The first confirmed observations of seismic anisotropy in the earth were the measurements of azimuthal velocity variations of P-waves (Hess, 1964).

The importance of seismic anisotropy was recognized by the oil industry from its first observation in a hydrocarbon reservoir in 1986 (Crampin, et al, 1986; Alford, 1986; Lynn and Thomsen, 1986). Since a shear-wave is also sensitive to seismic anisotropy

than a P-wave (e.g. Crampin and Radovich, 1982; Winterstein, 1990), the PS-wave is suitable for seismic anisotropy analysis as a P wave, because the upward wave-paths of the PS-wave is a shear-wave (S-wave) trajectory. Many geophysicists have realized that P- and S-wave velocities and anisotropic parameters, which can be estimated from P- and PS-wave reflection data, can help to characterize fractures or stress, discriminate lithology and predict pore pressure.

On entering an anisotropic medium, the S-wave generally splits into two S-waves with different velocities and polarizations, which are determined by the anisotropic symmetry of the medium. Several cases show the fast S-wave polarization is sensitive to local stresses (e.g. Gaiser and Probert, 2006), and the fast directions can be used to infer fluid flow directions, because the polarization of the faster shear wave is parallel to fracture strikes while the polarization of the slow shear wave is normal to the fracture strike. The magnitude of time-delay between fast and slow shear-waves can be used to measure fracture density along the ray paths.

1.2 Problems which may be solved by seismic anisotropy

1.2.1 Problems in fracture detection

Obtaining fracture information is very important in producing fracture reservoirs. Fractured hydrocarbon reservoirs have become a very important energy sources for potential reserve growth in order to meet increasing demands. Consequently, understanding fractured reservoirs plays an important role in sustaining the required energy supply. To characterize the subsurface fracture systems, an initial effort was applied to the use of shear-wave splitting (e.g. Crampin 1985). Due to the lack of quality shear-wave data, the focus shifted to the use of wide azimuth P-wave seismic data in the 1990's (e.g. Lefeuvre, 1994 and Lynn et al 1996). The use of azimuthal seismic anisotropy to detect natural fractured reservoirs using equivalent medium theory has been studied by many authors (e.g. Hudson, 1981; Schoenberg and Douma, 1988; Liu, Hudson, et al, 2000; Chapman, 2003) Parallel vertical crack orientations can occur when the vertical stress becomes greater than the minimum horizontal stress. A medium containing vertically aligned fractures with scale length much less than the scale of the seismic wavelength can be modelled by an equivalent azimuthally anisotropic medium

for seismic wave propagation. Many theoretical studies of crack-induced seismic anisotropy simplified the fractures as ellipsoidal cavities of low aspect ratio (e.g. Hudson, 1980, 1981).

Many studies based on equivalent medium theories reveal that shear-wave splitting and azimuthal variations of P-waves amplitudes and travel-time can be used as the diagnostic features of fractured media. However, despite the intensive effort in research and development related to seismic detection of fractured reservoirs, there are still many problems remained to be solved, and some of the relevant technologies have largely remained research tools rather than routine tools for practical application.

Numerical modelling is often used to evaluate the results of seismic fracture detection, but it is based on equivalent medium theory and does not necessarily reflect physical responses, thus it is more mathematical than physical. Unlike numerical modelling data, physical model data obtained from a scale model on a lab bench possess most of the features of field data, since they have a similar physical background and what applies to physical model analysis should also apply to field data analysis. Furthermore, accurate numerical solutions are very useful in understanding wave propagation and verifying the processing results. However, numerical results often fail to reveal the analytical insights into parameter dependency and relationships involving offset and target depth, for example. For this reason, analytical approximations are often derived to fill the gaps. In physical modelling, we know all fracture information within the model, and just need to find the links between the data attributes and the fracture properties, and study which method can be used to infer fracture information. Thus, an analysis with physical model data will provide an understanding of the physical basis for the methods for azimuthal anisotropy analysis.

A range of different seismic attributes such as P-wave traveltimes and amplitudes, and converted shear-wave splitting attributes can all be used to estimate fracture distribution. How should these results compare, and what are their merits and limitations? More importantly, how are we to examine these results for improving the reliability of estimated fracture parameters? The methodologies for acquiring physical model data are similar to those applied in the field, except that the data acquisition is carried out in the laboratory. This makes it possible to study how the factors associated with data

acquisition, such as signal to noise ratio, geometry, etc., affect fracture detection, and how these effects can be recognized in fracture characterisation results from field data analysis so as to avoid interpretation traps.

Variation in both the near surface and the overburden affects the data quality. How can we improve the data quality through innovative processing methods whilst preserving fracture information and what are other factors that will also significantly influence fracture estimation?

Any progress in, and solution to any of the above problems will certainly be very useful in advancing the characterization of sub-surface fractures and will benefit the hydrocarbon industry as a whole.

1.2.2 Problems in PS-wave data imaging

Due to the difference in P-waves and shear-wave velocities, the signature of PS-waves is inherently non-hyperbolic because of the asymmetric ray-paths and different methods from those for P-wave processing are required for PS-wave move-out correction (e.g. Tessmer and Behle, 1988; Zhang, 1992; Stewart et al., 2002). Besides asymmetric ray-paths, seismic anisotropy is another problem in PS-wave imaging. If a layered sequence of different media (isotropic or not) is probed with an elastic wave of wavelength much longer than the typical layer thickness (i.e. the normal seismic exploration context), the wave propagates as through it were in a homogeneous but VTI (transverse isotropy with a vertical axis of symmetry) medium.

Though various attempts have been made to extend the dip move-out correction (DMO) approach to address the VTI anisotropy issue (e.g. Rommel, 1996; Thomsen, 1999, Tsvankin and Grechka, 2000), anisotropic CCP binning and PS-waves DMO is strongly velocity dependent and this has severely limited their application. Thus using PS-wave anisotropic PSTM to replace the conventional processing flow of common conversion point (CCP) plus DMO has more advantages in anisotropic PS-waves imaging (e.g., Dai and Li, 2001; Dai, 2003; Li and Yuan,2003; Li, et al., 2007, etc.). Furthermore, we know that VTI anisotropy is mainly caused by marine sediments and may affect the seismic imaging quality, but the extent to which the anisotropy will affect the PSTM results and

how to compensate for the VTI effects are still important issues in PS-wave data processing.

1.2.3 Problems in oil-water discrimination

Geophysicists have devoted great efforts to find solutions to determine fluid saturations from seismic data with many studies, but with rather mixed results. Oil and water have similar bulk moduli, which means that the effects of oil and water saturation on pure P- and S-wave (shear-wave) are very similar, and this fact has impeded efforts to tell the two apart from analysis of seismic data. It is commonly believed that fluid information is to be inferred from the P-wave data, with shear-waves being insensitive to fluid, and indeed almost all successful fluid-detection methodologies have been based on analysis of the P-waves (e.g. Varela et al., 2006). Nevertheless the traditional seismic methods based on wave propagation in isotropic media have not been very successful so far.

However, fractured reservoirs are seismically anisotropic, and the rock physics relationships relevant to fractured, anisotropic rocks are subtler than those for the more familiar isotropic case. We have to take account of the effect of anisotropy on fluid substitution in the analysis, and many studies show the seismic characteristics of fluid-saturated HTI (transverse isotropy with a horizontal axis of symmetry) anisotropic media (Chapman, Maultzsch, et al., 2003). Recent theoretical advances in frequency dependent anisotropy have shown the possibility of using seismic anisotropy to detect fluid saturation. These theories allow anisotropic dispersion and attenuation to be related to rock and fluid properties (Chapman, Maultzsch, et al., 2003).

Oil and water have markedly different viscosities. Since the viscosity of fluids saturating a fractured medium will affect the medium elastic properties, it is theoretically possible to determine viscosity information from seismic data, and so to monitor fluid saturation changes. Thus, if we can find a robust seismic measurement which is sensitive to fluid viscosity we would greatly improve our chances to discriminate between oil and water saturation. However, besides viscosity, other factors such as frequency, angle of incidence, fracture density, etc., may also affect anisotropy and have combined effects on seismic data. Though the ability to detect a viscosity effect is of great potential relevance to the problem of oil-water discrimination, there are two questions to answer.

The first question is: What are the effects of the viscosity that will be present in seismic data? The second question is: Can the method be practical in determining fluid saturation in real data analysis?

1.3 Objectives and approaches

Nowadays, more and more 3D multi-component seismic data (marine and land) with wide-azimuth distribution are available. The progress in 3D multi-component seismic data acquisition technology, especially ocean-bottom seismic data acquisition, has made it possible to acquire high-quality converted wave (PS-waves) reflection seismic data with wide azimuth coverage, which provides more opportunity for the study of seismic anisotropy. Thus, the overall objective of my thesis is to investigate seismic anisotropy in 3D multi-component seismic reflection data, mainly focus on the study of using seismic anisotropy in 3D multi-component seismic data to characterize subsurface fractures, improve converted wave imaging and detect fluid content in fractured reservoirs, which are very important for fractured reservoir exploration and monitoring. Consequently, my research work mainly covers the following three aspects:

To use seismic anisotropy to characterize subsurface fracture information

Though techniques of using seismic data to characterize subsurface fracture distributions have been developed for many years, few of them have become routine tools in reservoir characterisation due to concerns about the reliability of the fracture characterisation results. I aim to analyze the factors that may affect the results and draw up guidelines for real applications. To reach this objective, I 1) investigate the effects of acquisition parameters on the use of P-wave anisotropic attributes for fracture characterisation by analysing two 3D physical model datasets; 2) analyse the effects of data processing on anisotropy analysis and develop innovative new methods that may lead to an improvement in fracture characterization and/or anisotropic imaging; 3) study fracture characterisation using both land and marine 3D converted shear-wave seismic data and evaluating the new methods for improving characterisation results; and 4) study the relationship between P-wave attribute versus direction (AVD) analysis and converted shear-wave analysis.

To study the effects of seismic anisotropy on PS-waves pre-stack time migration

If a layered sequence of different media (isotropic or not) is probed with an elastic wave of wavelength much longer than the typical layer thickness, the wave propagates as through it were in a homogeneous medium but with VTI anisotropy. How to compensate for the VTI effects is still an important issue and very useful in PS-wave data processing. To fulfil this study, I will investigate the anisotropic effects of VTI media on pre-stack time migration (PSTM) of converted wave data by applying two velocity models (one isotropic, the other anisotropic) to a real 3D dataset, so as to find some reference for real data analysis in the future.

To use seismic anisotropy to characterise fluid saturation

Oil and water have similar bulk moduli, and this has impeded efforts to tell the two apart from analysis of seismic data. However, the two fluids have very different viscosities, and if there is a robust seismic measurement for fluid viscosity, the chance to discriminate the two fluid saturations will increase. The ability to detect variations of viscosity has great potential relevance to the problem of oil-water discrimination. For this purpose, I study the effects of fluid viscosity on certain seismic attributes through numerical modelling, analyze the use of viscosity to detect oil-water saturation in fractured reservoirs, and perform theoretical analysis of wave propagation in vertically fractured rock to investigate frequency-dependent anisotropy. I also study the individual and combined effect of factors such as frequency, angle of incidence, fracture and density to obtain some insights into their effective use for the characterisation of fluid substitution.

1.4 Structure of the thesis

In Chapter 2 I review the publications covering the background theories involved in the subject, assessing what has been done and what remains to be done in the area.

In using seismic anisotropy to characterize subsurface fracture information, the equivalent medium theory provides a theoretical basis for using seismic methods to detect the sub-surface fracture systems which give rise to azimuthally anisotropic seismic wave propagation. Seismic attributes such as amplitudes and travel-time, are

azimuthally dependent and show elliptical distribution with azimuth. The role of seismic anisotropy could be to bridge the gap between the fractures determined by logs, and extrapolated from outcrop analogues, and those inferred from seismic data. The fracture properties can also be obtained by studying the rock stress distributions through shear-wave splitting analysis. The polarization of the faster shear-wave is parallel to the direction of fracture strike while the polarization of the slow shear-wave is normal to the direction of fracture strike, and the magnitude of time-delay between fast and slow shear waves can be used to measure fracture density along the ray paths.

For the effects of seismic anisotropy on PS-wave pre-stack time migration, PS-wave processing involves some inherent problems such as asymmetric ray-paths and common-conversion-point (CCP) binning, increased sensitivity to anisotropy, etc. PS-wave PSTM is a better approach in seismic imaging than conventional PS-wave processing strategy, which normally includes CCP binning, normal-move-out (NMO) correction, dip-move-out (DMO) correction and post-stack migration, which can be carried out by building a PS-wave stack velocity model from asymptotic common conversion-point (ACCP) gathers and using the common-imaging-point (CIP) gathers to update the migration velocity model.

In using seismic anisotropy to characterise fluid saturation, the Chapman squirt-flow model (Chapman, Maultzsch, et al., 2003) and the poroelastic equivalent medium theory indicate that the fluid viscosity in a saturated HTI medium can influence medium elastic properties and thus the Thomsen anisotropic parameters, which makes it theoretically possible to use seismic properties to infer fluid viscosity changes, so as to monitor fluid substitutions in production reservoirs.

In Chapter 3 I perform forward modelling to study the azimuthal variations of the attributes (i.e. amplitudes, travel time, etc.) of P- and PS-waves in an HTI model. I mainly focus on factors which may affect the feasibility of elliptical anisotropy analysis, with the objective of obtaining more insight into the practice of using azimuthal anisotropy analysis for fracture detection, and aiming to use the findings in the modelling analysis as a guideline in real data analysis and interpretation.

In addition to the numerical modelling of conventional P-wave azimuthal anisotropy, I also model the azimuthal distribution of PS-wave attributes and compare results, so as to

study the possibility of using the azimuthal variation of PS-wave attributes for fracture detection. It is revealed that both amplitudes and interval travel-time of the radial component of PS-waves can be used to infer fracture properties through ellipse fitting as for azimuthal P-wave attributes analysis.

In Chapter 4 I carry out azimuthal attributes analysis on two 3D physical model P-wave datasets. Because the physical model datasets have a similar physical background to a field dataset, it can provide the opportunity to understand the physical basis of the azimuthal analysis methods and help us to know the potential of applying them in field data. The methodologies for acquiring physical model data are similar to that applied in field surveys, except that the data acquisition is carried out in the laboratory. This makes it possible to study how the factors associated with data acquisition, such as signal to noise ratio, geometry, etc., affect the results of fracture detection and how to recognize these effects in field data analysis to avoid interpretation traps. The findings from the physical modelling analysis are used to guide the fracture detection in real data in Chapter 5.

Chapter 5 is actually the extension of the work in Chapter 3 and Chapter 4. Azimuthal attribute and shear-wave splitting analyses are performed on the Clair 3D-4C OBC (ocean bottom cable) data for seismic anisotropy, aiming to characterize the fracture properties of the reservoirs. VSP (vertical seismic profile) and 2D OBC data analysis had been carried out for seismic anisotropy in the area. The azimuthal P-wave stacking velocities and stack panels were used to infer fracture information. The results from different attributes reveal spatial variations of fracture orientation and density, and the fracture information derived from the interval travel times appears more reliable than the results from other seismic attributes. The PSTM results of the T-component show reflection events at the target zone, indicating that shear-wave splitting happens in the reservoir. However, the magnitude is not large enough to quantify the shear-wave splitting analysis across the whole section to obtain time-delays and polarization directions. Instead, the stacking velocity of the R-component shows evidence of azimuthal variations which can help to interpret fracture information, when used together with the P-wave data.

In Chapter 6 I investigate the sensitivity of anisotropic parameters on PS-waves pre-stack time migration, which shows that the effects of VTI anisotropy on both

P-waves and PS-waves decreases with time, but the imaging of PS-wave data is affected more by anisotropy than the imaging of P-wave data. The results of the anisotropic parameter analysis reveal that the P-wave anisotropy is very small but the S-wave anisotropy is very large and should not be ignored in PS-wave data processing. The overall PS-wave PSTM results based on the anisotropic velocity model are better than that based on the isotropic velocity model, and the improvement is mainly located in the upper part of the section.

In Chapter 7 I study the effects of a fluid-saturated HTI medium on elastic properties and seismic measurements, and the possibility to discriminate oil/water saturation though numerical modelling and real data analysis. In fractured reservoirs, the fracture density and orientation influences the permeability. The numerical modelling results show that variations of fluid viscosity can be revealed in certain anisotropic parameters and P- and PS-wave reflection coefficients. Both seismic frequency and viscosity have similar effects on elastic properties and have the potential to be used to monitor fluid substitution in producing fracture reservoirs.

In Chapter 8 I use a land 3D multi-component seismic data from Ken 71 survey to study pore-pressure and saturating fluid substitution in the reservoir. Due to the serious noise contamination in the Ken 71 PS-wave data, I develop a method which can automatically recognize and eliminate the strong noise point by point with little interference to useful signals. It adapts to the features of the strong noise and after the application of the method, the signal to noise ratio of the data is significantly improved, which makes it possible to use the data for fracture and fluid substitution analysis.

The analysis of shear-wave splitting changes due to pore pressure changes reveals the potential of discriminating between oil and water distributions. The split shear-wave shows consistent changes in amplitude dimming, time delay anomalies, which indicate pore pressure change due to water-flooding, meaning that shear-wave splitting is sensitive to an oil-water saturation change. The amplitude and travel-time anomalies on Ken 71 data are correlated with well information on fluid saturation. Water-saturated zones tend to be associated with higher shear-wave splitting than oil-saturated zones, and their amplitudes are dimmer. In the oil-saturated zones, big difference in PS-wave amplitude between the fast and slow shear-wave direction can be observed.

The publication and the abstracts for international conferences from my PhD project are listed in appendix A.

1.5 Datasets and software

1.5.1 Datasets used for the analyses

In the analyses, I used two 3D synthetic datasets, two pre-existing 3D P-wave physical model datasets, and one 3D OBC dataset and one 3D land multi-component seismic dataset. I created the relevant synthetic datasets with ANISEIS software.

Synthetic data I:

I created 3D synthetic three-component seismic datasets from a model with fracture densities of 10% and 18% to perform azimuthal anisotropy analysis. The offset of the data ranges from 25m to 1500m, the azimuth ranges from 0^o to 360^o, and the azimuth sampling interval is 10^o. The data was generated and analyzed in Chapter 3.

Synthetic data II:

I generated a 3D synthetic three-component seismic dataset from a model with a porous, cracked and fluid saturated HTI medium under an isotropic medium to study the effects of viscosity on seismic data. The data represents seismic waves propagating 1) in the direction of the fracture normal, 2) in the direction forming 45^o to fracture normal and 3) in the direction parallel to fracture strike. I used the data in Chapter 7.

Physical model data:

In the study of physical model subsurface fractures, I used two 3D datasets acquired in the lab with different geometries. Each dataset is equivalent to a field area size of $20km^2$, and they are acquired with different acquisition parameters. Both datasets have wide-azimuth offset coverage, which make them ideal for azimuthal anisotropy analysis. I analyzed the data for fracture characterisation in Chapter 4. The total original data size is 20GB.

Clair 3D OBC data:

I used the Clair 3D OBC dataset to perform azimuthal anisotropy analysis. The Clair reservoir comprises of a Devonian/Carboniferous fractured reservoir beneath a Base Cretaceous unconformity (Coney et al. 1993) with an oil column about 600m, and successful production is very much dependent on the ability to characterize the fracture system. The 3D OBC data were acquired by PGS in 2002 using the patch geometry where the sail lines are orthogonal to the receiver cables in order to obtain wide azimuth coverage. A total of twenty patches were acquired. I applied the 50GB data to the analysis in Chapter 5 and 6.

Shengli land 3D multi-component data

The data is from the Ken 71 survey of the Shengli Oilfield located in the Yellow River delta besides Bohai Sea, covering an area of 40 km^2. The 3D multi-component seismic data were acquired with digital micro-electro-mechanical system (MEMS) sensors over a mixed sand and shale sequence in the overburden. The data consisted of four swaths. The data are of good quality with some random noise and ground roll. The data size involved in the analysis is 500GB. The data was analysed in Chapter 8.

1.5.2 Software used

CXtools is a software package for multi-component seismic data processing developed by EAP. I used it for PS-wave data processing and seismic anisotropy analysis in Chapters 4, 5, 6 and 8.

RU (Rock Unix) is a toolkit developed by EAP for fracture modelling and anisotropic rock physics analysis. I used it for forward modelling and seismic anisotropy analysis in Chapters 3 and 7.

ProMAX is a commercial seismic data processing system. I applied it for geometry definition, data quality check, conventional velocity analysis, NMO correction, stack, plotting, etc.. I used the software in Chapters 4, 5, 6 and 8.

SU (Seismic Unix) is an open source seismic utilities package supported by CWP, I used it as the platform to run the anisotropic analysis programs which I developed.

ANISEIS is a commercial software for anisotropy analysis, I used it to generate synthetic seismograms for the anisotropic and cracked models defined in this thesis. I used it in Chapters 3 and 7.

Matlab is a commercial software package for performing mathematical calculations and visualizing data. I mainly used it for plotting synthetic diagrams in Chapters 4, 5 and 7.

Chapter 2

Review of seismic anisotropy

In this chapter I review the basic theories and methods which are relevant to my PhD project of using wide-azimuth multi-component seismic data to study seismic anisotropy effects for subsurface properties related to symmetries and fluid saturation, including azimuthal seismic attribute and shear wave splitting analysis for fracture detection, converted wave processing, and fluid substitution analysis.

2.1 Basic concepts

Seismic anisotropy

Seismic anisotropy is a term used in seismology to describe the directional dependence of seismic wave speed in a medium (rock) within the Earth. There are several definitions for the term seismic anisotropy, but they are basically the same. For example, Crampin (1989) defines seismic anisotropy as the directional variation of seismic properties (e.g. seismic velocity, arrival time, amplitude, polarizations, etc). Thomsen (2002) gives a simple and concise definition of seismic anisotropy as the angle dependent seismic velocity, where the velocity can be ray velocity, wave-front velocity, group velocity and phase velocity, interval velocity, vertical average velocity, NMO velocity and RMS velocity, etc., and the angle can be polar angle (from vertical), azimuthal angle, etc., depending on the context.

In geophysical exploration, the fine layering of a sedimentary basin may produce seismic anisotropic features if the individual layer thickness in the layer sequence is much smaller than the seismic wavelength, and the seismic wave will propagate as through it were in a homogeneous, but anisotropic medium (White and Sengbush, 1953, Backus, 1962). The aligned cracks may also produce anisotropy and can be used to determine the

direction of stress in the crust, because in most cases, cracks are preferentially aligned with the direction of maximum compressive stress. The first confirmed observations of seismic anisotropy in the earth were measurements of azimuthal velocity variations of P-waves (Hess, 1964).Anisotropy is also very important in production from oil reservoirs as fast directions can be synonymous with preferential fluid flow directions.

Heterogeneity

When talking about seismic anisotropy, we can not bypass the concept of heterogeneity, in which physical properties are dependent upon spatial position. In the scale of seismic exploration, heterogeneity may referred to the case where rock particles have a roughly preferred directional distribution, such as in sedimentary rocks which may have a coarse thin layer structure where the grains tend to land on their flat sides due to gravity, or in rock formations containing vertically aligned fractures caused by regional stress.

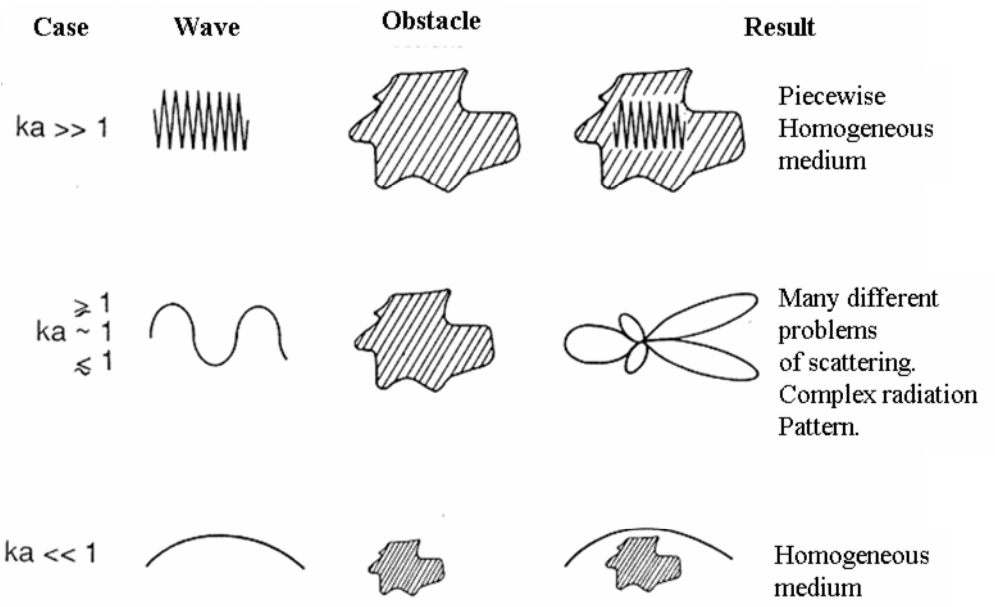

Figure 2.1.1: Relationships between anisotropy and heterogeneity. (Herraiz, M. and Espinosa, A. F., 1987), where **k** is the wave number, **a** is the scale length of the heterogeneities.

When the scale of the heterogeneity is smaller than the seismic wavelength, seismic anisotropy may be observed. Thus, seismic anisotropy utilizes the concept of scattering interference from sub-wavelength heterogeneities and may provide a way to characterize these specific examples of aligned heterogeneities. An ordered system of reservoir

heterogeneity may display seismic anisotropy diagnosed by shear-wave splitting, and the polarization of the fast split shear-wave (qS1), the time delay between the two split shear-waves (qS1, qS2), and the differential reflectivity at normal incidence may be used to quantify the heterogeneities.

Weak seismic anisotropy

The descriptive equations for anisotropic propagation of seismic waves are much more complicated than that for isotropic propagation. However, in most cases of interest to geophysicists, the seismic anisotropy is relatively weak (at least less than 20%), which allows the equations governing anisotropic propagation to be simplified considerably and much easier to be grasped intuitively (Thomsen, 1986). The Thomsen parameterization reveals that P-wave reflection travel time is governed by fewer independent quantities than those formally appearing in the expressions for velocities of waves propagating through VTI anisotropic media (model with a vertical axis of rotational symmetry, will be discussed later). This observation led to the introduction of the elliptical coefficient $\eta \approx \varepsilon - \delta$ that, along with conventional NMO velocity, makes it feasible to do time processing of P-waves in laterally homogeneous VTI media (Alkhalifah and Tsvankin, 1995). For example, although the orientation, density and size of fractures in rocks may vary with position, they are under regional stress control and tend to distribute in vertically aligned forms with fractures oriented parallel to the direction of maximum in-situ stress, thus can be simplified as vertically aligned fracture models (HTI anisotropy) in seismic anisotropy analysis.

2.2 Fundamentals of seismic anisotropy

2.2.1 Stress-strain's expression in Hooke's law

When seismic waves propagate far away from their source, they can be regarded as plane waves and the particle displacements caused by seismic wave can be assumed to be small enough for the relationship between stress tensor σ and strain ε to be sufficiently accurate when described by the generalized Hooke's law

$$\sigma_{ij} = \sum_{k=1}^{3}\sum_{l=1}^{3} c_{ijkl} e_{kl} \qquad i, j = 1,2,3 \tag{2.2.1}$$

where c_{ijkl} are the elements of the fourth-order elastic stiffness tensor matrix responsible for material properties, containing a total number of 81 elements (3 x 3 x 3 x 3) that connect the stress σ_{ij} and strain e_{kl} which is the strain tensor defined as (e.g. Tsvankin, 2005, pp.2)

$$e_{kl} = \frac{1}{2}\left(\frac{\partial u_k}{\partial x_l} + \frac{\partial u_l}{\partial x_k} \right) \qquad k,l = 1,2,3 \tag{2.2.2}$$

where u_i is the i^{th} components of the displacement vector and x_j are the Cartesian coordinates.

Or equivalently, the relationship between the stress σ_{ij} and strain e_{kl} can also be expressed as

$$e_{ij} = \sum_{k=1}^{3}\sum_{l=1}^{3} s_{ijkl}\sigma_{kl} \qquad i,j = 1,2,3 \tag{2.2.3}$$

where s_{ijkl} is normally referred as an elastic compliance constant.

Due to the symmetry of stresses and strains, the following relations exist (e.g. Mavko, et al., 1998, pp. 19)

$$c_{ijkl} = c_{jikl} = c_{ijlk} = c_{jilk} \tag{2.2.4}$$

The existence of unique strain energy potential also implies the relation (Aki and Richards, 2002, pp. 21-23)

$$c_{ijkl} = c_{klij} \tag{2.2.5}$$

Equation (2.2.4) and (2.2.5) allow the stiffness tensor to be condensed into a symmetric matrix of 6 x 6 according to Voigt notation by converting each pair of indices (*ij* and *kl*) into a single index through the mapping rule

$$11 \rightarrow 1,\ 22 \rightarrow 2,\ 33 \rightarrow 3,\ 32 \rightarrow 4,\ 31 \rightarrow 5,\ 21 \rightarrow 6$$

$$
\begin{array}{cc|cccccc}
ij & kl \rightarrow & 11 & 22 & 33 & 23 & 13 & 12 \\
\downarrow & & & & & & & \\
11 & & c_{11} & c_{12} & c_{13} & c_{14} & c_{15} & c_{16} \\
22 & & \cdot & c_{22} & c_{23} & c_{24} & c_{25} & c_{26} \\
33 & & \cdot & \cdot & c_{33} & c_{34} & c_{35} & c_{36} \\
23 & & \cdot & \cdot & \cdot & c_{44} & c_{45} & c_{46} \\
13 & & \cdot & \cdot & \cdot & \cdot & c_{55} & c_{56} \\
12 & & \cdot & \cdot & \cdot & \cdot & \cdot & c_{66}
\end{array}
$$

The number of independent constants of the stiffness matrix reduces from 81 to 21, and is sufficient to describe an anisotropic elastic medium. Written in matrix form, equation (2.2.1) has the form

$$
\begin{pmatrix} \sigma_{11} \\ \sigma_{22} \\ \sigma_{33} \\ \sigma_{23} \\ \sigma_{31} \\ \sigma_{12} \end{pmatrix} = \begin{pmatrix} c_{11} & c_{12} & c_{13} & c_{14} & c_{15} & c_{16} \\ c_{12} & c_{22} & c_{23} & c_{24} & c_{25} & c_{26} \\ c_{13} & c_{23} & c_{33} & c_{34} & c_{35} & c_{36} \\ c_{14} & c_{24} & c_{34} & c_{44} & c_{45} & c_{46} \\ c_{15} & c_{25} & c_{35} & c_{45} & c_{55} & c_{56} \\ c_{16} & c_{26} & c_{36} & c_{46} & c_{56} & c_{66} \end{pmatrix} \begin{pmatrix} e_{11} \\ e_{22} \\ e_{33} \\ 2e_{23} \\ 2e_{31} \\ 2e_{12} \end{pmatrix} \tag{2.2.6}
$$

which contains 21 independent elastic parameters. The relationship between subscripts and coordinate axes is described in Figure 2.2.1.

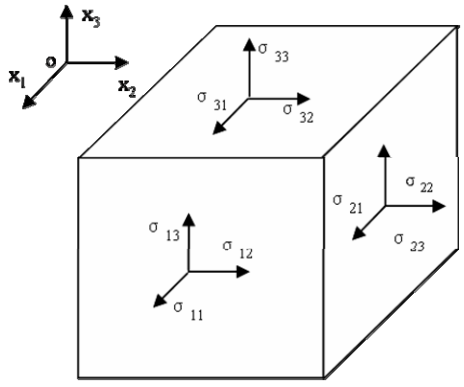

Figure 2.2.1: The relationship between subscripts and coordinate axes.

2.2.2 Seismic wave propagations in anisotropic media

Seismic wave equations

According to Newton's second law of motion, the wave equation within a continuum can be written as (Tsvankin, 2005, pp. 2)

$$\rho \frac{\partial^2 u_i}{\partial t^2} - \frac{\partial \sigma_{ij}}{\partial x_j} = f_i \qquad i, j = 1,2,3 \tag{2.2.7}$$

where ρ is the density, u_i is the i^{th} components of the displacement vector, σ_{ij} is the stress tensor component, f_i is the i^{th} external body force component imposed on the medium per unit volume, t is the time and x_j are the Cartesian coordinates. In equation (2.2.7), there is an implied summation over index j.

However, when studying seismic anisotropy, we usually assume the medium as being homogeneously anisotropic and the medium has no source of elastic energy. Under this assumption, the body force can be dropped and the wave equation becomes

$$\rho \frac{\partial^2 u_i}{\partial t^2} - \frac{\partial \sigma_{ij}}{\partial x_j} = 0 \qquad i, j = 1,2,3 \tag{2.2.8}$$

By combining Newton's second law of motion and generalized Hooke's law, the wave equation for linearly elastic, anisotropic and homogeneous media can be written as

$$\rho \frac{\partial^2 u_i}{\partial t^2} - c_{ijkl} \frac{\partial^2 u_k}{\partial x_j x_l} = 0 \tag{2.2.9}$$

Equation (2.2.9) relates particle displacements u_i to the stiffness matrix c_{ijkl} and is the base for seismic anisotropy analysis.

The most common trial solution for equation (2.2.9) is a plane wave, while other solutions can be constructed from the superposition of plane waves. The wave equation for the plane wave has the form (e.g. Tsvankin, 2005, pp. 3)

$$\begin{pmatrix} \Gamma_{11} - \rho V^2 & \Gamma_{12} & \Gamma_{13} \\ \Gamma_{21} & \Gamma_{22} - \rho V^2 & \Gamma_{23} \\ \Gamma_{31} & \Gamma_{32} & \Gamma_{33} - \rho V^2 \end{pmatrix} \begin{pmatrix} U_1 \\ U_2 \\ U_3 \end{pmatrix} = 0 \tag{2.2.10}$$

where Γ is the Christoffel matrix, which is determined by medium stiffness tensors and wave propagation directions

$$\Gamma_{ik} = c_{ijkl} n_j n_l \tag{2.2.11}$$

where Γ_{ik} is called Kelvin-Christoffel tensor and n_i is the direction cosine of propagation. A trial solution for plane wave is (Tsvankin, 2005, pp.3)

$$u_k = U_k e^{i\omega(n_j x_j / v - t)} \tag{2.2.12}$$

where U_k are the corresponding polarization components, ω is the angular frequency, v is the phase velocity, n_j are the components of the unit vector that is orthogonal to the plane wave front, x_j is the coordinate and t is the travel time.

In many publications, the Christoffel equation is expressed in a more compact form

$$\left(\Gamma_{ik} - \rho V^2 \delta_{ik}\right) U_k = 0 \tag{2.2.13}$$

where, i, k can be 1,2 or 3, V represents phase velocity, ρ represents density, δ_{ij} represents the Kronecker δ function with

$$\delta_{ik} = \begin{cases} 1 & for \quad i = k \\ 0 & for \quad i \neq k \end{cases} \tag{2.2.14}$$

The Christoffel equation describes a standard 3 x 3 eigenvalue (ρV^2) and eigenvector (U) problem for the symmetric matrix Γ. The three eigenvalues and three corresponding eigenvectors can be obtained by solving (e.g. Helbig, 1994)

$$\det\left(\Gamma_{ik} - \rho V^2 \delta_{ik}\right) = 0 . \tag{2.2.15}$$

The three solutions for ρV^2 give three phase velocities, representing the phase velocity of a compressional wave (P-wave) and two shear waves (S1-wave and S2-wave), whereas the three eigenvectors of the Christoffel matrix are the three corresponding polarization vectors. It means that when seismic waves propagate in a medium, there exist three body waves with mutually orthogonal polarization. In anisotropic media, the expressions 'quasi-compressional' wave (qP-wave), and 'quasi-shear' wave (qS1-wave and qS2-wave) are usually used for P-wave, S1-wave and S2-wave, because polarizations of body waves are not necessarily normal or parallel to the wave propagation directions (Crampin, 1989, pp. 765).

Phase and group velocities

The phase velocity is the velocity at which a point of constant wavelet phase travels in the direction normal to the wave surface while the group velocity (also called energy velocity or ray velocity) is the velocity at which a wave surface (group velocity surface) and wave energy travel in a given direction, which determines the direction and speed of energy propagation and is of primary importance in seismic travel time modelling and inversion methods. When seismic waves propagate in an isotropic non-attenuative medium, the group velocity and phase velocity coincide, but in generally anisotropic media, the group velocity is different from the phase velocity (Figure 2.2.2). The difference between the phase velocity vector and group velocity vector includes velocity dispersion with frequency and travel direction, etc., which is a feature of anisotropy.

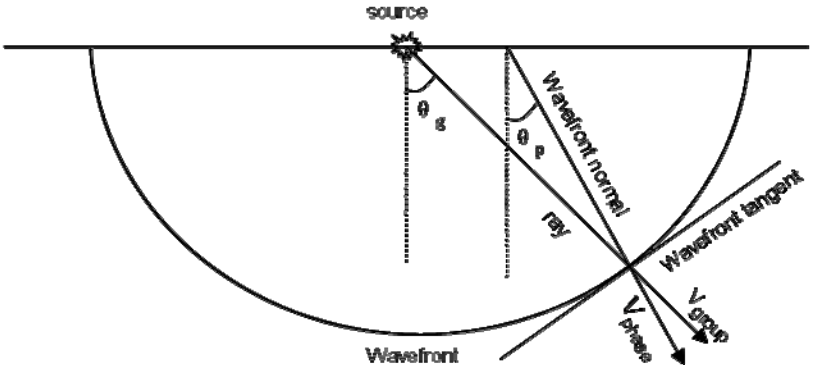

Figure 2.2.2: The relationship between group velocity V_{group} (ray velocity) vector and the phase velocity vector V_{phase} in an anisotropic medium. V_{group} is in the source-receiver direction while the V_{phase} direction is orthogonal to the wavefront. In general anisotropic media, group velocity is not the same as the phase velocity. In an isotropic non-attenuative medium, group velocity and phase velocity coincide.

Unlike the phase velocity which can be solved with the Christoffel equation, the group velocity depends on the corresponding phase velocities. The relationship between the group velocity and the phase velocity is given by equation (2.2.16) (Berryman, 1979)

$$V_{group} = grad^{K}(kV_{phase}) = \frac{\partial(kV_{phase})}{\partial k_1} i_1 + \frac{\partial(kV_{phase})}{\partial k_2} i_2 + \frac{\partial(kV_{phase})}{\partial k_3} i_3 \qquad (2.2.16)$$

where $K=(k_1, k_2, k_3)$ is the wave vector which is parallel to the phase velocity vector and has the magnitude of $k=\omega/V$ (ω is the angular frequency); i_1, i_2 and i_3 are the unit coordinate vectors. It can be further derived that the projection of the group velocity

vector in the phase velocity direction is equal to the phase velocity (Tsvankin, 2005, pp.7)

$$\left|V_{phase}\right| = \left(V_{group} \cdot \vec{n}\right) \tag{2.2.17}$$

Equation (2.2.17) indicates that the magnitude of the group velocity vector is always larger or equal to that of the corresponding phase velocity vector.

2.2.3 Classification of symmetry systems

Subsurface geological structures are often simplified with different symmetry systems to describe seismic anisotropy reflected in the distribution of the tensor matrix and from which the variation of the elastic response of seismic waves can be derived. For example, a fracture system with a preferential fracture alignment is often simplified as a hexagonal symmetry system because they have the same elastic tensor matrix.

The symmetry of a medium is reflected in the structure of the stiffness tensor c_{ijkl} and the number of independent constants, which determines the spatial pattern of velocities, polarizations and amplitudes of elastic waves travelling through the medium (Crampin, 1981). When described in a two-order stiffness matrix c_{ij} (equation 2.2.6), a general anisotropic medium needs 21 independent elastic constants to describe its elastic properties. However, the symmetry features of anisotropic media may reduce the number of independent elastic constants of the stiffness matrix.

Currently, there are eight physically realizable systems to describe anisotropic or crystalline symmetry systems, including Triclinic, Monoclinic, Orthorhombic, Trigonal, Tetragonal, Hexagonal, Cubic and Isotropic, with the number of independent elastic constants in the corresponding matrix being 21, 13, 9, 6, 6, 5, 3 and 2, respectively (e.g. Crampin, 1989, pp. 757-758). In terms of geophysical anisotropy, the earth model is often simplified as a Triclinic, Monoclinic, Orthorhombic, Hexagonal and isotropic models described below.

Triclinic model

The most general anisotropic medium is called triclinic model with three unequal axes intersecting at oblique angles. The stiffness matrix of a triclinic model has the following form with 21 independent elastic constants

$$C^{(TRI)} = \begin{pmatrix} c_{11} & c_{12} & c_{13} & c_{14} & c_{15} & c_{16} \\ c_{12} & c_{22} & c_{23} & c_{24} & c_{25} & c_{26} \\ c_{13} & c_{23} & c_{33} & c_{34} & c_{35} & c_{36} \\ c_{14} & c_{24} & c_{34} & c_{44} & c_{45} & c_{46} \\ c_{15} & c_{25} & c_{35} & c_{45} & c_{55} & c_{56} \\ c_{16} & c_{26} & c_{36} & c_{46} & c_{56} & c_{66} \end{pmatrix} \tag{2.2.18}$$

For a geophysical model, earth formations containing two non-orthogonal sets of non-vertically aligned fractures in finely layered strata can be regarded as a triclinic model. However, current seismic measurement technology is not sufficient to describe triclinic anisotropy.

Monoclinic model

A monoclinic model has three unequal crystal axes, two of which intersect obliquely and are perpendicular to the third axis. By taking the symmetry plane of a monoclinic medium to be orthogonal to the x_3-axis, the stiffness matrix for monoclinic medium has the form of (2.2.19) (e.g. Tsvankin, 2005, pp 9)

$$C^{(MON)} = \begin{pmatrix} c_{11} & c_{12} & c_{13} & 0 & 0 & c_{16} \\ c_{12} & c_{22} & c_{23} & 0 & 0 & c_{26} \\ c_{13} & c_{23} & c_{33} & 0 & 0 & c_{36} \\ 0 & 0 & 0 & c_{44} & c_{45} & 0 \\ 0 & 0 & 0 & c_{45} & c_{55} & 0 \\ c_{16} & c_{26} & c_{36} & 0 & 0 & c_{66} \end{pmatrix} \tag{2.2.19}$$

For a geophysical model, a monoclinic model can be used to represent the case where finely layered strata contain two non-orthogonal sets of vertically aligned fractures.

Though a monoclinic model has a single plane of mirror symmetry compared to a triclinic model and the matrix can be simplified into 13 independent elastic constants (Bakulin et al., 2000a, 2000b, 2000c), it is still difficult to use seismic data to describe monoclinic anisotropy.

Orthorhombic model

An orthorhombic model has three mutually orthogonal symmetry planes and contains 9 independent elastic constants. By taking each coordinate plane in Cartesian coordinate system (x_1, x_2 and x_3) as a plane of symmetry, the stiffness matrix for orthorhombic model can be simplified as (e.g. Tsvankin, 2005, pp. 10)

$$C^{(ORT)} = \begin{pmatrix} c_{11} & c_{12} & c_{13} & 0 & 0 & 0 \\ c_{12} & c_{22} & c_{23} & 0 & 0 & 0 \\ c_{13} & c_{23} & c_{33} & 0 & 0 & 0 \\ 0 & 0 & 0 & c_{44} & 0 & 0 \\ 0 & 0 & 0 & 0 & c_{55} & 0 \\ 0 & 0 & 0 & 0 & 0 & c_{66} \end{pmatrix} \tag{2.2.20}$$

For a geophysical model, the orthorhombic is used to describe finely layered horizontal sedimentary strata with vertically aligned fractures, which has the combined features of the Vertically Transverse Isotropy (VTI) model and the Horizontally Transverse Isotropy (HTI) model (e.g. Bush and Crampin, 1991; Wild and Crampin, 1991), or a fracture system with two orthogonal sets of aligned fractures (Bakulin et al., 2000a, 2000b, 2000c).

Hexagonal model

The hexagonal symmetry model is often referred as the Transverse Isotropy (TI) model which has a single axis of rotational symmetry and can be completely specified with 5 independent elastic constants. The two most discussed TI models in seismic anisotropy analysis are VTI (Vertically Transverse Isotropy) models and HTI (Horizontally Transverse Isotropy) models. Anisotropy studies based on VTI and HTI models are much simpler than those that are based on other anisotropic models, because the properties of seismic waves are determined by the angle between the direction of wave propagation and the symmetry axis. Another often mentioned TI model is the TTI (Tilt Transverse Isotropy) model, which means there is a tilted symmetry axis, with respect to the symmetry plane, which geologically represents the case where thin layers dip due to tectonic process, or a non-vertically aligned fracture system exists.

VTI model

A VTI model is a TI model with a vertical axis of rotational symmetry. By taking x_3 as the axis of the symmetry, the stiffness matrix can be expressed as (e.g. Markov et al., 1998, pp. 21)

$$C^{(VTI)} = \begin{pmatrix} c_{11} & c_{11}-2c_{66} & c_{13} & 0 & 0 & 0 \\ c_{11}-2c_{66} & c_{11} & c_{13} & 0 & 0 & 0 \\ c_{13} & c_{13} & c_{33} & 0 & 0 & 0 \\ 0 & 0 & 0 & c_{44} & 0 & 0 \\ 0 & 0 & 0 & 0 & c_{44} & 0 \\ 0 & 0 & 0 & 0 & 0 & c_{66} \end{pmatrix} \tag{2.2.21}$$

which has the same non-zero elements as that for orthorhombic media, except that only five independent elastic constants are needed to describe a VTI model.

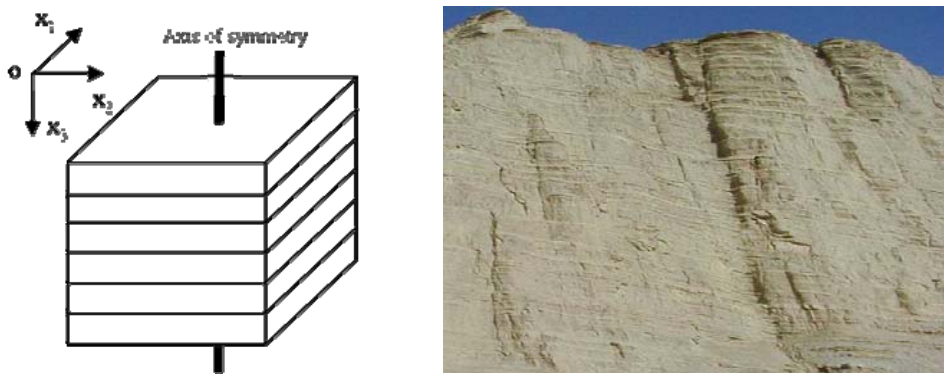

(a) VTI model (b) Outcrops from Tarim Basin, China

Figure 2.2.3: VTI model and outcrop example.

For a geophysical model, finely layered horizontal sedimentary strata with a single layer thickness scale much smaller than seismic wave length (e.g. Backus, 1962; Thomsen, 1986; Helbig, 1994), or a preferential alignment of minerals and grains during deposition such as in shales, where the anisotropy is caused by the interactions of reflections and transmissions through thin isotropic layers (e.g. White et al., 1983), can be regarded as a VTI model. When seismic waves travel in VTI media, the velocity difference between vertical and horizontal directions can be large enough to cause observable VTI seismic anisotropy.

VTI anisotropy is also referred to as polar anisotropy because seismic attributes vary with the polar angle. The treatment of VTI seismic anisotropy in seismic processing is discussed more extensively in Chapter 5.

HTI anisotropy

A HTI model is a TI medium with a horizontal axis of rotational symmetry, which is another special case of the TI model and needs five independent elastic constants to describe the elastic properties. By rotating a VTI medium 90^o clockwise about x_2 axis using a Bond transformation (Winterstein, 1990, pp. 1075) to make x_1 as the axis of symmetry, the stiffness matrix of a HTI model takes the following form (Li, 1997)

$$C^{(HTI)} = \begin{pmatrix} c_{11} & c_{13} & c_{13} & 0 & 0 & 0 \\ c_{13} & c_{33} & c_{33}-2c_{44} & 0 & 0 & 0 \\ c_{13} & c_{33}-2c_{44} & c_{33} & 0 & 0 & 0 \\ 0 & 0 & 0 & c_{44} & 0 & 0 \\ 0 & 0 & 0 & 0 & c_{66} & 0 \\ 0 & 0 & 0 & 0 & 0 & c_{66} \end{pmatrix} \tag{2.2.21}$$

where there are nine non-zero elements in the matrix from five independent elastic constants, which is similar to the case for a VTI medium.

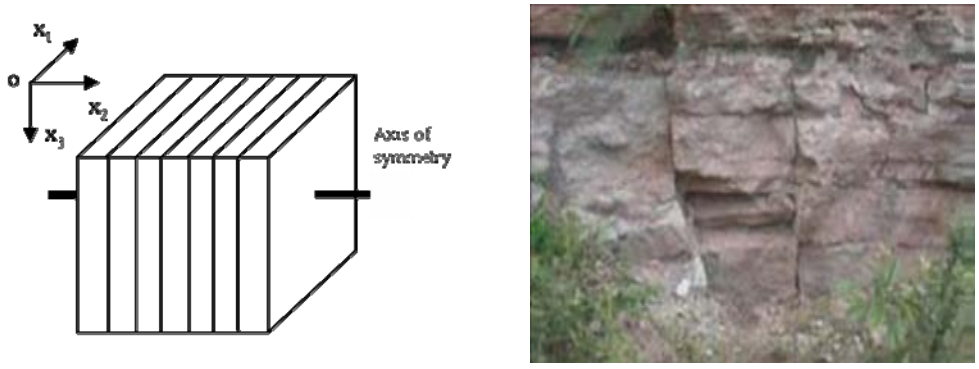

(a) HTI model (b) A field HTI case

Figure 2.2.4: The HTI model and outcrop example.

For a geophysical model, a HTI model is often used to represent the strata containing vertically aligned fractures or cracks (Figure 2.2.4), where the strike of open vertical fractures or cracks at depth is normally in the direction of maximum horizontal compressive stress (e.g. Crampin, 1987; Lorenze et al., 1996).

HTI anisotropy is usually referred to as 'azimuthal anisotropy' because the anisotropy attributes vary with azimuth. Unlike VTI anisotropy which is predominantly due to rock layers, HTI anisotropy is usually very sensitive to stress because it is usually due to aligned fractures. A detailed discussion of the analysis of HTI anisotropy with multi-component seismic data is in Chapter 7.

Isotropic model

When a medium is referred to as isotropic, it has the highest possible symmetry because any plane of the medium can be regarded as a symmetry plane and seismic wave propagation is equivalent in all directions. Isotropy is the most special case of anisotropic models.

For an isotropic model, there are only two independent elastic constants in the tensor matrix and any axis can be regarded as the direction of the symmetry axis, and c_{ijkl} is given by

$$c_{ijkl}^{(iso)} = \lambda\delta_{ij}\delta_{kl} + \mu(\delta_{ik}\delta_{jl} + \delta_{il}\delta_{jk}) \tag{2.2.22}$$

The stiffness matrix in two-index notation takes the following form as (2.2.23) (e.g. Tsvankin, 2005, pp. 13)

$$C^{(iso)} = \begin{pmatrix} \lambda+2\mu & \lambda & \lambda & 0 & 0 & 0 \\ \lambda & \lambda+2\mu & \lambda & 0 & 0 & 0 \\ \lambda & \lambda & \lambda+2\mu & 0 & 0 & 0 \\ 0 & 0 & 0 & \mu & 0 & 0 \\ 0 & 0 & 0 & 0 & \mu & 0 \\ 0 & 0 & 0 & 0 & 0 & \mu \end{pmatrix} \tag{2.2.23}$$

where λ and μ are Lame's constants which determine the velocity of P-wave and S-wave by

$$V_P = \sqrt{\frac{\lambda+2\mu}{\rho}} \quad ; \qquad V_S = \sqrt{\frac{\mu}{\rho}} \tag{2.2.24}$$

Of the geophysical models discussed above, the isotropic, hexagonal, orthorhombic and monoclinic symmetry systems are the four most used systems in analyzing subsurface symmetry systems and are particularly important in seismic anisotropy analysis. I mainly

focus on using multi-component seismic data to study the seismic anisotropy coming from hexagonal symmetry systems, including anisotropic imaging analysis based on VTI models, as well as fracture characterization and fluid property analysis based on HTI models, because these are most relevant to the characterization of sedimentary layering and aligned fractures.

2.2.4 Equivalent medium theory

To simplify the analyses of fracture induced seismic anisotropy, equivalent medium theory is widely used to represent a fractured medium in studying the elastic constants (Hudson, 1981, 1990; Hudson et al., 1996; Liu and Hudson, et al., 2000; Schoenberg, 1994, 1998; Schoenberg and Sayers, 1998). Based on Eshelby's derivation of the elastic responses of an ellipsoidal inclusion embedded in an infinite elastic solid (Eshelby, 1957, 1959), a number of equivalent medium models for rocks containing isolated fractures have been developed (e.g. O'Connell and Budiansky, 1974; Berryman, 1980; Hudson, 1981; Nishizawa, 1982). According to Crampin and Peacock's definition (2005), equivalent media are homogeneous solids with the same elastic properties as cracked rocks, which can be used as an approximation in mathematical modelling when cracks are much smaller than the seismic wavelength. The effects of vertically aligned fractures in isotropic background medium can be expressed with the effective compliance tensor of the whole medium which is the sum of the compliance tensor of the pure background medium (without fracture) and the compliance tensor of aligned fractures (Schoenberg and Sayers, 1995).

The Hudson model (Hudson, 1981) is a widely used model in the study of seismic anisotropy, which describes high frequency seismic response with no fluid movement by assuming zero matrix permeability, and the seismic wavelength is much longer than the crack size. Its derivation is based on the analysis of the mean wave field in an elastic solid medium containing penny-shaped cracks using scattering theory. The effective elastic tensor C is given by

$$C = C^{(0)} + bC^{(1)} + b^2C^{(2)} \tag{2.2.25}$$

where $C^{(0)}$ is the isotropic stiffness tensor of the background medium. $C^{(1)}$ is the first order correction due to the presence of cracks and thus is a function of the elastic

parameters of a un-cracked solid medium and the response of the isolated, cracks to normal and shear traction, and depends on the crack aspect ratio and the elastic moduli of the material filling the cracks. $C^{(2)}$ is the second order correction caused by crack-crack interaction. b is the crack density

$$b = N \cdot a^3 \tag{2.2.26}$$

where N is the number of cracks per unit volume and α is the crack radius.

In the interpretation of seismic anisotropy, the Hudson model is used to derive crack density from the measured magnitude of azimuthal anisotropy. However, when equation (2.2.26) is used to calculate the fracture density, a material with few large fractures may have the same fracture density as a material with many small fractures.

Another commonly used equivalent medium theory for fracture models is the linear slip model (Schoenberg, 1980), where fractures are modeled as planes of weakness with linear-slip boundary conditions. The stiffness tensor of the effective medium is obtained by adding excess compliance s_f for the fractures to the background compliance s_0 of the matrix rocks:

$$s = s_0 + s_f \quad . \tag{2.2.27}$$

The advantage of the expression (2.2.27) is that the compliance of each individual fracture set in the model can simply be added to obtain the overall compliance. The compliance tensor s_f contains only two independent elements: the normal fracture compliance Z_N and tangential fracture compliance Z_T. Since the effective elastic tensor of Schenoberg (1980) model is equivalent in form to the effective elastic tensor of the Hudson model (1981), Z_N and Z_T can equally be expressed in terms of micro-structural parameters (Liu ad Hudson, et al., 2000).

The equation (2.2.27) is very convenient in calculating the elastic constants of the media with lower symmetry than hexagonal, such as materials containing more than one set of aligned fractures (Schoenberg and Douma, 1988; Sayers and Kachanov, 1991; Schoenberg and Sayers, 1995; Schoenberg and Helbig, 1997; Sayers, 2002, etc.).

Equivalent medium theories for media containing aligned fractures establish the links between seismic anisotropy and fracture properties so that the fracture information may be derived from the anisotropic measurements on seismic data.

2.2.5 Thomsen's parameters for weak anisotropy

When anisotropy is less than 20 percent, it can be regarded as weak anisotropy and the equations governing anisotropy can be considerably simplified and are much easier to grasp intuitively (Thomsen, 1986). To address the anisotropy issues, Thomsen suggested the following convenient notation for VTI media with weak anisotropy (Thomsen, 1986, pp. 1956-1957)

$$\alpha = \sqrt{c_{33}/\rho} \quad ; \qquad \beta = \sqrt{c_{44}/\rho} \quad ; \qquad \varepsilon = \frac{c_{11} - c_{33}}{2c_{33}}$$

$$\gamma = \frac{c_{66} - c_{44}}{2c_{44}} \quad ; \qquad \delta = \frac{(c_{13} + c_{44})^2 - (c_{33} - c_{44})^2}{2c_{33}(c_{33} - c_{44})} \tag{2.2.28}$$

where, α and β are the P-wave and S-wave velocities propagating along the symmetry axis, respectively, ε and γ denote the magnitude of P-wave anisotropy and S-wave anisotropy, respectively, δ is related to wave-front ellipticity. For the media with weak anisotropy, $\varepsilon<<1$, $\delta<<1$, $\gamma<<1$. For isotropic media, ε, δ and γ are zero; if ε equals δ, the media have elliptical anisotropy features.

To geophysicists, most sedimentary rocks are weakly anisotropic. For example, most marine sediments show weak anisotropy and the laboratory measurements of shale samples reveal anisotropy of $\varepsilon<0.2$, $\delta<0.2$, $\gamma<0.2$ (Wang, 2002).

In terms of Thomsen's parameters for VTI media, the phase velocities of P-wave, SV-wave and SH-wave, which represent pseudo longitudinal wave, pseudo shear wave polarized normal to the pure shear wave and pure shear wave with no component of polarization in the vertical (x_3) direction, respectively, can be expressed as (e.g. Marko et al., 1998, pp. 25)

$$V_P(\theta) \approx V_P^V(\theta)(1 + \delta \sin^2\theta \cos^2\theta + \varepsilon \sin^4\theta)$$

$$V_{SV}(\theta) \approx V_S^V(\theta)(1+\frac{c_{33}}{c_{44}}(\varepsilon-\delta)\sin^2\theta\cos^2\theta) \tag{2.2.29}$$

$$V_{SH}(\theta) \approx V_S^V(\theta)(1+\gamma\sin^2\theta))$$

where θ is the angle between the wave-front normal and the symmetry axis (x_3 in Figure 2.3.5). The P-wave anisotropy parameter ε can be described through the fractional difference of the P-wave velocities between vertical and horizontal directions, and S-wave anisotropy parameter γ can be described through the fractional difference of the S-wave velocities in the vertical and horizontal directions

$$\varepsilon \approx \frac{V_P^H - V_P^V}{V_P^V} = \frac{V_P(90^0) - V_P(0^0)}{V_P(0^0)}$$

$$\gamma \approx \frac{V_{SH}^H - V_{SH}^V}{V_{SH}^V} = \frac{V_{SH}(90^0) - V_{SV}(90^0)}{V_{SV}(90^0)} = \frac{V_{SH}(90^0) - V_{SH}(0^0)}{V_{SH}(0^0)} \tag{2.2.30}$$

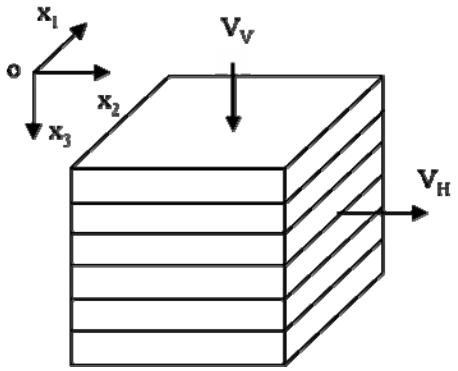

Figure 2.2.5: Vertical and horizontal velocity in a VTI medium.

Similarly, through Bond transformation (Winterstein, 1990, pp. 1075) to make x_1 instead of x_3 as the axis of the symmetry, Thomsen anisotropy parameters for HTI media can be defined as (Li, 1997, 1998b)

$$\varepsilon = \frac{c_{33} - c_{11}}{2c_{11}} \quad ; \quad \delta = \frac{2c_{66} + c_{13} - c_{11}}{c_{11}} \quad ; \quad \gamma = \frac{c_{44} - c_{66}}{2c_{66}} \tag{2.2.31}$$

The equation (2.2.31) is very useful in azimuthal anisotropy analysis for fracture characterization.

2.3 Fracture characterization with seismic anisotropy

Many studies have tried to predict effective properties of rocks containing cracks. For example, Hudson (1981) gives the basic theory for anisotropic elastic constants for both velocity variations and attenuation in media with parallel cracks. Sayers and Kachanov (1995) as well as Schoenberg and Sayers (1995) present methods for calculating the effective elastic constants for cracked and fractured rocks by assuming a linear relationship governed by fracture compliance, between displacement discontinuity across fractures and the applied tractions. Liu and Hudson et al. (2000) study the equivalent medium representation of three fractured rock models and give the analytic expressions for the fracture compliances for the three kinds of models. They show that it is possible to relate the measured compliance or stiffness directly to the statistics of the micro-structural details of fractures, and that the ratio of normal to shear fracture compliance is a good indicator for the properties of the fracture infill. Grechka and Tsvankin (1998) showed that the azimuthal dependence of NMO velocities (e.g., P-P and S-S) is an ellipse under the same general assumptions that result in the familiar hyperbolic form of reflection moveout. In addition, azimuthal amplitudes of the reflected P-wave have also been found to be approximately quadratic in sines and cosines of the azimuth as long as offsets do not exceed the reflector depth (e.g. Rüger, 1997). Bakulin et al. (2000a, 2000b, 2000c) devised a suite of techniques for quantitative fracture characterization.

In this thesis, the seismic anisotropy analyses for fracture characterization are based on a HTI model representing a set of vertically aligned fractures in an isotropic model. Using a HTI model to represent subsurface fractured rocks is currently the most effective and practical way in the interpretation of seismic anisotropy for fractured reservoirs. Basically there are two kinds of methods to carry out seismic anisotropy analysis for fracture interpretation, these are azimuthal seismic attribute analysis and shear wave splitting analysis.

2.3.1 Azimuthal attribute analysis for fracture characterisation

When the P-wave travels in a vertically aligned fractured medium, attributes such as travel time, NMO velocities and amplitudes on the P-wave data may show variations

with azimuth and can be used to derive fracture information. There are many studies of using azimuthal seismic amplitude analysis methods for the detection of fractures with preferential alignment (e.g., Lynn et al., 1999; Gray and Head, 2000; Liu, 2003; Hall and Kendall, 2003).

The normal moveout in azimuthally anisotropic media describes an ellipse in the horizontal plane to the same approximation that it is hyperbolic in time (Grechka and Tsvankin, 1998)

$$\frac{1}{v_{NMO}^2(\phi)} = \left(\frac{\cos(\phi-\phi_0)}{v_{\max}}\right)^2 + \left(\frac{\sin(\phi-\phi_0}{v_{\min}}\right)^2 \tag{2.3.1}$$

where, ϕ is the azimuthal angle, v_{max} and v_{min} are the maximum and minimum NMO velocities, ϕ_0 is the azimuth of the major axis of the ellipse. For HTI media, ϕ_0 denotes the fracture strike. The above equation can equally be written in terms of travel-time t

$$t^2(\phi) = t_{\max}^2 \cos^2(\phi-\phi_0+\pi/2) + t_{\min}^2 \sin(\phi-\phi_0+\pi/2) \tag{2.3.2}$$

For weak anisotropy, it can be approximated to the following form

$$t(\phi) = C_1 + C_2 \cos[2(\phi-\phi_0+\pi/2)] \tag{2.3.3}$$

where

$$C_1 = \frac{1}{2}(t_{\max}+t_{\min}) \;\; ; \qquad C_2 = \frac{1}{2}(t_{\max}-t_{\min})$$

The equation (2.3.3) provides a number of tools to derive fracture information from azimuthal Normal Move-Out (NMO) velocities and travel-time on seismic data with wide azimuth coverage.

The seismic amplitude is another attribute which can be used to perform azimuthal analysis for fracture information. It is based on the fact that the seismic reflectivity not only varies with the angle of incidence but also varies with azimuth in a HTI medium. By retaining only the second order terms for the angle of incidence θ, the P-wave reflection coefficient R_{pp} can be approximated to the form (e.g. Ruger and Tsvankin, 1997, Ikelle, 1997, Thomsen, 2002)

$$R_{pp}(\theta,\phi) = R_0 + G(\phi)\sin^2\theta \tag{2.3.4}$$

where R_0 is the reflection coefficient at normal incidence or Amplitude Variation with Offset (AVO) intercept, and G is the AVO gradient

$$G(\phi) = A + B\cos[2(\phi - \phi_0)] \tag{2.3.5}$$

where A and B are two constants. For a fixed angle of incidence θ_0, the relationship between P-wave reflection coefficient R_{pp} and azimuth ϕ can be simplified as

$$R_{PP}(\theta_0,\phi) = C + D\cos[2(\phi - \phi_0)] \tag{2.3.6}$$

where C and D are two constants. The equation (2.3.5) and equation (2.3.6) reveal that, at a fixed angle of incidence, both AVO gradients and reflection coefficients vary with azimuth in a $\cos(2\phi)$ relationship (or elliptical relation), which means the symmetry direction and anisotropic magnitude of a HTI medium can be interpreted from seismic amplitudes. The overall seismic attributes with azimuth on near offset traces can be unified with equation (2.3.7)

$$F(\theta,\phi) = A + B(\theta)\cos 2\phi \tag{2.3.7}$$

where, $F(\theta,\phi)$ can be regarded as the reflection coefficient, the inverse of the square of NMO velocity, travel time or interval travel time. $B(\theta)$ is a azimuth independent parameter.

In the practice of using azimuthal seismic attributes for fracture characterization, the following five steps are normally performed:

1. Choose an appropriate offset for a fixed θ;
2. Calculate $F(\theta,\phi)$ in every azimuth;
3. Carry out the elliptical attribute fitting, interpret the direction of the major axis of the fitted ellipse;
4. Calculate the major to minor axis ratio of the ellipse;
5. Plot and interpret seismic anisotropy.

In real data analysis, there are many factors that may cause deterioration to seismic attributes, such as acquisition geometry, noise etc., so that how to obtain reliable results can still remain a critical issue.

2.3.2 Shear-waves splitting for fracture characterisation

Shear wave splitting in anisotropic media

In the subsurface fracture system, maximum stress direction normally coincides with fracture strike and minimum stress direction is perpendicular to fracture strike. When a shear wave enters an anisotropic stress field, it splits into two quasi-shear waves, with one polarizing in maximum stress direction and another in minimum stress direction (Crampin, S. 2005, pp. 61). Shear-wave splitting is analogous to the birefringence of light travelling in a crystal. Figure 2.3.1 shows the polarization of fast and slow shear waves in a HTI medium. However, stress-aligned anisotropic symmetry is close, but not usually identical, to hexagonal symmetry (transverse isotropy) with a horizontal axis of symmetry (HTI-anisotropy).

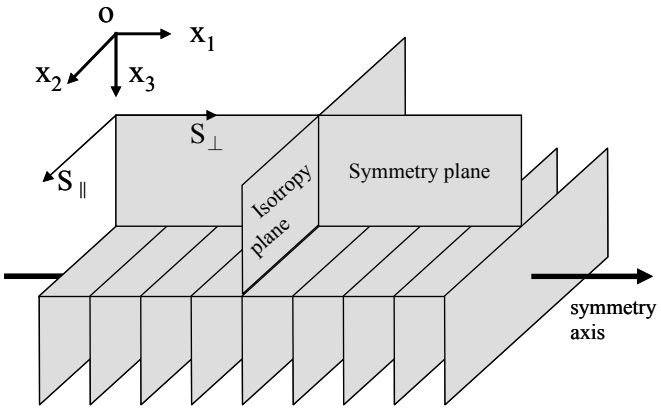

Figure 2.3.1: Polarizations of fast and slow shear waves in a HTI medium. When a shear wave enters an anisotropic medium, it splits into two shear waves in a symmetry plane, one has polarizations parallel to the symmetry plane(S||), another has the polarizations normal to the symmetry plane (S⊥).

The fracture properties can be obtained by studying the rock stress distributions through shear-wave splitting analysis. The polarization of the faster shear wave is parallel to fracture strikes while the polarization of the slow shear wave is normal to the fracture strike, and the magnitude of time-delay between fast and slow shear waves can be used to measure fracture density along the ray paths.

Shear wave splitting on multi-component seismic data

In geophysical exploration, multi-component seismic data provide the way to observe the phenomena of shear-wave splitting. If the sub-surface media are flat and isotropic, converted P- to shear-waves are contained on the radial component (R-component) data rather than in the transverse component (T-component) data. The R and T-component data are usually calculated with X and Y-component data recorded in the field data acquisition. If vertically aligned fractures exist and the angle between the fracture strike and the direction of seismic wave propagation is between 0^o and 90^o, the converted shear-wave will split into a fast shear-wave and a slow shear-wave with the fast shear-wave polarized parallel to, and the slow shear-wave perpendicular to, the strike of the fractures (Figure 2.3.2).

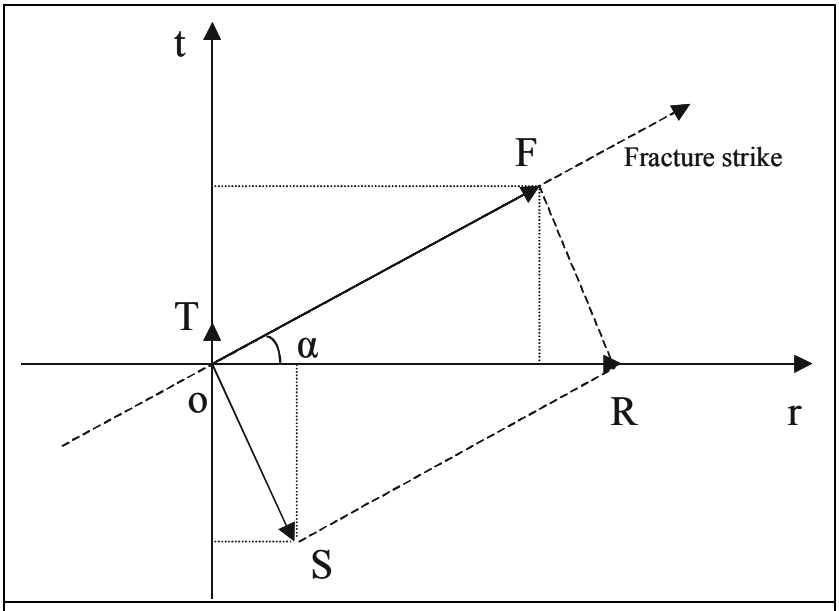

Figure 2.3.2: The relationship between Radial/Transverse components and Fast/Slow components. r-axis and t-axis denote radial and transverse direction, respectively; F and S represent the polarizations of fast and slow shear waves, respectively. α is the angle between the fracture strike and the radial component.

If an incident shear-wave travels along the **r**-axis, shear wave splitting will occur with the relationship of amplitudes between fast and slow shear-waves following equation (2.3.8) and equation (2.3.9)

$$\begin{cases} F(t+t_1) = S_i(t)\cos\alpha \\ S(t+t_2) = S_i(t)\sin\alpha \end{cases} \quad (2.3.8)$$

$$\tan\alpha = S(t+t_1) \Big/ F(t+t_2) \quad (2.3.9)$$

where, S_i denotes the amplitudes of the incident shear-wave which polarize along the r-axis; t_1 and t_2 represent the travel time of fast and slow shear waves, respectively. The amplitudes of radial and transverse component along ***r-*** and ***t-***axes can be expressed as equation (2.3.10)

$$\begin{cases} R_f(t) = F(t)\cos\alpha \\ T_f(t) = F(t)\sin\alpha \\ R_s(t) = S(t)\sin\alpha \\ T_s(t) = -S(t)\cos\alpha \end{cases} \quad (2.3.10)$$

and the amplitudes of the radial and transverse components can be expressed in terms of the amplitudes of the fast and slow shear-waves

$$\begin{cases} R(t) = F(t)\cos\alpha + S(t)\sin\alpha \\ T(t) = F(t)\sin\alpha - S(t)\cos\alpha \end{cases} \quad (2.3.11)$$

Which means that, if $\alpha = 0$, then $R(t) = F(t-t_1)$, $T(t) = 0$, only the fast shear-wave can be observed. If $\alpha = 90^o$, then, $R(t) = 0$, $T(t) = S(t-t_2)$, only the slow shear-wave can be observed. When α is between 0 and 90^o, both the fast and slow shear-waves can be observed. Equation (2.3.11) can be written in the form of equation (2.3.12) with amplitudes of the fast and slow shear waves as functions of the unknown angle α

$$\begin{cases} F(t) = R(t)\cos\alpha + T(t)\sin\alpha \\ S(t) = R(t)\sin\alpha - T(t)\cos\alpha \end{cases} \quad (2.3.12)$$

If the variable x is used to replace α, equation (2.3.12) becomes

$$\begin{cases} F'(t,x) = R(t)\cos(x) + T(t)\sin(x) \\ S'(t,x) = R(t)\sin(x) - T(t)\cos(x) \end{cases} \quad (2.3.13)$$

By taking equation (2.3.11) into account, we can transform equation (2.3.13) into

$$\begin{cases} F'(t,x) = F(t)\cos(x-\alpha) - S(t)\sin(x-\alpha) \\ S'(t,x) = F(t)\sin(x-\alpha) + S(t)\cos(x-\alpha) \end{cases} \quad (2.3.14)$$

If x is equal to α, the fast and slow shear waves will be separated completely. The angle between the **r**-direction and the fracture strike (**F**-direction) has the relationship

$$\tan\alpha = S'(t+t_1,\alpha) \Big/ F'(t+t_2,\alpha) \quad (2.3.15)$$

In practice, we can calculate the ratio of the fast to slow shear-waves with respect to every α and obtain the desired value of α according to equation (2.3.15).

2.4 Anisotropy from fluid saturation in a HTI medium

Effects of wave-induced fluid motion in an isotropic porous rock have been studied for many years; this is called fluid saturation analysis. Mukerji and Mavko (1994) and Thomsen (1995) find that the exchange of fluid between fractures or cracks and equant pores in the surrounding matrix rocks can have a strong influence on the predicted anisotropy of the rocks. Thomsen (1995) developed a model where fluids move between aligned fractures and equant pores in the matrix so that pressure gradients can be equalized in fracture-pore space and found his model agrees more with the laboratory measurements of Rathore et al. (1995) on samples containing aligned cracks in a porous matrix than the isolated crack model of Hudson (1981).

Frequency dependent anisotropy

Fluid permeability and saturation in fractures has been widely studied recently (Hudson et al., 1996; Tod, 2001; Chapman, 2003). When the fluid in a fractured media is allowed to move, the seismic wave induced pressure gradients will force fluid to move to reduce pressure gradients so as to reach a new pressure equivalence. However, the time needed for pressure relaxation is dependent on the mobility of the fluid, which is associated with the properties of fractures, pores and fluids. If fluid pressure relaxation takes much longer time than that given by the wave period, the un-relaxed state represents the high frequency limit, while if fluid pressure gradients throughout the pore space have sufficiently equilibrated within the time frame given by the wave period, the state is called the low frequency limit. Thomsen (1995) proposed a fracture model allowing

limited matrix permeability which can be used to simulate the low frequency seismic response. The state between high and low frequency limits is called the transition frequency band and the model representing such a case is called the squirt flow model (Mavko and Jizba, 1991) and the seismic anisotropy behaviour becomes frequency-dependent, which can be used to infer fracture and fluid properties. Chapman and Maultzsch et al (2003) takes the factors, such as fracture size, density and fluid viscosity influences fluid permeability, etc., into account to study frequency dependent seismic anisotropy.

Frequency dependent seismic anisotropy bridges the Hudson model and Thomsen model (Maultzsch and Chapman et al., 2003). The traditional equivalent medium theories for fractured rocks can be regarded as representing either the high or low frequency limits and the overall elastic property of the fractured medium is insensitive to the property of the fluid in the fractures.

Dispersion and attenuation

Many observations reveal that attenuation is larger in fluid-saturated rocks than in dry rocks, and the attenuation rate increases with the decrease of crack density of microcracks, which demonstrated fluid flow is a very important factor for dispersion and attenuation (e.g. Gardner et al., 1964; Toksöz et al,. 1979; Johnston and Toksöz, 1980; Johnson, 1981; Spencer, 1981; Winker, 1986). Though many studies suggest that characteristic frequencies for squirt flow are within the sonic and ultrasonic range (e.g. Nur and Winkler, 1980; Sams et al., 1997) while seismic frequency is beyond the low frequency limit, some observations on seismic data show the dispersive effects and attenuation associated with anisotropy and fractures (e.g. Liu et al., 1993; Horne and MacBeth, 1997). Kolk et al. (2001) analysed a 3D seismic data on a fractured carbonate reservoir and found increased shear-wave splitting together with attenuation of higher frequencies in a region that coincided with the gas-oil contact.

Dispersive equivalent medium theory

Many models have been developed to study the fluid motion in aligned fractured rocks and predict elastic constants as a function of frequency (e.g. Hudson et al., 1996; Kolk et al., 2001). Hudson et al. (1996) studied the flow between interconnected cracks and the

flow between cracks and smaller equant pores and formed the equant porosity model. The expressions for the stiffness constants are of similar form as in the earlier isolated crack model of Hudson (1981), except that the response of the crack to normal traction entering the first-order corrections is frequent-dependent. Theoretical predictions of the models were studied by Pointer et al. (2000). The equant porosity model predicts significant attenuation anisotropy at seismic frequencies for a range of rock properties commonly encountered in sedimentary rock (Pointer et al., 2000, Maultzsch and Horne et al., 2003). A further equivalent medium theory describing velocity dispersion is the BOSK model (Kolk et al., 2001), however, the actual flow mechanism leading to dispersion in the BOSK model is not clear (Hudson and Crampin, 2003).

Chapman (2003) establishes the poroelastic equivalent medium model for rocks with a lattice configuration of spherical pores, randomly oriented ellipsoidal micro-cracks and aligned ellipsoidal fractures.The pores and micro-cracks are at grain size scale. The fracture sizes are in meso-scale, which are much bigger than crack sizes but smaller than the wavelength. The aligned fractures give the model transversely isotropic features (hexagonal symmetry). Compared to the Hudson equant porosity model (Hudson et al., 1996) and the BOSK model (Kolk et al., 2001), the Chapman model (Chapman, 2003) has the advantage of taking account of the mechanical effect of the porosity, describing the squirt flow process explicitly by considering two scales of pore space heterogeneity, and that it is correct in its frequency limits.

When wave induced pressure gradients exist, the fluid in the model will be driven to move between adjacent voids to reach new stress equilibrium. The pressure gradients can be described with equation (2.4.1) (e.g. Chapman and Maultzsch et al., 2003, pp. 370)

$$\partial_t m_a = \frac{\rho_0 \kappa \varsigma_g}{\eta}\left(p_a - p_b\right) \tag{2.4.1}$$

where m_a is the fluid mass in element α, ρ_0 is the fluid density, κ is the permeability, ς_g is the pore size, η is the fluid viscosity, and p_a and p_b are the pressures in elements a and b.

In Chapman's model (Chapman, 2003), each element is assumed to be connected to six elements, and the resulting flow can be added linearly. Because the size of fractures is

larger than the micro-cracks and pores, it has more adjacent voids for exchange of fluid. To ensure that there is some spacing between the fractures, it is assumed that each pore or micro-crack is connected to at most one fracture, and that fractures are not connected to each other. It requires that the number of micro-cracks and pores must vastly exceed the number of fractures.

Based on the equation (2.4.1), Chapman and Maultzsch et al. (2003) derives the expressions for the expected mass flow out of the individual fracture, micro-crack and pore in terms of expected pressure gradients with the mass in each element of pore space is expressed as a function of inclusion pressure and applied stress. The effective elastic constants are calculated using an interaction energy approach (Eshelby, 1957) for the material with embedded inclusions where stress and strain inside the inclusions are calculated from the derived time dependent pressures. The detailed equations for the calculation of the elastic constants are given explicitly (Chapman and Maultzsch et al., 2003, pp. 370-375).

The effective stiffness tensor of the model is constituted by

$$C = C^{(0)} - \Phi_p C^{(1)} - \varphi_c C^{(2)} - \varphi_f C^{(3)} \tag{2.4.2}$$

where $C^{(0)}$ is the stiffness tensor of the isotropic rock matrix, $C^{(1)}$, $C^{(2)}$ and $C^{(3)}$ are the contributions from pores, micro-cracks and fractures, respectively, multiplied by the porosity Φ_p, the crack density φ_c and fracture density φ_f . The $C^{(1)}$, $C^{(2)}$ and $C^{(3)}$ are combined effects of the Lamé constants, fluid and fracture properties, frequency and relaxation time associated with the squirt flow.

Fluid flow between micro-cracks and pores is associated with the traditional squirt-flow frequency (Murphy, 1985; Winkler, 1986; Lucet and Zinszner, 1992; Sothcott et al., 2000)

$$f_m^c = 1/\tau_m \tag{2.4.3}$$

$$\tau_m = \frac{c_v \eta (1 + K_c)}{\sigma_c \kappa \varsigma_p c_l} \tag{2.4.4}$$

where c_v is the volume of an individual crack, η is the fluid viscosity, σ_c is the critical stress, κ is the permeability, ς_p is the pore size and c_1 is the number of connections to other voids. σ_c and K_c are defined by

$$\sigma_c = \frac{\pi \mu\, r}{2(1-v)} \tag{2.4.5}$$

$$K_c = \frac{\sigma_c}{k_f} \tag{2.4.6}$$

where r is the aspect ratio of the cracks, v is Possion's ratio of the rock matrix and k_f is the fluid bulk modulus.

The flow in and out of fractures is characterized by a lower frequency or larger time scale constant τ_f, which depends on the size of the fractures. The two time scale parameters have the following relation

$$\tau_f = \frac{a_f}{\varsigma_p}\tau_m \tag{2.4.7}$$

where a_f is the fracture radius, ς_p is the pore size. The larger relaxation time t_f (or its quivalent characterization frequency) plays an essential role in velocity dispersion and attenuation in seismic frequency range, which means that the anisotropy is frequency dependent.

2.5 Summary

Estimation of fracture-induced seismic anisotropy can be used to infer fracture direction and density. The equivalent medium theory provides a theoretical basis for using seismic methods to detect sub-surface fracture systems which gives rise to azimuthal anisotropy to seismic wave propagation. According to the equivalent medium theories, seismic attributes, such as amplitudes and travel-time, are azimuthally dependent and show elliptical distribution with azimuth. The role of seismic anisotropy could be to bridge the gap between the fractures determined by logs, and extrapolated from outcrop analogues, and those inferred from seismic data.

The fracture properties can also be obtained by studying the rock stress distributions through shear-wave splitting analysis. The polarization of the faster shear wave is parallel to fracture strikes while the polarization of the slow shear wave is normal to the fracture strike, and the magnitude of time-delay between fast and slow shear waves can be used to measure fracture density along the ray paths.

The Chapman squirt-flow model and the poroelastic equivalent medium theory indicate that the fluid viscosity in a saturated HTI medium can influence medium elastic properties and thus the Thomsen anisotropic parameters. This makes it theoretically possible to use seismic properties to infer fluid viscosity changes, so as to monitor fluids exchange in production reservoirs.

Chapter 3

Numerical modelling for P- and PS-wave azimuthal anisotropy

In this chapter I study the azimuthal variations of the attributes (amplitudes, travel time, etc) of P- and PS-waves in fractured media (HTI model) through numerical modelling. My study mainly focuses on the factors that may affect the feasibility of elliptical anisotropy analysis with the objective of obtaining more insight into the practice of using azimuthal anisotropy analysis for fracture detection, aiming to use my findings in the modelling analysis as a guide in real data analysis and interpretation.

In addition to the numerical modelling of conventional P-wave azimuthal anisotropy, I also model the azimuthal distribution of PS-wave attributes and compare results, so as to study the possibility of using the azimuthal variation of PS-wave attributes for fracture detection.

3.1 Introduction

The use of seismic anisotropy to characterize naturally fractured reservoirs started in the 1980's, and the underlying physics for this technology comes from the equivalent medium theory for seismic wave propagation in fractured media (e.g. Hudson, 1981; Liu and Hudson et al, 2000). According to this theory, in studying the behaviour of seismic waves, a medium containing vertically aligned fractures with a scale length much less than the seismic wavelength can be modelled with an equivalent azimuthally anisotropic medium. Numerical modelling based on equivalent medium theory reveals that P-wave amplitudes and travel-times are azimuthally dependent and can be used to detect fracture properties through azimuthal elliptical fitting. Figure 3.1.1a shows the relationship between the angle of incidence and azimuth and figure 3.1.1b explains the required azimuth

distribution to carry out the azimuthal seismic attribute analysis at a surface analysis point. In a reflection case from low-high impedance contrast, the major axis of the ellipse fitted to the amplitudes of the P-wave denotes the fracture strike (Figure 3.1.1c) and major axis of the ellipse fitted to the azimuthal interval travel time is normal to the direction of the fracture strike (Figure 3.1.1d). The major to minor axis ratio of the ellipse indicates the fracture density.

However, many requirements must be imposed on the data to make it really suitable for this practice. It is widely believed that a good azimuth-offset distribution is essential to get reliable results. However, analysis based on different attributes may have different requirements. For example, the analysis of azimuthal P-wave AVO gradients may be used as an indicator for fracture detection because its distribution with azimuth can be regarded as an approximately elliptical distribution at relatively near offset range. However, the optimal offset range that should be used in working with real P-wave data is not clear.

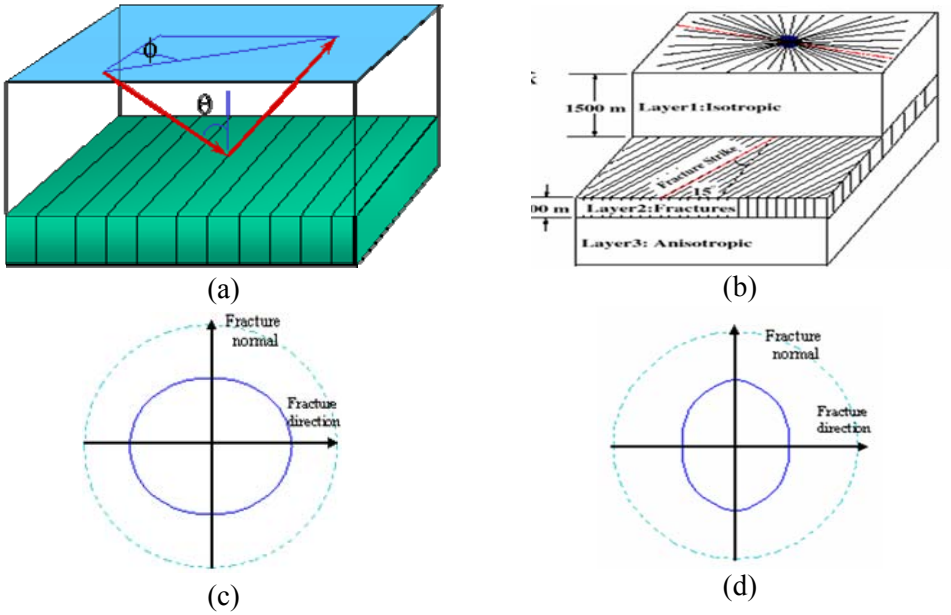

Figure 3.1.1: Azimuthal seismic anisotropy analysis. (a) relation between the angle of incidence (θ) and azimuth (ϕ); (b) wide azimuth seismic data acquisition, fracture properties of the middle layer (such as fracture direction and intensity) can be obtained by analyzing the azimuthal distribution of seismic attributes; (c) azimuthal variation of P-wave amplitudes - show an elliptical distribution with the major axis of the ellipse coinciding with fracture direction; (d) azimuthal interval travel time of P-wave displays elliptical distribution with the major axis in the direction of the fracture normal. The dashed line circle is used as the reference.

In addition to P-wave data, more and more converted wave (PS-wave) data with wide azimuth-offset coverage are becoming available. Do the attributes of PS-waves show similar elliptical variation with azimuth as the attributes of P-waves, and can they be used for elliptical anisotropy analysis? If so, this will provide additional opportunities to obtain fracture information, and the reliability of final fracture detection results will be enhanced with a combined and integrated azimuthal anisotropy analysis of P-wave and PS-waves data. Figure 3.1.2 is a Common Conversion Point (CCP) gather example of PS-wave data (Radial and Transverse component) from an Ocean Bottom Cable (OBC) survey in North Sea, which has been sorted in azimuth sequence. The event times show an obvious relation to azimuth on the R-component gather (Figure 3.1.2a). Especially at 1.5s, the events show a clear sinusoidal variation with azimuth, while the events on the T-component show polarity reversals with azimuth (Figure 3.1.2b). This means azimuthal anisotropy can be observed not only in P-wave data but also in PS-wave data.

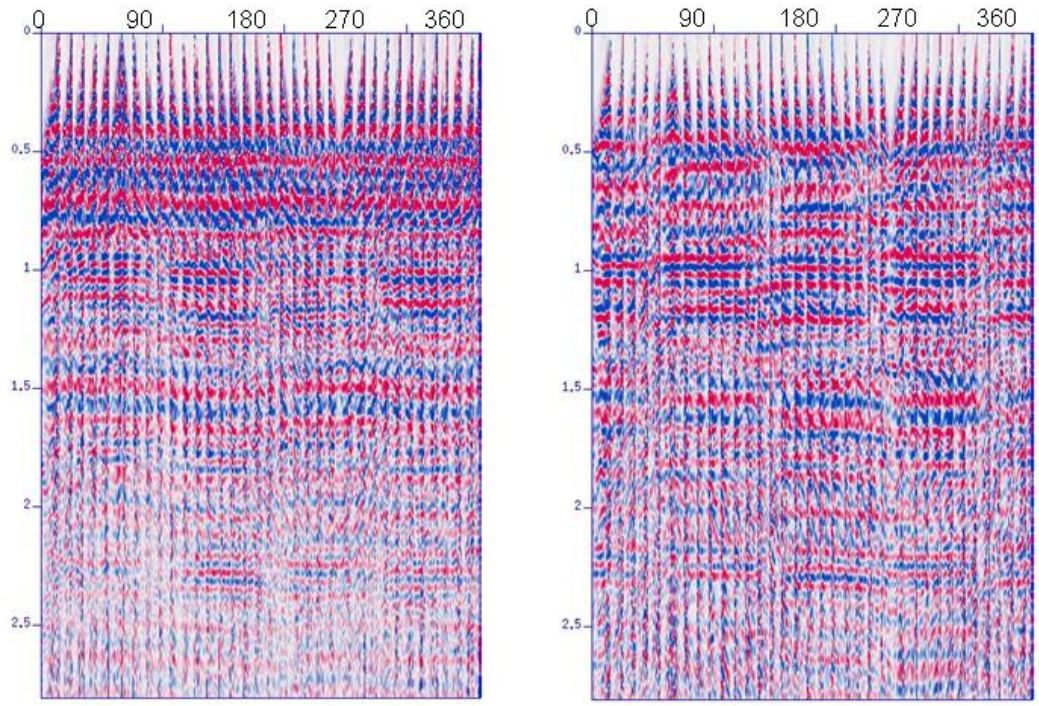

(a) Radial component (b) Transverse component

Figure 3.1.2: A PS-waves CCP gather example from North Sea OBC data. The traces in both (a) and (b) are sorted in azimuth (horizontal label on the top) sequence.

However, in contrast to wave propagation in isotropic media, there are no analytic expressions for PS reflectivity in anisotropic media, except for the VTI media and in the

symmetry planes of HTI media (Ruger, 1998). I study the azimuthal anisotropy of P- and PS-waves through numerical modelling to obtain more insight into the practice of using azimuthal anisotropy analysis for fracture detection, aiming to use my findings as a guide in real data analysis and interpretation. I especially study the possibility of using the azimuthal variation of PS-wave attributes for fracture detection. I do the modelling analysis by creating three-component seismic data with anisotropic modelling software (ANISEIS).

3.2 Model and data

The model I used to generate synthetic three-component data is shown in Figure 3.2.1. It is a simple three-layer model, so that results can be obtained directly. The top layer of the model is isotropic with P-wave velocity of 2000m/s. The middle layer of the model is a HTI medium simulating vertical aligned fractures in an isotropic medium. The fractures are simulated with aligned penny-shaped cracks in planar distribution (Liu and Hudson et al, 2000), and the aspect ratio and radius are 0.01 and 0.1, respectively. The fracture density is set to 10% and 18% separately to study the efforts of fracture density on azimuthal seismic response. The azimuth of fracture strike in the layer is 0^o. The material in the cracks is assumed to be a fluid with P-wave velocity of 1200m/s and density of $0.95g/cm^3$. Under the fractured layer is another isotropic layer.

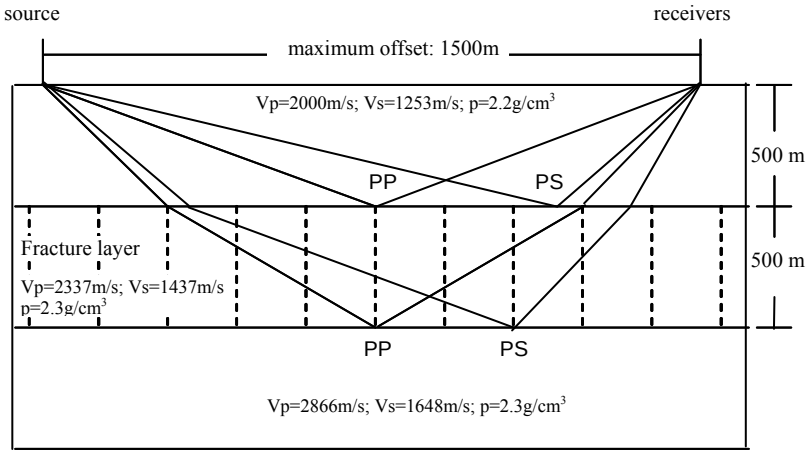

Figure 3.2.1: The three-layer model for numerical modelling. The offsets of the data range from 25m to 1500m, corresponding to straight ray-path incident angles ranging from 0^o to 37^o for the reflections at the bottom of the fractured layer.

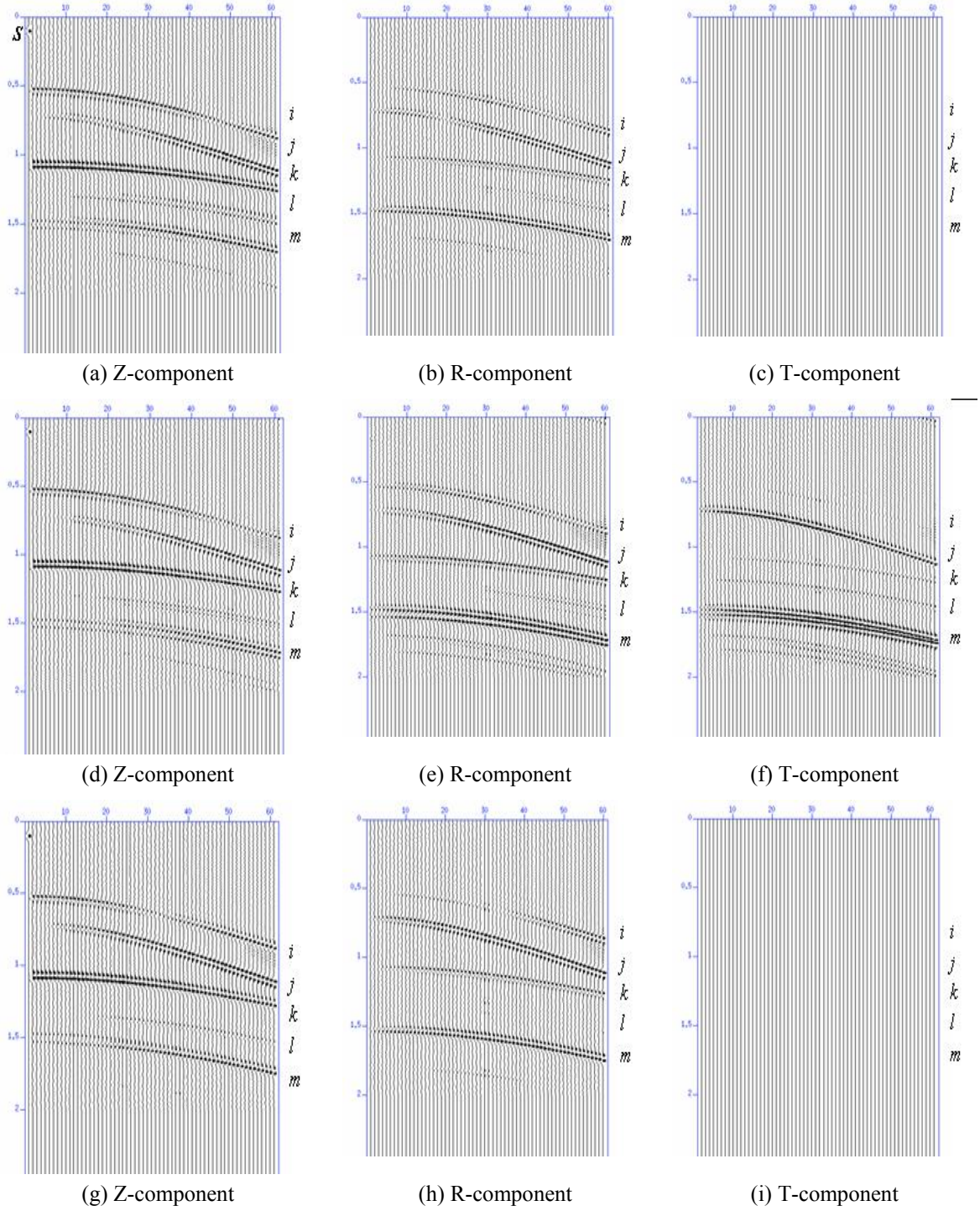

(a) Z-component (b) R-component (c) T-component

(d) Z-component (e) R-component (f) T-component

(g) Z-component (h) R-component (i) T-component

Figure 3.2.2: Synthetic data in source gather from the model in Figure 3.2.1. On (a), (b) and (c), seismic waves propagate along fracture strike; on (d), (e) and (f), seismic waves propagate at the angle of 45^{o} away from fracture strike; on (g), (h) and (i), seismic waves propagate in the direction of fracture normal. Figures on each panel represent the angle of incidence.

Figure 3.2.2 shows the synthetic three-component (radial, transverse and vertical) data in shot gathers based on the model in Figure 3.2.1. The offsets of the data range from 25m to 1500m, so that the straight ray-path incident angles range from 0^o to 37^o for the reflections at the bottom of the fracture layer. Since the ray-paths are not normally straight in practice, it is more convenient for us to use the offset-depth ratio to represent incident angle. The azimuth of the synthetic data ranges from 0^o to 360^o and the azimuth sampling interval is 10^o.

The data examples shown in Figure 3.3.2 represent the seismic waves propagating in the fracture normal direction, the direction at 45° to the fracture normal and the direction parallel to the fracture strike. Figure 3.3.2a, 3.3.2b and 3.3.2c are the synthetic data corresponding to the seismic waves propagating in the fracture normal direction; Note that the first trace in Figure 3.2.2a is the source wavelet for generating the synthetic data. Figure 3.3.2d, 3.3.2e and 3.3.2f are the synthetic data corresponding to the seismic waves propagating in the direction forming 45° to the fracture normal; Figure 3.3.2g, 3.3.2h and 3.3.2i are the data corresponding to the seismic waves propagating in the direction parallel to the fracture strike. Figures 3.3.2a, 3.3.2d and 3.3.2g are the Z-component, Figures 3.3.2b, 3.3.2e and 3.3.2h are the R-component; Figures 3.3.2c, 3.3.2f and 3.3.2i are the T-component.

3.3 P-wave azimuthal anisotropy

For the P-wave, there are four attributes that can be used for azimuthal anisotropy analysis, which are the amplitude, AVO gradient, velocity and travel time. The amplitude and AVO gradient are actually based on the same reflectivity attribute, and velocity and travel time are basically the same for a given ray-path. The travel time may show elliptical variation with azimuth in media with vertically aligned fractures and has the potential to be used to estimate fracture orientation and intensity (Booth and Crampin, 1983; Sena, 1991; Sayers and Ebrom, 1997). NMO velocity in HTI media also shows elliptical variation with azimuth (Grechka and Tsvankin, 1997, 1998). The azimuth dependence of P-wave seismic attributes suggests the possibility of detecting subsurface fracture information through azimuthal anisotropy analysis on seismic data.

The main motivation for me to do P-wave numerical modelling analysis is not to simply

confirm the above conclusions, but to further study the factors that might affect the results of azimuthally elliptical anisotropy in P-wave analysis, such as the offset to depth ratio (or the angle of incidence), the difference of the results from different attributes, etc..

3.3.1 Effects of offset on P-wave azimuthal anisotropy

Effects of offset on azimuthal amplitudes

Though the P-wave amplitudes of near offsets may be used for elliptical anisotropy analysis, how to choose an appropriate offset range to obtain optimal results is not so clear.

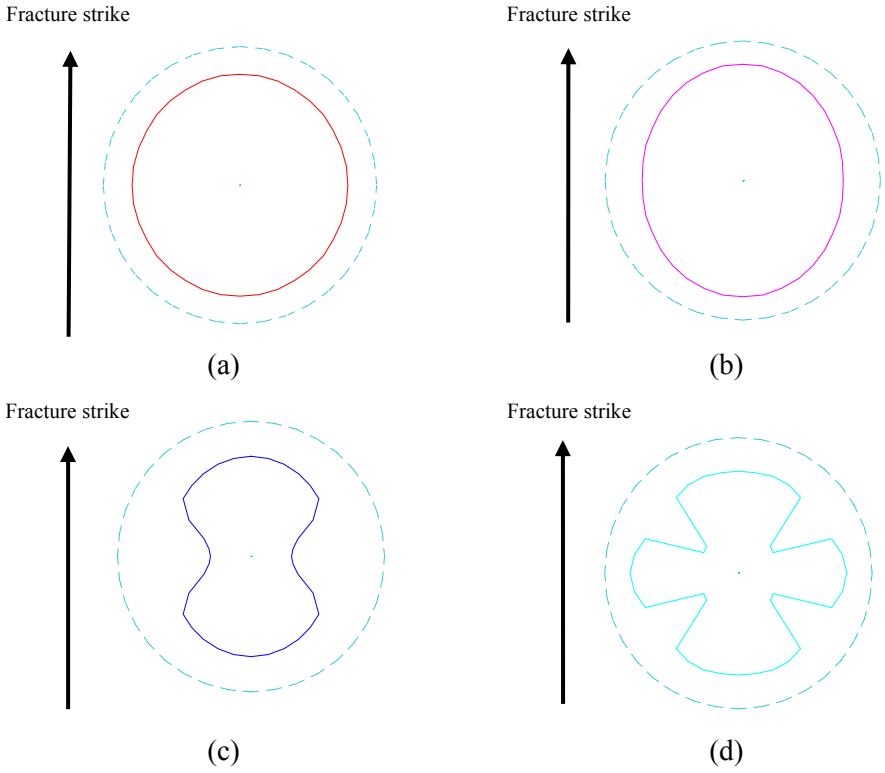

Figure 3.3.1: P-wave azimuthal amplitude distributions at the top of the fractured layer. (a), (b), (c) and (d) represent the offset-depth ratio of 0.2, 0.6, 1.0, 2.0, respectively. The dashed circle is used for reference circle.

Figure 3.3.1 shows the azimuthal distribution of P-wave amplitudes at the top interface of the fracture layer. It is obvious that not all amplitudes at different offsets show elliptical distribution with azimuth. When the offset-depth ratio is 0.2 (Figure 3.3.1a),

the amplitude distribution with azimuth is very close to a circle (use the dashed circle as a reference), which means that the amplitudes of near offset traces do not change significantly with azimuth, thus are not suitable for elliptical anisotropy fitting. The amplitudes with an offset-depth ratio of 0.6 display the ideal elliptical distribution with azimuth (Figure 3.3.1b) with the major axis coinciding with the fracture strike. When the offset-depth ratio is 1.0, the azimuthal amplitude distribution looks like 'peanut', but still be fitted for an ellipse with the major axis of the fitted ellipses in the direction of fracture strike (Figure 3.3.1c). However, in Figure 3.3.1d where the offset-depth ratio is 2.0, the amplitudes show a complicated 'Fan shape' distribution with azimuth and are not suitable for elliptical fitting. In this azimuthal amplitude modelling, the optimal offset-depth ratio for elliptical fitting is between 0.6 and 1.0.

In real data analysis for fracture detection where a noise problem is normally involved, the amplitude on very small offset traces or very large offset traces may be more ambiguous and we should be more cautious in choosing the appropriate offset ranges for elliptical anisotropy analysis.

Influence of offset on azimuthal travel time

Previous studies (Li, 1999) have demonstrated that the interval travel time of P-waves in a HTI medium can be used to infer subsurface fracture information through elliptical anisotropy analysis. However, as for azimuthal amplitude analysis, the offset may also influence the results of azimuthal anisotropy analysis of P-wave travel time. In the modelling analysis for azimuthal variation of interval travel time, I mainly study the influence of offset range, and try to obtain knowledge in choosing appropriate offsets for robust results.

Figure 3.3.2 shows the azimuthal distribution of travel-time within the fractured layer. When the offset-depth ratio is 0.2 and 0.5(Figure 3.3.2a, and Figure 3.3.2b), the azimuthal travel time distribution is very close to a circle (use the dashed circle a reference), which means the travel time is not very azimuth dependent and thus is not good for azimuthal anisotropy analysis. With increasing offset, the azimuthal distribution of travel time develops from a near-circle to a long ellipse. In figure 3.3.2c where the offset-depth ratio is 1.0, the travel time shows a clearly elliptical distribution with azimuth where the major axis is normal to the direction of fracture strike. When the

offset-depth ratio is 2.0 (Figure 3.3.1d), the travel time shows an even longer elliptical distribution with azimuth and is ideally suitable for elliptical fitting, which is very different to the situation represented by Figure 3.3.1.

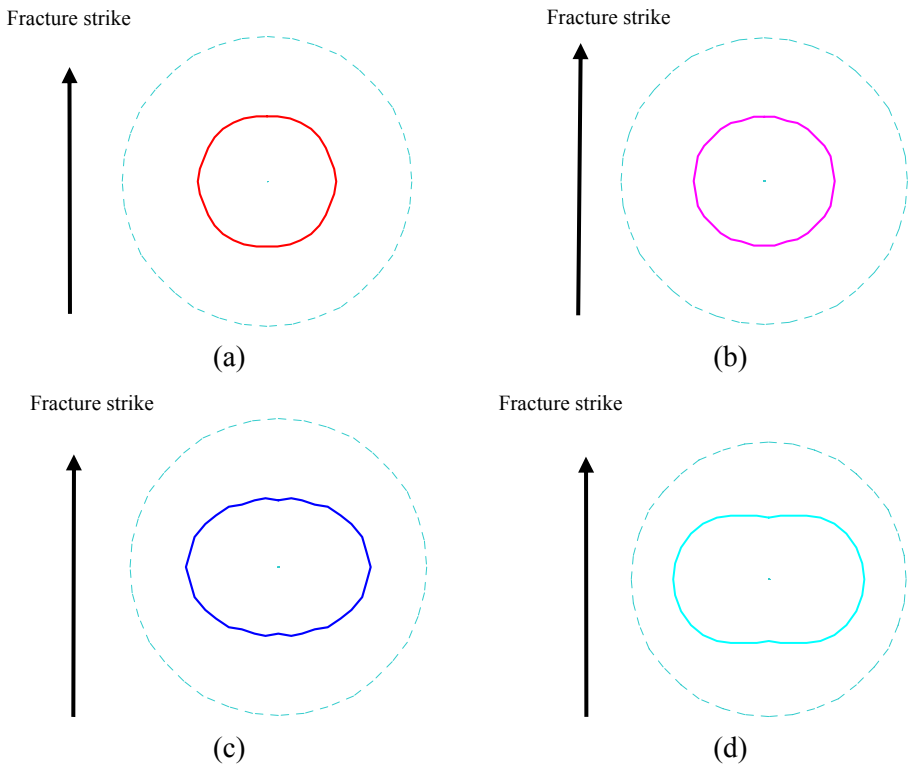

Figure 3.3.2: Azimuthal travel time within the fractured layer. (a), (b), (c) and (d) represent the offset-depth ratio of 0.3, 0.5, 1.0, 1.5, respectively. The dashed circle is for reference.

From the azimuthal travel time distribution shown in Figure 3.3.2, the optimal offset-depth ratios for azimuthal anisotropy analysis appear to be those larger than 1.0, which is opposite to the criteria of selecting offset range for azimuthal amplitude analysis. The modelling results reveal that, when using interval travel time for elliptical anisotropy analysis, we should use data with sufficiently large offsets, because azimuthal variation of interval travel time does not develop significantly on near offset traces.

3.3.2 Effects of fracture density on P-wave azimuthal anisotropy

Effects of fracture density on azimuthal amplitudes

Figure 3.3.3 shows the azimuthal amplitude distributions for different fracture densities.

Two offsets are used, to study the difference between the two ellipses at different offsets, with Figure 3.3.3a at the offset-depth ratio of 0.3 and Figure 3.3.3b at the offset-depth ratio of 0.5. The blue and red curves correspond to fracture densities of 10% and 18%, respectively. The figure reveals that the red curve which corresponds to a higher fracture density has a larger major to minor axis ratio at both offset ranges. It means that, at a suitable offset range where azimuthal amplitude can be fitted to an ellipse, the major to minor axis ratio can be used to represent relative fracture density.

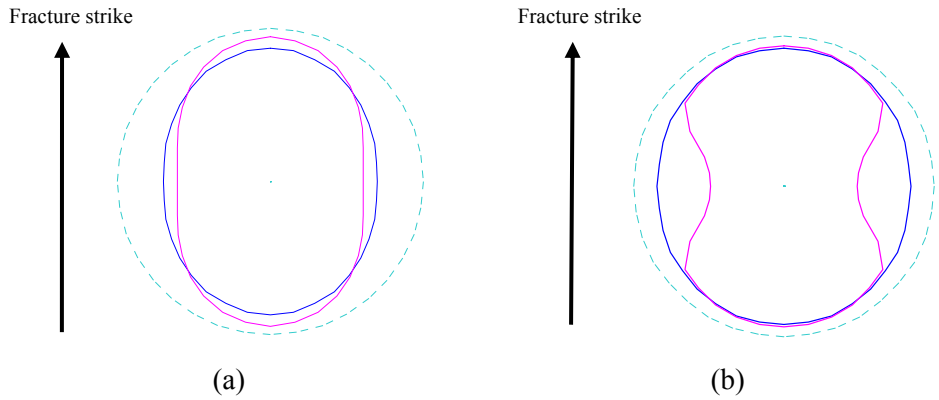

Figure 3.3.3: Azimuthal P-wave amplitudes at different fracture densities. (a) and (b) represent the offset-depth ratio of 0.3 and 0.5, respectively. The blue curve is for a density of 10% and the red curve is for a density of 18%. The dashed circle is for reference.

Effects of fracture intensity on azimuthal travel time

As for azimuthal P-wave amplitude analysis, the ratio of major to minor axis of the ellipse fitted to interval travel time also shows fracture density dependence. Figure 3.3.4 shows the azimuthal distribution of interval travel time for different fracture densities, where Figures 3.3.4a and 3.3.4b correspond to the results from data with offset-depth ratios of 1.0 and 1.5 respectively. The blue and red curves correspond to fracture densities of 10% and 18%, respectively. The figure reveals that, if the offset is large enough to allow azimuthal anisotropy of the interval travel time to develop significantly, the major to minor axis ratio of the fitted ellipse can be used to indicate relative fracture density.

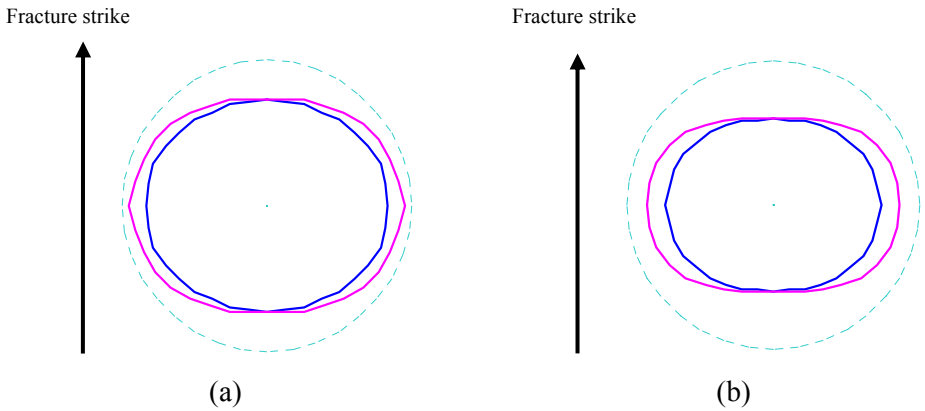

Figure 3.3.4: Effects of fracture density on azimuthal P-wave interval travel-time. (a) and (b) represent the offset-depth ratio of 1.0 and 1.5, respectively. The blue curve is for a density of 10% and the red curve is for a density of 18%. The dashed circle is for reference.

3.3.3 Summary

The results of P-wave modelling reveal that both amplitude and interval travel time may show elliptical variation with azimuth for HTI media, because the higher order term can be ignored. The major axis is in the direction of the fracture strike for the amplitude-fitted ellipse and is normal to the direction of fracture strike for the interval travel time fitted ellipse. At a fixed offset, the major to minor axis ratio proves to be fracture density dependent for both amplitude and travel time elliptical fitting, with larger major to minor axis ratio corresponding to higher fracture density. This feature makes it possible to use the major to minor axis ratio as a parameter to represent the relative fracture density distribution at a given offset.

However, in studying fracture density effects, I find that only the amplitudes on near offset traces are suitable for carrying out elliptical anisotropy analysis. If the offset-depth ratio is larger than 1.0, amplitudes do not show elliptical distribution with azimuth. In azimuthal travel time analysis, an opposite effect ito that of azimuthal amplitude analysis is found, so that the azimuthal variations can only be observed indata with sufficiently large offset. The offset restrictions in the numerical modelling analysis suggest that if all offsets are used for the elliptical anisotropy analysis, we may have false fracture information.

3.4 PS-wave azimuthal anisotropy

Another important motivation for the modelling analysis is to investigate the behaviours of azimuthal PS-wave attributes (amplitudes and interval travel time) in HTI media, compare it with the corresponding P-wave analysis and study the possibility of using azimuthal PS-wave attributes for fracture detection.

Figure 3.4.1 shows the azimuthal amplitude variations at the top of the fractured layer. The amplitudes of both the R-component and T-component of the PS-waves at the top of the fractured layer display large variation with azimuth. The amplitudes of the R-component show a nearly elliptical distribution with azimuth (Figure 3.4.1a) and the amplitudes of the T-component reveal zero-crossings and polarity reversals (Figure 3.4.1b), which can be used to infer fracture information (Li, 1998a).

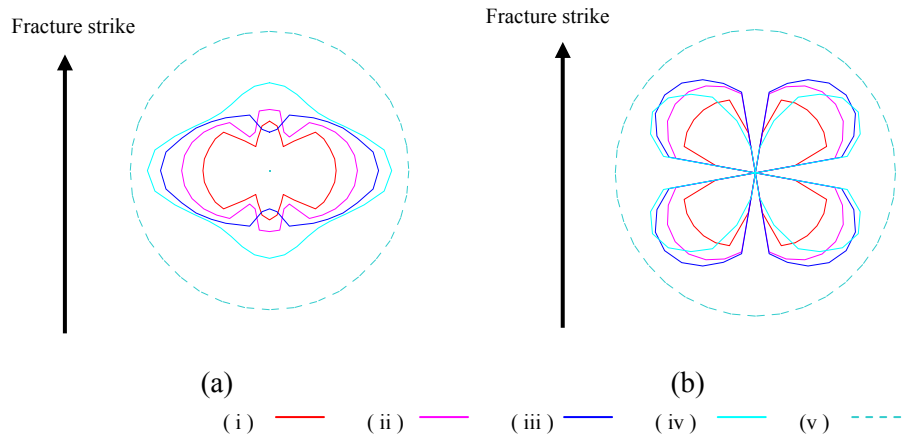

Figure 3.4.1: PS-waves azimuthal amplitude distributions at the top of the fractured layer. (a) R-component; (b) T-component. The color curves (i) to (iv) represent offset-depth ratios of 0.2, 0.6, 1.0, 2.0, respectively. The curve (v) is a circle for reference.

3.4.1 Effects of offset on PS-wave azimuthal anisotropy

Effects of offset on azimuthal amplitudes

Figure 3.4.2 shows that, at offset-depth ratios of 0.2, 0.6 and 1.0, the amplitudes of the R-component at the top of the fractured layer show a nearly elliptical distribution with azimuth, which is similar to that of the P-wave. It also reveals that the data suitable for elliptical fitting are those with offset-depth ratios ranging from 0.2 to 2.0, indicating that

wider offsets can be included for elliptical anisotropy analysis for R-component PS-wave data than the P-wave data. In contrast to the P-wave analysis where the major axis of the ellipse indicates the direction of the fracture strike, the major axis in R-component analysis is in the direction of the fracture normal.

Figure 3.4.3 shows that, at different offset-depth ratios, the amplitudes of the T-component at the top of the fractured layer show obvious azimuth dependence with zero-crossings and polarity reversals of amplitudes (Figure 3.4.4), which is very similar to that in Figure 3.1.2b. However, the azimuthal T-component shows very little offset dependence, which is different from the R-component.

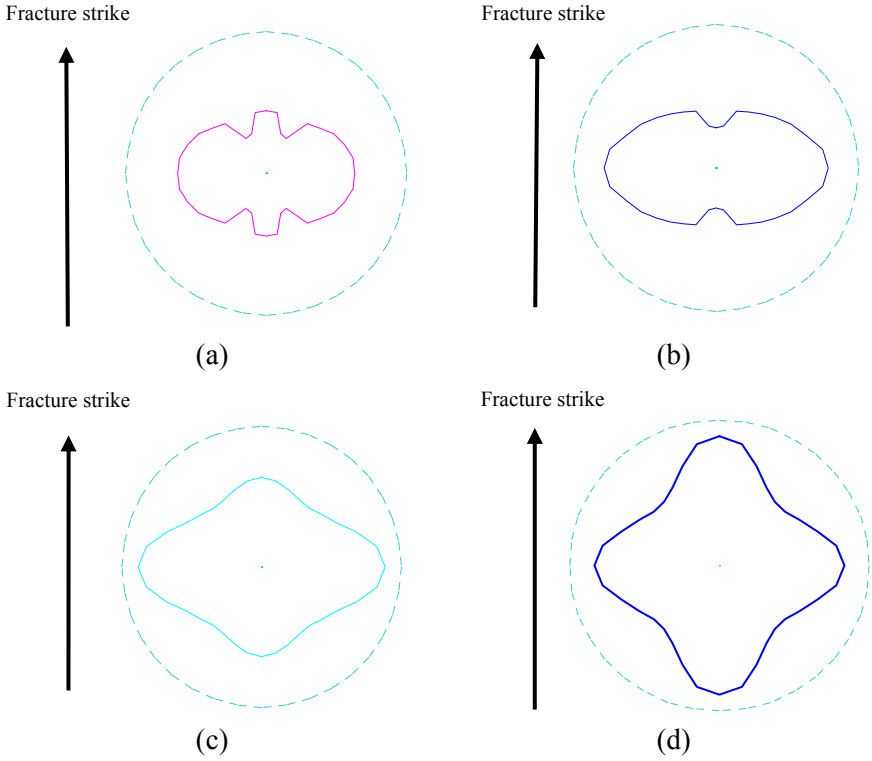

Figure 3.4.2: Azimuthal amplitude distribution of R-component at the top of the fractured layer. (a), (b), (c) and (d) represent the offset-depth ratios of 0.2, 1.0, 2.0, 3.0, respectively. The dashed circle is for reference.

.

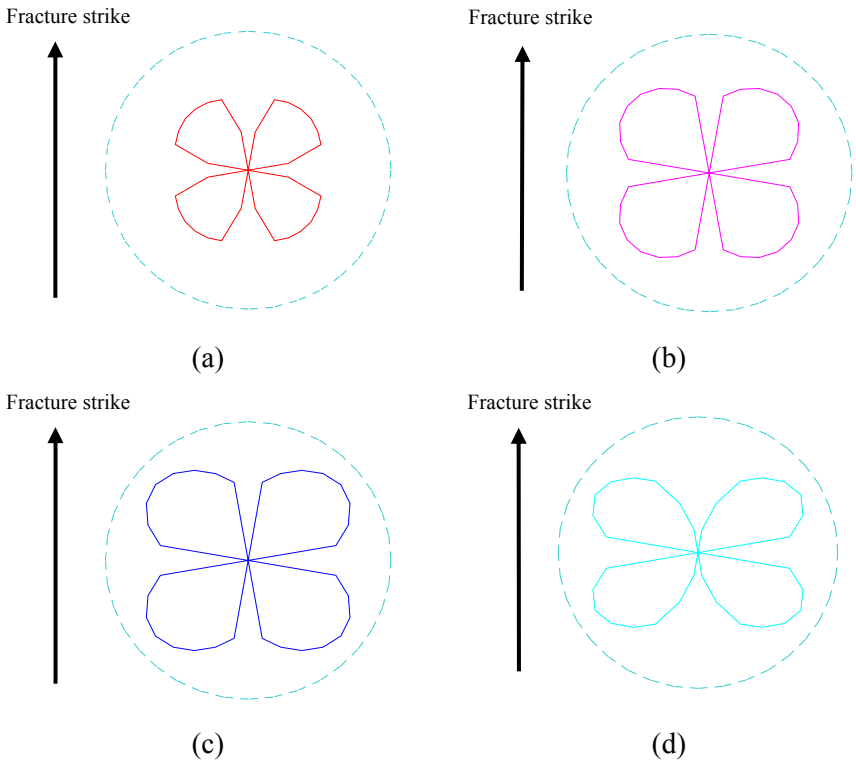

Figure 3.4.3: Azimuthal amplitude distribution of T-component at the top of the fractured layer. (a), (b), (c) and (d) represent the offset-depth ratios of 0.2, 1.0, 2.0, 3.0, respectively; the dashed circle is for reference.

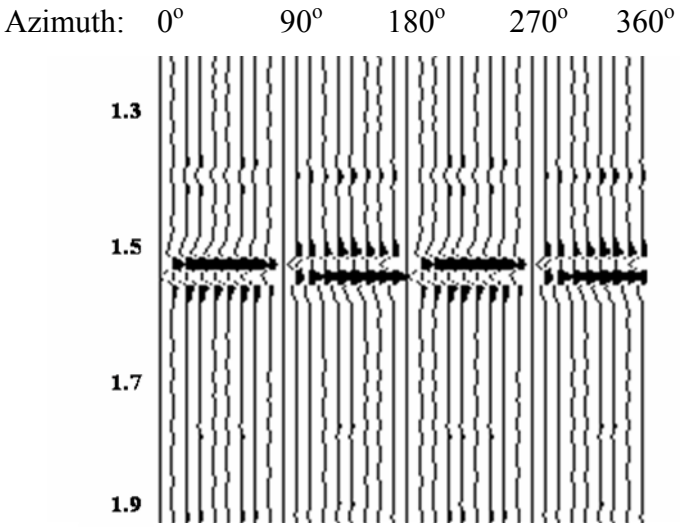

Figure 3.4.4: T-component traces of a CCP gather in azimuth sequence; the offset-depth ratio of the gather is 1.0.

Effects of offset on azimuthal travel time

Figure 3.4.5 is the azimuthal interval travel-time of the R-component within the fractured layer. When the offset-depth ratio is 0.3 and 0.5 (Figure 3.4.5a, and Figure 3.4.5b), the travel time distribution with azimuth is very close to a circle, which means the travel time shows little azimuthal anisotropy. However, when the offset-depth ratio is 1.0 (Figure 3.4.5c), the travel time shows an obvious azimuth dependence with a nearly elliptical distribution, and the major axis is normal to the direction of fracture strike. When the offset-depth ratio is 1.5 (Figure 3.4.5d), the travel time shows a longer elliptical distribution with azimuth than that in Figure 3.4.5c. It is consistent with the results obtained above for azimuthal P-wave analysis, showing that large offsets are required to allow azimuthal variations of interval travel-time to develop significantly to be observed.

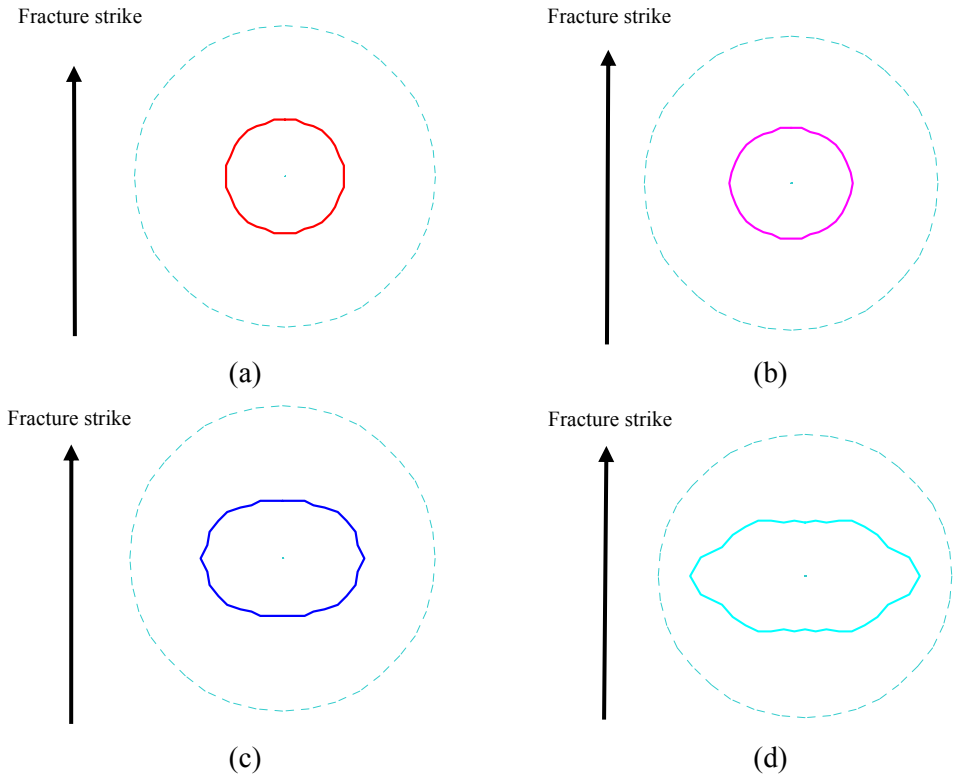

Figure 3.4.5: R-component azimuthal interval travel time in the fractured layer. (a), (b), (c) and (d) represent the offset-depth ratios of 0.3, 0.5, 1.0, 1.5, respectively. The dashed circle is for reference.

3.4.2 Effects of fracture intensity on PS-wave azimuthal anisotropy

Amplitude and fracture densities

Figure 3.4.6 is the azimuthal distribution of the amplitudes of R-component at different offset ranges, with Figure 3.4.6a at the offset-depth ratio of 0.2 and Figure 3.4.6b at the offset-depth ratio of 0.6. The blue and red curves correspond to fracture densities of 10% and 18%, respectively. It is seen that the red curve has a larger major to minor axis ratio for both offsets, indicating that the major to minor axis ratio of the ellipse fitted with the amplitudes of the R-component can be used as a parameter to describe relative fracture density.

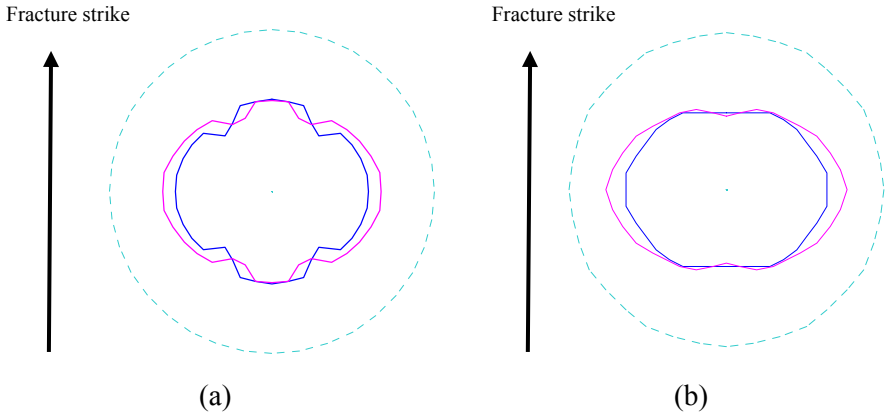

Figure 3.4.6: R-component azimuthal amplitude distribution with fracture density. (a) and (b) are the result for offset-depth ratios of 0.2 and 0.6, respectively. The blue curve is for a density of 10% and the red curve is for a density of 18%. The dashed circle is for reference.

Travel time and fracture densities

Figure 3.4.7 shows the azimuthal travel time at different offsets, with Figure 3.4.7a at offset-depth ratio of 1.0 and Figure 3.4.7b at the offset-depth ratio of 1.5. The blue and red curves correspond to fracture densities of 10% and 18%, respectively. The major to minor axis ratio of the ellipse show clear fracture densitydependence. The modelling results reveal that, when the offset is large enough to allow azimuthal anisotropy to develop significantly, the major to minor axis ratio of the fitted ellipse is fracture density rdependent and can be used to represent relative fracture density distribution. This conclusion is consistent with the results in the corresponding P-wave analysis.

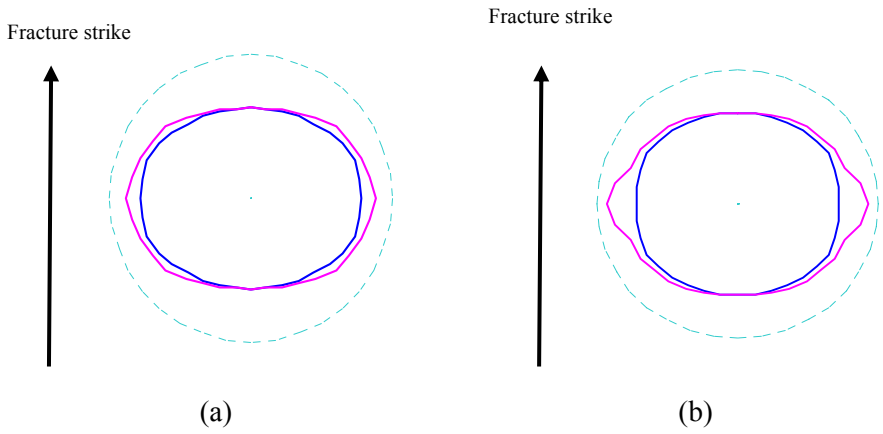

Figure 3.4.7: R-component azimuthal interval travel-time with fracture density. (a) and (b) represent offset-depth ratio of 1.0 and 1.5, respectively. The blue curve is for a density of 10% and the red curve is for a density of 18%. The dashed circle is for reference.

3.4.3 Summary

The modelling for azimuthal amplitudes of PS-waves reveals that both the R-component and T-component can be used to characterize fracture information. The elliptical distribution of the R-component amplitudes can be used to infer fracture properties with the major axis indicating the direction of fracture normal. The zero-crossings and polarity reversals of the T-component amplitudes show dependence on fracture properties and can be used to obtain fracture information. The azimuthal travel time of the R-component within the fractured layer at large offset traces also reveals clear fracture dependence by its elliptical variation.

The modelling results also demonstrate the restrictions of applicable offset range for the different attributes. When the amplitude is used for azimuthal anisotropy analysis, only the near and middle offset traces can be used, because the amplitudes on big offset traces (where offset-depth ratio is larger than 2.0) do not show elliptical distribution with azimuth. In the travel time analysis, travel times do not show a perceptible variation with azimuth on the traces with small offsets, thus only data with big offsets are suitable for analysis.

3.5 Comparison of azimuthal anisotropy between P- and PS-waves

3.5.1 Amplitude distribution with azimuth

Figure 3.5.1 displays the azimuthal amplitudes of P- and PS-waves at the offset-depth ratio of 0.6, showing that all amplitudes are dependent on the direction of fracture strike. The amplitudes of both the P-wave and the R-component of PS-waves show nearly elliptical distribution with azimuth. The major axis of the ellipse for the R-component is normal to the direction of fracture strike (Figure 3.5.1a), while the major axis is in the direction of fracture strike in P-wave analysis (Figure 3.5.1c). For T-component of the PS-waves, the azimuthal amplitudes demonstrate their fracture dependence through zero-crossings and polarity reversals.

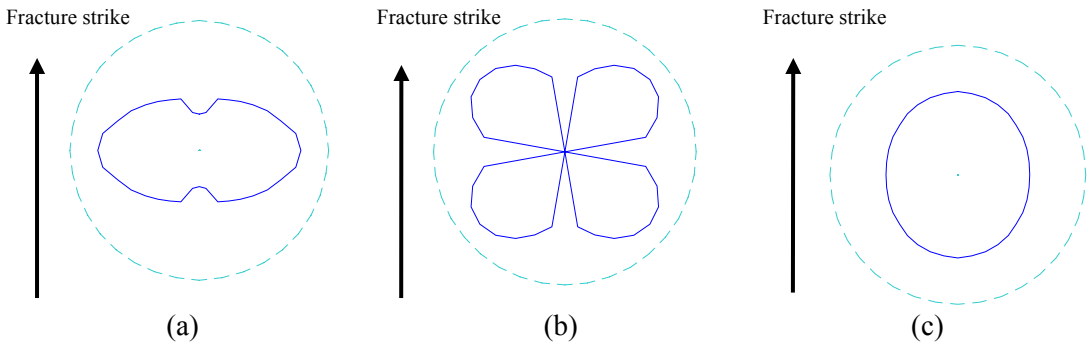

Figure 3.5.1: Amplitude distribution with azimuth for R-component (a), T-component (b) and P-wave (c). The offset-depth ratio is 0.6. The dashed circle is for reference.

Figure 3.5.2 shows the comparison of the azimuthal amplitude distribution for the R-component and P-wave at the top of the fractured layer, for different fracture densities and different offsets. At the same offset, the azimuthal amplitudes of the R-component display a clearer elliptical distribution than those of the P-wave and the offset range suitable for azimuthal amplitude analysis is larger. It means that a wider offset range can be included for elliptical anisotropy analysis for the R-component of PS-waves, than for the P-waves. In contrast to the major axis of ellipsis pointing towards the direction of fracture strike in P-wave analysis, it is in the direction of the fracture normal in R-component analysis.

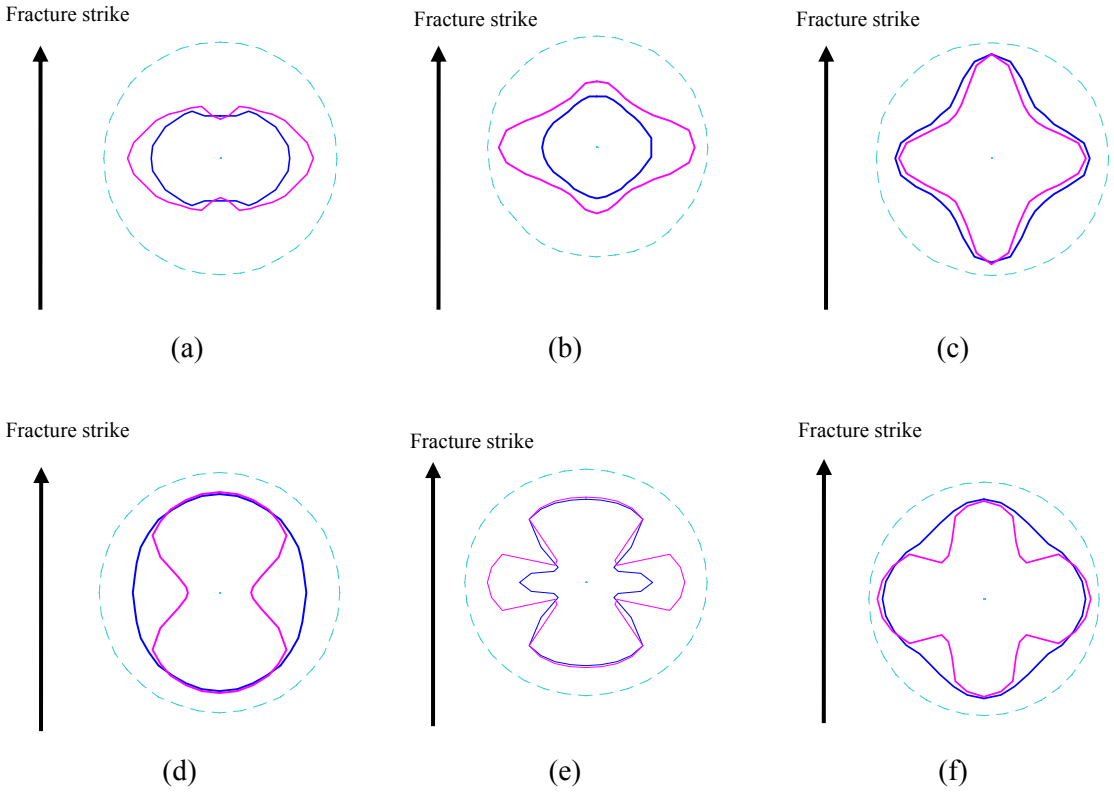

Figure 3.5.2: Azimuthal amplitude distributions at the top of the fractured layer with different fracture densities. (a), (b) and (c) are for PS-waves (R-compnent), with the offset-depth ratios of 1.0, 2.0 and 3.0, respectively; (d), (e) and (f) are for P-waves with the same offset-depth ratios as that in (a), (b) and (c). The blue curve is for a density of 10% and red curve is for a density of 18%. The dashed circle is for reference.

3.5.2 Travel time distribution with azimuth

Figure 3.5.3 shows the comparison of azimuthal interval travel-time between the R-component and P-wave at the offset-depth ratio of 1.0. Both sets of azimuthal interval travel times display elliptical distribution and the major axis is in the direction of the fracture normal. Figure 3.5.4 shows the azimuthal interval travel-time within the fractured layer for the P-wave and the R-component of the PS-waves, for different fracture densities and different offsets. It shows that the azimuthal variation of interval travel-time of the R-component and the P-wave consistently show an elliptical distribution with azimuth, with the major axis in the direction of fracture normal. It also reveals that, when the offset is large enough to allow azimuthal anisotropy to develop significantly, the major to minor axis ratio of the ellipse fitted to both waves can be used to represent relative fracture density distribution.

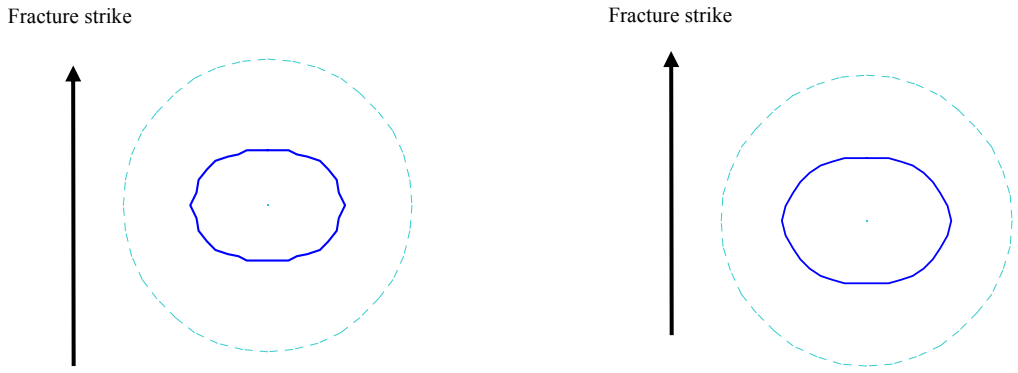

Figure 3.5.3: Azimuthal interval travel time of R-component (a) and P-wave (b). The offset-depth is 1.0. The dashed circle is for reference.

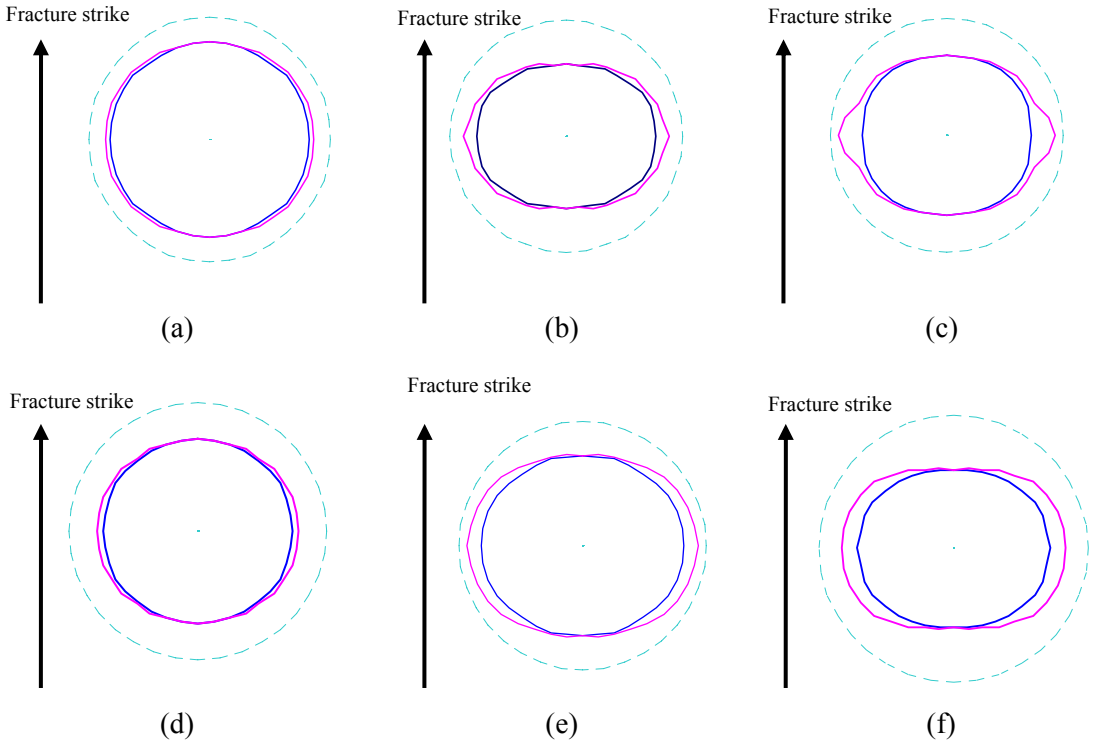

Figure 3.5.4: Azimuthal interval travel-time with fracture density. (a), (b) and (c) are for PS-waves (R-compnent), with offset-depth ratios of 0.5, 1.0 and 1.5, respectively; (d), (e) and (f) are for P-waves with the same offset-depth ratios as that in (a), (b) and (c). The blue curve is for a density of 10% and the red curve is for a density of 18%. The dashed circle is for reference.

3.5.3 Summary

A comparison of azimuthal P- and PS-wave attributes reveals similarities in elliptical anisotropy distributions. The amplitudes of both the P-wave and the R-component of PS-waves show nearly elliptical distribution on near offset traces. In a low-high impedance contrast case, the major axis of the ellipse fitted to the amplitudes of the P-wave is in the direction of the fracture strike, while the major axis from the R-component amplitude analysis is in the direction of the fracture normal. For the T-component of the PS-waves, the azimuthal amplitudes demonstrate i fracture dependence with zero-crossings and polarity reversals. For the same offset, the azimuthal amplitude variation of the R-component shows larger variation magnitude than that of the P-wave. It also reveals that a wider offset range of the R-component data can be included for azimuthal amplitude analysis than for P-waves. Whereas the major axis of the ellipse fitted to the P-wave azimuthal amplitudes is in the direction of the fracture strike, for azimuthal R-component analysis the major axis is in the fracture normal direction.. The azimuthal interval travel time shows elliptical distribution for both the P-wave and the R-component of the PS-waves, and the major axis is normal to the direction of the fracture strike.

The azimuthal interval travel-time within the fractured layer for the P-wave and the R-component consistently show an elliptical distribution with azimuth, and the major axis is in the direction of fracture normal. When the offset is large enough to allow azimuthal anisotropy to develop significantly, the major to minor axis ratio of the ellipse fitted to the travel time of both waves can be used as a parameter to characterize the distribution of relative fracture densities.

3.6 Conclusions

The modelling of azimuthal P-waves reveal that not all offsets are suitable for elliptical anisotropy analysis, as the data with very small offset do not show observable azimuthal amplitude variations, and the optimal offsets for elliptical fitting are limited to those with offset-depth ratios between 0.3 and 1.0. This means that, if we perform elliptical anisotropy analysis on the amplitudes of real P-wave data, we should be careful in choosing the appropriate offset to obtain reliable results.

The modelling results also show that the azimuthal interval travel-time variations can only be observed on data with offset-depth ratios larger than 1.0, because interval travel-time variations with azimuth can only develop significantly on traces with sufficiently large offset. Thus, we should focus more on the far-offset data if we use interval travel-time for elliptical anisotropy analysis on real data.

Both the amplitudes and interval travel-times of the R-component of PS-waves can be used to infer fracture information through elliptical anisotropy analysis, in a similar way to P-wave analysis. The azimuthal distribution of R-component amplitudes shows a better elliptical distribution than for P-waves. In contrast to P-waves, the major axis of the fitted ellipse is in the direction of the fracture normals. The overall offset range of PS-wave data suitable for azimuthal amplitude analysis is wider than that for P-waves. The azimuthal interval travel-times of PS-wave R-components display very similar elliptical distributions to those of P-waves and indicate good application potential for real data.

Chapter 4

Physical modelling for fracture detection

In this chapter I carry out azimuthal attributes analysis on the 3D P-wave datasets from two physical modelling datasets scaled to equivalent survey area of 20km^2 each, to study the physical bases of using azimuthal anisotropy for fracture detection. It is the extension of the study in Chapter 4. The findings from this physical modelling are aimed to help fracture detection in real data analysis, which is discussed in Chapter 5.

4.1 Introduction

Over the last few years, there have been many field scale studies of using azimuthal P-wave seismic data for fracture detection (e.g. Lynn et al., 1996; Liu and Li et al., 2000; Hall et al., 2000; Smith & McGarrity, 2001; Li, 1999; Wang and Li, 2006; amongst others). However, studies based on laboratory scale physical models are relatively rare in the recent past than numerical modelling studies (Luo and Evans, 2004), although physical modelling of shear wave splitting were well documented in the early 1990's (e.g. Slack et al. 1991; Brown et al. 1991; Cheadle et al. 1991). The motivation for physical modelling is to examine the suitability of using azimuthal seismic attributes of P-waves for fracture detection and to validate the numerical modelling. The purposes of doing this physical modelling are as follows:

To study the physical basis of using azimuthal analysis methods on seismic data for fracture detection. Azimuthal seismic anisotropy studies based on physical model data can help us understand the physical reasons for using azimuthal seismic attributes to detect fracture information. Though numerical modelling based on equivalent medium theories for azimuthal seismic anisotropy on HTI media in Chapter 3 reveals that fracture properties can be characterized by elliptical fitting, it is more mathematical than physical

and based on some assumptions. In contrast, an analysis with physical model data will provide an understanding of the physical basis of the azimuthal seismic methods. It will also help us to know the potential of applying them to field data, because physical model data have the same physical background as field data. Thus, I carry out an azimuthal seismic anisotropy study on the two 3-D physical P-wave modelling data for fracture detection, so as to obtain a better physical basis for using the methods for fracture detection on seismic data.

To obtain guidelines in the choice of seismic attributes and methods for fracture detection on field data. Unlike numerical modelling data, physical model data possess most of the features of field data, since they have the similar physical background and what applies to physical model analysis should also apply to field data analysis. In physical modelling, we know all fracture information within the model, and just need to find the links between the attributes of data and the fracture properties, and study which method can be used to infer fracture information. The attributes and methods applied in physical model data also provide the physical basis for detecting fracture information in field seismic data. In this study, I analyse different attributes of azimuthal P-wave seismic data, and use different analysis techniques to study the potential for using them for fracture detection in field data.

To study the effects of different acquisition parameters and structures on the capability for fracture detection. The methodologies for acquiring physical modelling data are similar to those applied in the field, except that the data acquisition is carried out in the laboratory. This makes it possible to study how the factors associated with data acquisition, such as signal to noise ratio, geometry, etc., affect fracture detection, and how to recognize these effects in fracture characterisation results from field data analysis so as to avoid interpretation traps. In the analysis of two physical modelling datasets with different geometry and data quality, I compare and investigate the effects of geometries and noise on the fracture characterization results.

The findings from this physical modelling data analysis are used to guide fracture detection in 3D seismic data with wide azimuth coverage acquired from a fractured reservoir; this is discussed in Chapter 5.

4.2 The structure of the physical models

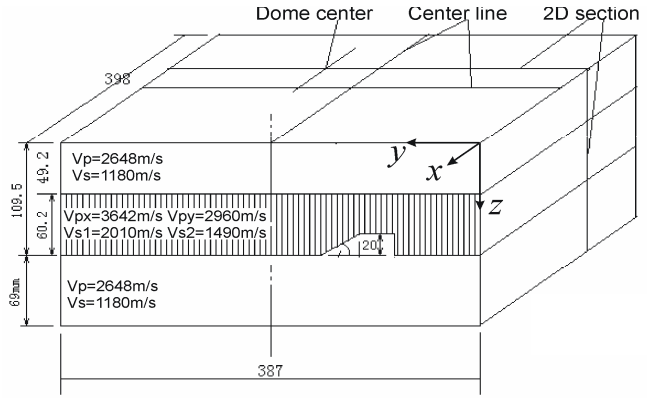

(a)

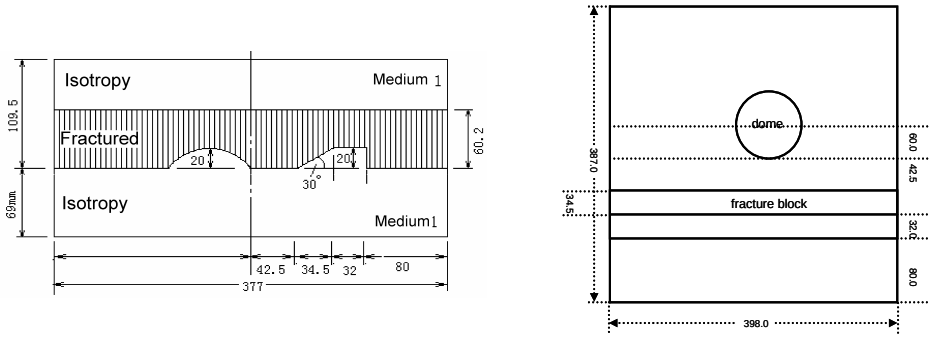

(b) (c)

Figure 4.2.1: Basic physical model for constructing acquisition models, consisting of three horizontal layers with the top and bottom layers being isotropic and the middle layer composed of epoxy-bonded fibre sheets to simulate vertical fractures with density around 20%. The measurements are in millimetres, and the model is scaled down in size by 1:10 000 with scale up in frequency by 10 000:1. (a) The parameters for the physical model; (b) a 2D section through the dome centre; and (c) a plane view of the structure within the fractured layer.

The two physical models for modelling are constructed from a basic model which consists of three horizontal layers (Figure 4.2.1) where the top and bottom layer are made from the same material (epoxylite) which is believed to be isotropic. The middle layer is constructed from a special industrial material which is azimuthally anisotropic (HTI medium) with simulated vertical fractures composed of epoxy-bonded fibre sheets. The layer is highly anisotropic with 20 per cent P-wave and S-wave anisotropy, and the fracture density is around 20%. There are two built-in geological features at the bottom of the fractured layer. One is a dome, and the other is a block simulating a normal and a

vertical fault. The model is constructed with a scale of 1:10 000 for spatial dimensions and time measurements, with a velocity scale of 1:1.

Table 4.2.1 shows the measured elastic parameters (c_{ij}, in $10^9 N/m^2$), and the corresponding anisotropic parameters for the fractured layer in Table 4.2.1 using the experimental method described in Cheadle et al. (1991). The density of the material is $1.45 g/cm^3$. In defining the elastic constants, the axes of *x*, *y* and *z* are represented by indices *1*, *2* and *3*, respectively. ε and γ are calculated with (Thomsen, 1986)

$$\varepsilon = (c_{33} - c_{11}) / (2c_{11})$$

$$\gamma = (c_{44} - c_{66}) / 2c_{66})$$

c_{11}	c_{22}	c_{33}	c_{44}	c_{55}	c_{66}	c_{12}	c_{13}	c_{23}	ε	γ
12.704	**19.233**	**22.162**	**5.858**	**3.299**	**3.219**	**7.865**	**8.199**	**9.320**	**0.372**	**0.410**

Table 4.2.1: The measured elastic parameters and the corresponding anisotropic parameters for the fractured layer in the middle of the basic model (Figure 4.2.1).

Two models are derived from the basic model for experiments simulating varying offset-depth ratios and acquisition geometries (Figure 4.2.2). The scaled-up Model I (Figure 4.2.2a) consists of a very thick water layer of 1470m on top of the basic model in order to maximize the data quality. The thick water layer ensures primary reflections from the studied interfaces of the basic model are free from multiple contaminations as a result of increasing the travel-time of multiples. The total thickness of the overburden above the fractured layer is 1962m, and the maximum offset-depth ratio is about 0.9 to the top of the fractured layer and about 0.7 to the bottom of the fracture layer. Model II (Figure 4.2.2a) consists of a thin water layer of 10m and another isotropic layer of 430m just above the basic model, which is designed to maximize the anisotropic effects and increase offset coverage relative to the target depth. The total thickness of the overburden in the basic model in Model II is reduced to 932m, and the maximum offset-depth ratio is about 2.2 to the top of the fracturde layer, and about 1.3 to the bottom of the fractured layer (Table 4.3.2).

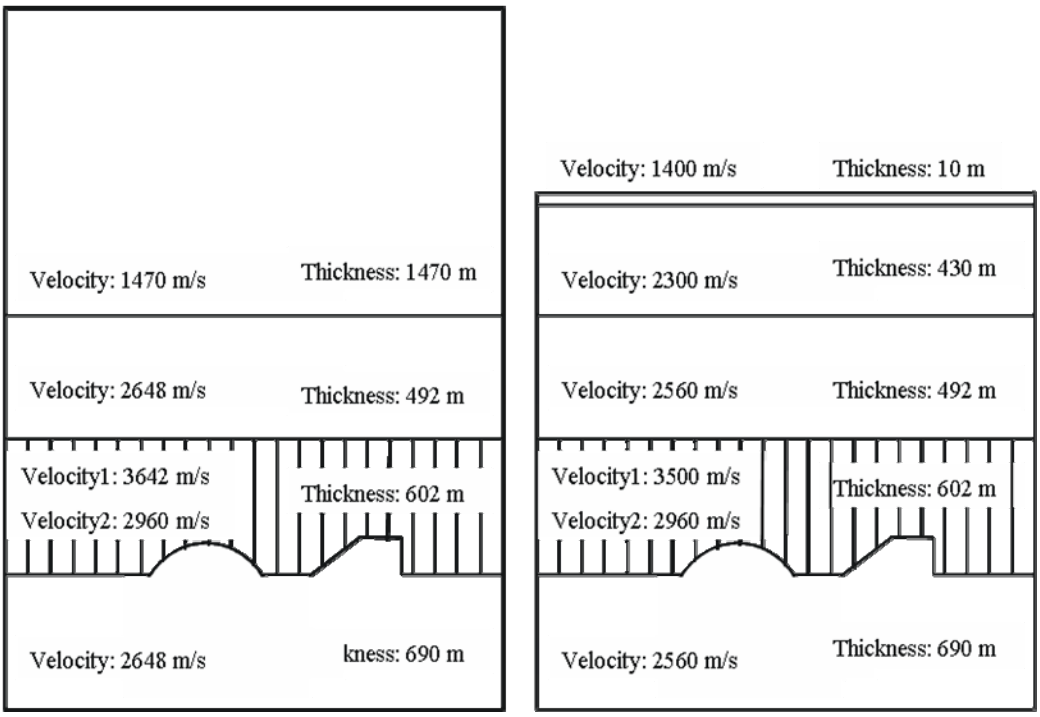

(a) (b)

Figure 4.2.2: Sectional view of Model I (a) and Model II (b) with dimension scaled up by 1:10,000. The basic model (Figure 4.2.1a) forms the bottom three layers of both experimental models. The maximum offset-depth ratio for Model I is about 0.9 to the top of fractured layer and 0.7 to the bottom; Model II consists of a thin water layer of 10m and another isotropic layer of 430m on top of the basic model. The maximum offset-depth ratio is about 2.2 to the top of the fractured layer and about 1.3 to the bottom.

4.3 Data acquisition

The 3D data acquisition for both models is conducted in a water tank (Figure 4.3.1). The acquisition system consists of an ultrasonic pulse source and receiver system, an analogue/digital converter, and a motor-driven positioning system. The maximum movement in the x, y and z directions are 230mm, 230mm and 100cm, respectively, and the positional error is less than 0.1mm. The dominant pulse frequency is 230 kHz for the acquisition which results a dominant bandwidth of 11-32Hz in the data.

Each of the two datasets is equivalent to a field area size of 20km^2, and they are acquired with slightly different acquisition parameters. Table 4.3.1 shows a detailed comparison of the acquisition parameters for models I and II. Both acquisition geometries for the two experimental models are designed to ensure wide-azimuth coverage (Figure 4.3.2). The

receiver lines (Y-direction) are perpendicular to the fracture planes and the shot lines (X-direction) (Figure 4.3.3).

Figure 4.3.1: Data acquisition on the physical model in the lab.

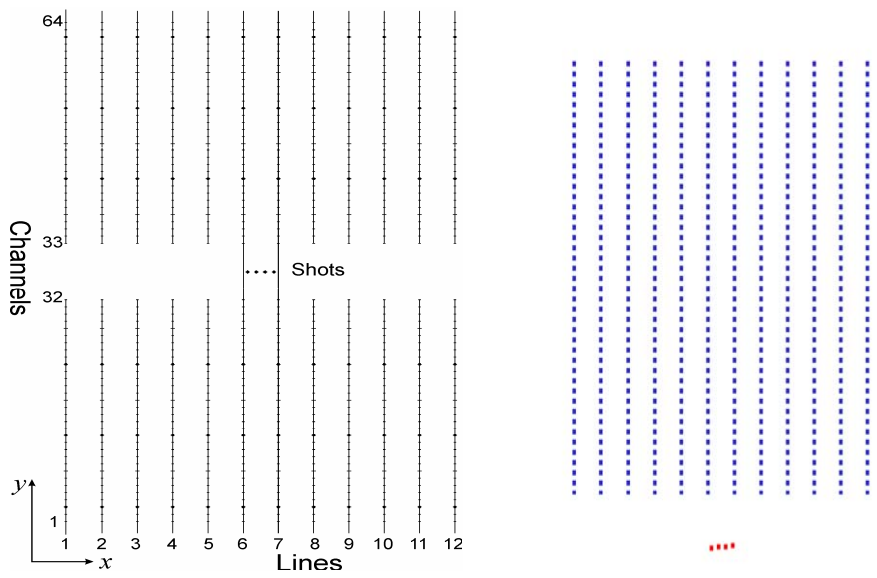

(a) (b)

Figure 4.3.2: Data acquisition system (a), and acquisition geometry (b). The shot points are located at the centre of the spread. There are 12 receiver lines and 48 receivers for each receiver line. The receiver line interval is 40m， and the shot line interval is 240m. The minimum and maximum offsets along the receiver line for a shot are 160 and 2040m, respectively.

4.3.1 Acquisition parameters

The 12L/4S/48 acquisition geometry (12 receiver lines for a shot; 4 shots for a shot line located in the centre of the spread; 48 receivers for each receiver line) is applied, and the cell size is 20m×20m. In the receiver line direction, the receiver interval is 40m，the layout is 0-160-2040m (i.e. the minimum and maximum offset along the receiver line for a shot are 160 and 2040m, respectively). The shot line interval is 240m. After firing four shots each time, the spread is moved to the next location. In the shot line direction：the receiver line interval is 240m，and the shot point interval is 40m. For Model II, the same style of shooting is used but the acquisition parameters (e.g. source interval, receiver interval, etc.) are changed for increasing efficiency. There are totally 15 swaths for each dataset.

Parameters	**Model I**	**Model II**
Shot line interval:	200m	240m
Receiver line interval:	200m	240m
Shot interval:	50m	40m
Receiver interval:	50m	40m
Minimum offset:	200m	160m
Maximum offset:	1750m	2040m
Sampling rate:	1ms	2ms
Recording length:	5s	8s
Number of channels:	768	576
Number shots:	2400	2340
Nominal fold:	48	32
Nominal bin size:	25mx25m	20mx20m
Target depth (to fractured layer bottom)	2564m	1534m

Table 4.3.1: Acquisition parameters for models I and II.

4.3.2 Coordinate definition

The coordinates are based on the station numbers, the unit of station number is 40m (the corresponding unit for the physical model is 4mm). Station numbers start from 0. In the X direction, the size of the model is 400mm, corresponding to the scaled size of 4.0 km, while in the Y direction, the size of the model is 380mm, corresponding to the scaled size of 3.8 km. The coordinates of the two experiment models at the four corners are (0, 2.5), (100, 2.5), (100, 97.5) and (0, 97.5), respectively.

The receiver lines are perpendicular to the X-axis. The line number starts from 101 with an increment of 1. The interval between two receiver lines is 6 times the station unit. Line 101 locates at 007.5 on the X-axis. The shot lines are normal to the Y-axis, The shot number starts from 501 with an increment of 1. The interval between two shot lines is 3 times the station unit. Line 501 locates at 5.0 on the Y-axis.

Figure 4.3.3 is the plane view for shots and receivers layout deployed for data acquisition as well as the model structure. The red lines (horizontal ones) represent shot lines and the blue lines (vertical ones) denote receiver lines. The green circular area denotes the dome location.

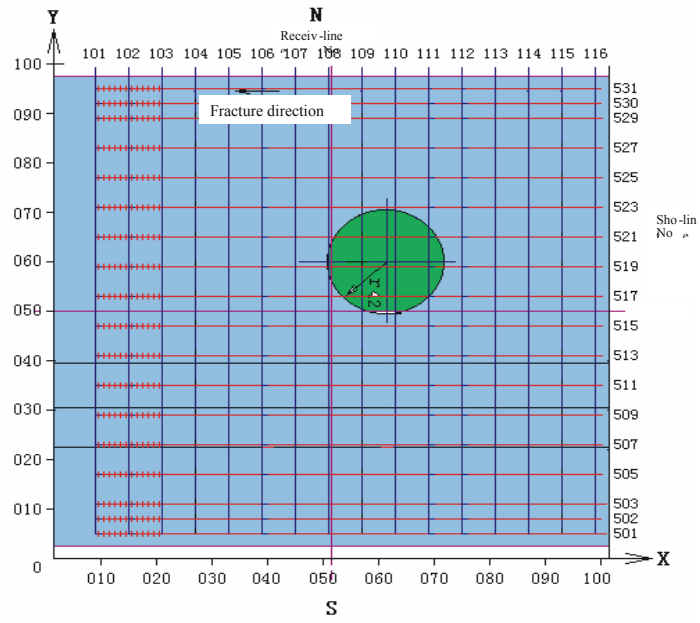

Figure 4.3.3: Layout of shots and receivers on the model. The red lines (horizontal ones) denote shot lines, the blue lines (vertical ones) denote receiver lines, and the green circle denotes the dome location.

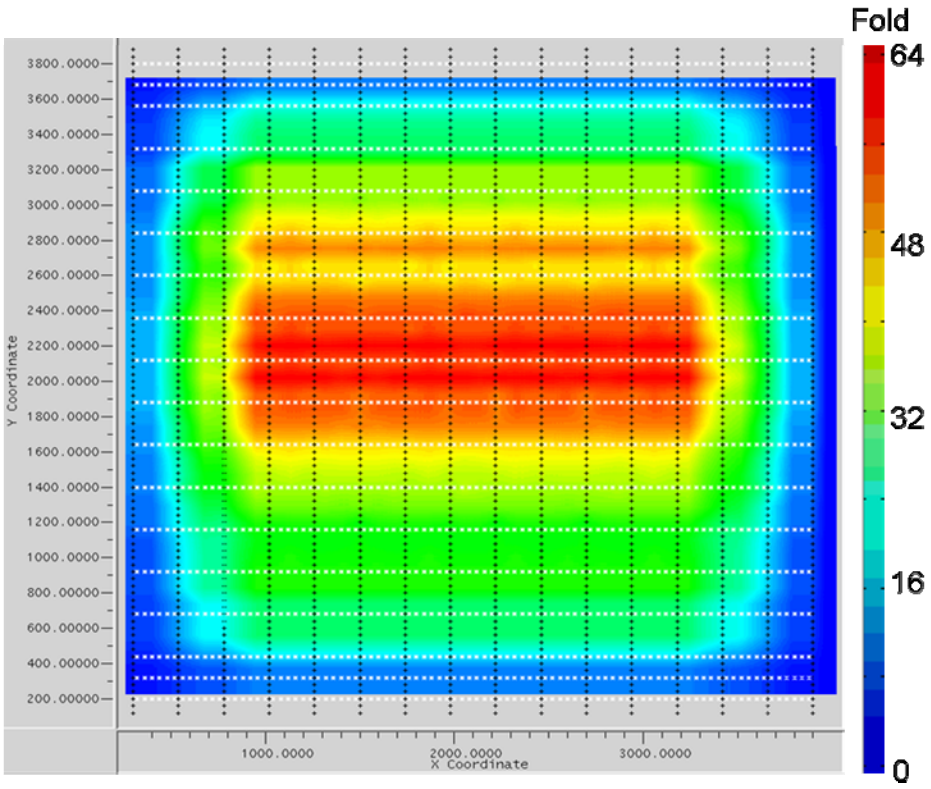

Figure 4.3.4: Fold distribution. The red colour denotes high folds.

The data sample interval in the laboratory is 0.2μs and there are 4096 samples in each trace, which is equivalent to field data with a record length of 8s and a sample interval of 2ms.

4.3.3 Data features

Though the two physical model datasets are acquired in the laboratory, they have almost the same features of field data, and are different from numerical data based on theoretical calculation. Figure 4.3.5 shows a shot-gather comparison of the two datasets. The data from Model I have a high signal to noise ratio, and all primary reflections are free from noise contamination, which means the results of fracture characterization should be free from the influence of noise. However in the data of Model II, the primary reflections suffer interference with multiples and refracted arrivals, and the reflection energy is weaker relative to the noise level. The overall data quality is quite similar to that of a field data with medium signal to noise ratio. The data is suitable for analyzing the influence of noise on fracture detection.

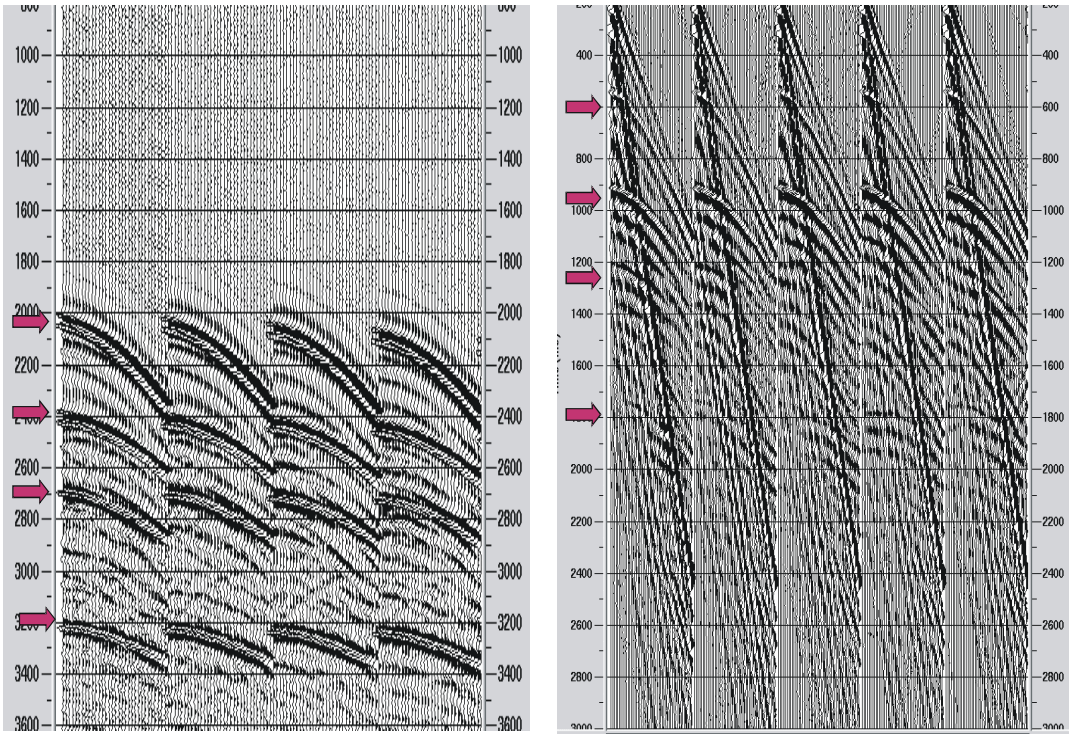

(a) (b)

Figure 4.3.5: Comparison of shot gathers from Model I (a) and Model II (b) (only four spreads are displayed in the panel). The data from Model I are almost free of noise with strong primary reflections, whereas the data from Model II contains several kinds of noises, including multiples, regular and random noises, and the energy of primary reflections are relatively weak compared with the noise. The four red arrows on each panel indicate the reflections from the four interfaces in the physical models in Figure 4.2.2.

Both the datasets have good azimuth coverage (Figure 4.3.6), and thus meet the azimuth requirements for performing azimuthal seismic anisotropy analysis for fracture detection.

	Model I	Model II
Maxoffset/ Target depth	0.89 (top) 0.68 (bottom)	2.19 (top) 1.33 (bottom)
S/N	high, free from noise	reasonable, more similar to real data
Azimuthal coverage	wide	wide

Table 4.3.2: Comparison of parameters for Model I and II.

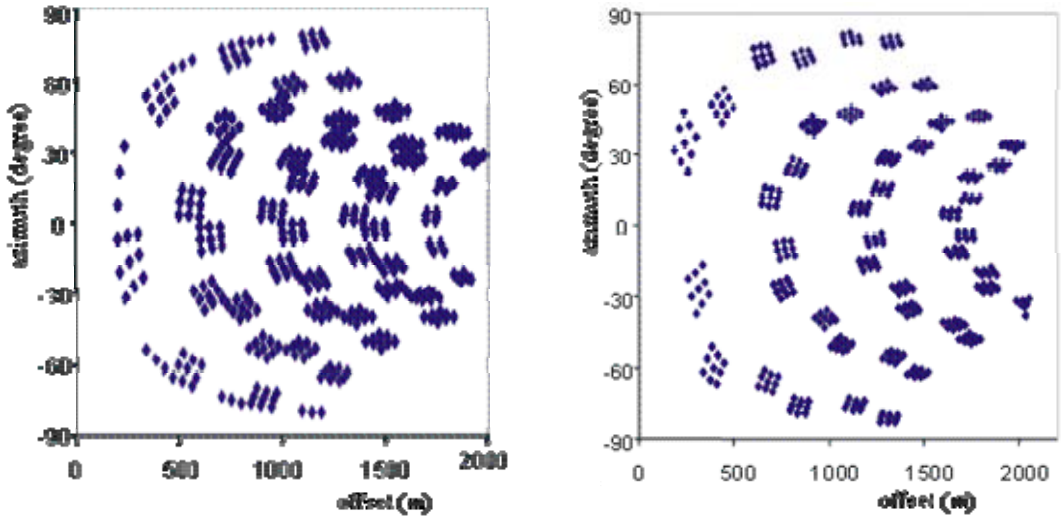

(a) (b)

Figure 4.3.6: Offset-azimuth coverage for the two modelling datasets: (a) Offset-azimuth coverage for Model I, and (b) Offset-azimuth coverage for Model II. The vertical axis is the azimuth in degrees from Y-axis.

4.4 Initial data processing

When analysing azimuthal attributes in the two physical model datasets for the study of fracture detection, I carry out the analysis in two stages: initial data processing, which is the same as that of conventional seismic processing for field data, and azimuthal seismic attribute analysis on pre-stack gathers for fracture detection. The main purpose of initial data processing on this physical modelling analysis is to obtain stack volume to guide travel-time and amplitudes picking on the corresponding pre-stack data for azimuthal anisotropy analysis. In field data analysis for azimuthal anisotropy, the initial processing is also to obtain structure information of the target layer in the survey area and perform an initial appraisal of whether the data are suitable for inferring fracture information through azimuthal seismic attribute analysis.

Like any other analysis based on seismic attributes, the azimuthal amplitude analysis is sensitive to the noise on the data. However the results from amplitude analysis require much more control for data quality than that those from travel-time analysis. For a dataset with high noise level, it is necessary to apply pre-stack noise-removal procedure to reduce noise so as to improve the reliability of the fracture characterisation results.

4.4.1 Processing flow

Before starting the initial data processing, special attention was paid to the noise level on the data. I thoroughly checked it in the data from Model I and Model II, and designed the appropriate processing strategy for each dataset. For the data from Model I, I found that the signal to noise ratio of the data is so high that the noise does not present a problem for analysis based on amplitude attribute (Figure 4.3.5a). Thus, I applied a relatively simple and straightforward processing flow for the data from Model I, which includes: geometry assignment, de-convolution, muting, CDP sorting, velocity analysis, normal moveout correction, stacking and post-stack migration (Figure 4.4.1).

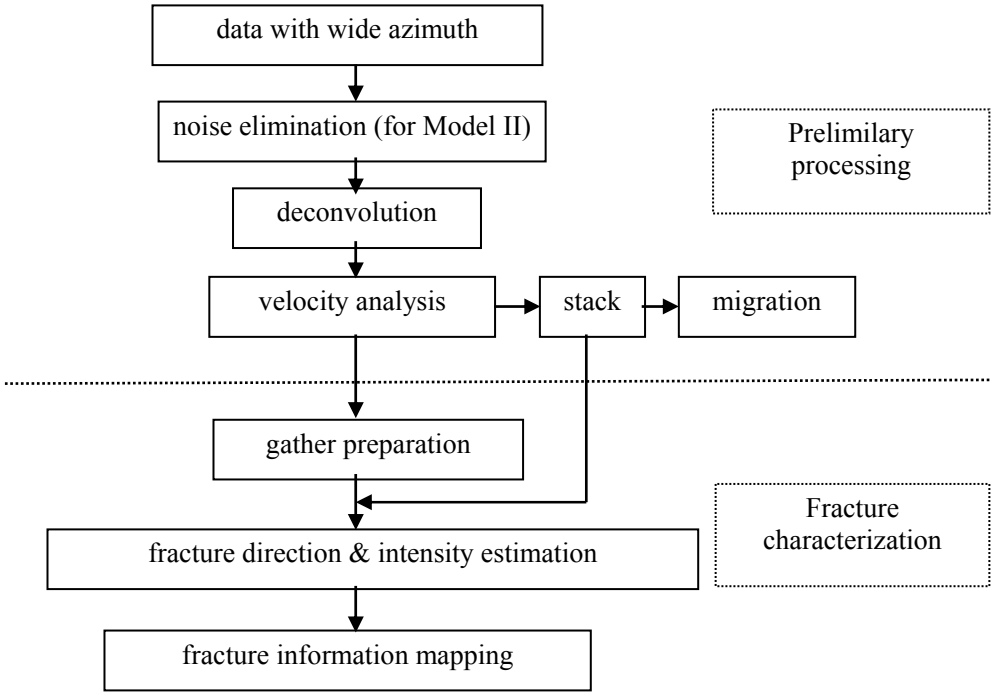

Figure 4.4.1: Processing chart for the data from Model I and Model II.

However for Model II, the data are heavily contaminated with several kinds of noise (Figure 4.3.5b) and the overall data quality in terms of noise level is much lower than that from model I and is similar to poor quality field data. Since the noise can seriously distort the results of fracture information inferred from azimuthal amplitudes analysis, it is necessary to apply a noise attenuation procedure to improve the signal to noise ratio before it can be used for azimuthal seismic anisotropy analysis. In addition to the

processing flow for Model I, I apply a pre-stack noise attenuation procedure for the data processing for Model II.

In order to study the effects of noise on the fracture detection results, I use exactly the same processing procedure and parameters for the data from Model I and Model II, except the noise attenuation applied to Model II. After the pre-stack noise attenuation, the signal level in the data of Model II has been remarkably increased (**Figure** 4.4.2).

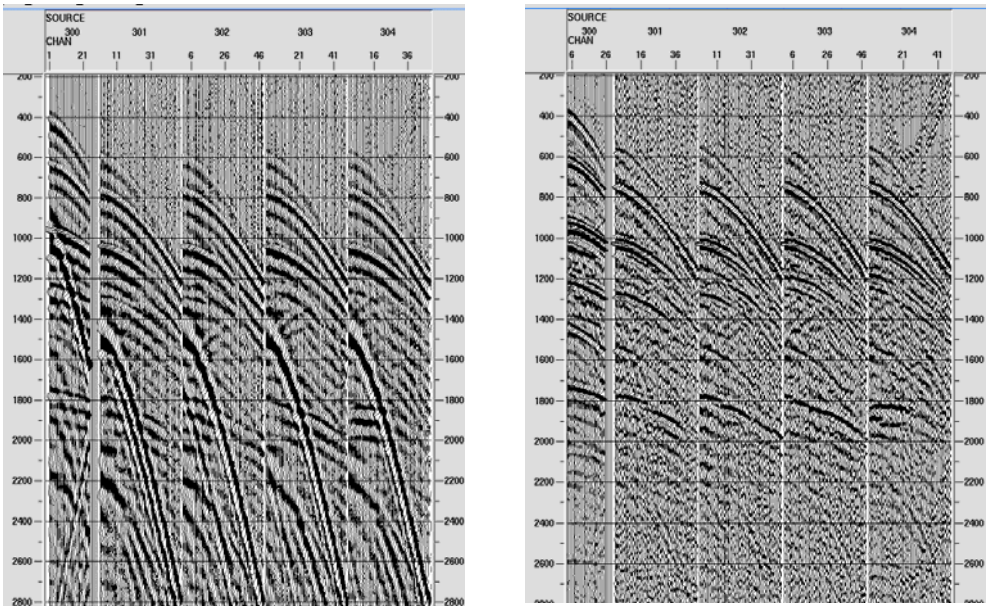

(a) (b)

Figure 4.4.2: Comparison of data (a) before and (b) after noise removal and deconvolution.

4.4.2 Preliminary results

Despite the simple processing flow, the quality of the stack volume for Model I is quite high and almost free of noise effects at the studied interfaces. Figure 4.4.3 shows an inline section extracted from the 3D stack and migration volume of Model II, showing that both the dome and the fault block in the fracture layer are perfectly imaged, which means the azimuthal analysis of the data will have very little effects arising from noise. Figure 4.4.4 shows the inline section extracted from the migration volume of Model I and Model II. The two sections have been matched and trimmed to focus on the basic model shown in Figure 4.2.1b. After noise attenuation processing, there are still some

traces of noise in the data, but the overall noise level is very low relative to the signal energy and the data are acceptable for azimuthal analysis for fracture detection.

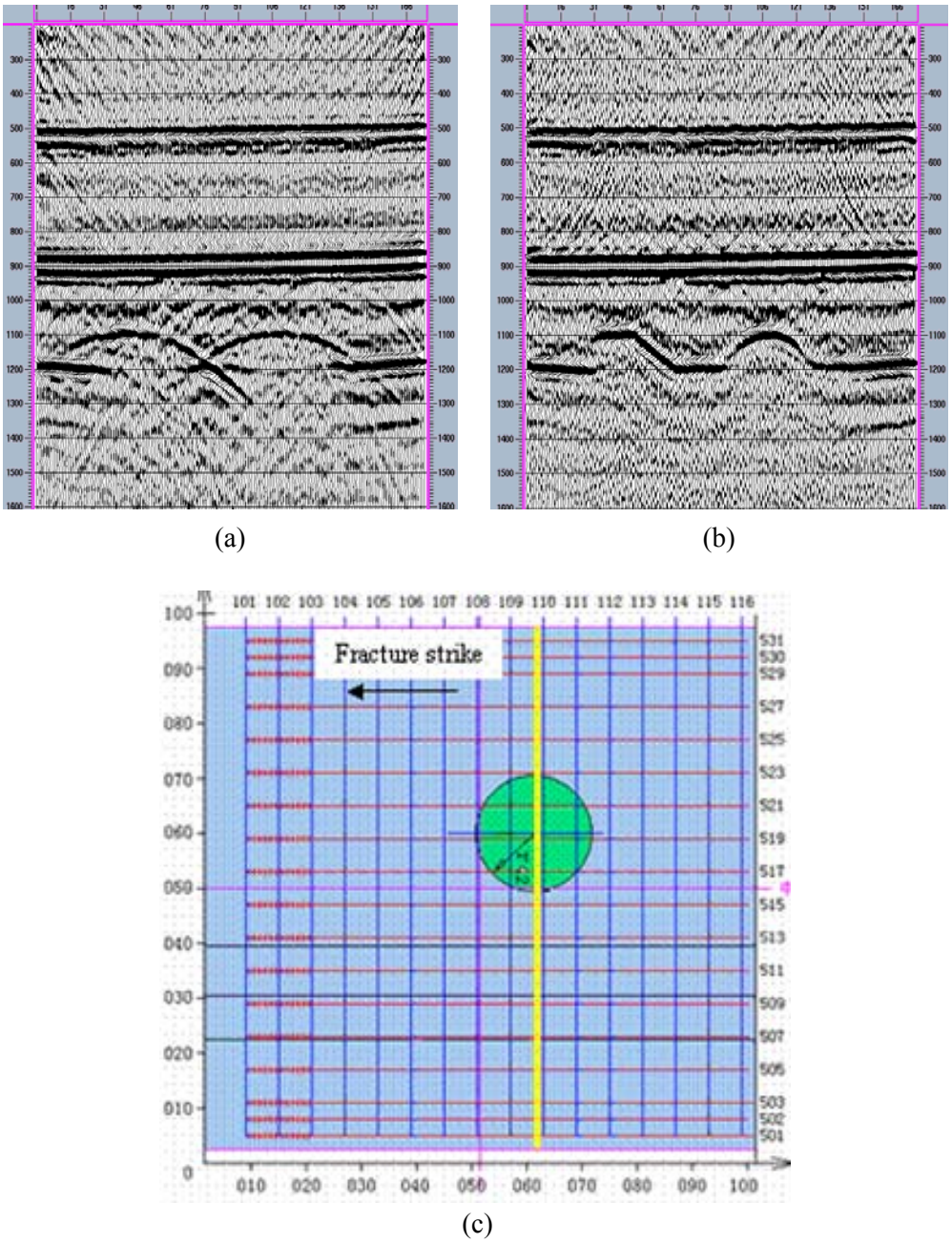

Figure 4.4.3: Inline sections extracted from the 3D stack and migration volume of Model II, showing the azimuthal analysis has very little noise interference. (a) stack section; (b) migrated section; and (c) location of the section (yellow line) on the models.

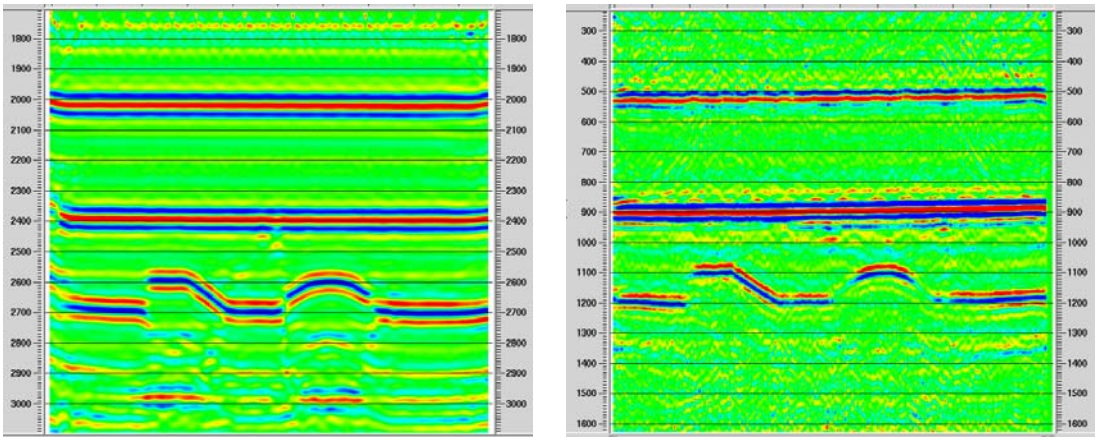

(a) (b)

Figure 4.4.4: Post-stack migration from Model I (a) and Model II (b). The two sections have been matched and trimmed to focus on the basic model shown on Figure 4.2.1b. The processing procedures for the data from Model II include all the procedures applied to the data from Model, and pre-stack noise attenuation.

4.4.3 Dominant frequency

In the initial data processing, through I apply exactly the same predictive deconvolution method and parameters on the two datasets, the time resolutions in the migration volume are slightly different. The time resolution in the results from Model II is a bit higher than that in Model I and the frequency band of the results from Model II is wider than that from Model I (Figure 4.4.4), because I use a smaller prediction gap for the Model II data. However, unlike other seismic inversions where signal frequency is important, what really matters in azimuthal attribute analysis are the signal amplitudes and travel-times. Dominant frequency does not have a significant effect on fracture detection results. Thus the frequency difference between the two datasets does not affect the comparability of the results in terms of azimuthal seismic anisotropy.

4.5 Azimuthal variations of P-wave attributes

Numerical modelling of wave propagation in such a medium predicts that the P-wave seismic attributes, such as travel time, velocity and reflected wave amplitudes will vary with azimuth, diagnostic of fracture-induced anisotropy (Liu and Li et al, 2000; Hall et al., 2003). To verify this, I examine the azimuthal variations in P-wave attributes for

both models. The numerical modelling results in Chapter 3 also indicate the variation. For the Model I data, I investigate whether azimuthal variations in travel time and normal moveout velocity are still observable, then I apply the same analysis on the data from Model II for comparison, in order to study the effects of offset coverage on the fracture detection results from azimuthal seismic analysis.

4.5.1 Anisotropy in NMO velocity analysis

In the initial analysis of the physical model data, I find that phenomena due to azimuthal anisotropy can be seen on the pre-stack gathers. Figure 4.5.1 is a snapshot taken from velocity analysis of Model II data, showing that, after normal moveout correction, the reflection event coming from the top interface of the fracture layer is properly flattened, but the reflection event coming from the bottom interface of the fracture layer shows some irregular time disturbances at offsets larger than 500m. The time disturbances here are not caused by statics, because there is no cause to generate a statics problem in this physical modelling. Also, the time disturbances have different characteristics to those caused by statics, because the time shifts appear on a whole trace rather just on a certain time zone of a trace. There is another possibility, that the time disturbances can be caused by structure, but corresponding location is far from the dome or fault block, where there is no chance to gain travel time variations. Then, the only possibility left is that these time disturbances are caused by the fracture layer in the model.

After further analysis, taking the azimuth of the traces into account, I find that these time disturbances can be perfectly explained using azimuthal seismic anisotropy. The P-wave propagates slower along the direction of fracture normal than along the direction of fracture strike, which means that, for a HTI medium, the travel-time of a reflected seismic wave varies with azimuth. When an intermediate velocity is used to correct the moveout on traces with different azimuth, it over-corrects the moveout of the events in data for the fracture strike direction, but under-corrects the moveout of events in data for the fracture normal direction, and this appears as time disturbances at certain time zones of the traces.

It also suggests that, in field data analysis, if we see similar phenomena and the time disturbance mainly locates on seismic traces with reasonably large offset and different

azimuths, this may indicate the presence of azimuthal seismic anisotropy and further investigation may be needed for confirmation. A simple method is to sort the super CMP gather with similar offset ranges in azimuth sequence. If the time disturbance on the reflective event shows a regular distribution with azimuth, the seismic waves may have travelled through a medium with HTI features.

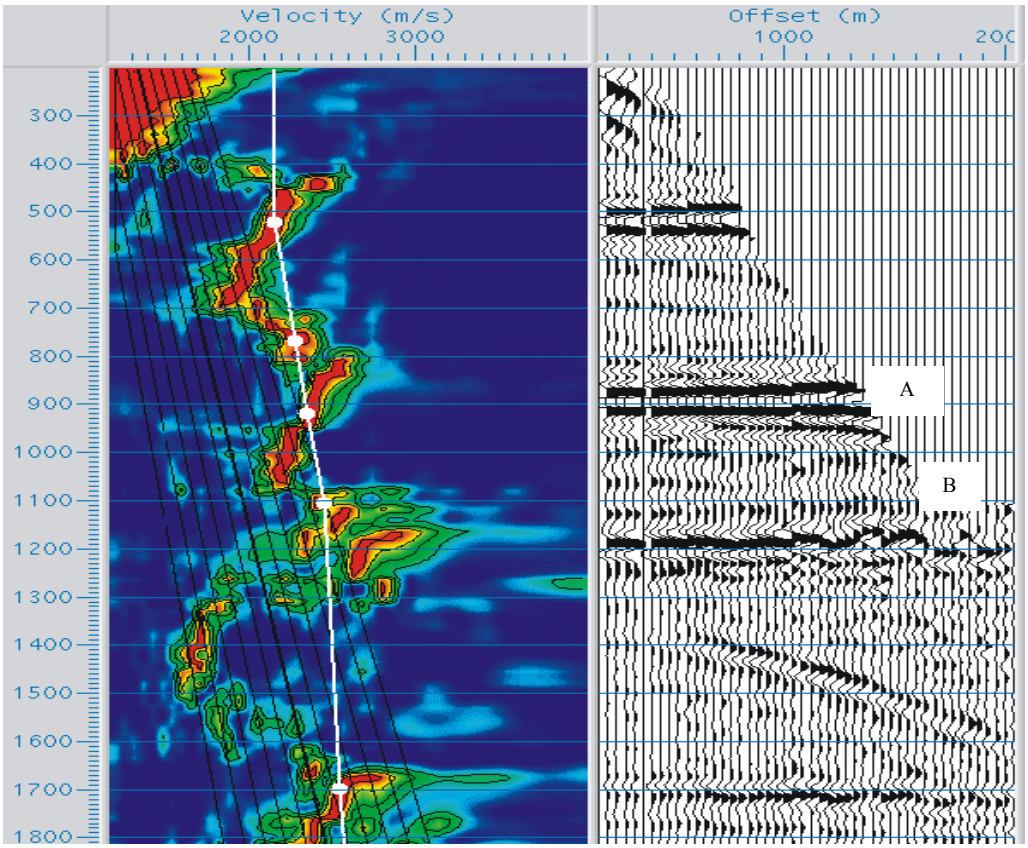

Figure 4.5.1: Azimuthal anisotropic phenomena in velocity analysis. The lower event shows some irregular time variation (point B), because the wave propagates slower along the fracture normal than along the fracture strike. When an intermediate velocity is used to correct the moveout, it over-corrects the moveout of the events in the fracture strike direction, and under-corrects the moveout of the events in the fracture normal direction.

4.5.2 Effects of offset coverage

Figure 4.5.2 show azimuthal attributes variations for Model I. For model I, the maximum offset-depth ratio is 0.9 to the top of the fracture layer, and it is reduced to 0.7 for the bottom of the fracture layer. I simply separate a gather into two sub-gathers according to offset ranges, where the offsets of one gather range from 0m to 800m and the offsets of the other sub-gather range from 800m to 2000m. All traces within one sub-gather are

supposed to have the same offset value. Since the offsets are small relative to the depth of the fracture layer, there is no visible azimuthal time variation on the events from the bottom of the fracture layer (note that there is a small time disturbance on the traces, generated in laboratory data acquisition, not resulting from the fracture layer in the model).

For the data from Model II (Figure 4.5.3), the offset-depth ratio to the top interface of the fracture layer is 2.2 and to the bottom interface of the fracture layer is 1.34. The top event of the fracture layer corresponding to interface 2 is properly flattened, but the bottom event of the fracture layer shows obvious azimuthal variation in terms of residual normal moveout.

Figure 4.5.2 and Figure 4.5.3 reveal that, if offset range is not sufficiently large relative to the depth of the studied interface, the magnitude of azimuthal time variation is very small and not sufficient to provide fracture information.

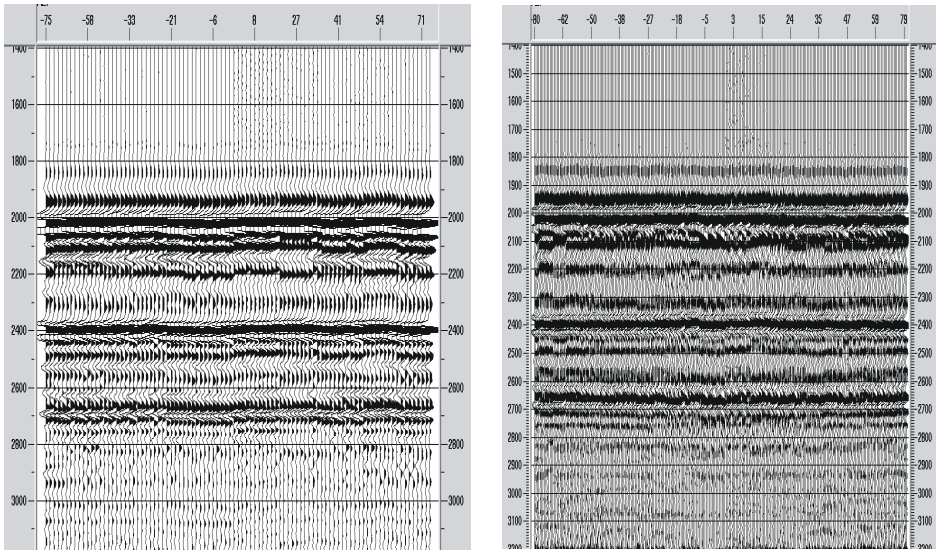

(a) (b)

Figure 4.5.2: Comparison of common-offset CDP gathers sorted in azimuth sequence for Model I. (a) offset range: 0-800 m; (b) offset range 800-2000m. For both offset ranges, the azimuthal variation in traveltime is weak.

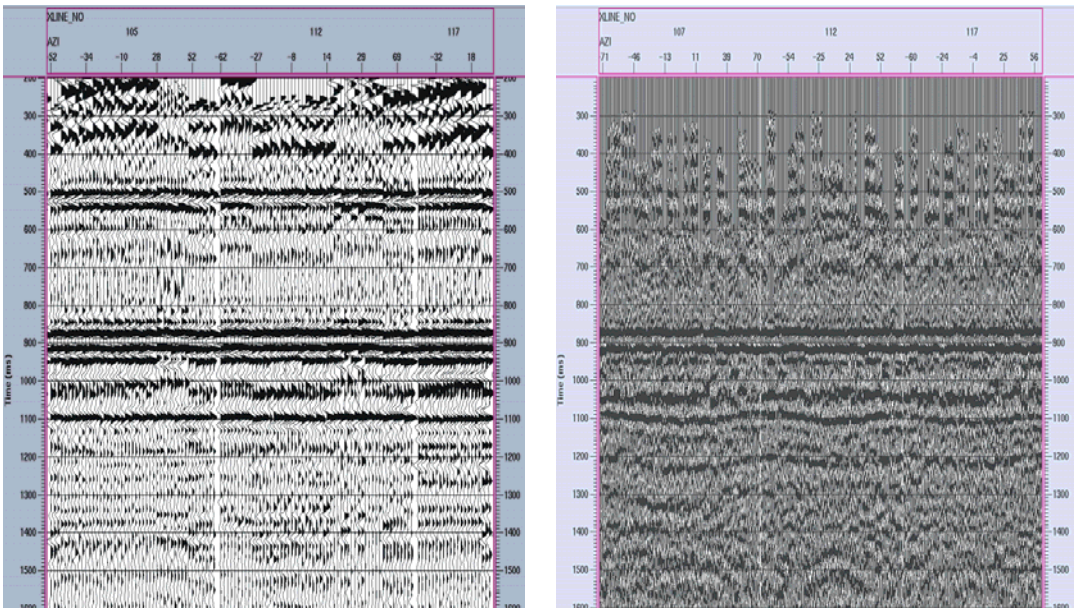

(a) (b)

Figure 4.5.3: Comparison of common-offset CDP gathers sorted in azimuths sequence for Model II; (a) offset range: (0-800) m; (b) offset range: (800-2000)m; CMPs 105, 112 and 117. The sinusoidal variation in the common-offset gather is clear.

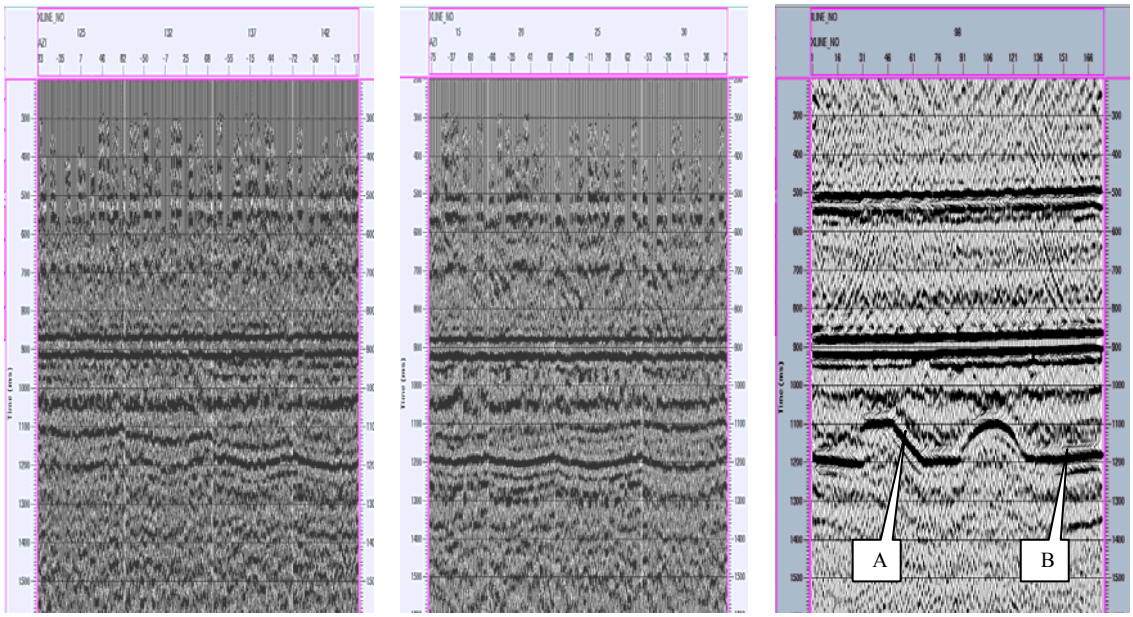

(a) (b) (c)

Figure4.5.4: The azimuthal travel time from different locations. (a) is from point 'A' and (b) is from point 'B' in panel (c), both show clear sinusoidal variation with azimuth.

4.5.3 Azimuthal travel time

First, I perform azimuthal travel time analysis on the data of Model I. Strictly speaking, in azimuthal travel time analysis, all the traces involved at an analysis point should have the same offset to avoid the effects of residual normal moveout. However, the number of traces which meet this condition is usually not enough for azimuthal anisotropy analysis. A practical approach is to take all the traces within a certain offset range as having the same offset, so that more traces can be included for the analysis. Figure 4.5.5 shows a super CMP gather from Model I, which has been binned and sorted into 18 azimuthal sub-gathers with 10^o bin size. After NMO correction, the top reflection event of the fracture layer is properly flattened, however, the bottom reflection event shows azimuthal residual moveout for some azimuth, which is associated with azimuthal velocity variation within the fractured layer. However, due to the lack of offset coverage, this azimuthal variation is not fully developed.

Figure 4.5.6 shows the azimuthal variations of P-wave residual normal moveout for Model II. In gathers with azimuth around -50^o and around 40^o, the bottom event is also reasonably flattened, but in gathers with azimuth around 0^o, the bottom event shows under-correction. However, in gathers with azimuths around -80^o and around 80^o, the bottom event is over-corrected. These phenomena proves the fact that the P-wave propagates slower along the fracture normal than along the fracture strike, while at an intermediate azimuth, the wave propagates with a velocity faster than at the fracture normal direction, but slower than at the fracture strike direction. Consequently, when an intermediate velocity for an intermediate azimuth is used to correct the moveout, it will over-correct the events at the fracture strike direction, but under-correct the event at the fracture normal direction. This physical modelling result confirms these observations, which are more accurate and consistent compared with previous studies due to the improved data quality and experimental setup. However, due to the lack of reasonably large offset coverage, the azimuthal variation in residual move-out has not been ideally developed.

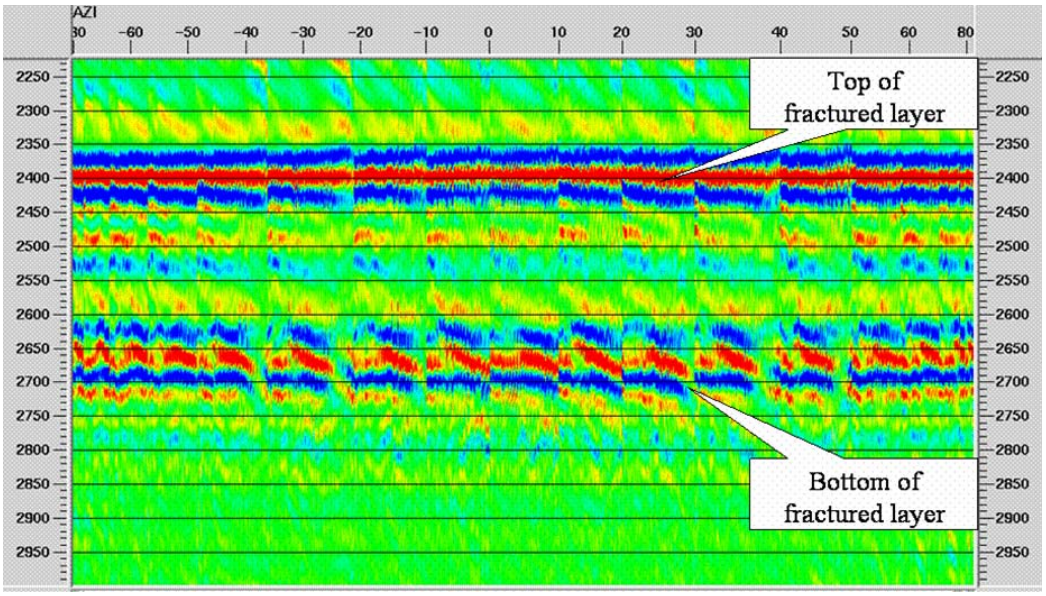

Figure 4.5.5: Azimuthal variations of residual normal moveout for Model I. The super-gather for model I is binned into 18 azimuthal gathers with 10o azimuth bins and 100m offset bins. NMO (normal move-out) correction is applied to the azimuthal gathers using a single velocity function.

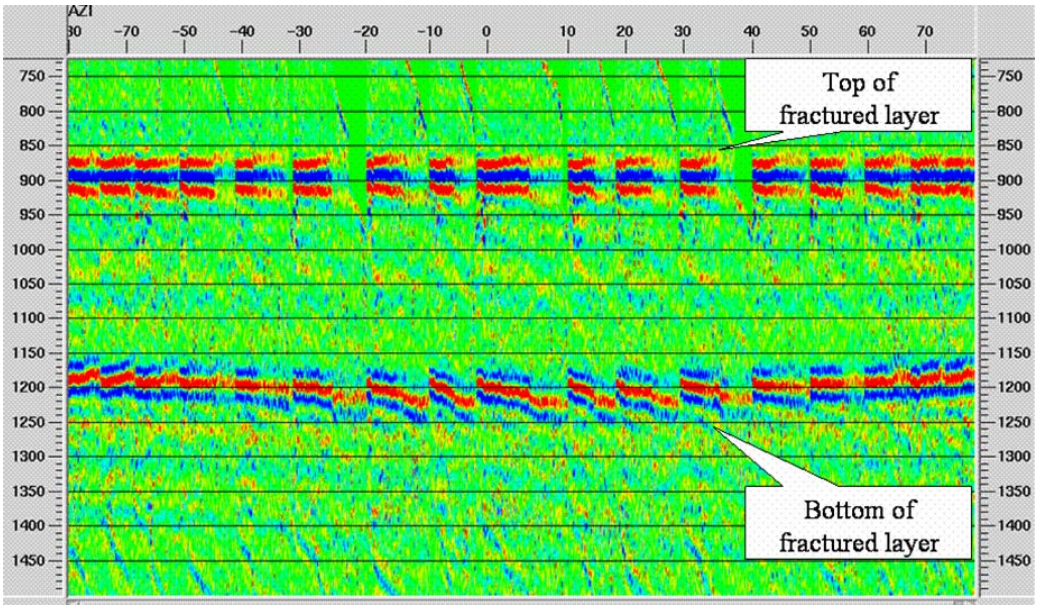

Figure 4.5.6: Azimuthal variations of residual normal moveout for Model II. In gathers with azimuths -50^o and 40^o, the event from the bottom of the fractured layer is properly flattened, and in the gathers with azimuth around 0^o, the event from the bottom of the fractured layer is under-corrected, but in gathers with azimuths around -80^o and 80^o, the event from the bottom of the fractured layer is over-corrected.

4.5.4 Azimuthal velocity

I then perform azimuthal velocity analysis on the data from Model I. I divide the super-gather for normal NMO velocity analysis into six sub-gathers according to azimuth (the azimuth interval is 30°), and carry out velocity analysis separately. Due to the azimuthal symmetry, I always use the azimuth range -90° — 90° instead of 0° — 360° in azimuth grouping, and azimuth 0° denotes the Y axis. Figure 4.5.7 shows the azimuthal velocity analysis on a sub-azimuth supergather (azimuth interval is 30°), and Figure 4.5.7a is the location in the section for the velocity analysis.

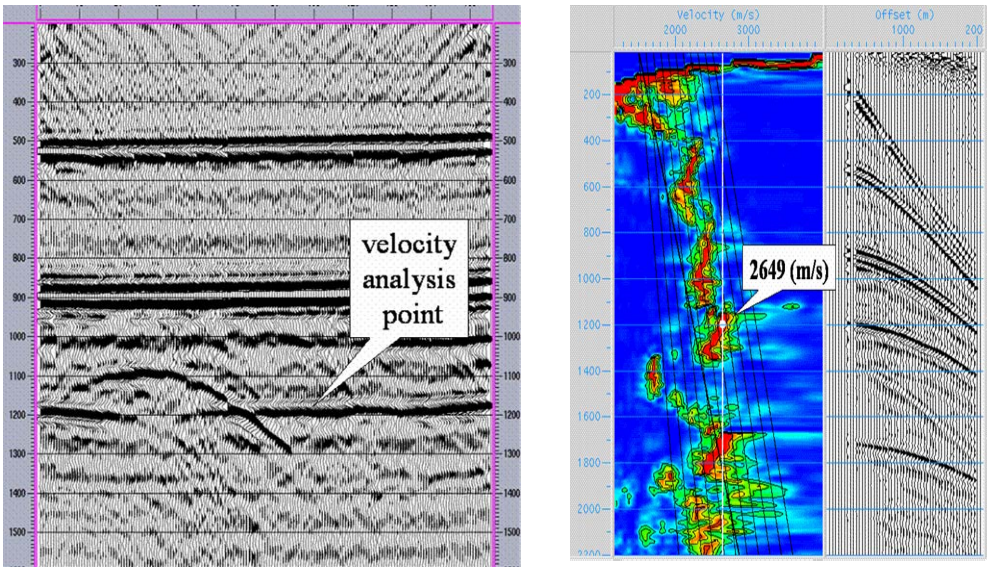

(a) (b)

Figure 4.5.7: Azimuthal velocity analysis (the azimuth interval is 30°).

Figure 4.5.8 shows velocity spectrum sections with different azimuths for the bottom interface of the fractured layer. The white dots on the spectra denote time points for picking velocities and white vertical lines are the reference lines for velocity comparison. Both the white lines on the spectra and the picked velocities on the right show the variation with azimuth, but the variation magnitude is small in comparison with the absolute velocity values. When I plot the velocities in terms of azimuth, it reveals a slightly elliptical distribution with the slow axis coinciding with the fracture normal direction (Figure 4.5.8b).

The above analysis confirms that, on the data from Model I, azimuthal variations in travel time and velocity can be observed, similar to that expected from numerical modelling results (Liu, 2003). However, due to the lack of sufficient offset coverage relative to the depth of the fractured layer, the variation is not well developed. For this reason, a second experiment was conducted for Model II that has an increased offset-depth ratio.

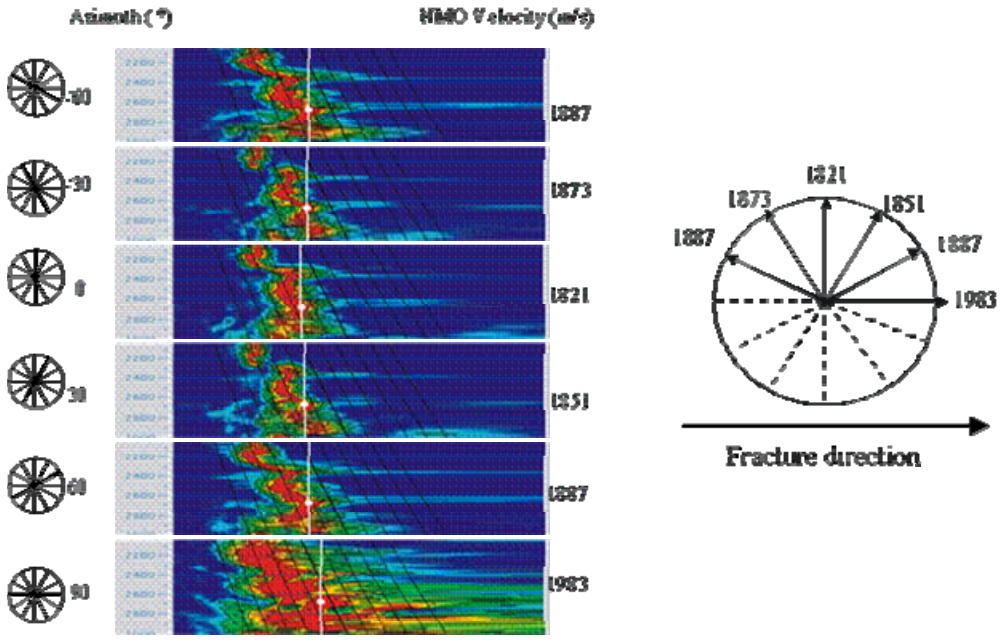

(a) (b)

Figure 4.5.8: Azimuthal stacking velocities for Model I. (a) Azimuthal NMO velocity variations; (b) fitted velocity ellipse. The variation is weak but can still be resolved reliably as indicated by the travel time variation in Figure 4.5.5.

Compared with Figure 4.5.5, the switch from under-correction to over-correction is much more developed in Figure 4.5.6 as a result of increased offset-depth ratio. As shown in Figure 4.5.6, in gathers with azimuths -50^o and 40^o, the event from the bottom of the fractured layer is properly flattened, and in the gathers with azimuth around 0^o, the event from the bottom of the fracture interface is under-corrected, but on gathers with azimuths around -80^o and 80^o, the event from the bottom of the fractured layer is over-corrected. The sinusoidal variation in the common-offset CDP gather is also more profound and significant (Figure 4.5.6b). The azimuthal velocity variation is also much clearer, giving rise to a more flat ellipse (Figure 4.5.9b).

Numerical modelling results reveal that azimuthal P-wave velocities can be approximately described by an ellipse (Liu, 2003) and the major axis of the ellipse coincides with the fracture strike. This can be clearly observed in Figure 3.5.9b. In comparison, the corresponding velocity variations in Figure 3.5.8b for model I are much smaller due to insufficiently large offset coverage relative to the depth of the fractured layer.

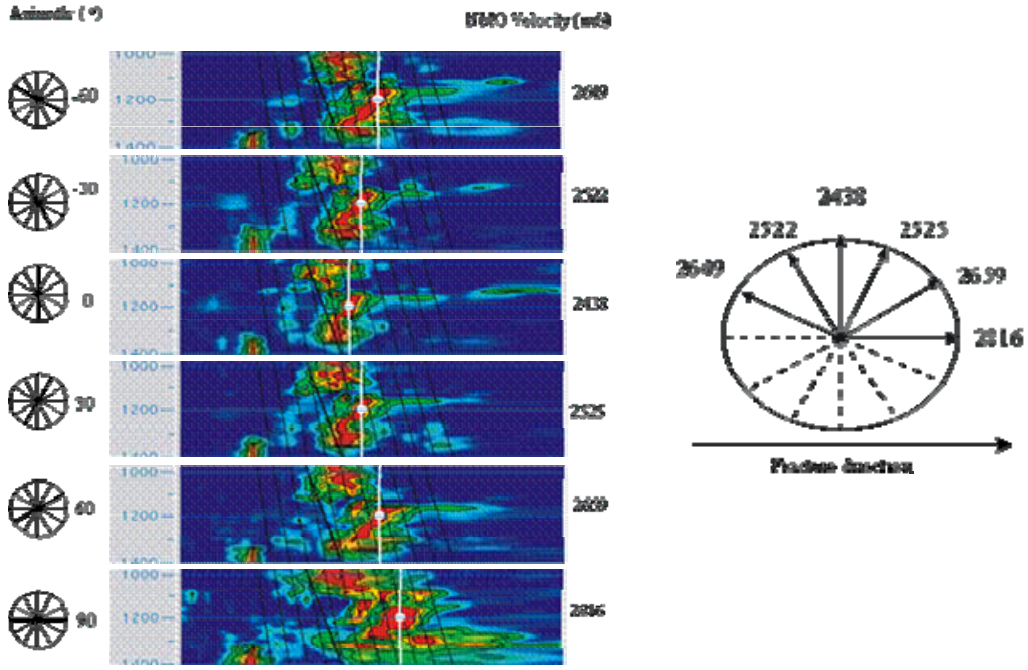

(a) (b)

Figure 4.5.9: Azimuthal NMO velocities. (a) Azimuthal Stacking velocity variation and (b) the fitted velocity ellipse of Model II.

The above 3D physical modelling analysis confirms the numerical findings based on the equivalent medium theory in Chapter 3. However, sufficient offset coverage is required to reveal these variations. The experiment shows that an offset-depth ratio of at least 1.0 is required to quantify these azimuthal variations reliably. Note that there exists a variety of equivalent medium theories for a porous fractured medium (e.g. Hudson 1981; Sayers and Kachanov, 1995; Liu and Hudson et al., 2000). Though the numerical modelling is based on the equivalent medium theory of Hudson (Hudson, 1981; Liu and Hudson et al., 2000), the findings here are not influenced by the choice of the

corresponding theory. It shows that differences in anisotropic effects due to these different wave propagation theories are negligible (Liu and Hudson et al., 2000).

4.6 Estimation and comparison of fracture parameters

4.6.1 Fracture parameters and methods

In the estimation of fracture parameters, I use the major axis direction to represent fracture strike and the major to minor axis ratio to represent fracture density, which means isotropy represented by a circle would give a fracture density of 0.0. As shown previously, the azimuthal variation of P-wave velocity can be approximately described by an ellipse. This is also true for interval travel-time as shown in Li (1999) and for amplitude and AVO gradient (Rüger and Tsvankin, 1997). For travel-time or interval travel-time, the minor axis of the ellipse indicates the fracture strike, and for velocity, the fracture strike coincides with the direction of the major axis. For the amplitude attribute, this depends on the impedance contrast. For a low to high impedance contrast, such as in the physical model studies here, the major axis of the ellipse indicates the fracture strike; while for a high to low impedance contrast, the fracture strike is indicated by the minor axis. The major to minor axis ratio is proportional to fracture density.

I use two methods to extract the fracture information from azimuthal P-wave attributes: full-azimuth surface fitting and narrow-azimuth stacking. The first method fits an elliptical surface to data from all available azimuths and offsets by a least-square fitting technique. The second method divides the data into a number of narrow-azimuth volumes; here I chose 18, with 10^{o} azimuthal bins. Corresponding to these two methods, there are four principal seismic attributes: travel-time, amplitude, velocity and AVO gradient, which may be used to extract the fracture information. The surface fitting method is suitable for the travel-time and amplitude attributes. The narrow-azimuth method is suitable for the velocity and AVO gradient attributes.

Both methods require the picking of travel-time and amplitudes of the top and bottom of the target events on the pre-stack volume. Manual picking is impossible due to the workload and possible human picking errors. There are many tools to carry out time picking. In this physical modelling analysis, I developed an automatic time and

amplitude picking method for pre-stack data by calculating the envelopes of the traces and picking the maximum envelop amplitude. To ensure reliable travel-time and amplitude picking, the events are first manually picked on the post-stack volumes and then used as control points for pre-stack automatic picking. All travel-time and amplitude attributes are picked in this way.

The above methods and attributes analysis were applied to both datasets. I compared these results in order to evaluate the merits of different methods and different attributes, and assess the effects of noises, acquisition parameters and azimuthal structure variations on these attributes.

4.6.2 Results and comparison

Here I show the results for four attributes for comparison: top amplitudes (reflection from the top of the fracture layer) and its AVO gradient, interval travel-time and bottom travel-time (travel time of the bottom reflection event). Excepting for the gradient attribute, the other three attributes are analysed using the surface-fitting method; the AVO gradient is analysed using the narrow-azimuth stacking method.

For Model I, the surface-fitting method applied to the top amplitude attribute gives the best results (Figure 4.6.1a). The fracture strike is in the horizontal direction, and the fracture density is about 0.2, with a very uniform distribution, indicating a single set of fractures. This agrees with the physical model. Also, the underlying structural features, as expected, do not affect the results. In contrast, the AVO gradient attribute by narrow-azimuth stacking does not give satisfactory results (Figure 4.6.2a). The estimated fracture strike and fracture density are similar to those in Figure 4.6.1a, but the distribution shows stripes parallel to the vertical direction, indicating the effects of the acquisition footprint, enhanced by the binning and stacking process due to the lack of sufficient offset coverage relative to the depth of the fractured layer.

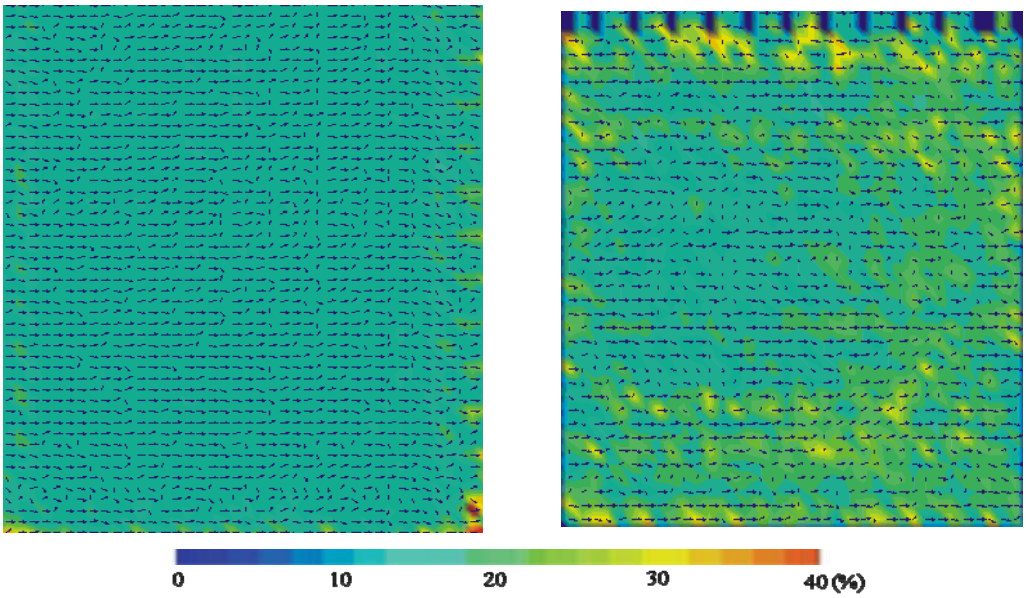

Figure 4.6.1: The fracture characterisation from azimuthal amplitude (reflection from the top interface of the models) analysis on (a) model I and (b) model II. The colour displays the percentage fracture intensity interpreted from the ratio of the major to minor axis of the attribute ellipse. The superimposed short lines indicate the fracture strike.

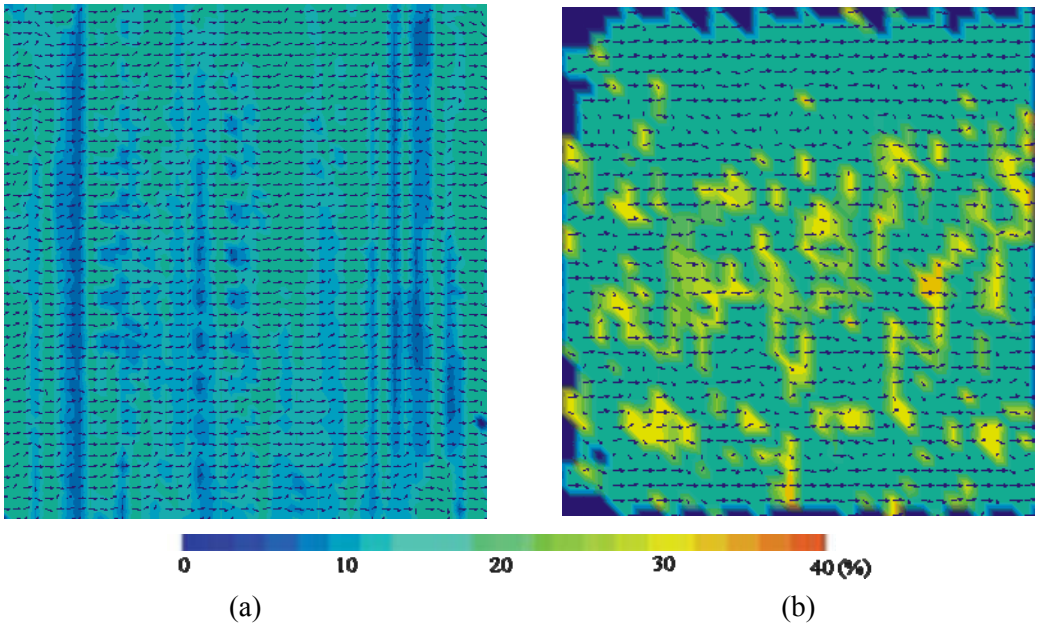

Figure 4.6.2: The fracture characterisation from AVO gradient attributes analysis on (a) Model I and (b) Model II. The colour contour displays the percentage fracture intensity interpreted from the ratio of the major to minor axis of the attribute ellipse. The superimposed short lines indicate the fracture strike. The stripes parallel to the y-axis for Model I indicate the effects of the acquisition footprint.

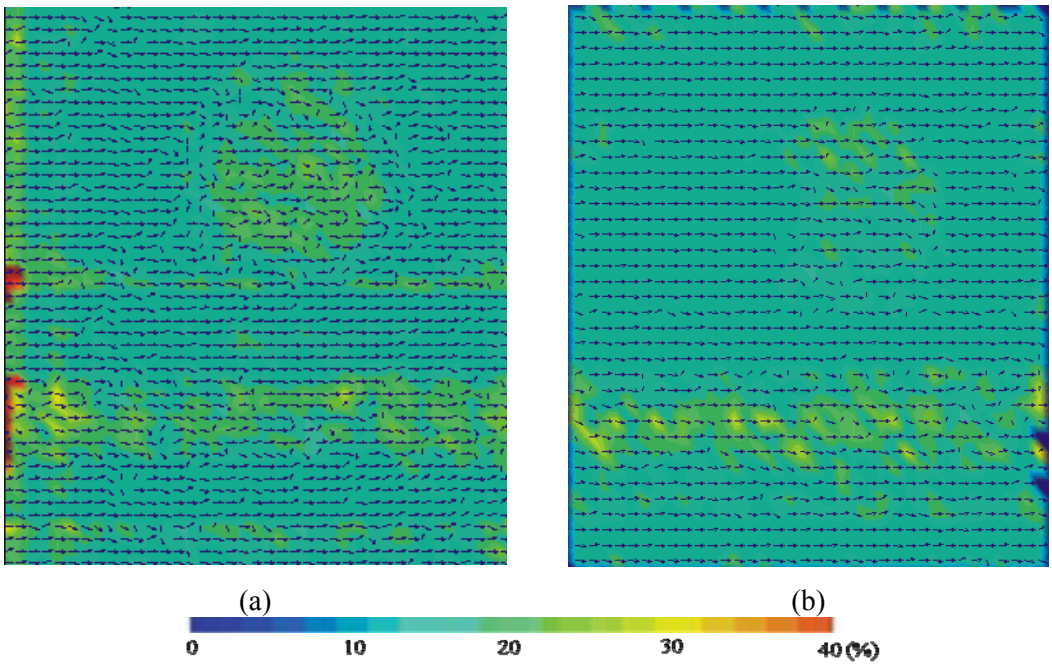

Figure 4.6.3: The fracture characterisation from interval travel-time attributes analysis on (a) model I and (b) model II. The colour contour displays the percentage fracture intensity interpreted from the ratio of the major to minor axis of the attribute ellipse. The superimposed short lines indicate the fracture strike.

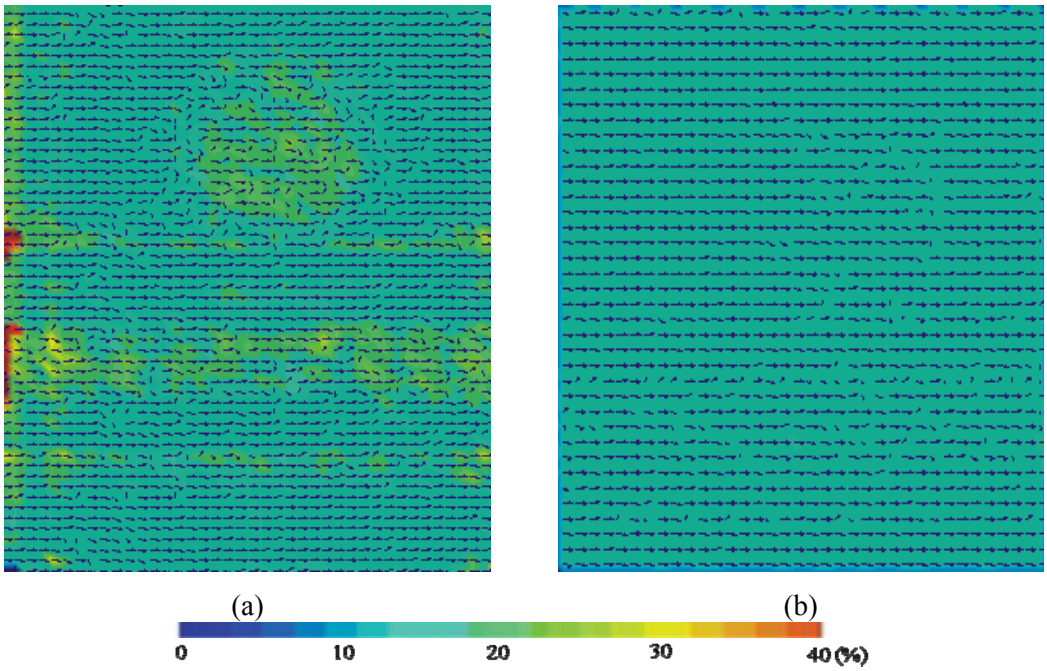

Figure 4.6.4: The fracture characterisation from bottom travel-time attributes analysis on (a) model I and (b) model II. The colour contour displays the percentage fracture intensity interpreted from the ratio of the major to minor axis of the attribute ellipse. The superimposed short lines indicate the fracture strike.

The result from the interval traveltime by the surface-fitting method shows a very clear structural imprint of the dome and the fault block (Figure 4.6.3a). In areas outside these two zones, the estimated fracture parameters show a very uniform distribution with the fracture strike along the X-axis and an average fracture density of 0.2, agreeing with the physical parameters very well. The result from the bottom travel-time shows similar features to the interval travel-time (Figure 4.6.4a).

In contrast, for model II, the results from the amplitude attribute are affected by the presence of noise on the data, and are less reliable (Figure 4.6.1b). The orientation estimation varies more significantly compared with those in Figure 4.6.1a for model I, and the estimated fracture density is scattered due to noise interference. The binning and stacking process further enhance the noise effects, as shown in Figure 4.6.2b.

It is the surface-fitting method applied to the bottom travel-time attribute which gives the best result (Figure 4.6.4b), with the fracture orientations mainly along the horizontal direction, and with a very uniform distribution of fracture density. Also the effects of the structural imprint are reduced by the increased offset-depth ratio to the fracture layer, which means the magnitude of the anisotropic variation is greater than that caused from structural variation. The interval travel-time gives similar results but is slightly affected by the presence of the fault (Figure 4.6.3b).

4.7 Discussion

I have analysed the azimuthal anisotropy in both physical modelling datasets, regarding the physical model data as field data, to estimate fracture parameters and obtained the following findings.

Choice of Attributes

The amplitude is the most sensitive attribute. For data with high signal to noise ratio, even when the offset-depth ratio to a target interface is very small (*offset to depth equals 0.9*), fracture parameters can still be determined accurately from the amplitude attributes (Figure 4.6.1a). However, the presence of noise will significantly distort the result (Figure 4.6.1b) even with sufficient offset coverage (*offset to depth ratio equals 2.0*).

Therefore, for the use of the amplitude attribute, it is more important to reduce the noise level and preserve the reflection amplitude than to increase the offset coverage.

The use of travel-time attributes requires sufficient offset coverage to allow the azimuthal travel-time variation to be sufficiently developed. For insufficient coverage (offset-depth ratio is less than 1.0), the attribute will be heavily influenced by the structural imprint as well as the acquisition foot print (Figures 4.6.3a and 4.6.4a), and these effects are substantially reduced when the offset coverage is doubled (Figures 4.6.3b and 4.6.4b).

Application of methods

The surface fitting method to all offsets and all azimuths is preferred to the narrow-azimuth method. The latter enhances the acquisition footprint when the offset-depth ratio is not sufficiently large (Figure 4.6.2a), and also enhances the noise response even the offsets are doubled (Figure 4.6.2b), though the acquisition footprint is reduced.

Acquisition parameters

The offset and azimuthal coverage is critical for the success of using azimuthal P-waves for fracture detection. The offset-depth ratio to the target interface is a good parameter to gauge whether the offset coverage is sufficient or not. The experiment for Model I reveals that the offset-depth ratio to the target interface should at least be larger than 1.0. Only in a noise-free environment, may there be sufficient sensitivity from the amplitude attribute to resolve the fracture parameter for offset-depth ratio to the target interface approaching 0.9 (Figure 4.6.1a). Large offset coverage makes it possible to use the travel-time attributes. A reliable estimation from travel-time attributes required an offset-depth ratio of 1.0 or more (Figure 4.6.3b and 4.6.4b).

Effects of structure

The azimuthal structure variation will leave a significant imprint on the estimated results, particularly if the offset-depth ratio is not sufficiently large (Figures 4.6.3a and 4.6.4a). However, these effects may be compensated for by increasing the offset coverage and by the use of travel-time attributes. When the magnitude of azimuthal variation due to

anisotropy exceeds that due to structural variations, the structural imprint will be significantly reduced (Figures 4.6.3b and 4.6.4b).

The effect of offset-depth ratio in fracture detection is more obvious in CMP gathers analysis. Figure 4.7.1 shows an inline migration section crossing the middle of the dome and the fault block of the physical model. Two areas in the section are selected to analyse the effect of structure and offset-depth ratio in fracture detection. Figure 4.7.2a displays four consecutive CMP gathers at area A, with offset ranging from 0m to 800m, and the traces within a gather are sorted in azimuth sequence. There is a weak sinusoidal time variation at the bottom event of the fractured layer (half period). The data at area B (Figure 4.7.2a) are the same as that in Figure 4.7.2a, but there is no obvious sinusoidal time variation at the bottom event. This shows that, when the offset to depth ratio is small, the effects of seismic anisotropy can be reduced by the presence of structural variation.

Figure 4.7.3 displays the same four consecutive CMP gathers with offset ranging from 800m to 1600m. Figure 4.7.3a displays the data in area A. The travel time has a very obvious sinusoidal variation at the bottom event of the fracture layer (half period). In the data of area B, obvious sinusoidal time variation at the bottom event of the fractured layer can also be seen. This shows that, with a larger offset to depth ratio, the effects of seismic anisotropy become more obvious. The effect of structural variation can be greatly reduced by increasing the offset-depth ratio.

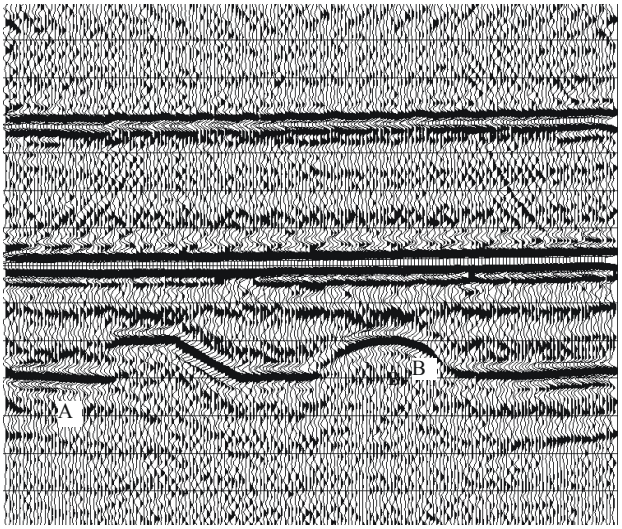

Figure 4.7.1: Migrated inline section of Model II, which crosses the middle of the dome and the fault block. Two points (A & B) are selected to analyse the effect of structure and offset-depth ratio on fracture characterisation, where A is at the flat bottom of the fracture layer, B is at the slope side of the dome.

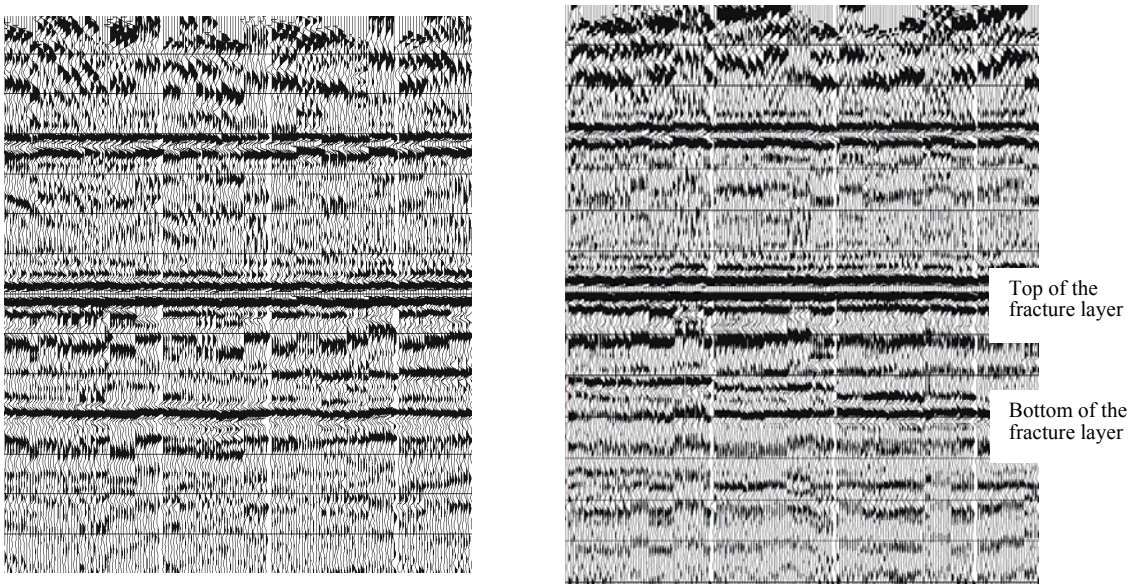

(a) (b)

Figure 4.7.2: Four consecutive CMP gathers at different points on model I. (a) at point A; the offset ranges from 0 to 800m; the traces within each gather are sorted in azimuth sequence. There is a weak sinusoidal variation at the bottom event of the fractured layer (half period); (b) at point B, the same as that in (a) but no obvious sinusoidal variation at the bottom event.

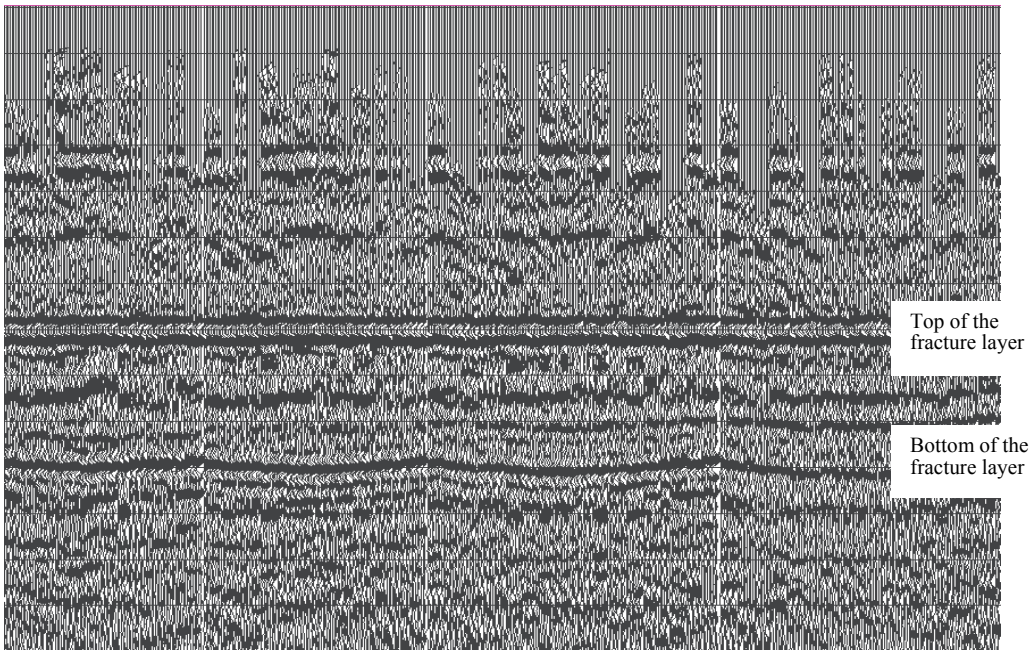

(a)

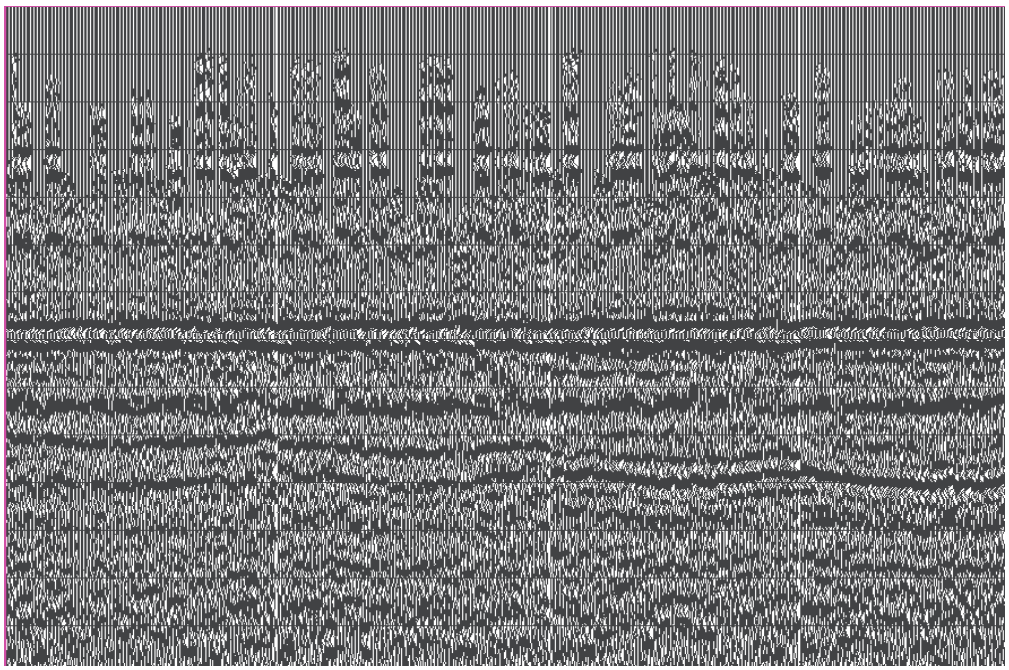

(b)

Figure 4.7.3: Four consecutive CMP gathers at different points on model I. (a) at point A, and the offset ranges from 800 to 1600m. The traces within each gather are sorted in azimuth sequence. There is very obvious sinusoidal variation at the bottom event of the fractured layer (half period); (b) at point B; the same as that in (a) and obvious sinusoidal variation at the bottom event can also be seen.

4.8 Conclusions

In the two physical modelling studies for fracture detection, I have carried out azimuthal anisotropy analysis on the two P-wave datasets equivalent to 20km^2 each and confirm the numerical modelling results based on the equivalent medium theory. Two methods (full-azimuth/full-offset and narrow-azimuth/full-offset) have been used and four seismic attributes are analyzed for fracture parameter estimation. The results from the narrow-azimuth stacking method appear to be influenced by the acquisition footprint and the noise, but those from full-azimuth and full-offset surface fitting agree with the physical parameters.

The offset-depth ratio to the target interface is a key parameter for the successful application of azimuthal analysis methods on P-wave data. It affects the choices of attributes and choice of processing methods. Smaller offset-depth coverage may only be applicable to amplitude attributes with high quality data; whilst large offset coverage makes it possible to use travel-time attributes, which are less sensitive to noise, reducing the effects of the acquisition footprint as well as the structural imprint. A reliable estimation from travel-time attributes required an offset-depth ratio of 1.0 or more.

The amplitude is the most sensitive attribute. It is particularly sensitive to the presence of noise but not very sensitive to variation of the offset-depth ratio. A small amount of noise will significantly distort the fracture detection results, even with sufficient offset coverage (offset to depth ratio reaches 2.0). For data with a high signal to noise ratio, even when the offset-depth ratio to a target interface is very small (offset to depth ratio equals 0.9), reliable fracture information can still be estimated from amplitude attribute. Therefore, for the use of the amplitude attribute, it is important to reduce the noise and preserve the amplitude than just increase the offset coverage.

Fracture detection results from the azimuthal travel-time analysis at more dependent on the offset to depth ratio, because it needs large offset coverage to allow the azimuthal variation to be sufficiently developed. If the offset coverage is not large enough (offset to depth ratio is less than 1.0), the results will be heavily influenced by structural imprints as well as acquisition footprints.

Chapter 5

Seismic anisotropy analysis in Clair OBC data

In this chapter I perform azimuthal anisotropy analysis on both P- and PS-wave data, and then carry out shear-wave splitting analysis to characterize the fracture properties of the reservoirs. I also apply PSTM (Pre-Stack Time Migration) approach to the converted-wave data to improve imaging and compensate for possible structure-related azimuthal variations. This chapter is the extension of my work in Chapters 3 and 4 to real field data. A major difference is a greater degree of complexity in the real earth and a lower signal to noise ratio.

5.1 Introduction

The Clair Oil Field lies about 75 km west of the Shetland on the UK continental shelf, and the water depth is around 140m. Oil production from the reservoir started in 2005. The reservoir comprises Devonian-Carboniferous fractured formations beneath a base Cretaceous unconformity with an oil column about 600m (Coney et al. 1993). Studies on oriented core and field analogue data indicate that the Clair reservoir contains a variety of fracture types, orientations and scales. Effective oil production is dependent on the ability to characterize the fracture systems. A 3D Ocean Bottom Cable (OBC) dataset with wide azimuth was acquired in 2002, which is ideal to carry out fracture characterisation for the reservoir. Here, I analyze a patch of the 3D OBC data to assess whether seismic anisotropy can be observed and how it can be used to infer fracture information for the reservoir.

5.2 Review of anisotropy analysis in the reservoir

A series of approaches have been used to evaluate the potential of seismic anisotropy for fracture characterization in the Clair reservoir which is commonly supposed to be a

fracture-type reservoir. The first initiative was the acquisition of a multi-azimuth walkaway VSP in October 1996 to investigate whether the azimuthal variations of P-wave attributes could aid fracture characterization (Horne et al. 1998). This led to a feasibility study of using crossed 2D and 3D data from older surveys to map fracture orientations and density. Smith and McGarrity (2001) successfully correlated the fracture density measured from velocity anisotropy to flow rates in production wells. However, the intersecting points from these older surveys are very sparse. In May 2000, three 2D OBC lines coinciding with the walk-away VSP were acquired, serving as a feasibility test for the 3D OBC survey.

The VSP data and the data from three OBC lines from the Clair field have previously been studied by (Edinburgh Anisotropy Project (EAP) in 2003. The results show no significant azimuthal variations in the overburden above the base Cretaceous. There is also no visible converted wave splitting in the overburden, which is further confirmed by the analysis of the VSP data. However, for the target layer, the presence of azimuthal anisotropy can be identified and even quantified. The P-wave and PS-wave (PS-wave) interval velocity over the reservoir show 10% to 15% azimuthal variations (Fig 5.2.1).

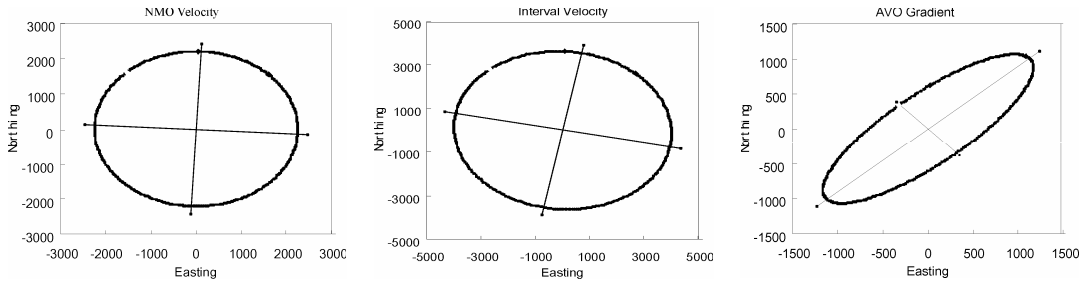

(a) (b) (c)

Figure 5.2.1: Azimuthal distribution of moveout velocities at the intersecting point from the 2D data: (a) 2D NMO stacking velocity for the overburden, and (b) 2D interval velocity of the target. (c) shows the variation of the interval velocity of the target from the super gather with six narrow-azimuth bins (from EAP annual report 2003).

The 2D OBC data have only an average signal to noise ratio, which may limit the reliability of the results to some extent.

5.3 Data Acquisition

Acquisition geometry

In the acquisition of the 3D OBC data, four parallel multi-component cables were deployed on the seabed (Figure 5.3.1). Each cable is 6 km long with 240 receiving channels, and the receiver group interval is 25 m. There are in total 45 sailing lines in each patch with 243 shots per sailing line, and the interval between two adjacent sailing lines is 245m. Though the original sampling rate is 2ms, the data I received for the fracture characterisation has been re-sampled to 6ms to reduce the overall data size.

Figure 5.3.2 shows the offset-azimuth distribution of a typical CMP super-gather. The traces within each gather display wide azimuth-offset coverage, which is essential for azimuthal anisotropy analysis. The colour panel on the right displays the CMP distribution and fold information. The red spot indicates the location of the analysis point having the offset-azimuth distribution on the left.

Clair Patch14	
Sail line spacing	245m
Sail lines per patch	45
Shot interval	25m
Shots per sail line	243
Receiver lines per patch	4
Group interval	25m
Groups per receiver line	240
Maximum inline offset	2500m
Maximum xline offset	2500m
Sampling rate	2ms
Records length	4s

(a)

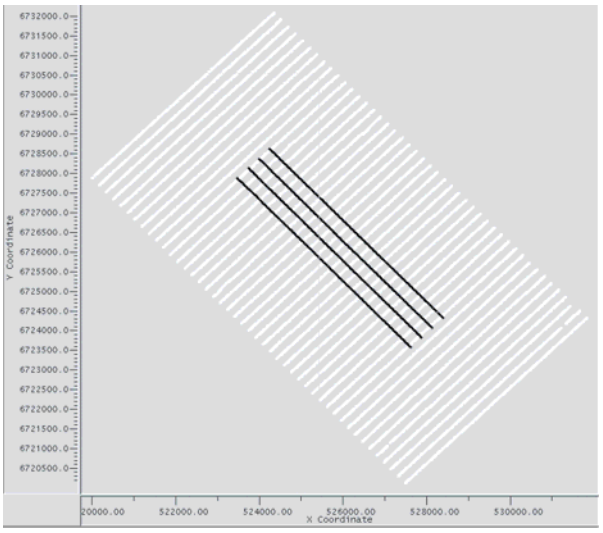

(b)

Figure 5.3.1: Acquisition parameters for the Clair 3D OBC data. (a) Acquisition parameters; (b) The deployment of sources and receivers in the patch. The white lines indicate the shot locations and the four black lines indicate the OBC cables.

Data quality

Though multiples are normally a problem for the streamer seismic data due to the hard

seabed in the area, it does not appear to be a big issue for the OBC data, and the data I received for the analysis had already been pre-processed and performed with multiples suppression. However, the overall signal to noise ratio of the data is poor (Figure 5.3.3 and Figure 5.3.4, note that only two spreads of a shot gather is displayed).

I process the vertical component data first to assess if any azimuthal variations in P-wave attributes can be observed in the OBC data. The P-wave azimuthal attribute analysis includes initial data inspection, brute stack for assessing image quality, analysis of azimuthal variations of P-wave stack velocity and AVO gradients. I apply exactly the same workflow as for the physical modelling in Chapter 4. AVO gradients are analysed for the event at 1.4s, the stack velocity and bottom travel time are used for the event at about 1.8s and the interval travel time applied is between 1.4 and 1.8s.

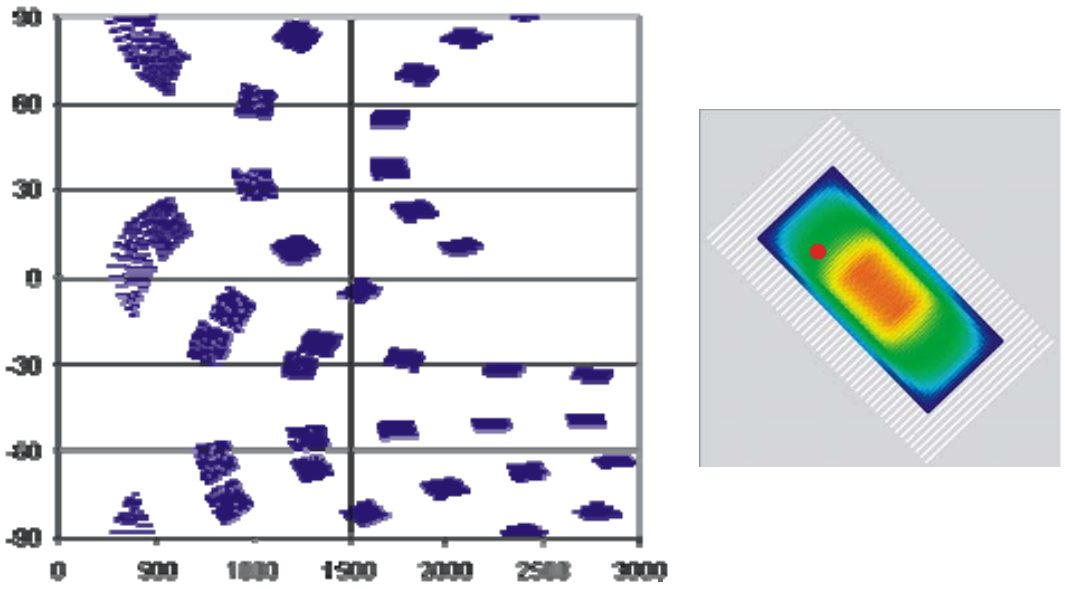

(a) (b)

Figure 5.3.2: Offset-azimuth coverage of a super CMP gather (a). The horizontal axis is the offset in metres, and the vertical axis is azimuth in degrees; (b) the CMPs distribution and fold information of the acquisition patch. The red spot indicates the point having the offset-azimuth distribution on the left.

In the PS-wave data, the time interval of interest is between 2.5s and 3.2s. Notice that although some reflections are visible in the R-component data, it is hard to discern reflection signals in the T-component data (Figure 5.3.4).

Offset coverage

According to the brute stacks (Figure 5.4.1), the target interval in the stack section is between 1.4 and 1.8s. The maximum offset of the original data is around 3000m, but there is no data for the far offset traces at the target interval due to interference with refracted arrivals. The maximum effective offset for the target layers is less than 2000m (Figure 5.3.5). This means that the effective offset range for the target must be considered instead of the apparent offset range from the acquisition.

Figure 5.3.6 shows the shot coverage with respect to a receiver. The red area denotes the sources which can be recorded by the receiver (the green point). However, only a smaller range of recorded sources (within the green circle) can be used for azimuthal anisotropy analysis, because the sources outside the circle contain no information at all (Figure 5.3.5).

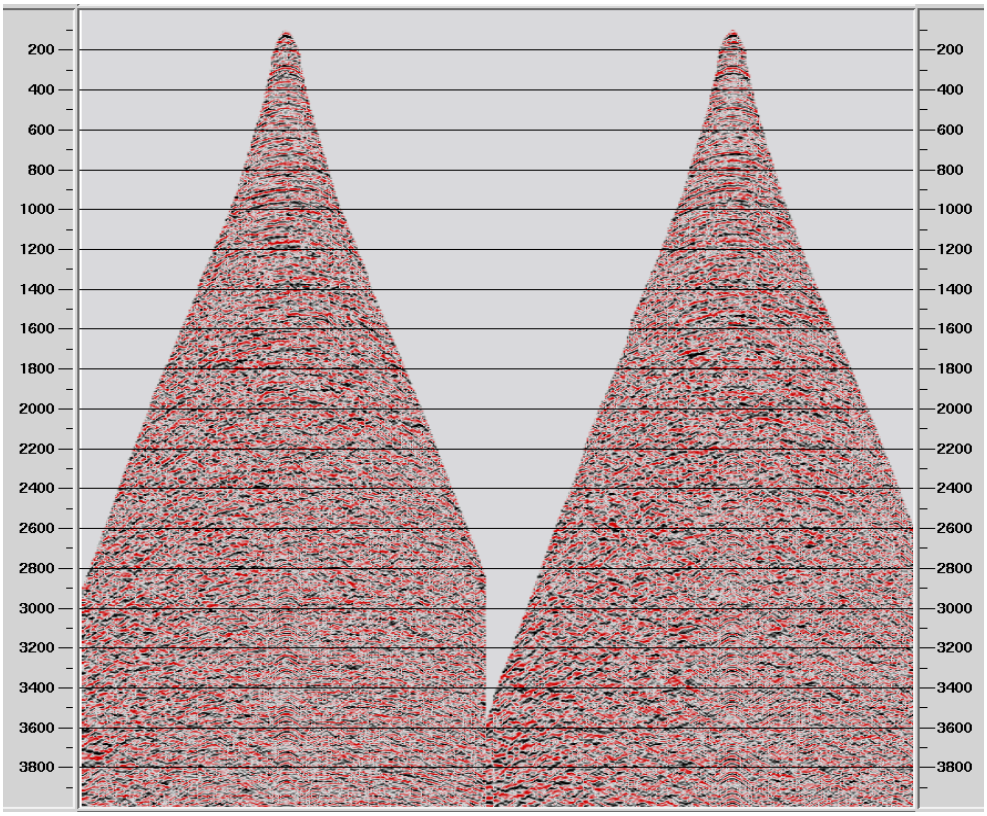

Figure 5.3.3: Z-components in shot gather (two spreads of a shot gather) from the 3D OBC dataset. The reflection events of interest are between 1.4s and 1.8s on the traces with zero offset.

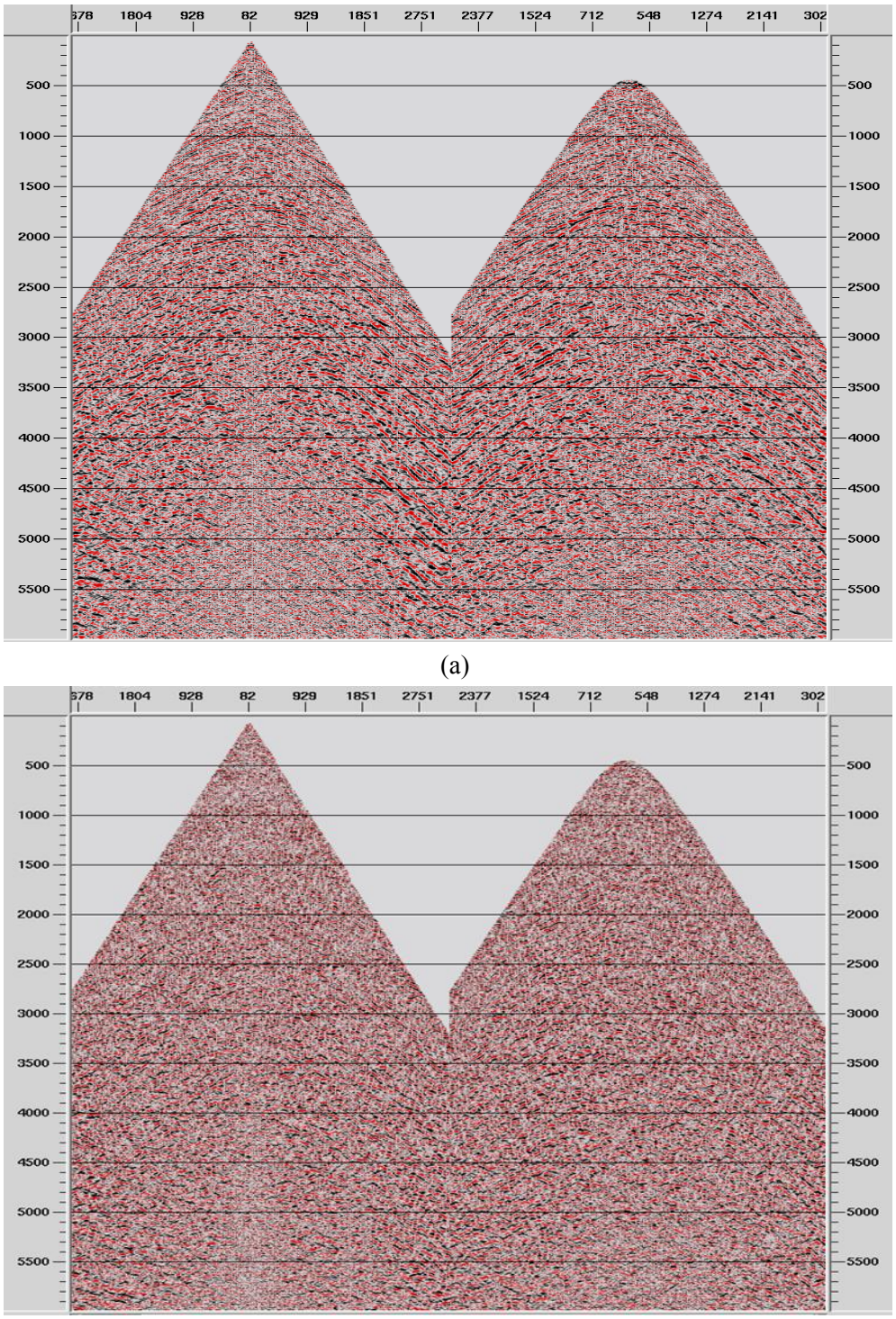

(a)

(b)

Figure 5.3.4: R-component (a) and T-component (b) of the OBC data from the shot gather (two spreads). The target interval is between 2.5s and 3.2s for the traces of aero offset. Reflection events can be observed on the data of R-component, but not on the T-component.

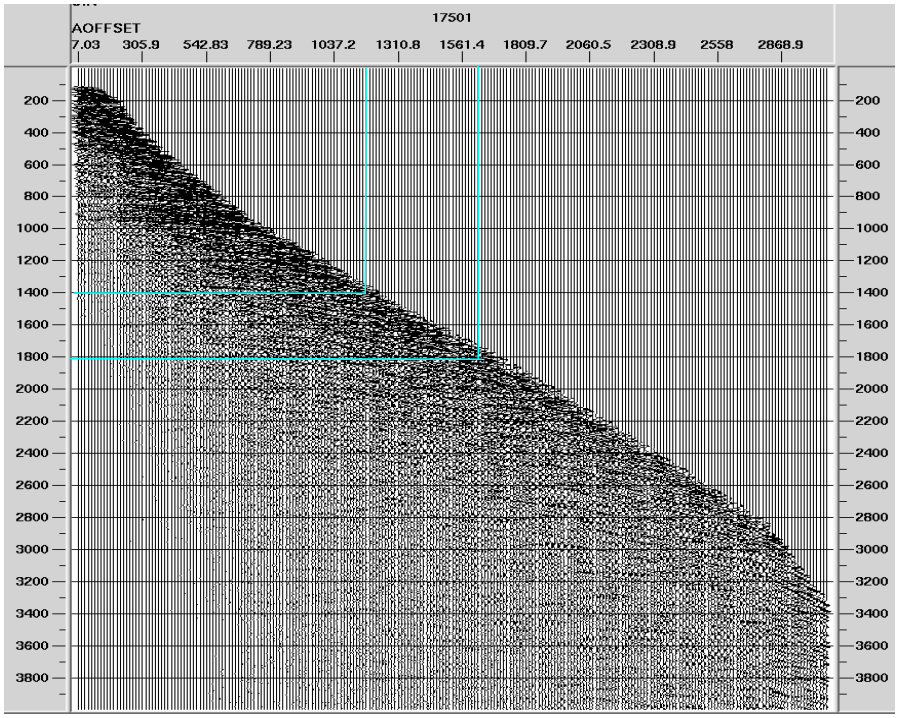

(a) a source gather.

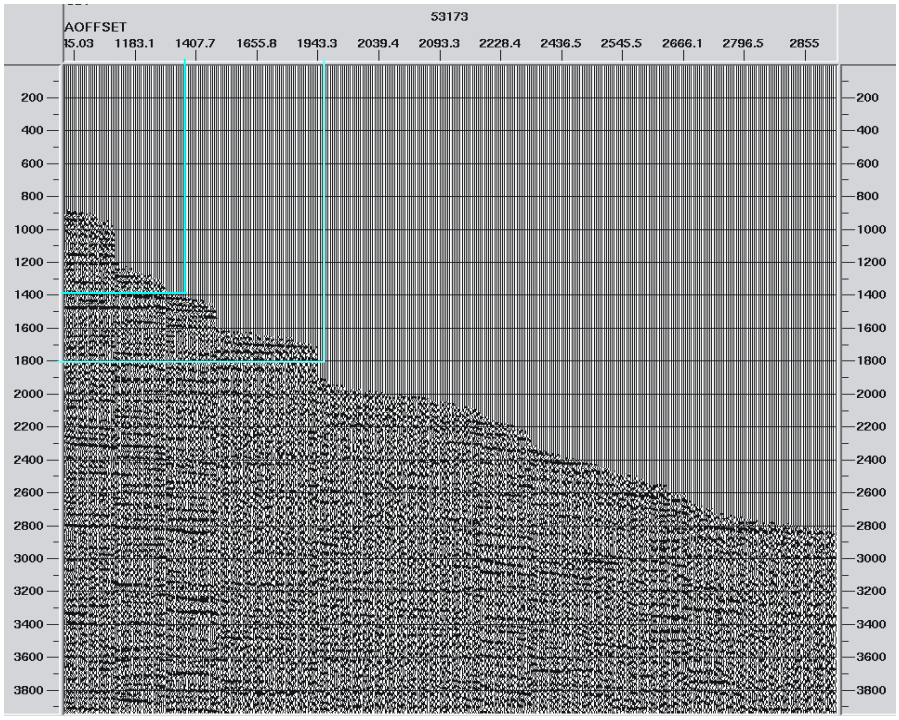

(b) a CMP gather with NMO correction.

Figure 5.3.5: Effective offset coverage of Z-component data with respect to the target layer. The effective offset is indicated by the blue lines.

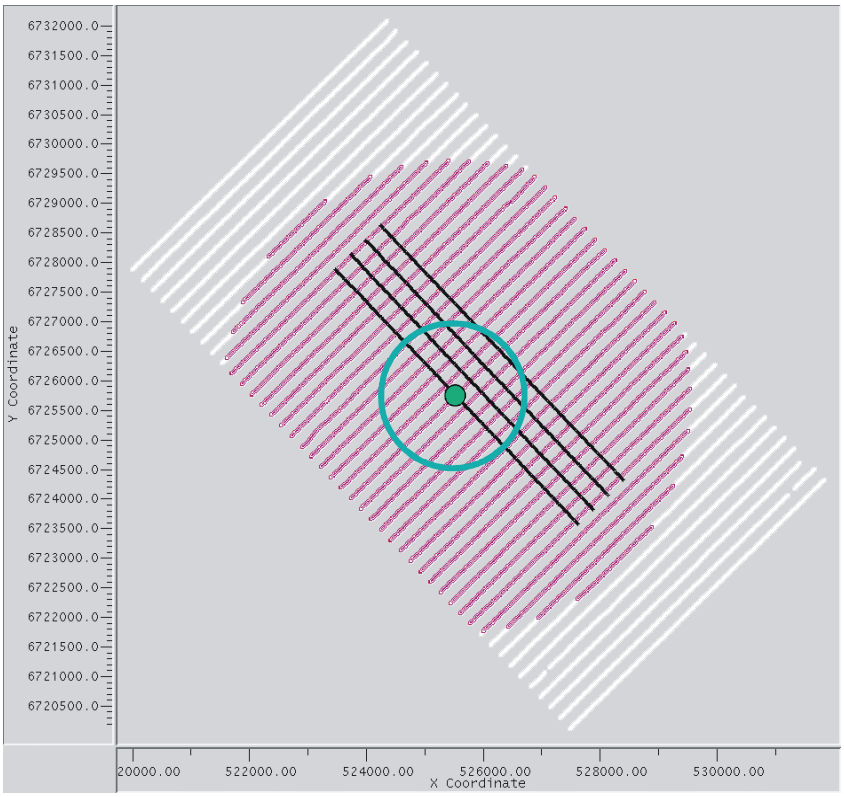

Figure 5.3.6: The sources recorded within a receiver. The red area denotes the sources that have been recorded by the receiver (green spot in the picture), However, only sources within the green circle can contribute to the azimuthal anisotropic attributes analysis for the target layer, because the sources outside the circle contain no information for the target layer of interest.

5.4 Azimuthal P-wave analysis

The results of both numerical and physical modelling of azimuthal P-waves reveal that the amplitude and travel time can be used to infer fracture information through elliptical fitting. The NMO velocity in HTI media also shows elliptical variation with azimuth (Grechka and Tsvankin, 1997, 1998). Figure 5.4.1 shows an inline P-wave stack section from the data. Note that the time interval of interest is between 1.4s and 1.8s on the left of the section. Compared with that of the previous 2D survey (Li and Wei et al. 2004), the data quality has been significantly improved. Six inline stack sections (compressed horizontally) (Figure 5.4.2) and a cross-line section (Figure 5.4.3) of the 3D P-wave stack volume are displayed to gives an overview of the 3D data quality.

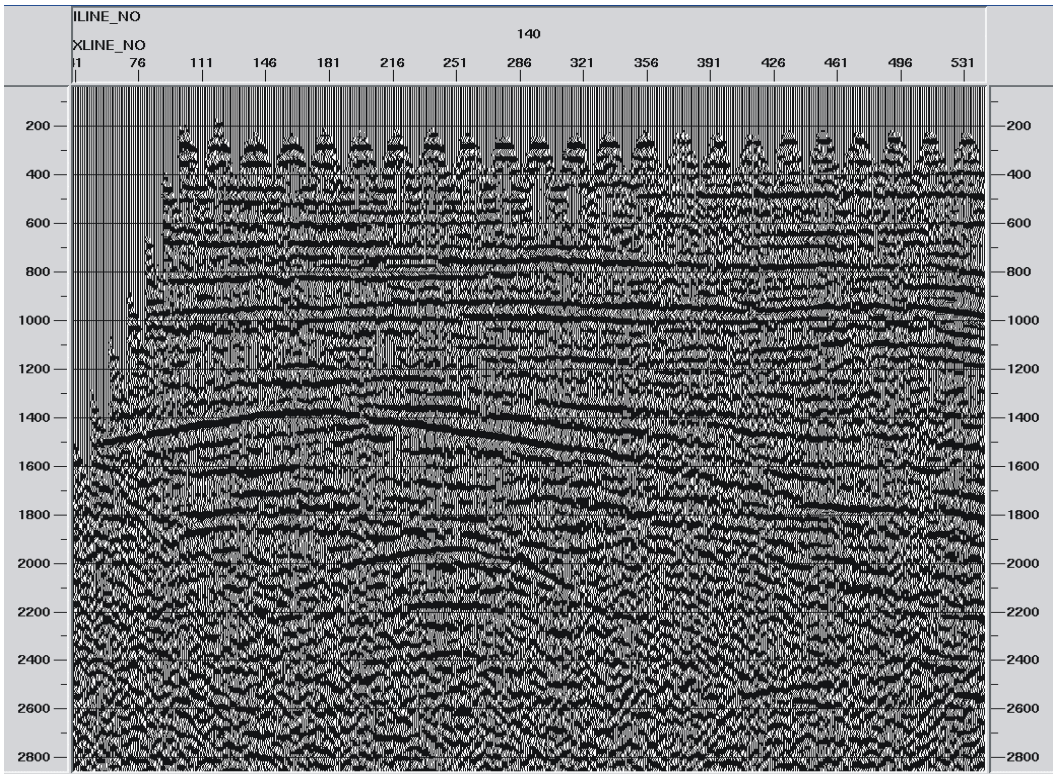

(a)

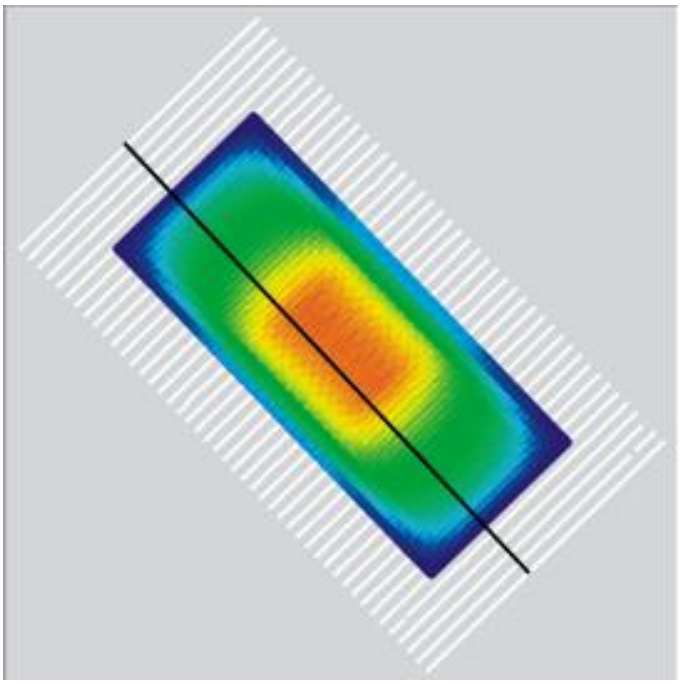

(b)

Figure 5.4.1: An inline stack section of the patch (a). (b) location of the section in the acquisition patch.

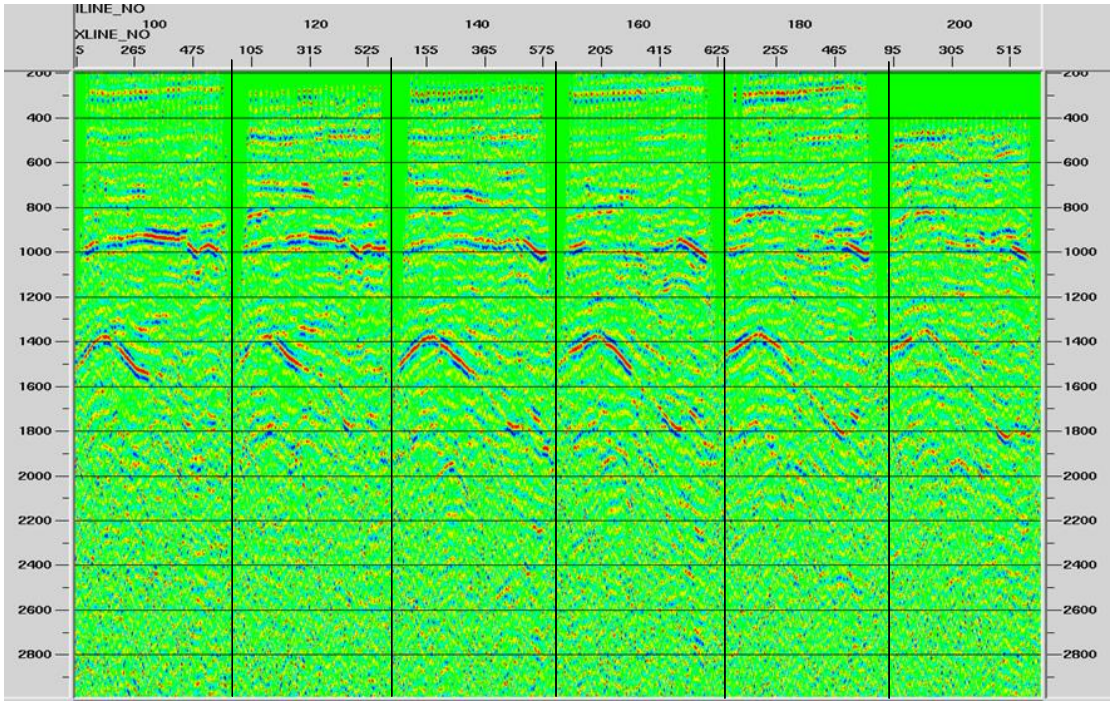

Figure 5.4.2: Six inline stack sections decimated from the P-wave 3D stack volume at an interval of twenty inlines.

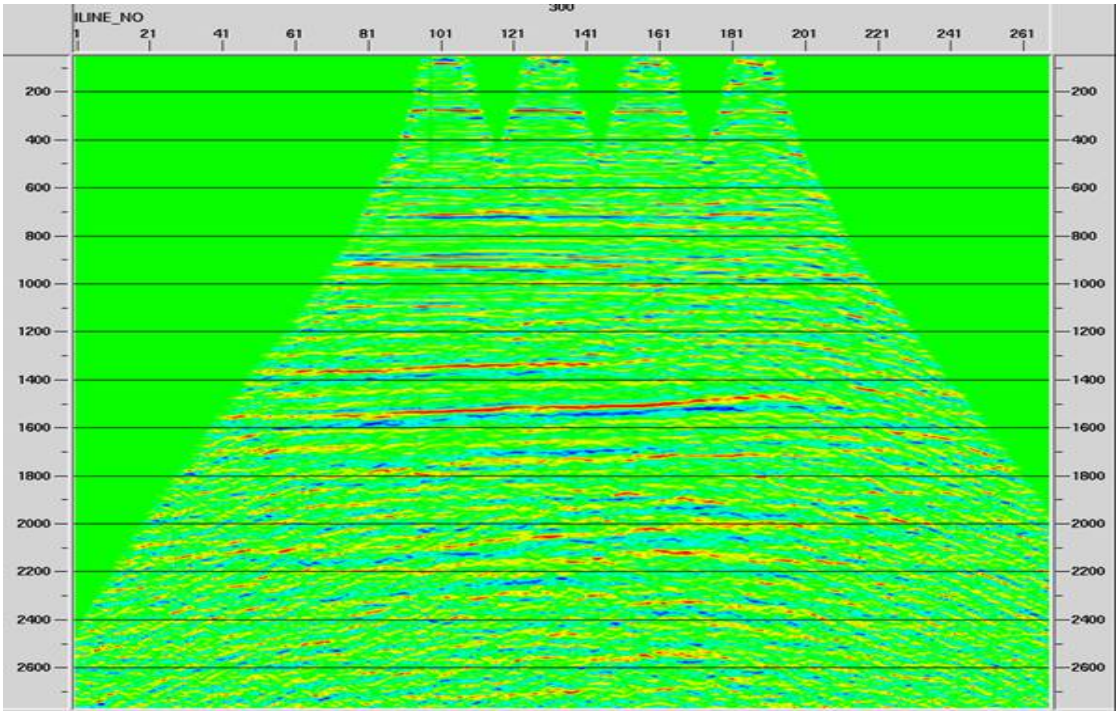

Figure 5.4.3: A cross-line section of the P-wave stack volume.

5.4.1 Azimuthal NMO velocities

During the data processing to get the stack results, I did azimuthal NMO velocity analysis first on the data using Promax software to perform a preliminary check of azimuthal anisotropy. Figure 5.4.4 shows the six azimuthal NMO velocity spectra, with the corresponding azimuth shown on the top of the spectra. As discussed in section 5.3 for data acquisition, the applicable offset-azimuth coverage is not as large as expected, and the resolution of the stack velocity spectra appears to be very low for picking the right NMO velocities. However, I focus on picking at the reflection time corresponding to the bottom of the reservoir, which is around 1.8s. When the velocities from the six spectrum panels are picked and mapped according to azimuth, nearly elliptical variations of the velocity are observed, indicating azimuthal anisotropy exists within the reservoir (Figure 5.4.5). The major axis of the ellipse roughly means the fracture strike is in the direction of N45^{o}E, which agrees with the previous results from the VSP and 2D OBC data in the area (Li and Wei et al. 2004).

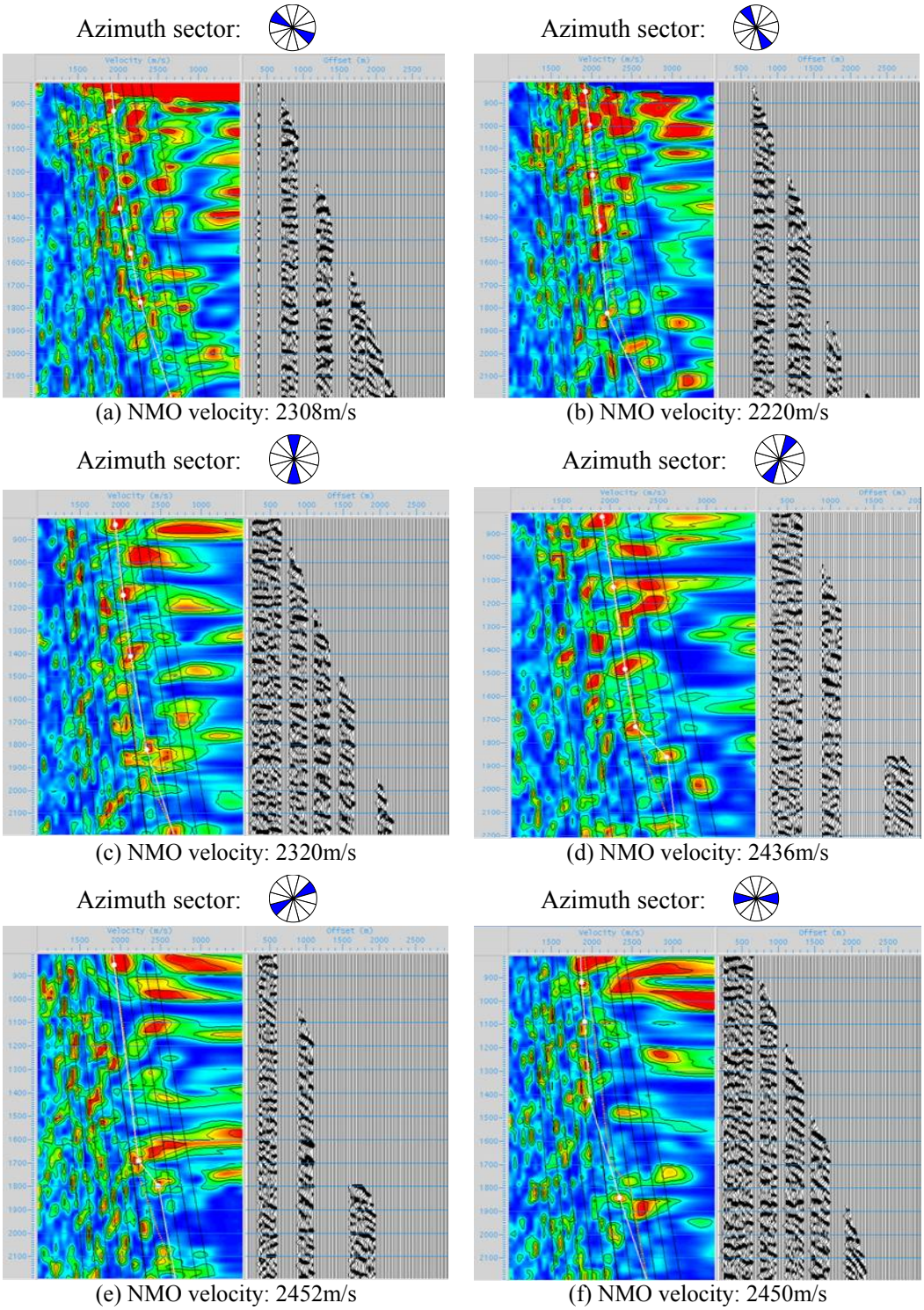

Figure 5.4.4: Azimuthal P-wave NMO velocity analysis. The left part in each panel is a velocity spectrum and the right is the azimuthal gather.

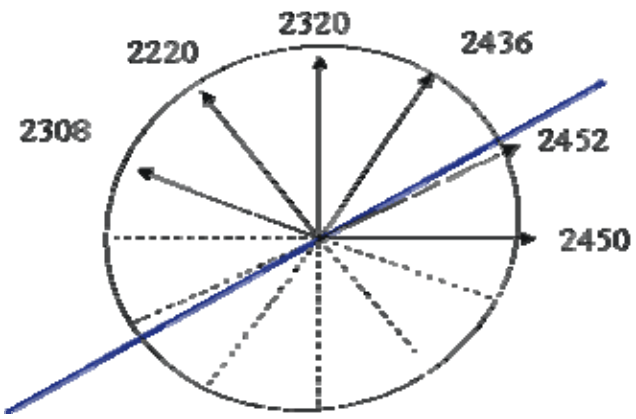

Azimuth (o)	NMO velocity (m/s)
-60	2308
-30	2220
0	2320
30	2436
60	2452
90	2450

(a) (b)

Figure 5.4.5: Azimuthal NMO velocity distribution at 1.8s. (a) Elliptical velocity variations with azimuth. The major axis of the ellipse denotes a fracture strike of nearly N45oE. (b) The picked NMO velocities at different azimuths at 1.8s.

5.4.2 Azimuthal stack panels

According to the results of numerical modelling in Chapter 3, and 3D physical modelling in Chapter 4, if aligned fracture exists then the reflection coefficients on the top of the fracture layer should show an elliptical distribution with azimuth. For a low to high impedance contrast, the reflection coefficient along the fracture strike should be larger than the reflection coefficients along any other direction, while the reflection coefficients along the fracture normal should be the smallest. Figure 5.4.6 displays the azimuthal stack panels with six azimuths. The stack section in the direction of N45^{o}E shows the strongest reflection events, which suggests a fracture strike of N45^{o}E. In the direction of N45^{o}W, the event is the weakest, indicating the direction of fracture normal. This result agrees with that obtained from azimuthal NMO velocity analysis. Since both azimuthal NMO velocity and azimuthal stack panel analyses give a fracture orientation of N45^{o}E, the confidence of the N45^{o}E as the "true" fracture strike in the analysis point has been increased.

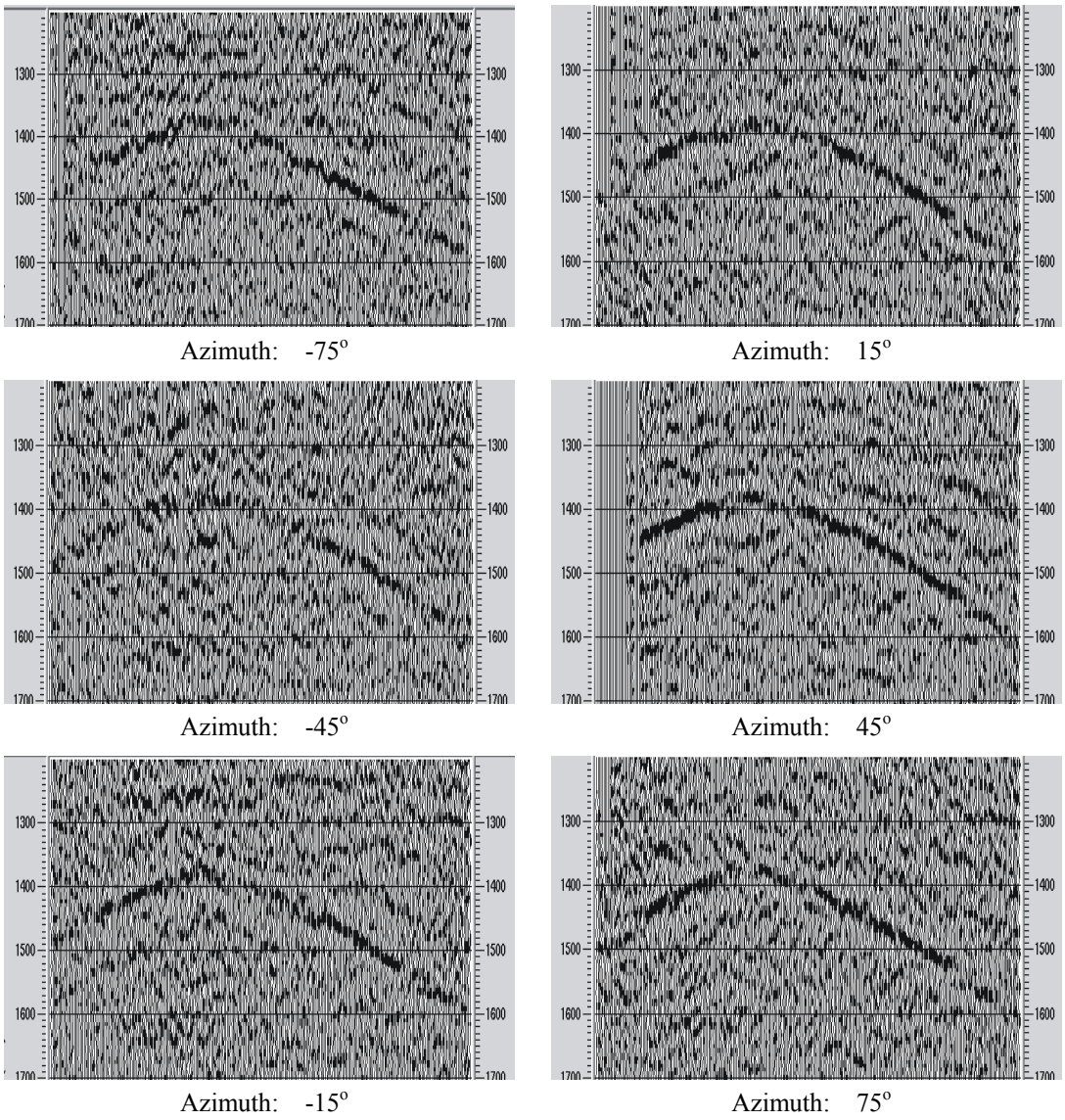

Figure 5.4.6: Azimuthal P-wave stack panels. The reflection event of the stack in the direction of N45°E shows the strongest amplitude. In the direction of N45°W, the amplitude of the event is the weakest.

5.4.3 Fracture parameter estimation

According to the features of the data, I use two methods to extract the fracture information on the P-wave data: full-azimuth surface fitting and narrow-azimuth stacking. The full azimuth method fits an elliptical surface on the data with all available azimuths and offsets by a least-square fitting technique, which is suitable for the travel-time and amplitudes. The narrow azimuth method divides the data into a number of narrow-azimuth sections and is suitable for the velocity and AVO gradient attributes;

the methods require the picking of travel-time and amplitudes of the top of the target events on the pre-stack volume. Since manual picking is impractical for so much data, I developed an automatic time and amplitude picking method on pre-stack data by calculating the envelopes of the traces and picking the maximum envelope value.

Figure 5.4.7 shows the fracture distribution from the analysis of top reflection amplitudes. The colour represents fracture density with the ratio of the major to minor axis of the attribute ellipse, and the superimposed short lines indicate fracture strikes. The 3D physical modelling study in Chapter 4 reveals that the analysis based on amplitudes is very sensitive to signal to noise ratio. Since the signal to noise ratio of the data is marginal, the fracture information derived from the amplitude analysis may have been affected by noise, and therefore becomes less reliable. Thus other approaches also need to be used to reduce the uncertainty and increase the reliability of the results.

Figure 5.4.8 shows the fracture attributes derived from the analysis of AVO gradients. There are stripes parallel to the OBC lines, which are very similar to those in the 3D physical modelling analyses in Chapter 4 (Figure 4.6.2), indicating it is the acquisition footprint of the OBC geometry rather than real fracture information.

Both results from the interval time and travel time show a relatively stable fracture distribution (Figure 5.4.9 and 5.4.10a). For clarity, the strike and density from azimuthal travel times are shown separately. The 3D physical modelling proves that azimuthal travel time is more robust than azimuthal amplitude attribute analysis when the signal to noise ratio is low, because travel time is less sensitive to noise than the amplitudes. Also, I find that picking travel time on the data is much easier than picking amplitudes. Therefore, the fracture information derived from the travel times should be more reliable than that from the amplitude analysis. However, the result from the bottom travel time is less reliable due to the fact that the variation in the fracture density is very small and over-smoothed.

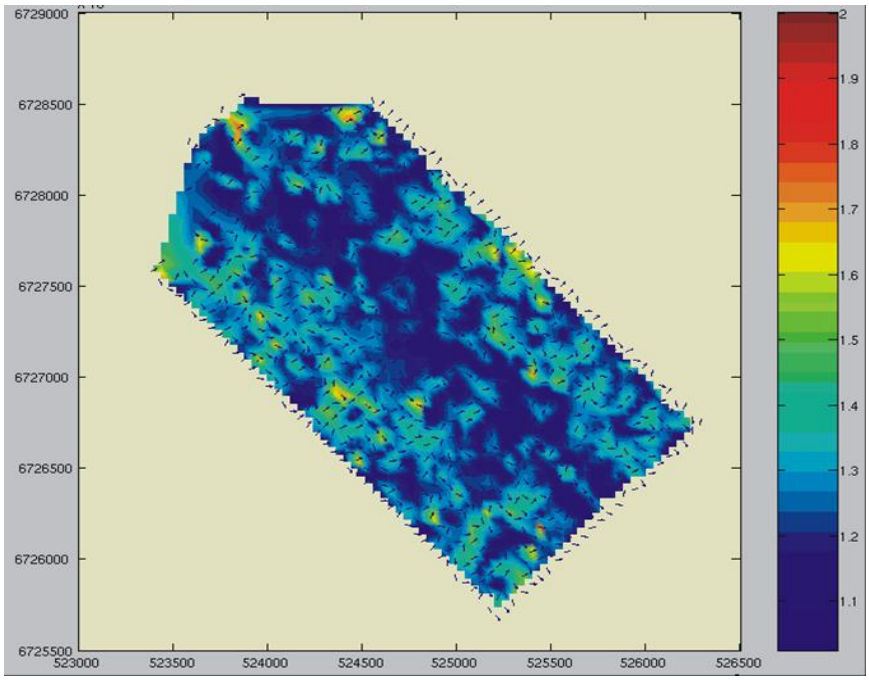

Figure 5.4.7: Fracture density and strike distributions from P-wave amplitude analysis. The colour denotes fracture density represented with the ratio of the major to minor axis of the attribute ellipse; the superimposed short lines indicate the fracture strikes.

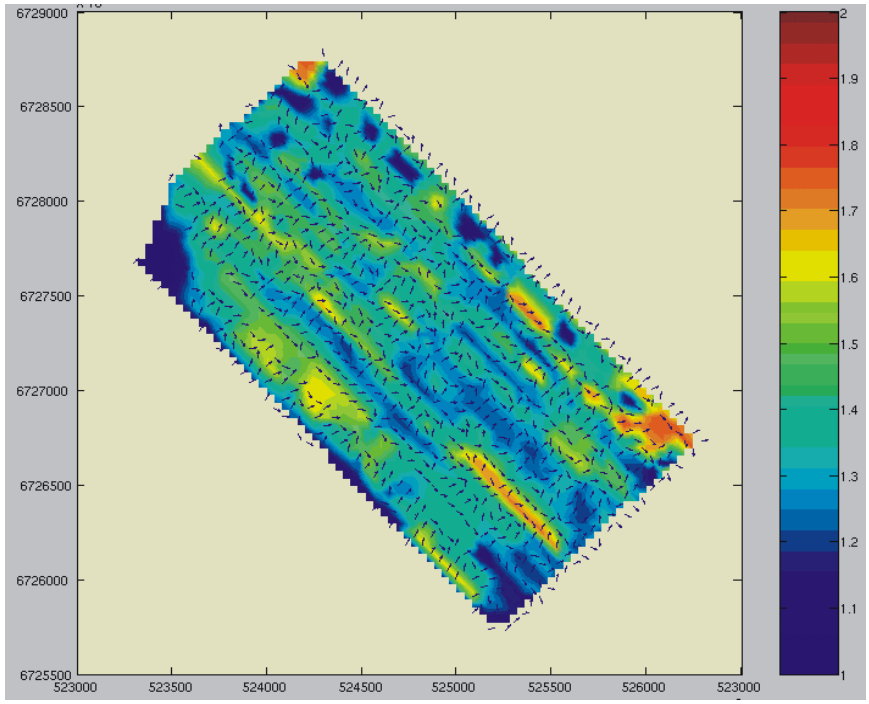

Figure 5.4.8: Fracture strike and density from azimuthal AVO gradient. The stripes parallel to the OBC lines are the acquisition footprint.

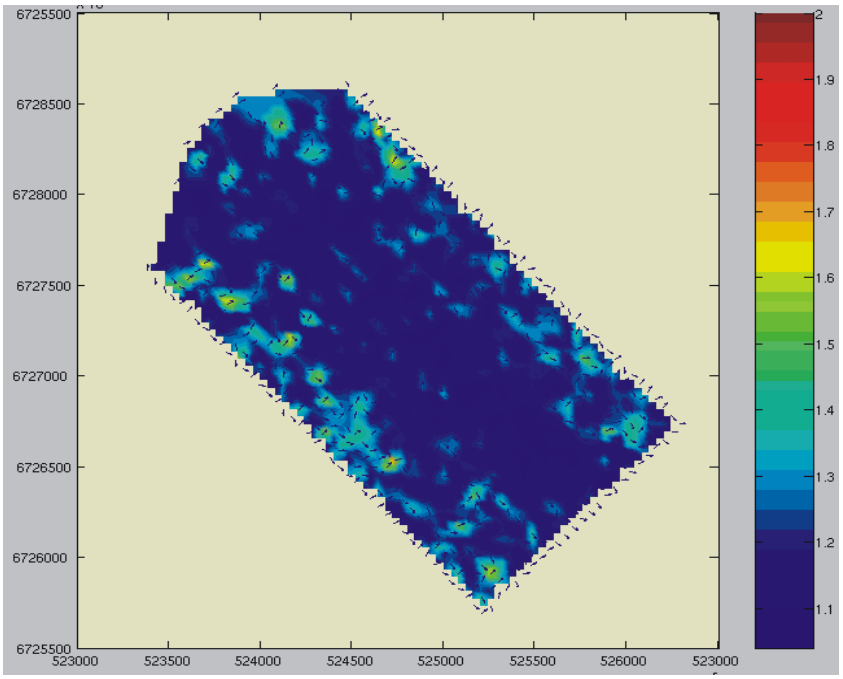

Figure 5.4.9: Fracture strike and density from azimuthal interval travel time.

5.4.4 Summary of azimuthal P-wave analysis

The 3D OBC data has wide offset-azimuth coverage, but the refractions after the first arrivals limit the effective offset range. Only the data with offset less than 2000m can be used for the azimuthal attribute analysis. This means that the offset range designed for field data acquisition does not guarantee sufficient offset coverage for the target interval, and the effective offset range for the target interval analysis should be taken into account.

Consideration of data quality is essential in using azimuthal P-wave anisotropic attributes analysis to obtain reliable results. Due to possible noise contamination in amplitudes, the analyses of azimuthal NMO velocities and stack panels are used to characterise fracture strike and both gives a fracture strike in the direction near N45^{o}E, which agree with that in previous VSP and 2D OBC data analysis.

All results from different attributes reveal spatial variations of fracture orientation and density. However, the fracture attributes derived from the interval travel time appear more reliable than the results from other attributes according to the conclusions from physical modelling in Chapter 4.

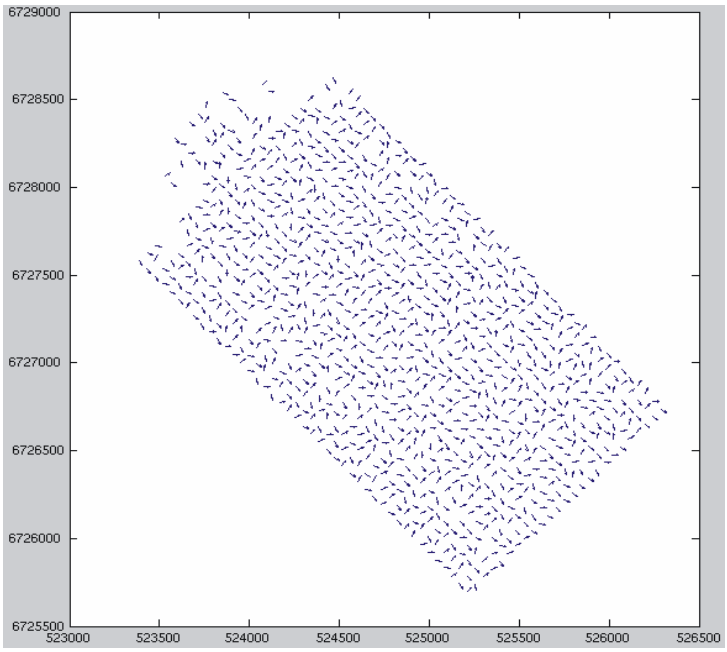

(a)

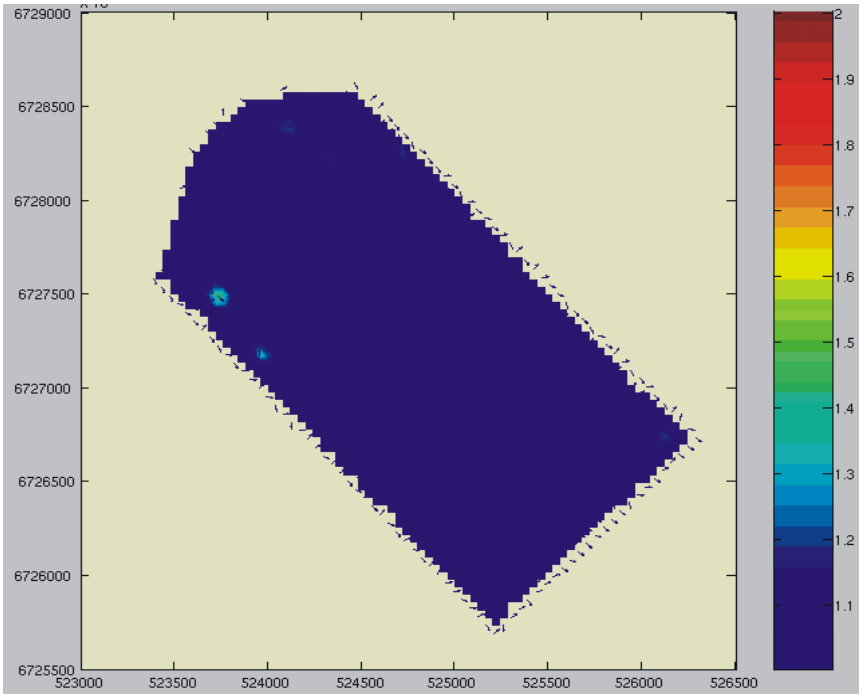

(b)

Figure 5.4.10: Fracture density and strike distribution from azimuthal interval time. (a) fracture strike from the bottom travel time; (b) fracture density from the bottom travel time.

5.5 Analysis of PS-waves for seismic anisotropy

In surveys with multi-component data acquisition, shear-wave splitting can be used as a diagnostic feature of aligned fractures in rocks. When a shear-wave propagates in fractured media, it splits into two components with one component travelling faster than the other one. For vertically propagating shear-waves in a HTI fractured medium, the faster split shear-waves shall polarize in fracture planes and the slower split shear-wave shall polarize orthogonally to the fracture planes. The two polarization directions form the principal axes of the fractured medium. The difference in velocity between the fast and slow split shear-waves is mainly dependent on fracture density. Therefore, there are two attributes associated with shear-wave splitting: polarizations of the faster waves and the time-delay between the faster and slower waves. The fast polarization gives the fracture orientation and the time-delay gives the fracture density.

In this analysis of Clair OBC data, an important purpose is to identify the presence or absence of shear-wave splitting in the converted-wave data, and if any, to quantify polarizations and time-delays of the shear-wave splitting. Another purpose is to characterize fracture information in the converted-wave data with azimuthal analysis methods.

5.5.1 Converted-wave data processing

For shear-wave splitting analysis, the first thing is to process the converted-wave. The quality of the Z-component of the OBC data proved to be moderate (as shown in Figure 5.3.3). However, the quality of the other two components (radial and transverse component, as shown in Figure 5.5.1) appears to be less satisfying. This is because, in addition to the low signal to noise ratio encountered in the P-wave data, PS-wave data processing also involves other issues, such as the asymmetric ray-path and conversion-point calculation. Normally, reflection amplitudes on the T-component roughly indicate the magnitude of shear-wave splitting and weak reflection events usually mean weak or no shear-wave splitting. From the initial check on the data, I can hardly see any meaningful reflection events on the shot gather of the T-component because of the low signal to noise ratio (Figure 5.3.4). However, I continued to carry out further shear-wave splitting analysis by processing the 3D converted-wave data and checking the magnitude

of shear wave splitting on the stack/migration volume. I applied exactly the same processing flow and parameters on both R- and T-components of the OBC data so that the true magnitude of shear wave splitting can be obtained.

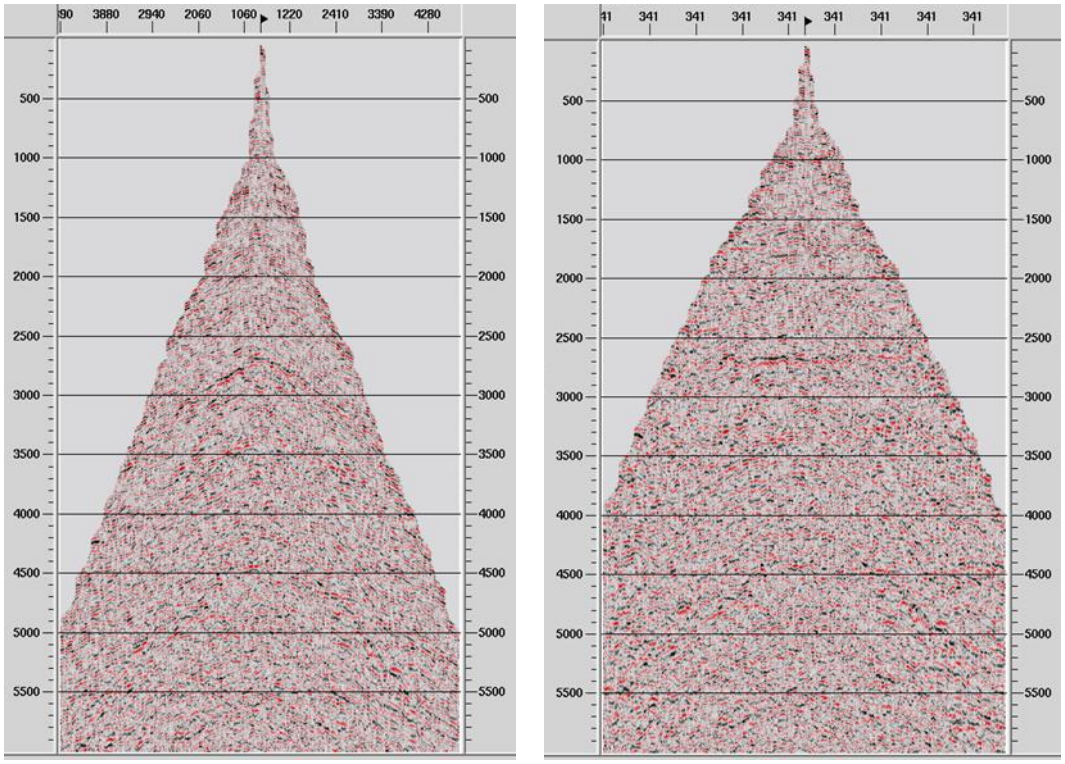

(a) (b)

Figure 5.5.1: An ACCP (asymptotic common conversion point) gather before (a) and after (b) NMO correction. The time interval of interest is between 2.5s and 3.2s at the zero offset.

Figures 5.5.2 and 5.5.3 show the stack section of R- and T-component from the stack processing. The image quality on the section of R-component data is moderately good and the reflection events at the top and bottom interface of the target layer at around 1.4 and 1.8s can be observed. While on the section of T-component, only very weak coherent events are visible. From the analysis of the stack volume of the R- and T-component, it means that, though shear-wave splitting presents, the signal to noise ratio of the T-component is too low to perform traditional analysis of polarization and time delay. Thus other methods are needed to carry out the analysis for fracture properties in the reservoir.

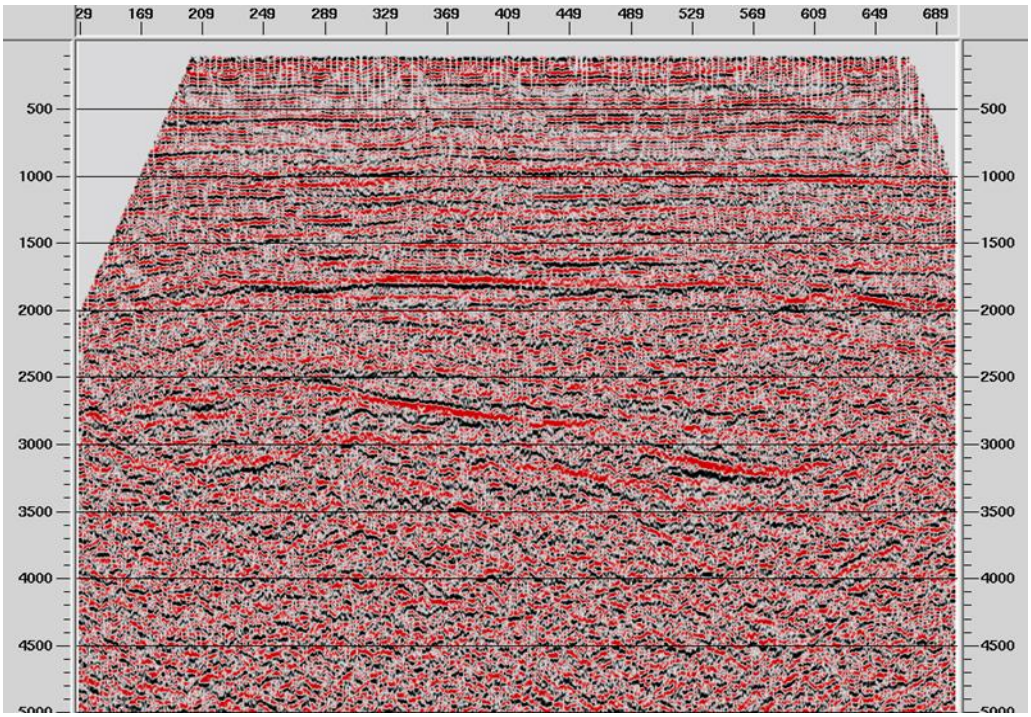

Figure 5.5.2: A section of the R-component.

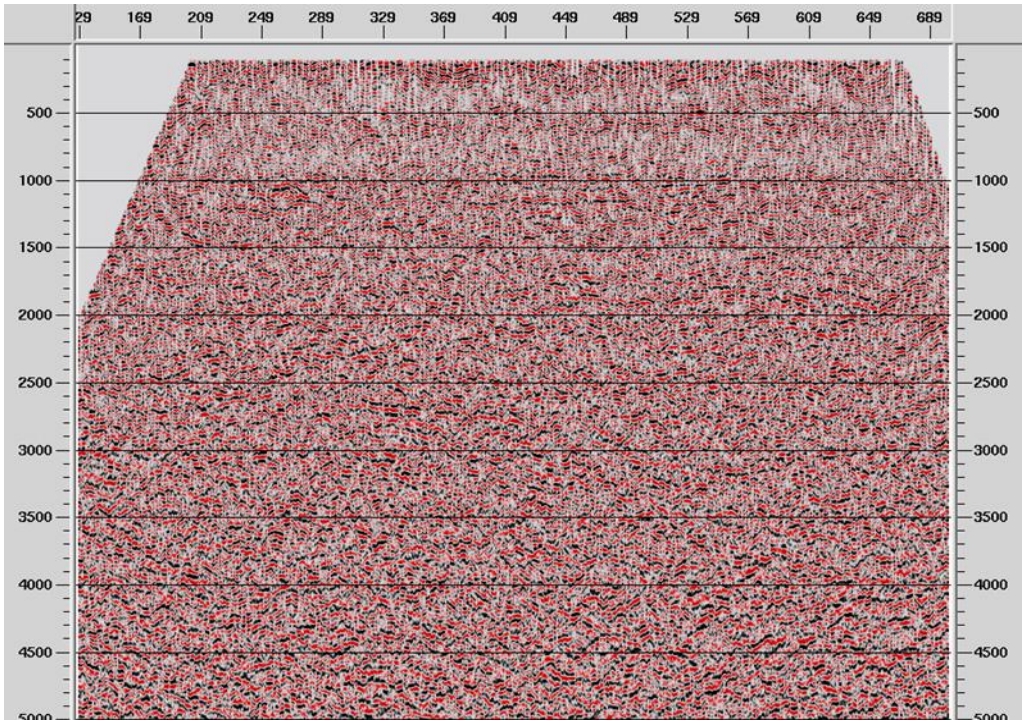

Figure 5.5.3: The stack section of the T-component.

Figure 5.5.4 shows the anisotropic velocity analysis on the R-component data. The velocities picked on the stack velocity spectra and that picked on the pre-stack time migration velocity spectra are very close in value. On the ACCP gather after the NMO (normal move-out) correction, the event is still slightly dipping (as indicated by the arrow in Figure 5.5.4).

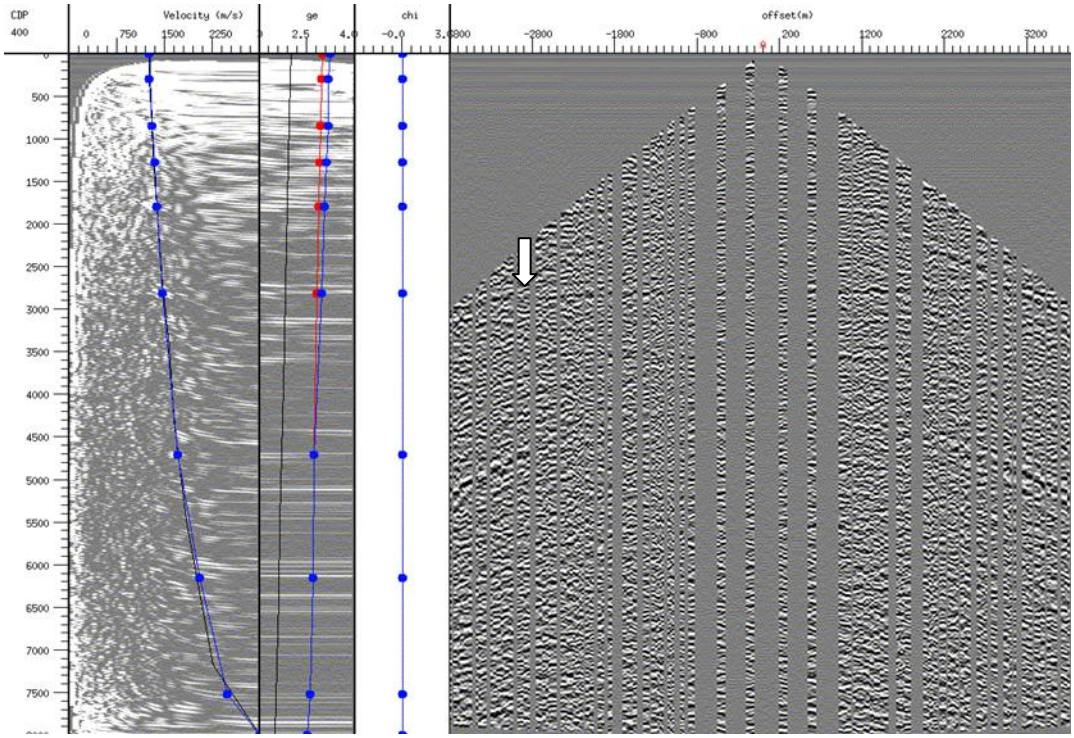

Figure 5.5.4: NMO velocity analysis on the R-component of the Clair 3D OBC data.

5.5.2 Azimuthal velocities of PS-waves

The reflection events on Figure 5.5.3 indicate that, though shear-wave splitting happens at the reservoir, the relatively low signal to noise ratio of the T-component prevents to carry out quantitative analysis in terms of polarization and time-delay analysis. However, the numerical modelling analysis in Chapter 3 reveals that the azimuthal variations of PS-wave stacking velocity can be used to extract fracture information.

Figure 5.5.5 shows the stacking velocity spectra from the gather of R-component with the corresponding azimuth displayed on the top of the spectrum. To do this, a super-gather with full azimuth coverage is divided into four azimuthal sub-gathers according to azimuth ranges and then the velocity spectrum is calculated on each sub-supergather,

respectively. The azimuthal stacking velocities picked from the spectra at the bottom of the target layer (3.2s) show some azimuthal variations, giving a fracture strike of N45^{o}E.

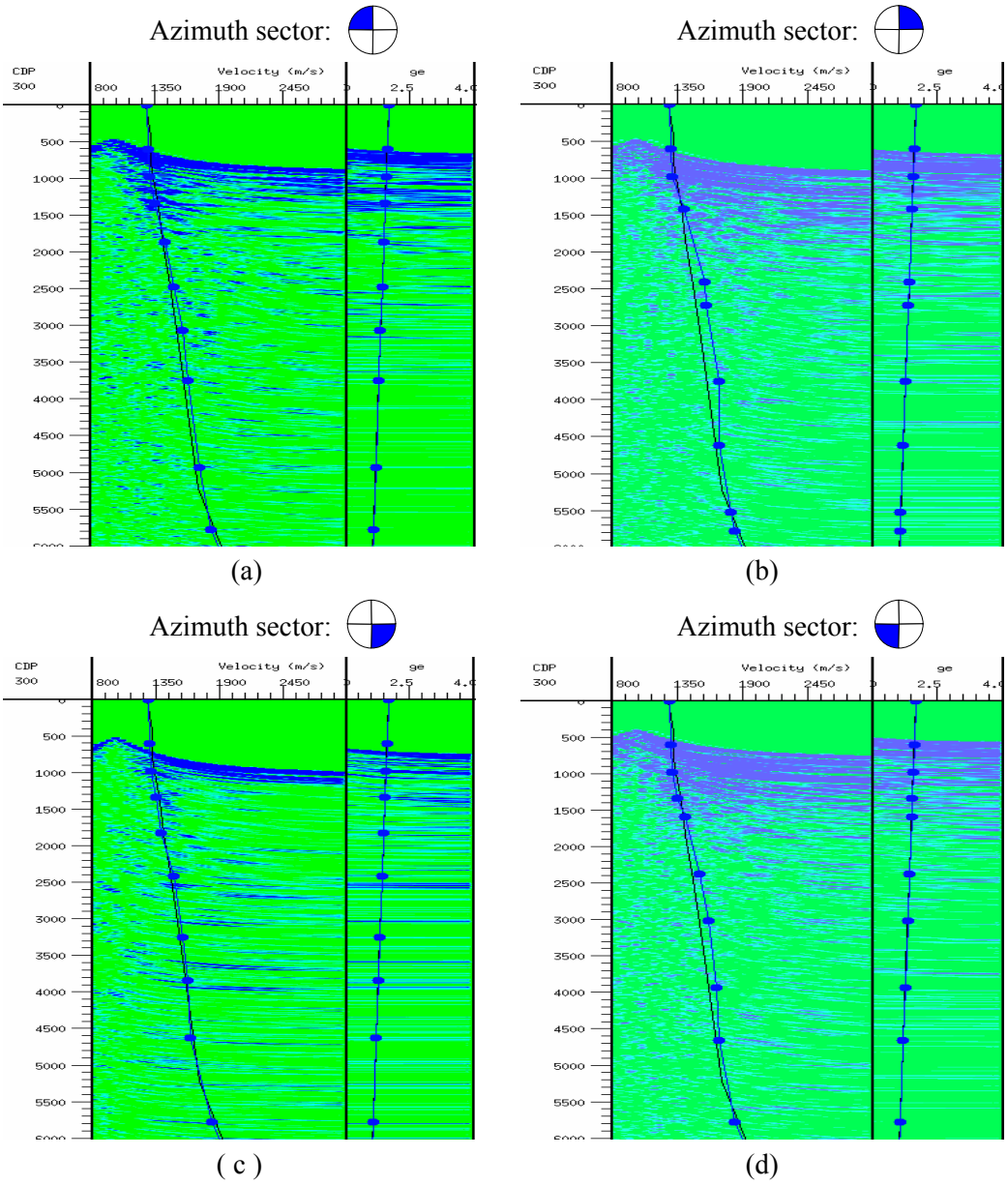

Figure5.5.5: Azimthal PS-wave stack velocity analysis. A super-gather with full azimuth coverage is divided into four azimuthal sub-gathers according to azimuth ranges and then the velocity spectrum is calculated on each sub-supergather (a), (b), (c) and (d), respectively. The velocities picked at 3.2s at each spectrum are: (a) azimuth:45^{o}, velocity: 1592m/s; (b) azimuth:45^{o}, velocity: 1622m/s; (c) azimuth: 45^{o}, velocity: 1561m/s; (d) azimuth:315^{o}, velocity: 1609m/s.

5.5.3 Summary of PS-wave analysis

Analysis of the conventional stack sections of the data shows the presence of shear wave splitting, but the T-component is of low signal to noise ratio. Compared with stack processing approaches, PSTM processing strategy can improve image quality and compensate possible structure-related azimuthal variations, and thus provides more information in shear-wave splitting analysis. In the resulting T-component data, much clearer reflection events become visible at the target zone. However, the magnitude is not large enough to quantify the shear-wave splitting analysis across the whole section to obtain time-delays and polarization directions.

The stacking velocity of the R-component shows evidence of azimuthal variations and has been used to infer anisotropy properties on its own. The azimuthal velocities at the bottom of the target layer give a fracture strike of N45^{o}E.

5.6 Conclusions

Though the data has wide offset-azimuth coverage, the refractions after the first arrivals limit the effective offset range to be less than 2000m. This means that the offset range designed for field data acquisition does not guarantee a sufficient offset coverage for the target interval, and the effective offset range for the target interval analysis should be taken into account.

The azimuthal P-wave stacking velocities and stack panels show azimuthal variations and can be used to infer fracture information. Both azimuthal stack velocity and stack panels give a consistent estimation of fracture orientation at N45^{o}E, which agrees with that in previous VSP and 2D OBC data analysis. The results from different attributes reveal spatial variations of fracture orientation and density, and the fracture information derived from the interval travel times appears more reliable than the results from other seismic attributes.

I carried out azimuthal attribute and shear-wave splitting analyses on the Clair 3D/4C OBC data for seismic anisotropy, aiming to characterize the fracture properties of the reservoirs. The PSTM results of T-component show reflection events at the target zone, indicating that shear-wave splitting happens at the reservoir. However, the low signal to

noise ratio of the T-component makes it difficult to quantify the shear-wave splitting analysis across the whole section to obtain time-delays and polarization directions. Instead, the stacking velocity of R-component show evidence of azimuthal variations which can help to interpret fracture information (orientation), when used together with the P-wave data.

Chapter 6

Anisotropic effects on PS-wave imaging: field data analysis

In this chapter I investigate the anisotropic effects of VTI media on pre-stack time migration (PSTM) of the converted-waves (PS-waves), by building and applying two velocity models (an isotropic velocity model and an anisotropic velocity model) to a real dataset. The main purpose of this study is to obtain some insights on the magnitude of anisotropic effects of VTI media on PS-wave PSTM results through analysis of a real 3D multi-component seismic dataset, so as to obtain guidance for similar real data analysis. The data I used for the analysis is from the same Clair 3D OBC dataset which I have used for the fracture analyses in Chapter 5, the details of the data set have been discussed there.

6.1 Introduction

A converted-wave with a down-going compressed-wave (P-wave) and an up-going shear-wave is referred to as a PS-wave (Thomsen, 1999). Due to the difference in P-wave and shear-wave velocities, the move-out signatures of PS-waves are inherently non-hyperbolic because of asymmetric ray-paths, therefore different methods are required for the PS-wave move-out correction (e.g. Tessmer and Behle, 1988; Zhang, 1992; Stewart et al., 2002). The approaches for the PS-wave normal move-out (NMO) correction and common conversion point (CCP) binning were presented by Tessmer and Behle (1988), followed by Harrison (1992) for the DMO (dip moveout) and post stack migration.

Besides asymmetric ray-paths, anisotropy is another issue in PS-wave data processing. The formations of sedimentary layers (i.e. shales, thin layer sequences) often give rise to VTI features. If a layered sequence of different media (isotropic or not) is probed with an

elastic wave of wavelength much longer than the typical layer thickness (i.e the normal seismic exploration context), the wave propagates as through it were in a homogeneous but VTI anisotropic medium (Backus, 1962). Though various attempts have been made to extend the DMO approach to address the anisotropy issue (e.g. Rommel, 1996; Thomsen, 1999, Tsvankin and Grechka, 2000), anisotropic CCP binning and PS-wave DMO are strongly velocity dependent and this has severely limited the application ability of converted waves. Thus using PS-wave anisotropic PSTM to replace the processing flow of CCP binning, DMO, attack and post stack time migration has more advantages in anisotropic PS-wave imaging (Li and Druzhinin, 2000; Dai and Li, 2001; Dai, 2003, etc.). Many factors affecting PSTM have been studied. For example, Dai and Li (2006, 2008) investigated the effects of migration velocity errors on travel-time accuracy in prestack Kirchhoff time migration and the image of PS-waves with a numerical analysis. However, the compensation for anisotropic effects from a VTI medium is an important issue in PS-wave PSTM and needs more case studies to obtain further insights to it.

To study the accuracy and sensitivity of anisotropic parameter estimation in PSTM, I used 3D OBC data set from the Clair field where the presence of VTI anisotropy is mainly caused by marine sediments.

6.2 PS-wave anisotropic processing

Normally, field multi-component data consists of X- , Y- and Z-components and most of the signals in X- and Y-components come from a P-wave to a S-wave conversion upon the reflection at an interface (thus called PS-waves). The Z-component consists mainly of P-waves and can be regarded as P-wave data. The workflow for processing P-wave data applies in Z-component data processing, which mainly includes field statics, pre-stack noise attenuation (such as multiple removal, ground-roll attenuation, etc.), de-convolution, residual statics, NMO, DMO, stack and migration, etc.. However, due to specific issues such as noise suppression, S-wave receiver statics, asymmetric ray-paths, different travel velocities of P- ans S-wave, conversion point calculation, move-out correction, etc., the processing flow for the PS-wave is different from that for the P-wave.

Because the PS-wave is inherently non-hyperbolic due to the asymmetric ray-path (Figure 6.2.1), the CCP positioning depends on not only the acquisition geometry but also the ratio of P and S-wave velocities. Thus the common midpoint (CMP) binning method for P-wave NMO, which is related to the acquisition geometry, is not suitable for common conversion point (CCP) binning in PS-wave processing. In a single isotropic layer where velocity is supposed to be invariant with depth, the CCP position can be calculated for the asymptotic common conversion point (ACCP) positioning method (e.g. Thomsen, 1999). In a layered medium where velocity is depth-dependent (Figure 6.2.1b), the exact CCP position has been intensively studied (e.g. Tessmer and Behle, 1988, Zhang, 1996). Thomsen (1999) uses the ratio of vertical velocity, NMO velocity and effective velocity to calculate CCP position. Li and Yuan (2001) extended Thomsen's (1999) CCP calculation methods by taking VTI anisotropy into account.

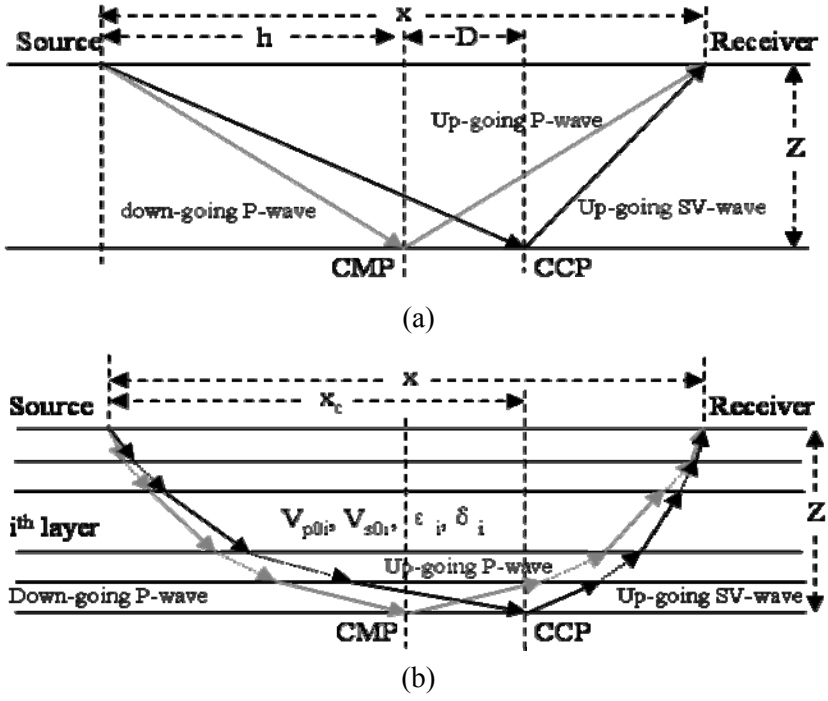

Figure 6.2.1: P- and PS-wave ray-paths in isotropic and VTI media. (a) P- and PS-waves path in isotropic media. (b) P- and PS-wave paths in horizontally layered media. x is the offset, x_c is the distance between source point and conversion point, V_{p0i} , V_{s0i}, ε_i and δ_i are Thomsen (1986) interval parameters.

For a PS-wave stack processing scheme, it normally includes common conversion point calculation, normal move-out corrections, dip move-out corrections, stacking and post-stack migration, involving inherent problems such as asymmetric ray-paths (Figure

6.2.1) and conversion-point binning. The results from PS-wave data processing are more sensitive to anisotropy than that of P-waves because the ray-paths of a PS-wave are more velocity-dependent than that of a P-wave.

Because PS-wave pre-stack time migration can bypass the procedures of common conversion point binning, normal move-out correction and dip move-out correction and post-stack migration and thus overcomes the limits of stack processing, it is widely regarded as a better alternative imaging approach than conventional stack processing schemes (e.g., Li and Druzhinin, 2000; Dai and Li 2001; Dai, 2003, Li and Dai et al., 2007). In PSTM processing, the image at a point in the CIP gather is constructed by summing the energy from all possible scatter points with given vertical travel-time and offset over all different available source and receiver locations, i.e., amplitudes are summed along a diffraction curve and relocated to the scatter point defined by the positions of the source and receiver. The travel-time is calculated according to the P-wave velocity and anisotropy parameters, the S-wave velocity and anisotropy parameters, which constitute the migration velocity model.

Normally, PS-wave PSTM can be carried out in four steps (Dai & Li 2001, Li and Wei et al. 2004; Dai and Li, 2007a, 2007b): the first step is to build a PS-wave stack velocity model, because in the building of migration velocity, the initial model is calculated from the stack velocity model. It means that conventional stack processing is also involved in a PSTM workflow. The second step is to convert the stack velocity model into an initial migration velocity model to carry out initial PSTM to obtain common image point (CIP) gathers for migration velocity analysis. The third step is to use the CIP gathers to update the migration velocity model and iterate the procedure until a satisfactory result is obtained. The updating is performed by analyzing the residual move-out in the CIP gathers. The last step is to implement PSTM with the updated velocity model for final PSTM results. Based on my experiences in P-wave data processing and the features of PS-waves, I established a processing flow for the PS-wave anisotropy analysis (Figure 6.2.2), where both the P-wave and PS-wave have been involved.

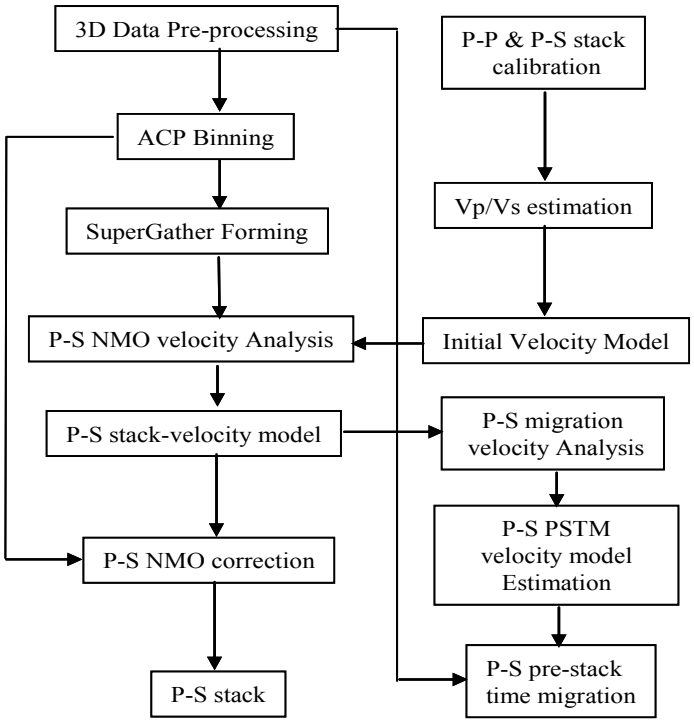

Figure 6.2.2: PS-wave PSTM processing flow applied in Clair PS-wave data.

6.3 Anisotropic velocity models

6.3.1 Velocity model building

Tsvankin and Thomsen (1994) studied the general PS-wave zero-dip response in VTI media with complicated forms. Simplified forms with less accuracy have also been developed (Thomsen, 1999; Cheret et al, 2000). Despite the asymmetric ray-paths in horizontally layered media, the PS-wave can still be described as hyperbolic for small offset to depth ratio as the first approximation

$$t_c^2 \approx t_{c0}^2 + \left(\frac{x}{v_{C2}}\right)^2 \tag{6.3.1}$$

where t_{c0}, v_{C2} and x are the vertical PS-wave travel time, PS-wave RMS velocity and offset, respectively. However, even for a single horizontal layer, the equation (6.3.1) is only sufficiently accurate when the offset to depth ratio is less than 0.7 (Yuan, 2001).

To obtain simplified and practical move-out correction methods with good accuracy, Li and Yuan (2003) give the equations to study the PS-wave zero-dip response in

horizontally layered VTI media, which is controlled by four parameters, including PS-wave stacking velocity V_{C2}, vertical velocity ratio γ_0, effective velocity ratio γ_{eff} and PS-wave effective anisotropy coefficient χ_{eff}. The four parameters (V_{C2}, γ_0, γ_{eff} and χ_{eff}) are referred to as the PS-wave stacking velocity model and can be picked directly in anisotropic velocity analysis as shown in Figure 6.3.1, where on the left is a semblance panel, followed by the velocity ratio and anisotropy parameter χ_{eff}, and on the right is an ACCP gather after NMO correction. Although all four parameters can be picked in this procedure, normally only the PS-wave velocity and anisotropic parameter χ_{eff} are updated in the process.

Normally, γ_0 is estimated through a coarse correlation of the P- and PS-wave stack sections which can be obtained by processing the P- and PS-wave data using hyperbolic methods, because the move-out signature of PS-wave is not very sensitive to γ_0 (Li and Yuan 2003) and thus cannot be determined from move-out signature analysis. However, a prevous study show that γ_0 allows an error of 10% while the PS-wave velocity error should not exceed 2% for an optimal PS-wave image (Dai and Li, 2002).

Once γ_0 is determined, the next step is to estimate the offset-dependent parameters V_{C2}, γ_{eff}, χ_{eff} from the PS-wave move-out signature (Dai, 2003). Each of the three parameters controls a particular aperture of primary influence: V_{C2} controls the hyperbolic move-out signatures at the offset range where the offset-depth ratio is less than 1.0 ($offset/depth<1.0$), because there the move-out signatures can be assumed as hyperbolic and are not sensitive to asymmetric ray-paths and anisotropy; γ_{eff} controls the non-hyperbolic move-out signature at the intermediate offsets ($1.0<offset/depth<1.5$) due to the asymmetric ray-path, where move-out signatures are not sensitive to anisotropy; χ_{eff} controls the non-hyperbolic move-out signatures at far offsets ($1.5<offset/depth<2.0$) due to anisotropy. According to these features, all three parameters can be determined by judging whether the events have been flattened.

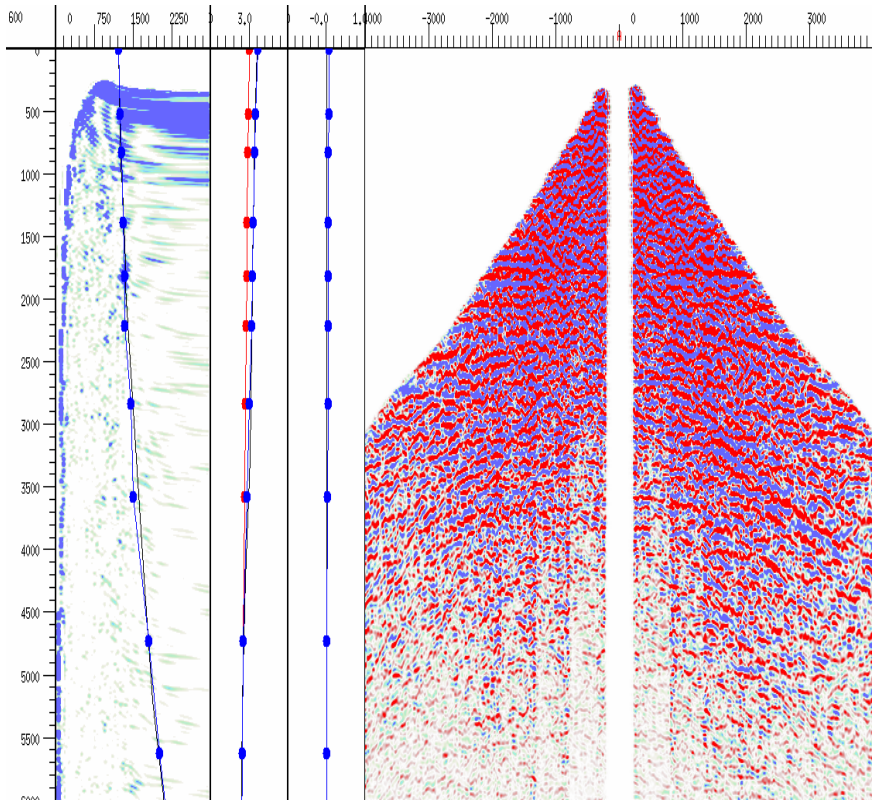

Figure 6.3.1: PS-wave anisotropic velocity analysis. (a) V_{C2} spectrum, the vertical axis represents time in ms, and the horizontal axis represents velocity in m/s; (b) γ_0/γ_{eff} ; (c) χ_{eff} ; (d) ACCP gather.

For anisotropic PS-wave PSTM, the most important thing is to build a reasonable velocity model which is specified by five parameters: γ_0, V_{P2}, V_{S2}, η_{eff} and ζ_{eff} representing the vertical velocity ratio, P- and S-wave stacking velocity, and P- and S-wave anisotropic parameters, respectively. The five parameters can directly be obtained from the stack velocity model containing γ_0, γ_{eff}, V_{C2} and χ_{eff} (Li and Yuan, 2003; Dai, 2003). A stack velocity model based on ACCP gathers is different from a PSTM velocity model based on CIP gathers, but it can be used as an initial PSTM velocity model and then updated through PSTM velocity analysis. Thus, to build a PSTM velocity model, the first step is to build a PS-wave stack velocity model and use it to generate initial CIP gathers for further velocity analysis. It normally needs several iterations before a reasonable PSTM velocity model is built. The events in a CIP gather after NMO correction is similar to that in the ACCP gather after NMO correction (Figure 6.3.2).

6.3.2 Links between stack and PSTM anisotropic velocity models

The parameters of a stack velocity model are inherently linked to that of the PSTM velocity model, and there are analytical links between the parameters describing these two processes. The PS-wave kinematic response in inhomogeneous VTI media is separated into two parts: the response in horizontally layered VTI media and the response from a point scatter. The former controls the stacking process and the latter controls the PSTM process. In terms of stack processing, the PS-wave travel-time in horizontally layered VTI media is determined by the PS-wave stack velocity, vertical velocity ratio, effective velocity ratio and PS-wave anisotropic parameter. In contrast, the PS-wave diffraction time from a point scatter is determined by the vertical velocity ratio, P-wave stack velocity, S-wave stack velocity, P-wave anisotropic parameter and S-wave anisotropic parameter. The P-wave and S-wave velocity have the following relation to PS-wave velocity (Li and Yuan 2003):

$$\begin{aligned} V_{P2}^2 &= V_{C2}^2 \frac{\gamma_{eff}(1+\gamma_0)}{1+\gamma_{eff}} \\ V_{S2}^2 &= V_{C2}^2 \frac{(1+\gamma_0)}{\gamma_0(1+\gamma_{eff})} \end{aligned} \tag{6.3.2}$$

The links between PS-wave anisotropic parameter χ_{eff} and P-wave anisotropic parameter η_{eff} as well as S-wave anisotropic parameter ζ_{eff} are given by (Li and Yuan, 2003):

$$\begin{aligned} \eta_{eff} &= \frac{\chi_{eff}}{(\gamma_0 - 1)\gamma_{eff}^2} \\ \zeta_{eff} &= \frac{\chi_{eff}}{(\gamma_0 - 1)} \end{aligned} \tag{6.3.3}$$

Thus, there is a one-to-one analytical link between the stack velocity model and PSTM velocity model. The equations (6.3.2) and (6.3.3) can be used to convert a stack velocity model (V_{C2}, γ_0, γ_{eff} and χ_{eff}) into an initial PSTM velocity model (γ_0, V_{P2}, V_{S2}, η_{eff} and ζ_{eff}).

Figure 6.3.2 shows the anisotropic velocity analysis in the R-component of Clair PS-wave data. In the ACCP gather after the NMO correction, the event is still slightly dipping (as indicated by the arrow in Figure 6.3.2b). However on the corresponding CIP gather from PSTM velocity analysis, the event has been well flattened (Figure 6.3.2a),

which will help to improve the image quality. The velocities anisotropic parameters picked on the stack velocity spectra (left panel of figure 6.3.2b) and that picked on the pre-stack time migration velocity spectra (left panel of figure 6.3.2a) are very close in values. Figure 6.3.3 shows two CIP gathers for stacking to generate PSTM results. Figures 6.3.4 shows the R- and T-component sections from the final 3D PSTM volume of PS-waves, which reveals improved image quality compared to that of the stack sections (Figure 5.5.2 in Chapter 5). On the resulting T-component, much clearer reflection events are visible at the target zone, which means that S-wave splitting can be observed better on the PSTM data than stack data for the Clair reservoir.

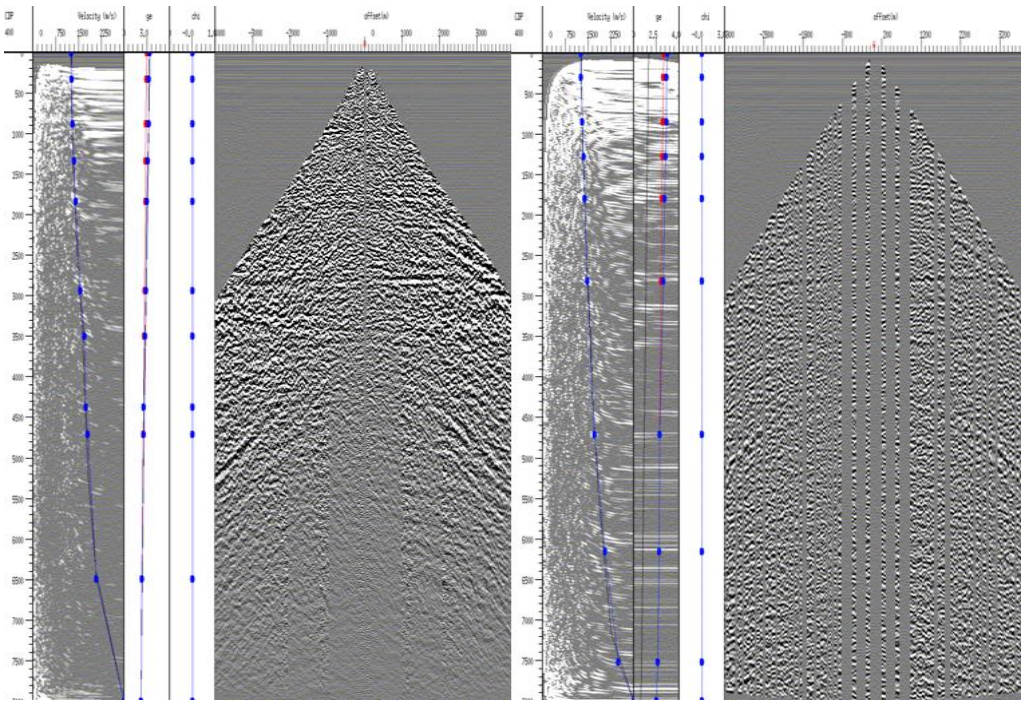

(a) (b)

Figure 6.3.2: Anisotropic velocity analysis on the R-component of the Clair 3D OBC data. (a) PSTM velocity analysis; (b) stack velocity analysis.

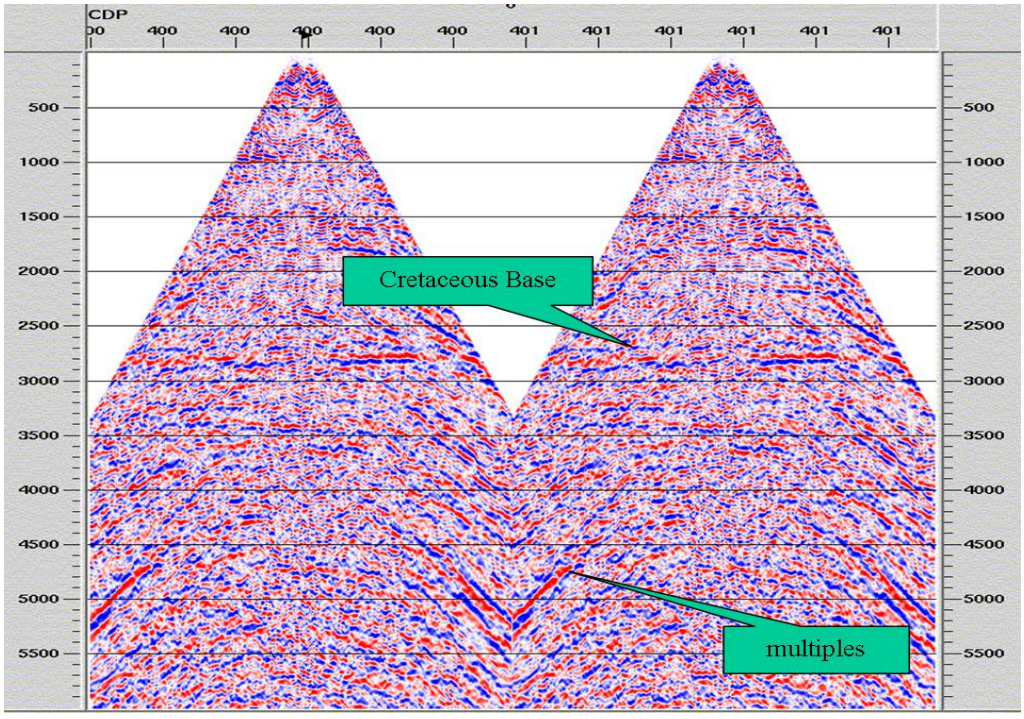

Figure 6.3.3: Two CIP gathers for PSTM results.

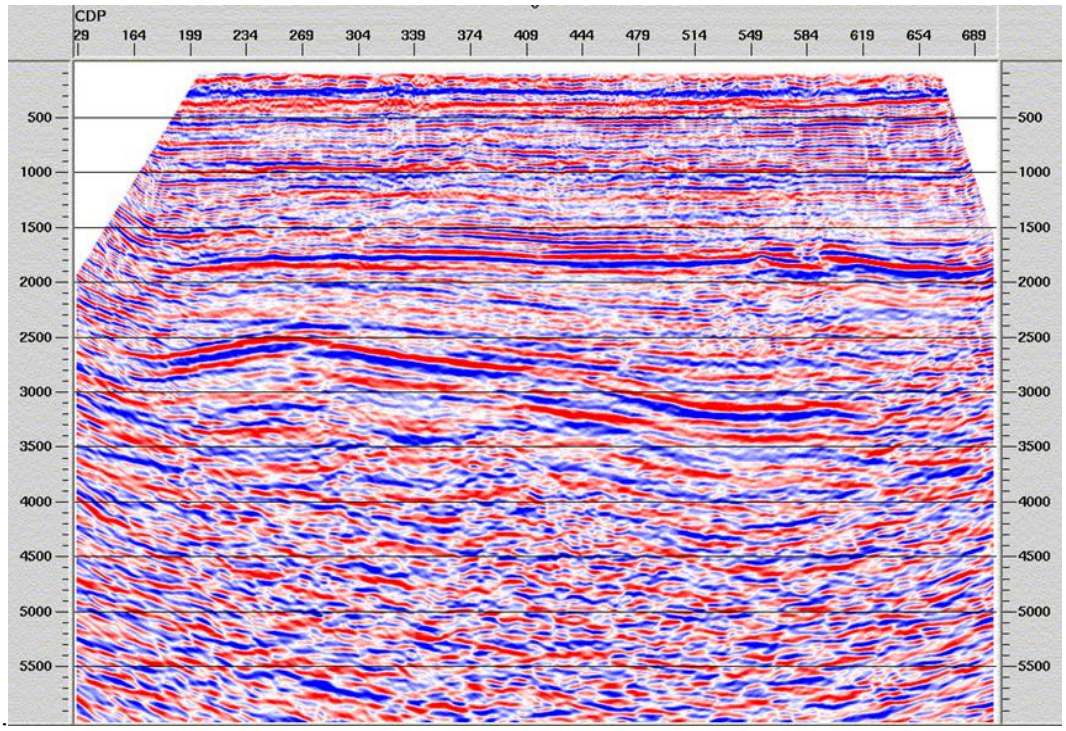

(a) R- component.

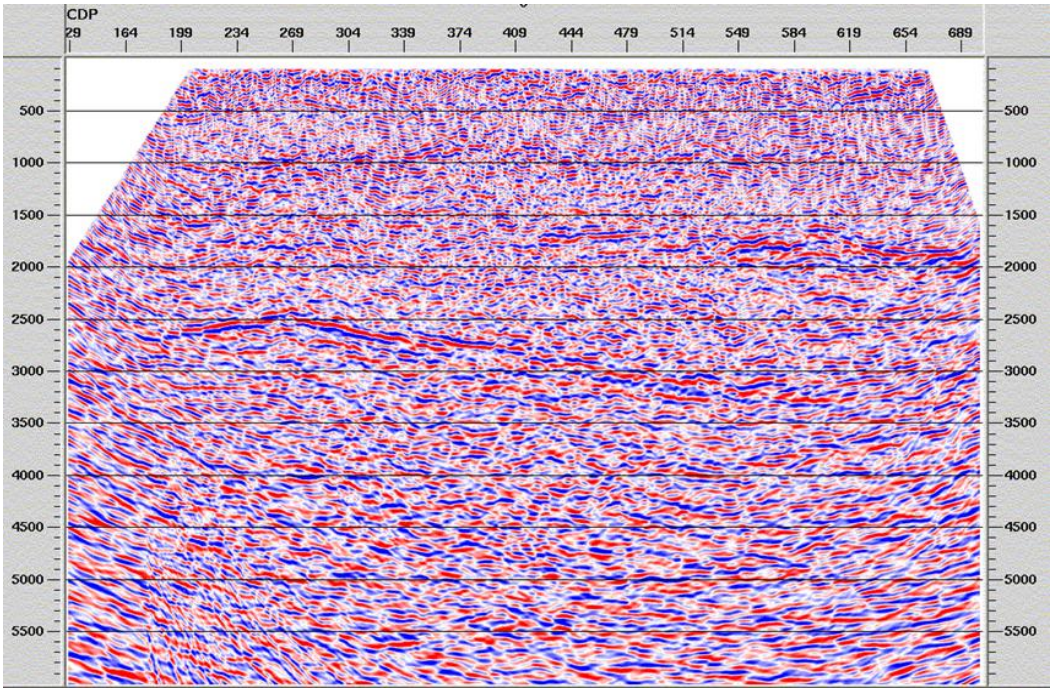

(b) T-component.

Figure 6.3.4: Inline section from the PSTM volumes of Clair OBC data.

6.4 Anisotropic effects

To analyze the anisotropic effects on PS-wave PSTM results, I carried out the PSTM with two sets of velocity models: one is an anisotropic velocity model which consists of four parameters (V_{P2}, V_{S2}, η_{eff} and ζ_{eff}); another is the isotropic velocity model which contains two parameters (V_{P2}, V_{S2}). The CXtools I used in the analysis is developed by EAP (Dai, 2003) and it takes anisotropy into account. Though it is developed to handle vertical transverse isotropy (VTI anisotropy) and the Clair oil field is assumed to exhibit horizontal transverse isotropy (HTI anisotropy) due to vertical aligned fractures. The analysis in Chapter 5 indicates that the HTI anisotropy in the overburden is relatively weak, thus the tools for VTI anisotropy analysis on the OBC data can be used for the upper part (above a HTI layer), because the presence of VTI mainly locates in the shallow part.

Anisotropic processing produces not only an image of the subsurface but also supplies information for a subsurface velocity and anisotropy model. The velocity models (four parameters) I built from the Clair PS-wave 3D OBC data are shown in Figure 6.4.1. The P-wave velocities range from 2200 to 3109 (m/s), while the S-wave velocities range from 690 to 1138 (m/s). The overall trend of variation in the P-wave and S-wave velocities follows the structural trend (Figure 6.3.4). In the P-wave anisotropy profile (figure 6.4.2a), the anisotropy varies from 0.1% to 0.5%, which is very small and can be ignored. However, in the S-wave anisotropy profile (figure 6.4.2b), the anisotropy varies from 1% to 5% which is an order of magnitude higher than the P-wave anisotropy. This explains why we can ignore the VTI anisotropy for the P-wave data, but we should not ignore the anisotropic effects in PS-wave data. Figures 6.4.2a and 6.4.2b also show that the anisotropy parameters decrease with depth.

Figures 6.4.3a and 6.4.3b are the PSTM results based on the two different velocity models respectively. In the PSTM section earlier than 2.5s, the PSTM result using the anisotropic velocity model is better than that the isotropic PSTM result in terms of both event continuity and focusing. However, in the lower part of the section, both are close in terms of imaging quality, which means that the effect of anisotropy becomes weak with depth. The results indicate that for shallow targets, in PS-wave processing we need to pay more attention to anisotropic effects which may arise from VTI media. If the target is very deep,

VTI anisotropy will not affect the imaging quality much, and we may just bypass the anisotropic analysis in PS-wave data analysis.

6.5 Discussion

In this chapter I have analyzed Clair OBC data to understand and quantify anisotropic sensitivities associated with PS imaging in the presence of VTI anisotropy. I demonstrated how anisotropic parameters can be estimated from 4C seismic data, and how such information can be used for improving subsurface imaging. Both isotropic and anisotropic processing flows have been introduced and applied to the data set. I found that the isotropic results for both Pand C-wave give unsatisfactory images. Determination of the anisotropy in the data showed that the C-wave anisotropy is stronger than the P-wave anisotropy.

PS-wave processing is different to P-wave processing and involves some inherent problems such as asymmetric ray-path and conversion-point binning, increased sensitivity to anisotropy, etc. PS-wave PSTM is a better approach than the conventional PS-wave processing scheme comprising CCP binning, NMO, DMO and post-stack migration, which can be carried out by building a PS-wave stack velocity model from ACCP gathers and using the CIP gathers to update the migration velocity model.

Though signal to noise ratio of the data often limits the image quality, anisotropy may also play a significant role. Both P-wave and converted S-wave anisotropy decrease with vertical travel time, but the converted S-wave data are more affected by anisotropy than the P-wave data. From the results of the anisotropic parameter analysis, the P-wave anisotropy is very small (less than 1%), but the S-wave anisotropy varies from 1% to 5%, and cannot be neglected for PS-wave processing. The PS-wave PSTM result based on the anisotropic velocity model is better than that based on the isotropic velocity model, and the improvements are mainly located in the upper part of the section.

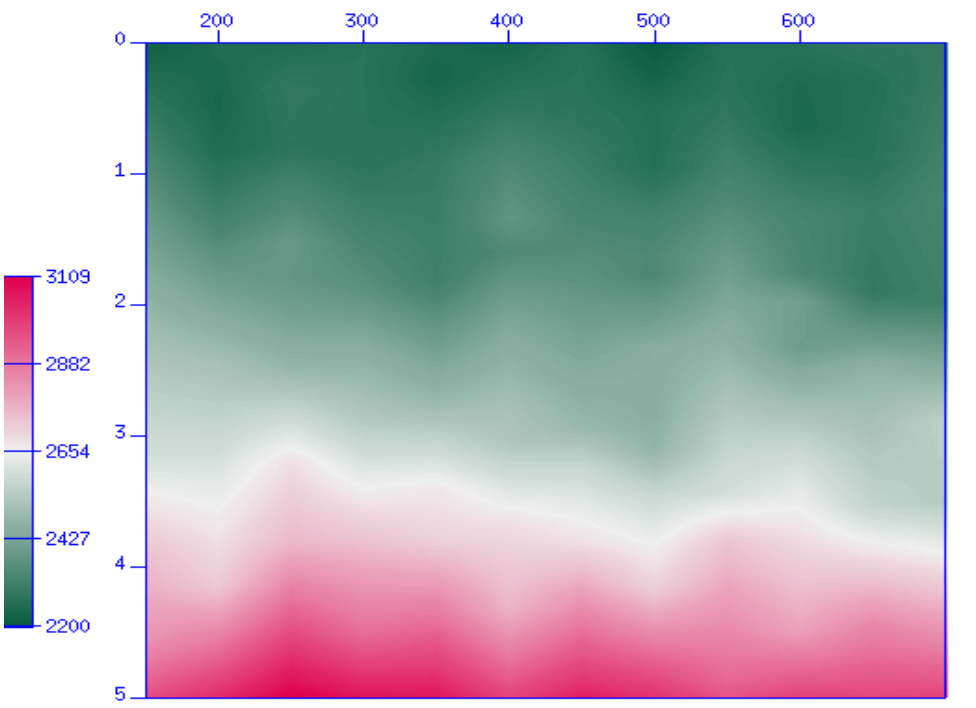

(a) V_{P2}

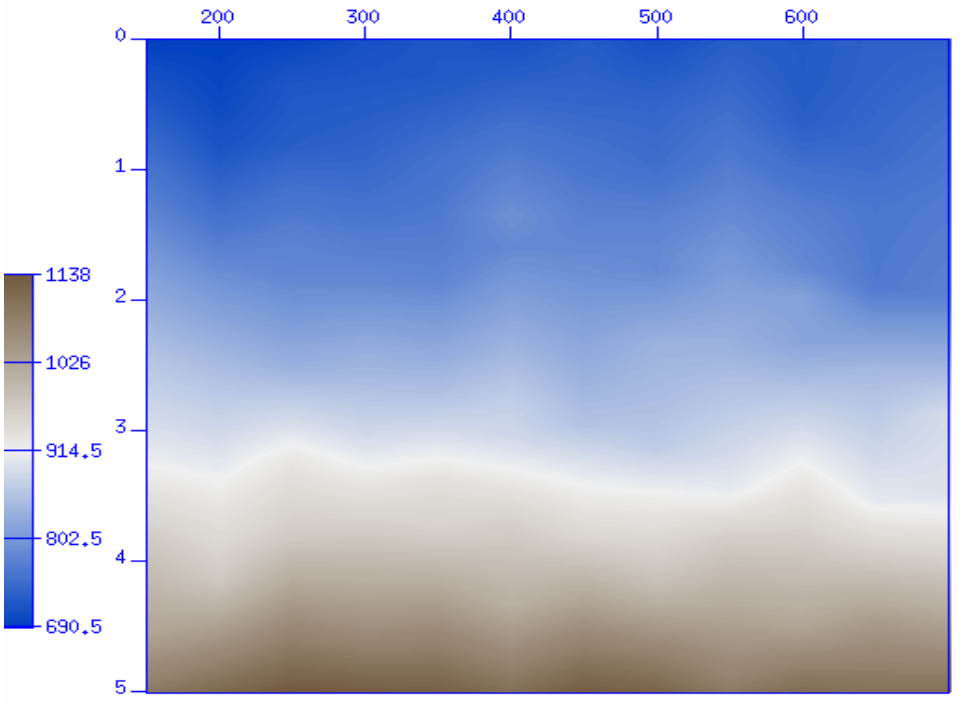

(b) V_{S2}

Figure 6.4.1: PSTM anisotropic model. The vertical axis denotes time in seconds.

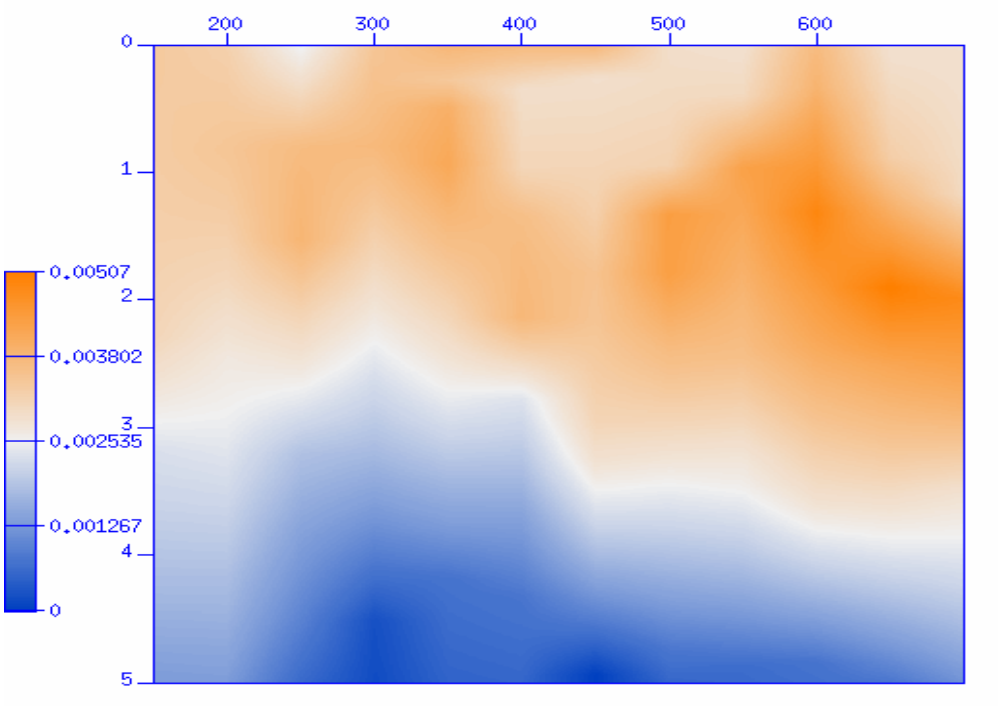

(a) η_{eff}

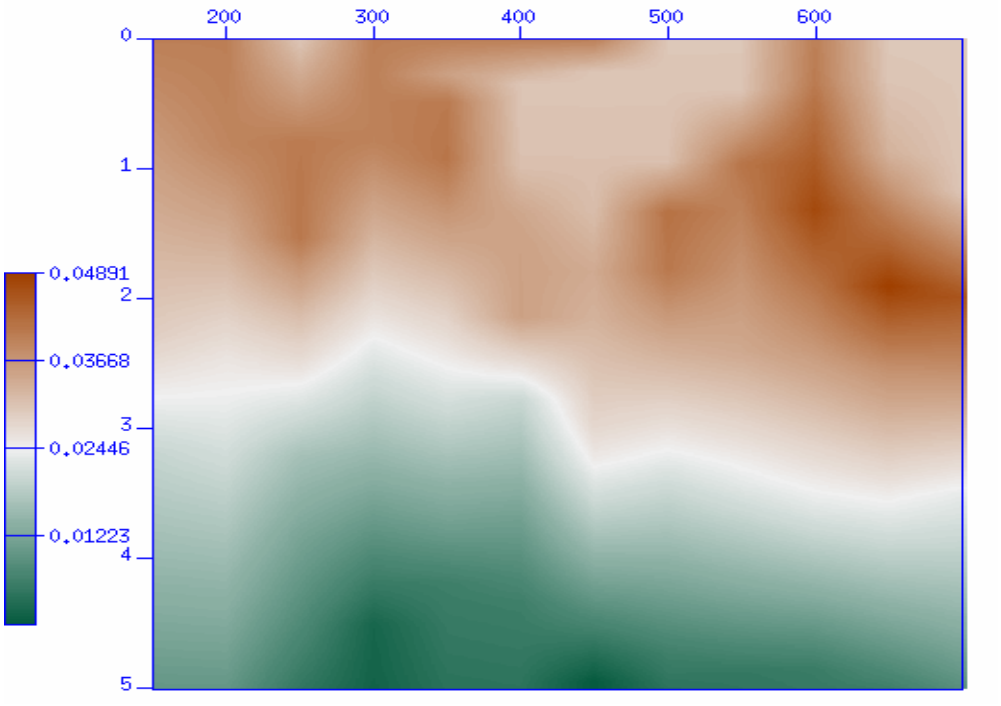

(b) ζ_{eff}

Figure 6.4.2: PSTM anisotropy model. The vertical axis denotes time in seconds.

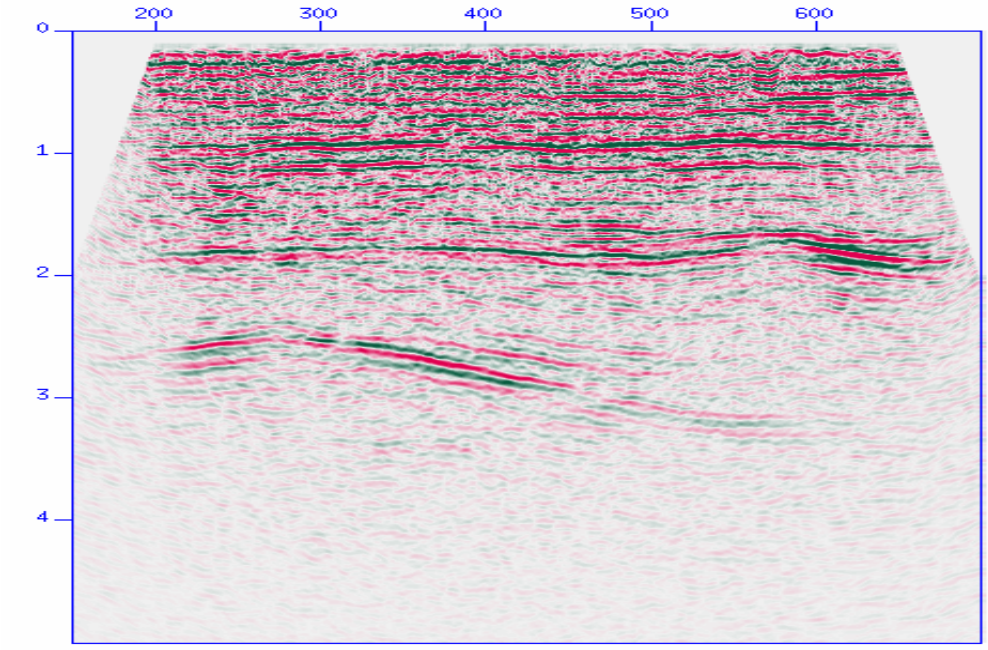

(a)

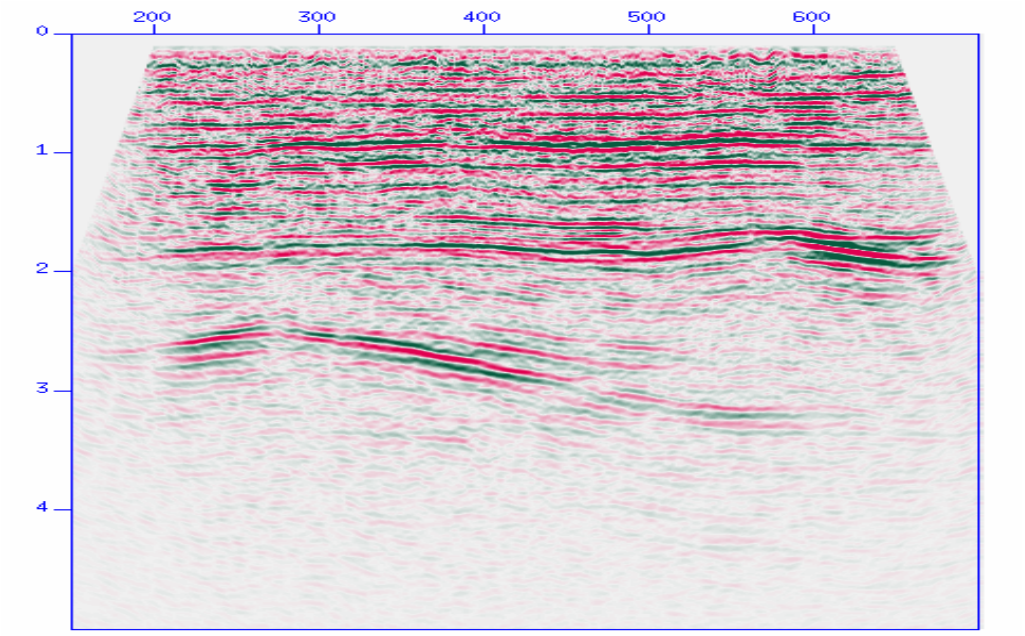

(b)

Figure 6.4.3: R-component PSTM. (a) Section based on the isotropic velocity model, bypassing the anisotropic parameters shown in Figure 6.4.1c and 6.6.1d; (b) section based on the four-parameter anisotropic velocity model in Figure 6.4.1.

Chapter 7

Fluid detection with seismic anisotropy: synthetic study

In this chapter I carry out numerical analyses to study the effects of viscosity， frequency, angle of incidence and fracture density on the seismic anisotropy of the fluid-saturated HTI medium. In particular, I examine the viscosity dependency through the three Thomsen anisotropy parameters, which may be linked to the seismic measurements ΔR_{pp} (P-wave amplitude difference between parallel and perpendicular to fracture strike) and ΔR_{ps} (PS-wave amplitude difference between parallel and perpendicular to fracture strike), so as to study the possibility of using multi-component seismic data to monitor fluid substitution in producing reservoirs.

7.1 Introduction

How to effectively monitor fluid substitution in producing reservoirs is an important issue for reservoir engineers, especially in cases where water injection is involved to drive oil towards a producing well to improve productivity. Geophysicists have devoted great efforts to the problem of determining fluid saturation from seismic measurements and many studies have been carried out for such a purpose, with mixed results. (Landro and Stronen, 2003; Kolk, *et al*, 2001; Varela et al., 2006). This is because the effects of oil and water saturation on pure P- and S-wave (shear wave) velocities are very similar, and the impedance variation is very small. It is commonly believed that fluid information is to be derived from the P-wave data, with shear-waves being insensitive to fluid, and indeed many successful fluid-detection examples have been based on analysis of the P-wave (e.g. Lumley, *et al.*, 1994; Johnston, *et al.*, 1998; Korneev, *et al.*, 2004).

However, when considering fractured reservoirs which are usually simplified as HTI models, we encounter the phenomenon of seismic anisotropy, and the rock physics relationships relevant to fractured, anisotropic rocks are subtler than those for the more familiar isotropic case. We have to take account of the effect of anisotropy on fluid substitution in the analysis, and many studies show links between fluid-saturated HTI media and the characteristics of seismic anisotropy (e.g. Chapman and Maultzsch et al., 2003). Many studies reveal the links between the fluids in HTI media and anisotropic seismic properties. For example, based on Hudson's model, it shows that the normal to shear compliance ratio is directly related to pore or fracture fluids and theoretically at least it is possible to estimate pore or fracture fluids direct from seismic data (Liu and Li et al., 2000). Recent theoretical advances in frequency-dependent anisotropy have shown the possibility of using seismic anisotropy to detect fluid saturations (Chapman and Maultzsch, 2003). These theories allow anisotropic dispersion and attenuation to give information on rock and fluid properties.

The exchange of fluids between fractures, cracks and pores in the surrounding matrix rocks can have a strong influence on the predicted anisotropy of the rocks (Mukerji and Mavko, 1994; Thomsen, 1995). Chapman and Maultzsch et al. (2003) point out that if the reservoir contains fluid-filled micro-cracks and meso-scale heterogeneities, anisotropic fluid substitution predicts a strong effect on the slow shear-wave between water and oil saturation due to the change in fluid viscosity. Furthermore, the changes in pore-fluid pressure will also cause the compliant cracks to open and close dynamically and hence modify the effective elastic constants of the fluid-filled rock, further enhancing S-wave splitting (Zatsepin and Crampin, 1997). Consequently, S-wave splitting can be used to monitor changes in the reservoir due to changes in the fluid saturation and stress field induced by the production process. S-wave splitting is known to be sensitive to the fracture properties and fluid bulk modulus and it has long been hoped that analysis of S-wave splitting in multi-component data would be able to improve our ability to detect fluid substitution in fractured reservoirs. Queen and Rizer (1990) give a good method of using seismic S-waves to characterize fractures and predict fluid flow direction. However, only a few open fractures may control the fluid flow and the stress controls fracture distributions and thus fluid flow pathways (Queen et al., 1992).

Oil and water have similar bulk moduli, and this fact has impeded efforts to tell the two apart from analysis of seismic data using elastic models. However, the two fluids often have markedly different viscosities, and if we can find a robust seismic measurement for fluid viscosity we would greatly improve our chances to discriminate between the two fluids. Thus the ability to detect a viscosity effect is of great potential relevance to the problem of oil-water discrimination. Since the viscosity of fluids saturating a fractured medium will affect the medium inelastic properties, it is theoretically possible to infer viscosity information in seismic data by estimating seismic attenuation, and so to monitor fluid saturation changes. This is particularly important for the oil-water case, as oil and water can have much bigger difference in viscosity than other physical properties.

For this purpose, I investigate the effects of fluid viscosity on certain seismic attributes through numerical modelling and analyze the use of viscosity to detect oil-water saturation in fractured reservoirs. I first carry out a theoretical study of wave propagation in vertically fractured rock to analyze frequency-dependent anisotropy. For angles of incidence typical of seismic reflection data, I find that it is the slow-shear wave which suffers most attenuation and whose properties are most sensitive to fluid viscosity. Further to this, I demonstrate that the converted shear wave (PS-wave) amplitude in the fracture normal direction can be very sensitive to the fluid, even when the P-wave attributes are insensitive to fluid.

Besides viscosity, other factors such as frequency, angle of incidence, and fracture density will also affect anisotropy and have combined effects on seismic data. Thus I investigate the individual and combined effect of these factors to obtain clearer insights of how to effectively use them for fluid characterization.

7.2 Seismic propagation and fluid mobility

As we already know, when a seismic wave passes by, rocks will be slightly deformed to produce stress as well as strain to allow the wave to propagate forward. If the pores, cracks and fractures in rocks are saturated with non-isolated fluids, the stress generated by the seismic wave will force the fluids to be pumped in and out of thin pores and cracks to equilibrate pressure; this causes seismic wave dispersion and attenuation. The

time required to relax the stress is determined by rock background properties such as porosity, fracture sizes and densities, as well as the fluid properties. Lower mobility requires more time or lower seismic frequency for fluid stress to equilibrate. Bigger fracture size and density normally increases fluid permeability, while viscosity influences fluid substitution speed in places where a pressure difference exists; higher viscosity means the fluid takes more time to react to pressure gradients. Seismic frequency, rock background properties and fluid viscosity affect the time for fluid pressure to equilibrate during seismic propagation, and thus affect seismic properties. The substitution of fluids between fractures and equidimensional ('equant') pores occurring during the passage of a seismic wave will affect the anisotropic elastic properties (Thomsen, 1995). The distributions of aligned cracks also contain grain-scale equant pores which can significantly influence seismic attenuation. The effects of squirt flow in media with aligned cracks was analysed for seismic attenuation (Point, T., et al., 2000), which may provide very useful information for seismic anisotropy analysis.

I here assume fracture distributions in porous rocks are approximately aligned and vertical. Traditional techniques for modelling the elastic properties of such systems make use of static equivalent medium theories in the long wavelength limit. Such theories have many features in common, and the simplest can be shown to be consistent with the notation of Schoenberg (Schoenberg and Douma, 1988), in which the "excess compliance" associated with the fracture network can be written in terms of two parameters, the normal compliance (Z_N) and shear compliance (Z_T) of the fractures. A typical assumption is that Z_T will be insensitive to fluids whereas Z_N will decrease with increasing fluid bulk modulus. Theories which assume that the cracks are penny shaped allow explicit computation of Z_N in terms of the fluid properties, either assuming that the cracks are fluid-isolated or allowing fluid communication with the surrounding rock (Thomsen, 1995).

Such theories demonstrate that for near-vertical propagation, shear-wave splitting can vary markedly with fluid saturation. The predicted change in shear-wave splitting arising from a given change in fluid properties varies markedly between the different theories, but the models do predict a consistent trend. Fluids with lower bulk moduli give rise to increased Z_N values, and this tends to lead to an increase in measured S-wave splitting,

for near vertical propagation. It is the slower quasi-shear wave whose velocity changes with the fluid; the faster wave is a pure-shear wave whose velocity is insensitive to fluid bulk modulus in accordance with Gassmann's relation.

More complex theories attempt to predict the anisotropic dispersion and attenuation which is generated by fluid-saturated fracture systems. In these theories a central role is played by the fluid mobility parameter which is the ratio of permeability to fluid viscosity (Batzle et al., 2006). The fluid mobility is associated with a "characteristic frequency", which divides the frequency range into broadly three bands; a low frequency range, a transition band and a high frequency range. The low and high frequency ranges correspond to the static cases in which we assume fluid-communicating or fluid-isolated cracks respectively. The behaviour in the transition band is rather different, since in this case the velocities change rapidly with frequency and attenuation occurs.

In the case in which we have a single vertical fracture set, theoretical models predict that the attenuation should be strongly anisotropic. Waves propagating in the plane of the fractures are predicted to suffer very little attenuation, but in the plane perpendicular to the fractures strong attenuation can take place.

7.3 Frequency dependent anisotropy

Chapman (Chapman and Maultzsch et al., 2003) introduces the squirt-flow model to study frequency-dependent anisotropy and established the poro-elastic equivalent medium theory to distinguish crack size by measuring and interpreting frequency-dependent seismic attenuation; there are some good examples for the study (Maultzsch ad Chapman et al., 2003; Liu and Maultzsch et al., 2003). In the calculation of elastic constants, the factors that may affect fluid mobility, such as fluid density, viscosity, permeability, fracture and crack density and porosity are taken into account in the explicit expressions. Once all elastic constants are obtained, we can calculate the three Thomsen anisotropic parameters containing the effects of rock background structure and fluid properties as well as the seismic frequency supposed. Chapman and Maultzsch et al. (2003) also give the parameterization method for the model, so that the specification of a reference elastic tensor can be avoided, and studied the effects of three different fluid saturations on the anisotropy. The Chapman model and the

parameterization method underlie the basis of studying effects of viscosity on elastic constants, which can be further used to calculate Thomsen anisotropic parameters containing the effects of fluid properties, and thus help to find a solution to discriminate fluid distribution in fractured reservoirs through certain seismic properties.

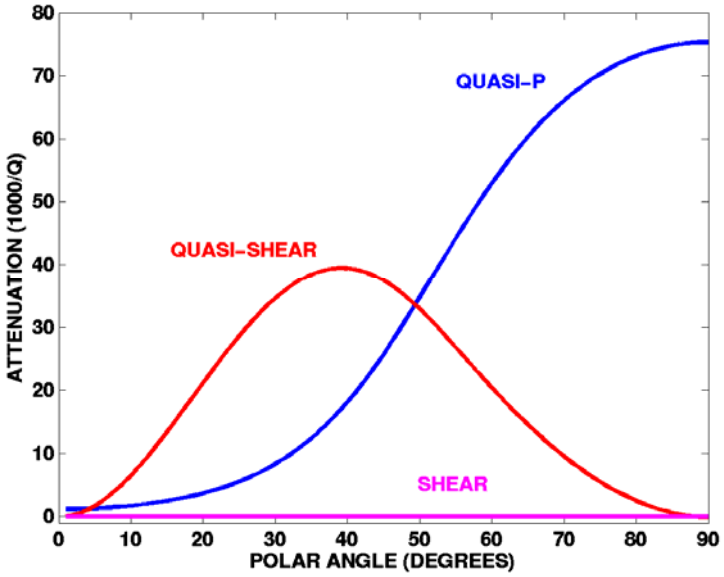

Figure 7.3.1: Calculated attenuation for the 3 wave modes as a function of polar angle (0° is vertical, 90° is horizontal) for propagation in a vertical plane, perpendicular to the vertical parallel fractures.

Figure 7.3.1 demonstrates typical behaviour of the model, assuming propagation in a plane perpendicular to the fractures, for three wave modes (P wave, fast S-wave and slow S-wave) as a function of polar angle (Chapman, 2003). We set the convention that for a vertical fracture set, a polar angle of 0° corresponds to vertical propagation while 90° is horizontal and parallel to the fracture normal. The fast (pure) S-wave should suffer no fluid-related attenuation, but both the P-wave and slow shear wave can be strongly attenuated. This behaviour comes about because the attenuation is assumed to occur due to the relaxation of fluid-pressure gradients between the fractures and the surrounding pore-space. The pure S-wave does not compress either the fractures or the pore-space and so can create no such attenuation. Both the P-wave and quasi-shear do compress the fractures relative to the pore-space and thus create attenuation. The effect is most pronounced for the P-wave, which suffers the highest absolute attenuation of any of the

waves when it propagates at 90°. Nevertheless the polarisations of the P- and quasi-shear are at right angles to one another, and this means that the angle of maximum attenuation differs for the two modes. In particular, while the P-wave has maximum attenuation for horizontal propagation the maximum quasi-shear attenuation occurs for propagation around 45°. In reflection seismology we are typically concerned with angles of incidence between around 0° and 45°. A striking conclusion to be drawn from Figure 7.3.1 is that for such angles of incidence, the greatest effect of the fracture related attenuation should be on the quasi-shear wave. Furthermore, for these angles of incidence the quasi-shear mode is typically the slow shear-wave.

The strong attenuation of the slow S-wave has many implications, but in this study we focus on the implications for fluid-substitution. For each wave-mode and for each direction of propagation, the behaviour is predicted to resemble that of a standard linear solid. Figure 7.3.2 shows the predicted velocities as a function of non-dimensional frequency corresponding to the model discussed above for all wave-modes propagating at 30° from vertical and for two different viscosities. Figure 7.3.2a demonstrates the predicted P-wave behaviour. The velocities increase with frequency, but the change is modest since there is little attenuation in this direction. When the viscosity is increased the dispersion curve shifts to lower frequencies, creating a frequency band in which the velocity is sensitive to viscosity. Figure 7.3.2b shows the corresponding shear-wave behaviour. The faster shear-wave is not attenuated, and so its velocity does not depend on viscosity. The slow-shear wave suffers more attenuation than the P-wave and this corresponds to a greater frequency dependence of the velocities. This leads to a frequency band in which the slow shear-wave is very sensitive to the viscosity.

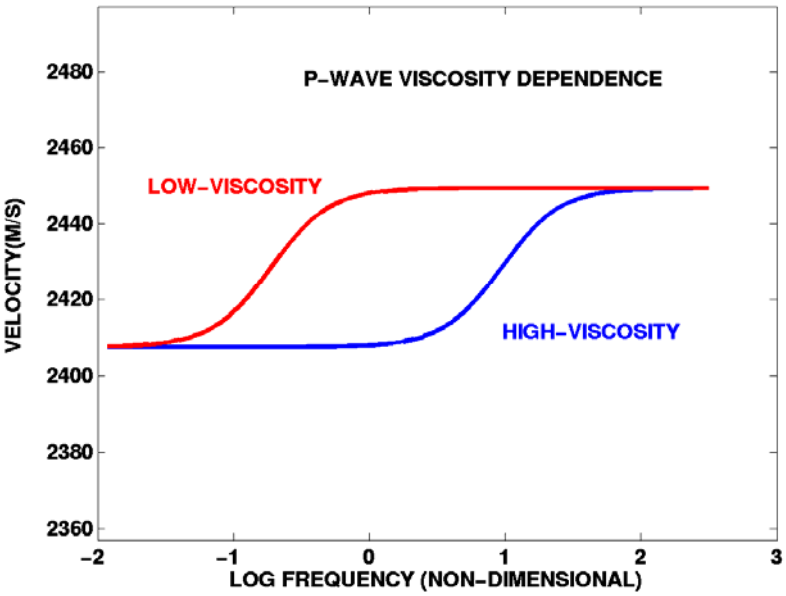

(a)

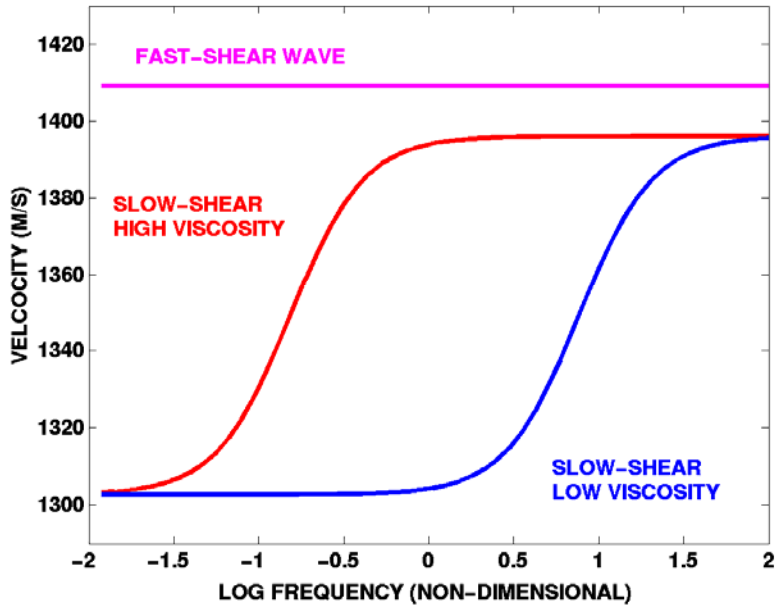

(b)

Figure 7.3.2: Velocity as a function of non-dimensional frequency for P-wave (a) and fast and slow shear-waves (b), for two different viscosities. Propagation is perpendicular to the fractures, with a polar angle of 30°.

Substituting one fluid for another involves changing at least the fluid bulk modulus, viscosity and density. In the water-to-oil case, the oil typically has a slightly lower bulk

modulus and density than the water, but a much larger viscosity. Fluid-substitution theories which ignore the viscosity typically suggest that oil-water discrimination is practically impossible. Since we expect theoretically that the slow shear-wave should be dependent on viscosity in fractured media, it is worth considering whether this effect can be used for oil-water discrimination in fractured reservoirs.

It has also been observed that S-wave splitting is very sensitive to pore-pressure change and is the principal seismic diagnostic for the detection of pressure effects (Angerer *et al.* 2002). The correlation of S-wave splitting with saturation can be modeled using fluid substitution as proposed by Chapman (2003), incorporating pore pressure effects based on the evolution of micro-cracked rocks (Zatsepin and Crampin, 1997). The effects of saturation on the P- and the fast S-wave velocity is very small (less than 1%), as revealed by the modelling (Figure 7.3.3a) and confirmed by core analysis in the laboratory. However the substitution of water for oil changes the fluid viscosity, which induces a change in the slow (quasi) S-wave velocity as high as 4% (Figure 7.3.3b), hence leading to a significant increase in shear-wave splitting for the water saturation case as compared with the oil case (Figure 7.3.3c). Moreover, the fluid substitution due to water flooding also changes the pore-fluid pressures, thus modifying the crack aspect ratios and further enhancing shear-wave splitting. The driving mechanism for the model is fluid migration by flow or dispersion along pressure gradients between cracks at different scale lengths.

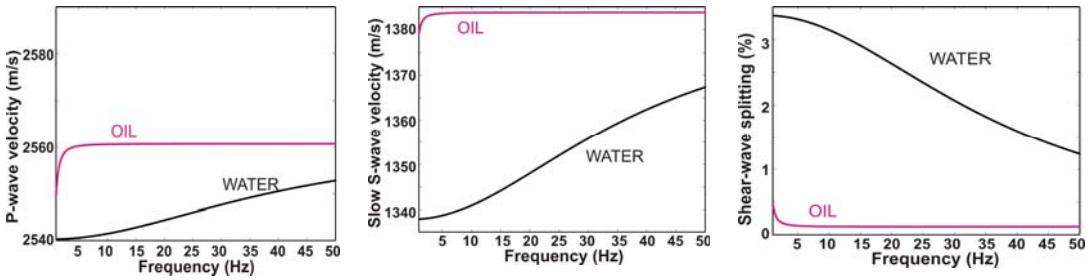

(a) (b) (c)

Figure 7.3.3: Effects of oil-water saturation for the thin sand at depth 1.5km in the study area, calculated using the formula by Chapman and Maultzsch et al. (2003). (a) P-wave velocity; (b) slow S-wave velocity; (c) S-wave splitting.

Certainly, shear-wave splitting is sensitive to oil-water substitution in the modelling framework we describe. Figure 7.3.4 shows S-wave splitting as function of frequency for oil and water saturation. In the low-frequency limit, oil saturation gives rise to higher values of shear-wave splitting, since the lower oil bulk modulus makes the fractures more compliant than the water-saturated case. In the high frequency limit there is little effect of the fluid for thin cracks, although oil will give higher values of shear-wave splitting if we assume much fatter cracks. Between these cases we have again a transition zone corresponding to the frequency dependence of the slow-shear velocity, as shown in Figure 7.3.2. We note that within the transition zone the sensitivity to fluid is greater than, and the direction of the change opposite to, that predicted in either low or high frequency limit. This behaviour has implications for PS-wave reflectivity. I demonstrate this effect with a numerical example, in which the parameters have been taken from the logging data at the Ken 71 reservoir of Shengli Oilfield, the seismic data from the same reservoir is to be discussed in Section 7.7.

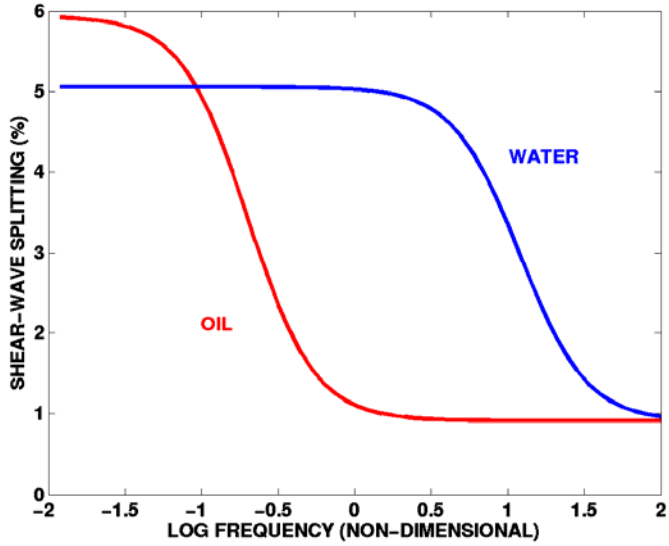

Figure 7.3.4: Predicted values of S-wave splitting as a function of frequency for oil and water saturation.

To further demonstrate the behaviour I calculate synthetic seismograms for a simple model (Figure 7.7.1), with an isotropic layer overlying a fractured layer with horizontal transverse isotropy, where the angle of incidence is taken to be up to 45°. Figure 7.3.5

shows the P- and PS-wave reflection coefficients for waves propagating parallel and perpendicular to the fractures, for both water and oil saturation. As expected, for the P-wave reflection there is very little sensitivity to the fluid in either direction. This is because of the low contrast in bulk modulus between oil and water and little viscosity dependence for these angles of incidence; indeed the bulk modulus and viscosity effects even tend to cancel each other out. Likewise, when we assume propagation parallel to the fracture strike the PS amplitude is predicted to be insensitive to the saturating fluid. This is not the case for propagation perpendicular to the fracture strike, however. In that case the PS-wave reflection is sensitive to the saturating fluid. This is because of the effect of the fluid viscosity for shear-wave propagation in that direction.

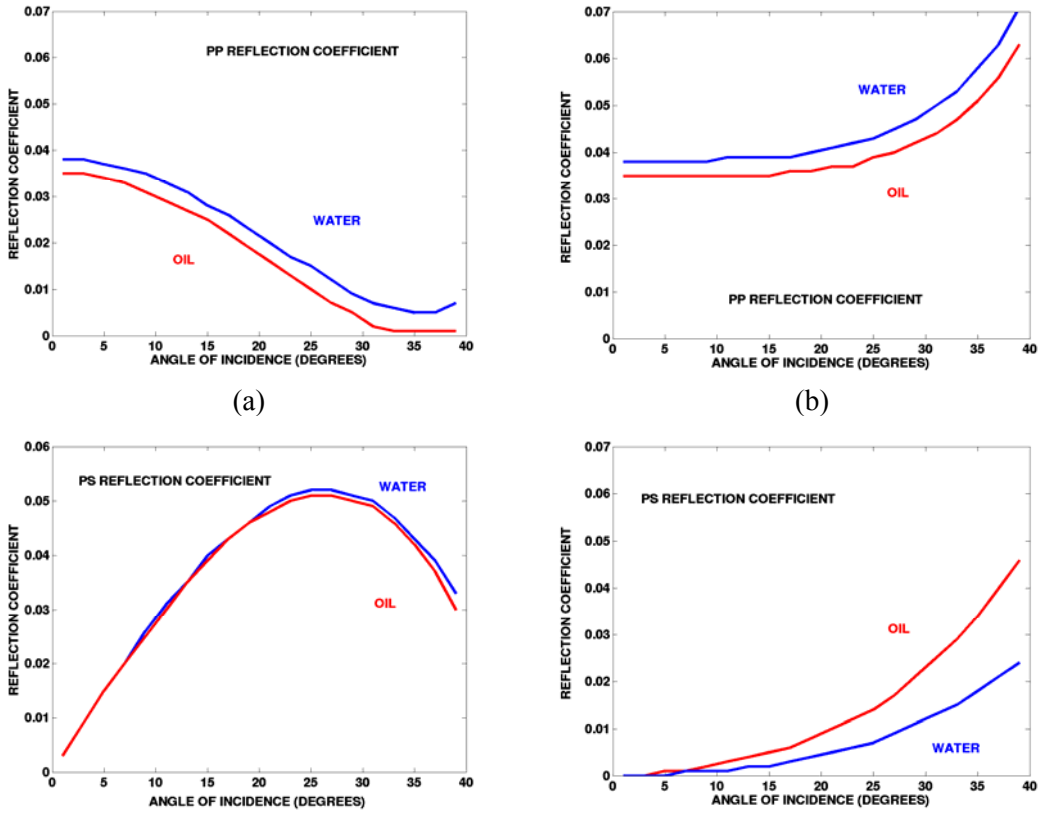

Figure 7.3.5: Computed values for the reflection coefficient. Top diagrams are for P-wave, bottom for PS-waves. Left diagrams are parallel to the fractures, and right are perpendicular.

7.4 Seismic measurement for fluid viscosity in a HTI medium

The communication of fluids between fractures and equant pores which occurs as a seismic wave passes by will influence the elastic properties of the medium (Thomsen, 1995). Liu ad Li et al. (2000) show that the normal to shear compliance ratio is directly related to isolated pore or fracture fluids and it is possible to estimate fluid saturation with seismic data. Chapman ad Maultzsch et al (2003) introduce the squirt-flow model to study frequency dependent anisotropy and establishes the poro-elastic equivalent medium theory which takes frequency, fluid viscosity, fracture and crack density and porosity into account in the calculation of elastic properties. Batzle et al. (2006) proposes the concept of fluid mobility as the ratio of permeability to viscosity to study frequency-dependent seismic velocities in the laboratory. These studies show that seismic frequency, fracture density and fluid viscosity will all have an important potential influence on the seismic anisotropy.

Since fluid saturation influences medium elastic properties, it should affect seismic reflection coefficients. However, inferring fluid properties directly from seismic reflection data seems to be very ambitious since there are so many factors that may have influenced the seismic amplitudes, and fluid properties are obviously not the major one. Furthermore, in oil exploration, what we really want is fluid information in space, not the real fluid properties. Thus, if we are able to obtain information on the variations of fluid properties in the form of seismic properties, together with other information, we may reach the aim of monitoring fluid changes. Thus, what really matters in the detection of fluid saturation is to find a seismic property whose variations can represent fluid property variations in space. Here, I use the method proposed by Li (1998a) to reach for this objective, in which the Thomsen anisotropic parameters for a HTI medium are included. To apply the method, we need to know the orientation of the preferred fracture strike, which can be estimated directly from seismic data (Thomsen, 2002). Though anisotropy information is contained in seismic reflection coefficients for a fluid-saturated HTI medium, it can be hard to interpret. To simplify the analysis, I focus attention on the reflection amplitude difference between the P- and PS-wave for the fracture parallel and fracture normal directions, respectively. Instead of calculating absolute reflection coefficients, we just need to calculate the differences of the P- and

PS-wave reflection coefficients for the fracture parallel and fracture normal directions (Li, 1998a)

$$\Delta R_{pp} = \frac{1}{2}\left(\delta - 2\varepsilon + \frac{8\beta_0^2}{\alpha_0^2}\gamma\right)\sin^2 i \tag{7.4.1}$$

$$\begin{aligned}\Delta R_{PS} = \frac{\sin i}{2\cos j}\Bigg[&\frac{\alpha_0^2}{\alpha_0^2-\beta_0^2}(\delta-2\varepsilon)+\frac{4\beta_0}{\alpha_0}\gamma\cos i\cos j\\ &-\frac{\alpha_0\beta_0}{\alpha_0^2-\beta_0^2}(\delta-2\varepsilon)\cos i\cos j-\frac{4\beta_0^2}{\alpha_0^2}\gamma\sin^2 i\\ &+(\delta-2\varepsilon)\sin^2 i-\frac{\alpha_0^2}{\alpha_0^2-\beta_0^2}(3\delta-4\varepsilon)\sin^2 i\Bigg]\end{aligned} \tag{7.4.2}$$

where, δ, ε and γ are the three Thomsen anisotropic parameters for HTI medium, which contain the effects of rock background properties, fluid properties as well as the supposed seismic frequency. α_0 and β_0 are the average P- and S-wave background velocities of the upper (isotropic) medium and lower (HTI) medium, and i and j are the average propagation angles of the upper and lower medium for the P- and converted S-wave, respectively. Since ΔR_{pp} and ΔR_{ps} have included the effects of fluid properties, they should be able to be used to infer the fluid information.

7.5 Factors affecting Thomsen anisotropic parameters

The Chapman squirt-flow model and the poroelastic equivalent medium theory have demonstrated the fluid viscosity in saturated HTI medium can affect medium elastic properties and thus the Thomsen anisotropic parameters, which make it theoretically possible to use seismic properties to infer fluid viscosity changes, so as to monitor fluid exchange in production reservoirs. Thus, if we calculate the elastic constants of a model (Chapman and Maultzsch et al., 2003), we also have the three Thomsen anisotropic parameters which contain the information on rock matrix and fluid properties (Thomsen, 1986). Figure 7.5.1 shows the variations of the three Thomsen parameters with viscosities. The figures on the lateral axis denote the relative values of viscosity compared to water, for which viscosity is supposed to be 1.0. The fracture density is 8% and the angle of incidence is 27°. We can see that both ε and δ slightly decrease as

viscosity increases, while γ remains a constant value with respect to viscosity, revealing that γ is insensitive to viscosity.

However, when the squirt-flow model (Chapman and Maulzsch et al., 2003) is used to calculate elastic properties, besides fluid viscosity, the frequency, fracture and crack density and porosity are also involved, which will influence the anisotropic properties of the medium. Figure 7.5.2 shows the distribution of Thomsen anisotropy parameters with fracture density, where the frequency and viscosity used in the diagram are 15Hz and 20.0, respectively. It shows that all three anisotropy parameters change with fracture density: γ and ε increase with fracture density, but δ decreases with fracture density. Figure 7.5.3 shows the changes of anisotropy parameters with frequency, where fracture density is 8% and viscosity is 20.0. The changes for ε and δ mainly occur within the frequency band of 10 - 30 Hz, while γ appears to be insensitive with respect to frequency, which is similar to figure 7.5.2.

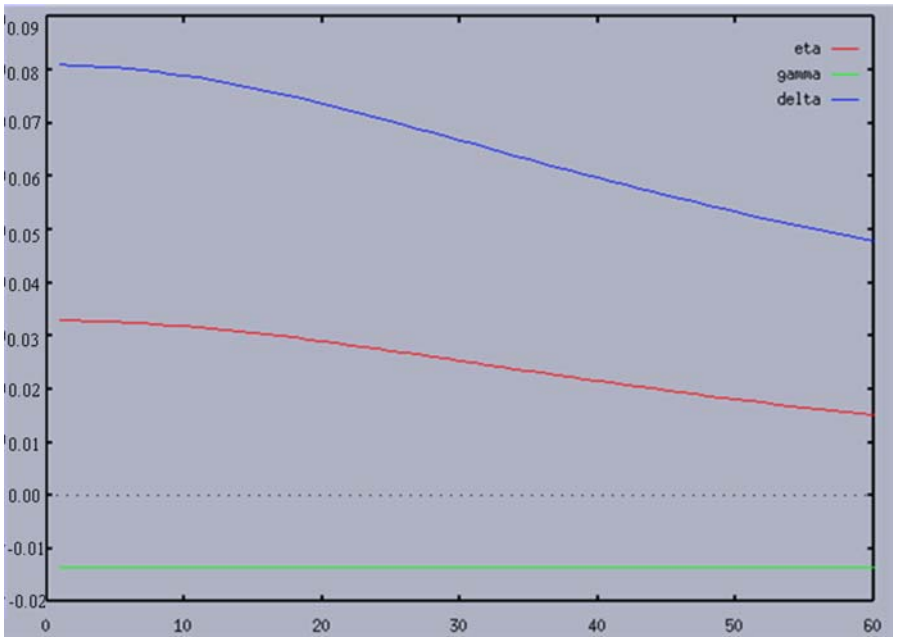

Figure 7.5.1: Viscosity (as is represented by the horizontal axis; the figures on the axis indicate the relative values to water, the same for the following diagrams in this chapter) effects on Thomsen parameters ε (red curve), γ (green curve) and δ (blue curve). The fracture density, angle of incidence and frequency used here are 8%, 27^{o}, 15Hz, respectively.

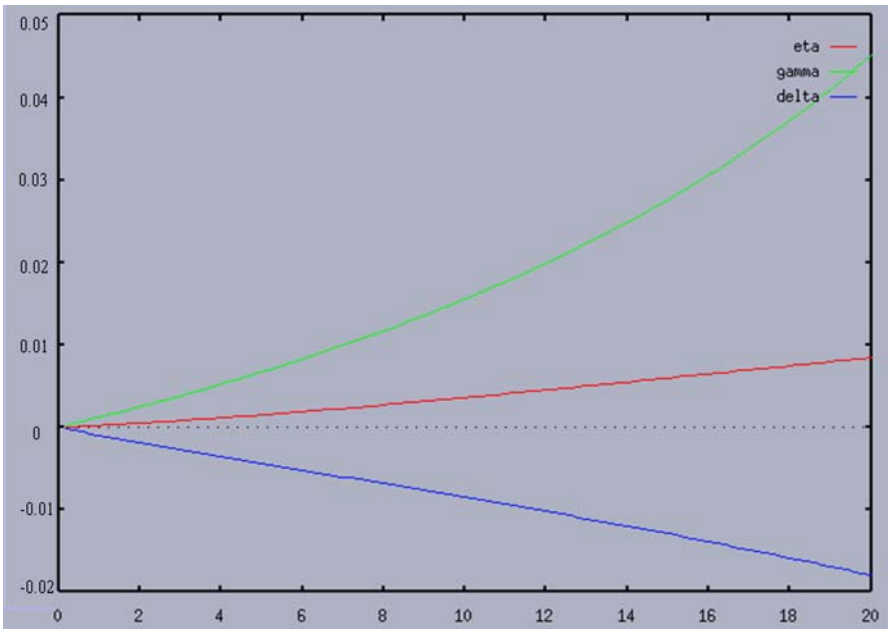

Figure 7.5.2: Variation of Thomsen parameters ε (red curve), γ (green curve) and δ (blue curve) with fracture density. The angle of incidence, viscosity and frequency used here are 27°, 20 and 15Hz, respectively.

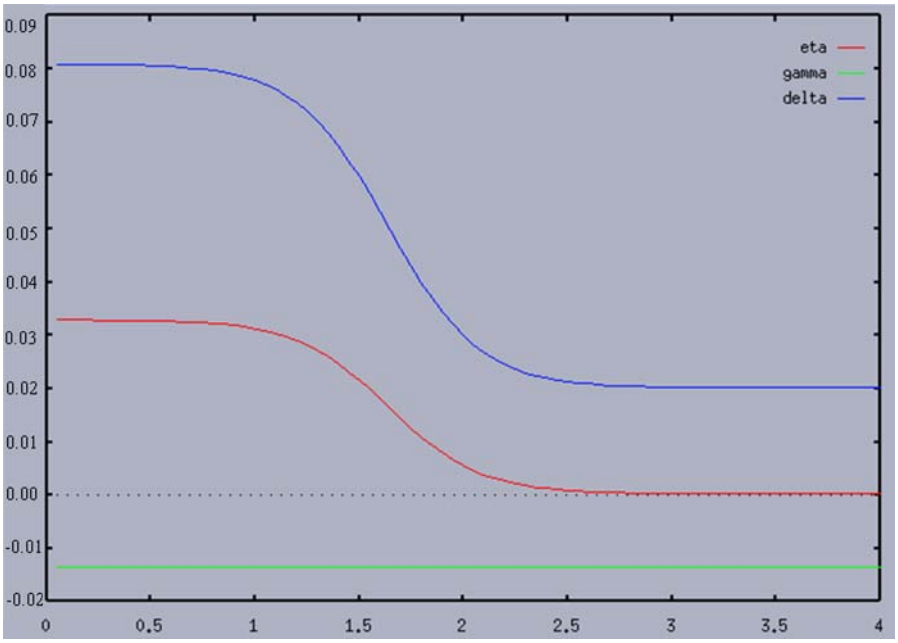

Figure 7.5.3: Variation of Thomsen parameters ε (red curve), γ (green curve) and δ (blue curve) with frequency. The angle of incidence, viscosity and fracture used here are 27°, 20 and 8%, respectively.

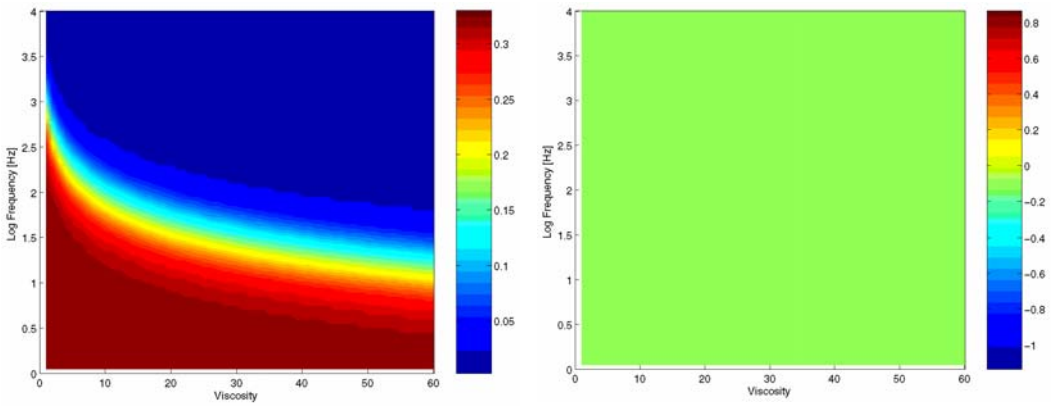

(a) (b)

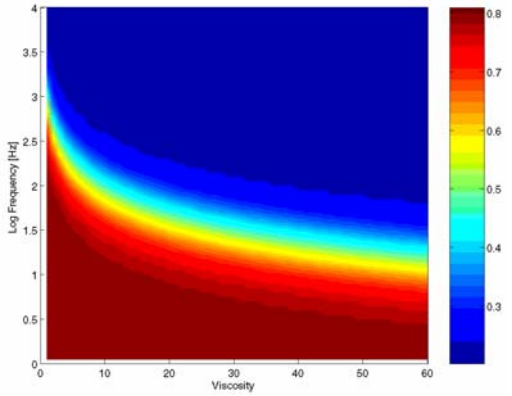

(c)

Figure 7.5.4: Variations of Thomsen parameters ε (a), γ (b) δ (c) with viscosity and frequency. The fracture density and angle of incidence used here are 8% and 27°, respectively.

Figure 7.5.4 displays the variations of the three Thomsen parameters in the two-dimension plane of fracture density and frequency. It reveals that both seismic frequency and viscosity have very similar effects on medium elastic properties, yet within the seismic frequency band of 10-30Hz, ε and δ change more dramatically with frequency than with viscosity, and γ is constant. Figure 7.5.5 displays the three Thomsen parameters changing with viscosity and fracture density. It shows that, when fracture density is small (less than 2%), ε does not change with viscosity, while for a moderate fracture density (8%), ε changes most when viscosity is less than 30.0. γ changes with fracture density, yet it has no resolution for viscosity.

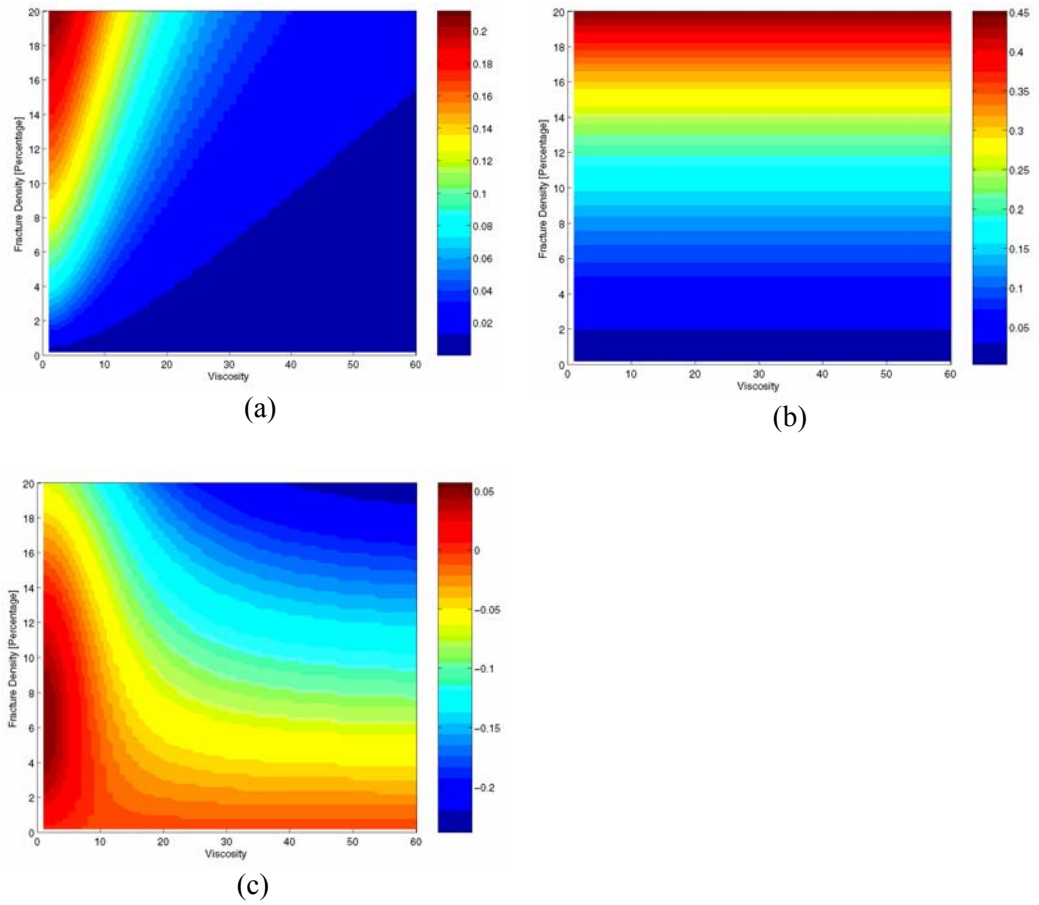

Figure 7.5.5: Variation of Thomsen parameters ε (a), γ (b) and δ (c) with viscosity and fracture density. The frequency and angle of incidence used here are 15Hz and 27°, respectively.

The above results prove that variations of fluid viscosity can be revealed in the two Thomsen anisotropic parameters ε and δ. Both seismic frequency and viscosity have similar effects on medium elastic properties, yet within the seismic frequency band, ε and δ changes more dramatically with frequency than with viscosity.

7.6 Variation of P- and PS-wave reflections with viscosities

Figure 7.6.1 shows the relationship of P- and PS-wave reflection amplitudes ΔR_{pp} and ΔR_{ps}, which are the seismic measurements defined by equations 7.4.1 and 7.4.2, with viscosity. The value of viscosity used in the analysis is the relative value compared with water whose viscosity is 1.0 basic unit. It shows that both ΔR_{pp} and ΔR_{ps} increase with viscosity, yet the increase in the PS-wave amplitude, ΔR_{ps}, is much larger than the

increase in the P-wave amplitude, ΔR_{pp}, which means ΔR_{ps} is much more sensitive to fluid viscosity than ΔR_{pp} within a certain viscosity range.

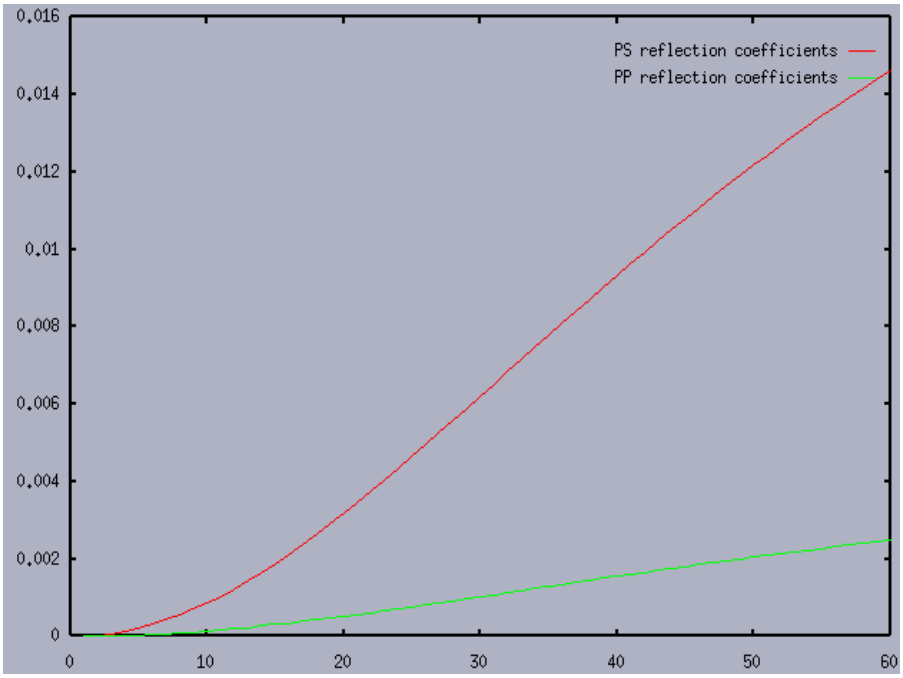

Figure 7.6.1: Variation of ΔR_{pp} (green) and ΔR_{ps} (red) with viscosity. Fracture density: 8%; angle of incidence: 27°.

Figure 7.6.2 shows the variation of ΔR_{pp} and ΔR_{ps} with fracture density. Both ΔR_{pp} and ΔR_{ps} increase when fracture density increases, but the amplitude of ΔR_{ps} is much bigger than that of ΔR_{pp}, which is similar to that in figure 7.6.1, except that the amplitude of ΔR_{pp} and ΔR_{ps} in figure 7.6.2 is much larger than that in figure 7.6.1, which means that both the P-wave and the S-wave are less sensitive to viscosity than to fracture density. It also verifies the fact that, at seismic angles of incidence which normally range from 0° to 45°, the slow S-wave is strongly attenuated and dispersed in the fracture normal direction, while the P-wave and fast S-wave suffer little fracture related attenuation in the fracture strike direction. Figure 7.6.3 displays the distribution of ΔR_{pp} and ΔR_{ps} with frequency, where around the frequency of 30 Hz, there are rapid increases in ΔR_{pp} and ΔR_{ps} with frequency, but the size of increase of ΔR_{ps} is much higher than that for ΔR_{pp}, which indicates a higher potential of using the PS-waves than the P-wave to study frequency-dependent anisotropy.

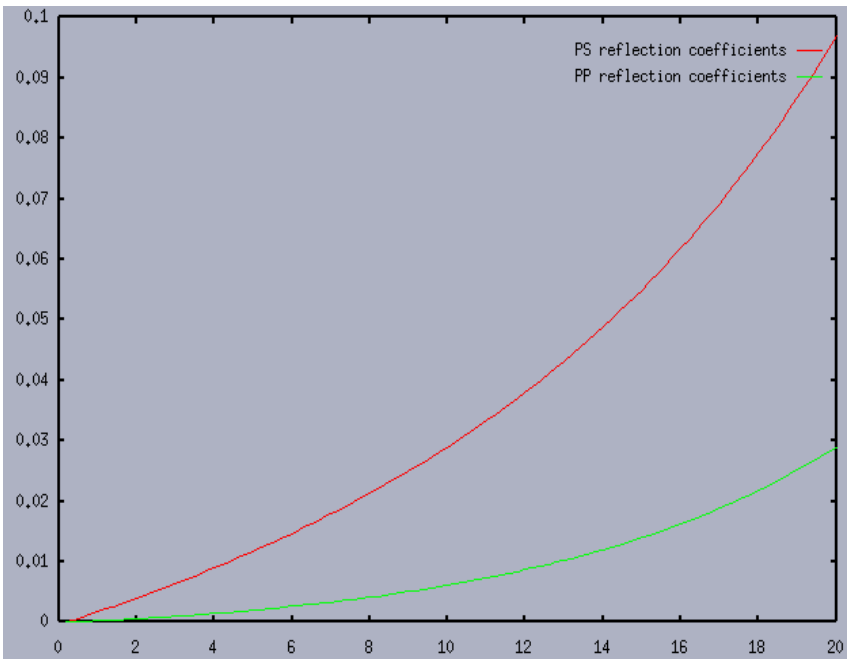

Figure 7.6.2: Variation of ΔR_{pp} (green) and ΔR_{ps} (red) with fracture density. Frequency: 15Hz; viscosity (relative value): 20.0.

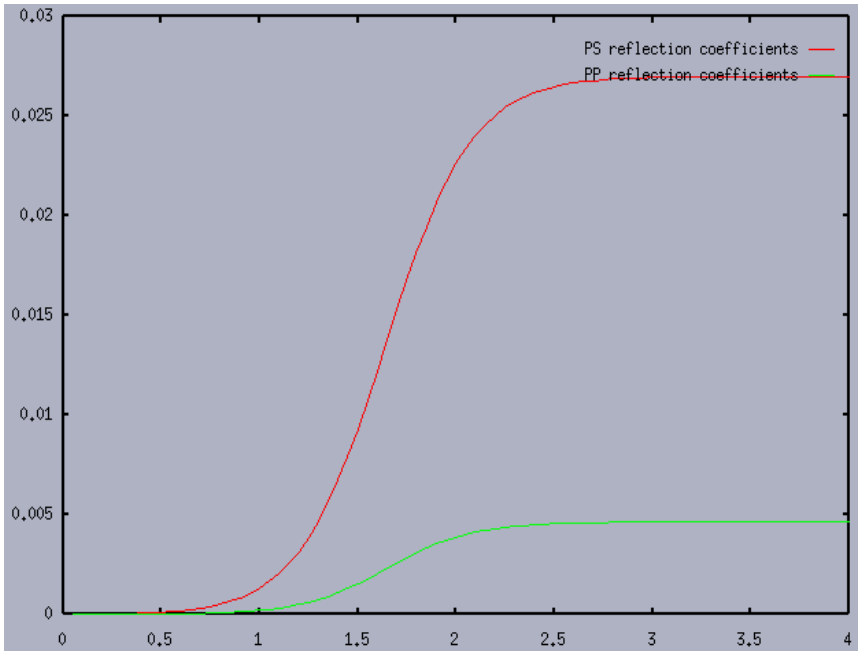

Figure 7.6.3: Variation of ΔR_{pp} (green) and ΔR_{ps} (red) with frequency (log Hz). Viscosity: 20; fracture density: 8%.

Since figures 7.6.1, 7.6.2 and 7.6.3 reveal that ΔR_{ps} is much more sensitive to viscosity than ΔR_{pp}. I focus my study on using ΔR_{ps} in further analysis. The frequency, fluid

viscosity, fracture and crack density affect the anisotropic properties of the medium, which will have combined effects on the distributions of ΔR_{pp} and ΔR_{ps}. Figure 7.6.4a is the distribution of ΔR_{ps} in the plane of fracture density and angle of incidence, showing that if the angle of incidence is smaller than 10^o, the ΔR_{ps} carries little information on fracture density, and if the fracture density is lower than 4%, it is impossible to use ΔR_{ps} to infer any viscosity information. Figure 7.6.4b is the distribution of ΔR_{ps} with viscosity and angle of incidence, which reveals that, to describe the viscosity with ΔR_{ps}, the angle of incidence should be larger than 20^o. Figure 7.6.4c is the distribution of ΔR_{ps} with frequency and angle of incidence, showing that ΔR_{ps} is sensitive to frequency changes only within a certain frequency band (10 – 100Hz) and the angle of incidence should be larger than 20^o. Figures 7.6.4a, 7.7.3b and 7.7.3c reveal a minimum angle of incidence requirement for ΔR_{ps} to be sensitive to frequency, fracture density and viscosity, thus the angle of incidence used for figures 7.6.4d, 7.7.3e and 7.7.3f is 27^o.

Figure 7.6.4d is the distribution of ΔR_{ps} with viscosity and frequency, showing that, within a normal seismic frequency band (10-100Hz), ΔR_{ps} is sensitive to viscosity and can be used to infer fluid viscosity. However, when viscosity is less than 10.0, the change of ΔR_{ps} is very small within this seismic frequency band, yet gradually increases with viscosity, though the resolution in terms of viscosity is still low. Figure 7.6.4e displays the ΔR_{ps} variation with viscosity and fracture density, revealing that the viscosity and fracture density have similar effects on ΔR_{ps}, and the smaller the fracture density, the lower will be the sensitivity to viscosity. The fracture density should be at least larger than 2% for changes of ΔR_{ps} with viscosity to be observed. However, if the viscosity is bigger than 30.0 (relative to water), the reflection amplitude change rate with viscosity becomes quite small. Figure 7.6.4f displays the ΔR_{ps} variation with frequency and fracture density, showing that only if frequency is higher than 10 Hz can the ΔR_{ps} be used to describe fracture densities.

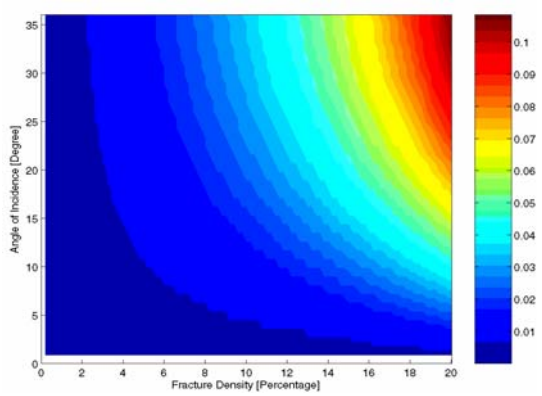

(a) ΔR_{ps} with fracture density and incidence angle. Frequency: 15Hz; viscosity: 20.0.

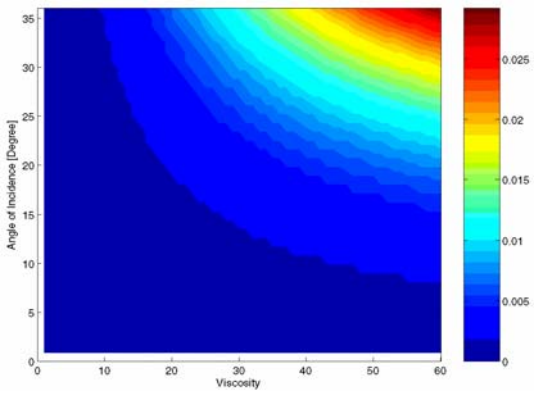

(b) ΔR_{ps} with viscosity and incidence angle. Fracture density: 10%; frequency: 15Hz.

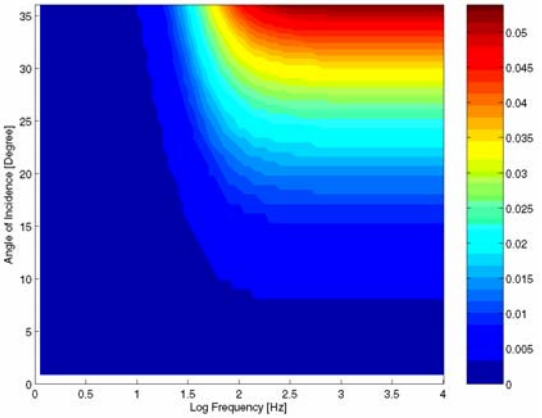

(c) ΔR_{ps} with frequency and incidence angle. Fracture density: 10%; viscosity: 20.0.

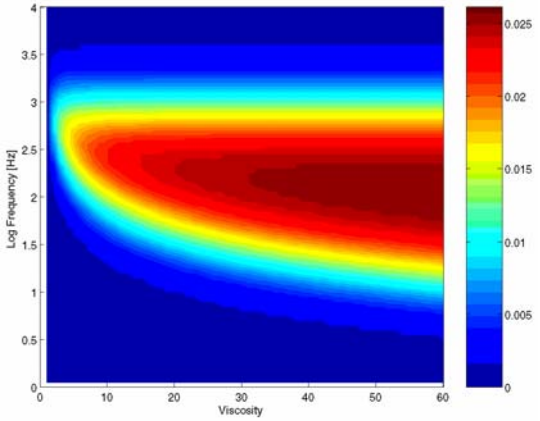

(d) ΔR_{ps} with viscosity and frequency. Fracture density: 10%; incidence angle: 27^{o}.

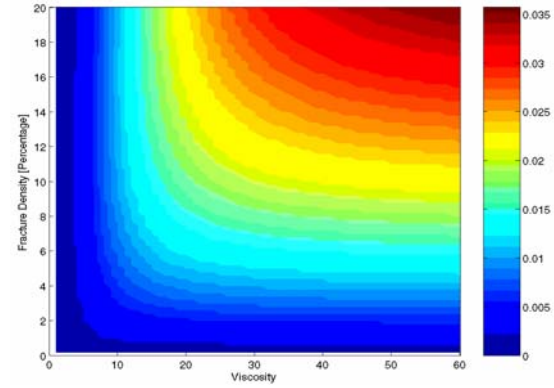

(e) ΔR_{ps} with viscosity and fracture density. Frequency: 15Hz, incidence angle: 27^{o}.

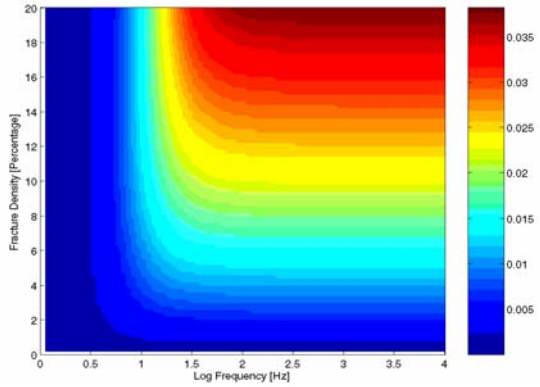

(f) ΔR_{ps} with frequency and fracture density. Viscosity: 20.0; incidence angle: 27^{o}.

Figure 7.6.4: Variations of seismic measurement ΔR_{ps} with fracture density, angle of incidence and viscosity

7.7 Synthetic data analysis

The analyses in section 7.4 reveal that the amplitudes of the PS-wave are sensitive to the saturated fluids in the HTI medium. Here, I do further analysis on the synthetic data to examine the theoretical possibility of using seismic data for the characterisation.

To generate the synthetic data, I establish a three-layer model with a porous, cracked and fluid saturated HTI medium under an isotropic medium to stimulate a fractured reservoir in sandstones under shale layers (Figure 7.7.1). The elastic and inelastic constants of the model are calculated with the methods proposed by Chapman and Maultzsch et al. (2003), which include the effects of fracture density, seismic frequency, angle of incidence and fluid viscosity. The Thomsen anisotropy parameters for the HTI medium are calculated from the elastic constants (Thomsen, 1986). In the general case, an incident P-wave will generate three reflections corresponding to the P, PS1 and PS2 modes. If we confine ourselves to propagation in the symmetry planes however (parallel and perpendicular to the fracture strike), only two reflections, one P-wave and another PS-wave, will be generated. To study the effects of fluid saturation, I generate two sets of data, one dataset corresponds to oil saturation and another dataset corresponds to water saturation.

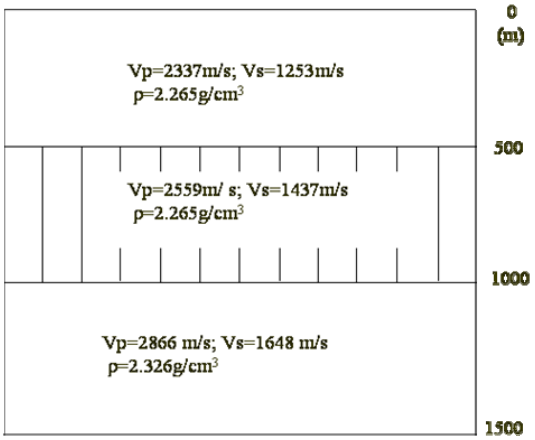

Figure 7.7.1: The model with a middle fluid-saturated HTI medium.

The P-wave amplitudes show very little difference between oil saturation and water saturation, no matter if the wave propagates parallel or perpendicular to the fracture strike (Figure 7.7.2). This is consistent with Figure 7.3.5, indicating the seismic

measurement ΔR_{pp} is not sensitive to viscosity. But for the PS-wave data, this is not the case. When the PS-wave propagates in the direction of fracture strike, very little amplitude difference can be observed, no matter if the fracture is water saturated or oil saturated (Figure 7.7.3a). However, when the PS-wave propagates normal to the direction of fracture strike, a strong anomaly between oil saturation and water saturation is present (Figure 7.7.3b). Figures 7.7.2 and 7.7.3 prove the fact that the PS-wave propagating normal to the fracture strike has good potential for fluid characterisation.

To make this effect clearer, I pick the amplitudes of the reflections direct from the synthetic data for different modes and directions. As in Figure 7.7.3, the P-wave amplitudes show very little difference between oil saturation and water saturation (Figure 7.7.4). For the PS-wave, if it propagates in the direction of fracture strike, the amplitudes are almost the same for all angles of incidence (Figure 7.7.5a). However, when the PS-wave propagates perpendicular to the fracture strike, it show large amplitude difference between oil saturation and water saturation (Figure 7.7.5b), and the large amplitude difference mainly locates on the traces with larger angles of incidence which correspond to the seismic traces for far offsets.

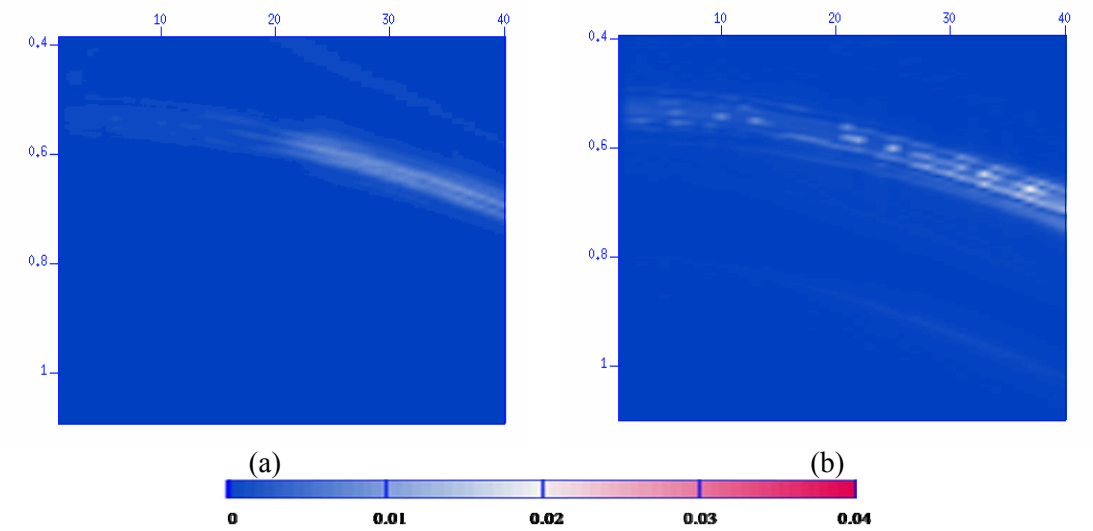

Figure 7.7.2: P-wave amplitude envelope difference between oil saturation and water saturation. (a) P-wave propagates in the fracture strike direction; (b) P-wave propagates in the fracture normal direction.

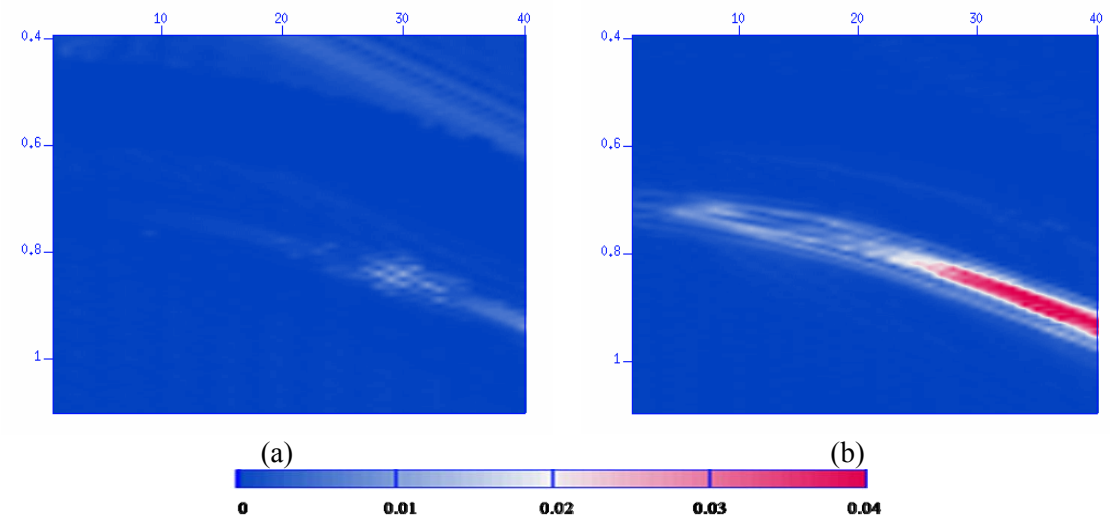

Figure 7.7.3: PS-wave amplitude envelope difference between oil and water saturations. (a) PS-wave propagates in the fracture strike direction; (b) PS-wave propagates in the fracture normal direction.

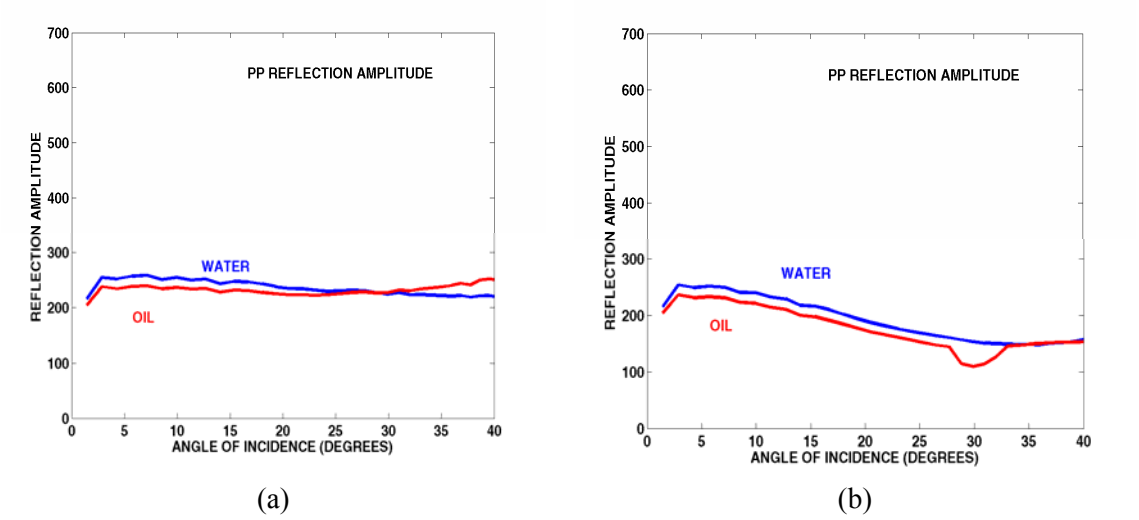

Figure 7.7.4: P-wave amplitudes of the synthetic seismograms with oil/water saturation. (a) propagation parallel to the fracture strike; (b) propagation normal to the fracture strike.

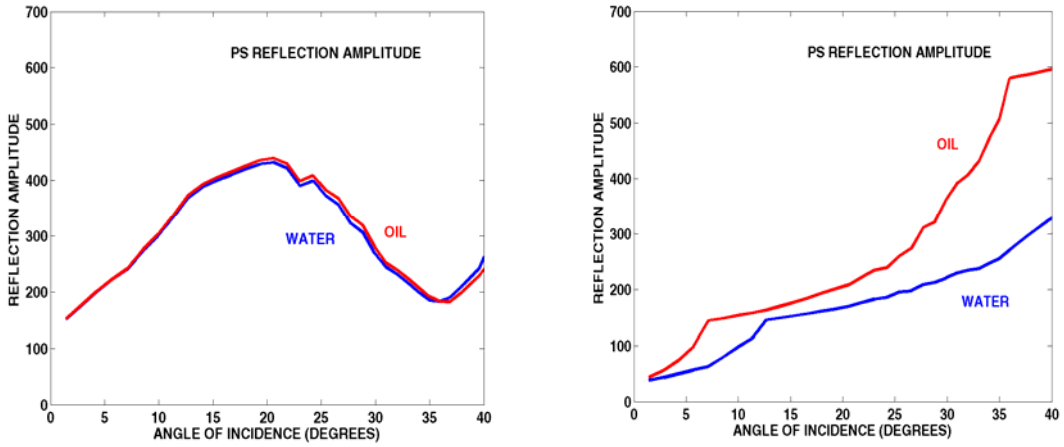

(a) (b)

Figure 7.7.5: PS-wave amplitudes of the synthetic seismograms with oil/water saturation. (a) propagation parallel to the fracture strike; (b) propagation normal to the fracture strike.

7.8 Conclusions

Discriminating oil from water is one of the most challenging problems in exploration geophysics, and how to effectively monitor fluid substitution in producing reservoirs is an important issue for reservoir engineers, especially in cases where water injection is involved to drive oil towards a producing well to improve productivity. Many studies reveal links between the fluids in HTI media and anisotropic seismic properties. Rock physics studies reveal that seismic frequency and fracture density influence the elastic properties of a fluid- saturated HTI medium which can be studied through seismic anisotropy. The Chapman squirt-flow model and the poroelastic equivalent medium theory demonstrate that the fluid viscosity in a saturated HTI medium can influence the medium elastic properties and thus the Thomsen anisotropic parameters. This makes it theoretically possible to use seismic properties to infer fluid viscosity information. The synthetic study based on rock physics reveals the theoretical possibility of using seismic properties to infer fluid viscosity and monitor fluid substitutions in producing reservoirs.

The numerical modelling reveals that seismic frequency, angle of incidence, fracture density and fluid viscosity influence the anisotropy of the fluid saturated HTI medium. It demonstrates the effects of fluid viscosity on medium elastic properties and seismic reflectivity as well as the possibility of using them to discriminate oil-water distribution

in fractured reservoirs. My study shows dependence of the Thomsen anisotropy parameters, also ΔR_{pp} and ΔR_{ps}, on the fluid properties and proves the variations of fluid viscosity can be revealed by two Thomsen anisotropic parameters (ε and δ) as well as P- and PS-wave reflection amplitudes. Though both ΔR_{pp} and ΔR_{ps} respond to fluid saturation, under some important circumstances ΔR_{ps} is more sensitive to these factors than ΔR_{pp}. The PS-wave amplitude in the fracture normal direction can be very sensitive to the fluid, even when the P-wave attributes are insensitive to fluid. I thus conclude that it has more potential to provide us with fluid information.

The modelling also reveals that seismic frequency and fluid viscosity have equivalent influence on elastic properties, and within the seismic frequency band, the changes of ε and δ with fracture density are more detectable than the changes with viscosity. To observe viscosity change with ΔR_{ps}, the required angle of incidence should be larger than 20^{o} and the fracture density should be larger than 4%. Thus there is a minimum angle of incidence requirement for the fluid influence to be detectable.

Chapter 8

Fluid detection with seismic anisotropy: real data analyses

In this chapter I perform an analysis for fluid detection using a 3D multi-component dataset from Ken 71 reservoir which has undergone water flooding, and the water/oil saturated zones have been roughly located from the analysis of logging data.

8.1 Introduction

The Ken 71 reservoir of the Shengli Oilfield is in the Yellow River delta besides Bohai Sea, covering an area of 4 km^2. The reservoir is in a gentle anticline with heavy faulting and consists of mainly thin sands buried in a sand-shale sequence at depths from 1 to 2 km. The average sand thickness is about 50-80m and average porosity is between 20-30%. Average oil column is 26m, and the estimated total oil reserve is about 13 million tons. The reservoir was discovered in 1978 and oil production started in 1981 with water flooding following in 1988. The water-flooding in the reservoir altered the fluid composition and the pore-fluid pressure. Up to July 2005, cumulative oil production reached 4.92 million tons and cumulative water production was 4.37 million tons. Since the average recovery rate is about 40% in the reservoir, 60% residual oil is believed to be still left in place. In 2005, an integrated programme of reservoir geophysics, including the acquisition of high resolution 3D3C seismic data covering around 120km^2, together with cores, logs, 3D VSPs, and crosswell seismic was implemented, aiming to locate the by-passed oil in the area (Figure 8.1.1).

My synthetic study based on rock physics, the Chapman squirt-flow model and poroelastic equivalent medium theory (discussed in Chapter 7) reveals the theoretical possibility of using multi-component seismic data to infer fluid viscosity information to

monitor fluid substitution in producing reservoirs. Thus, the Ken 71 3D3C dataset is a good experimental dataset to examine whether the oil-water substitutions can be discriminated using seismic anisotropy associated with viscosity, so as to prove the application potential of this approach for oil-water discrimination.

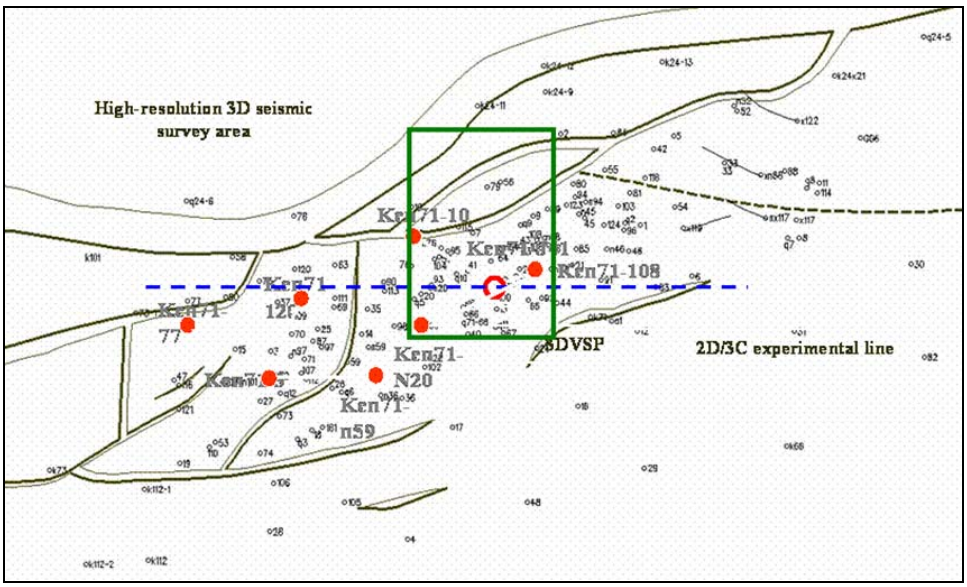

Figure 8.1.1: Ken 71 survey area. The 3D multi-component data for the analysis in this chapter is within the green rectangle. The red circle is the well location for calibration; the blue dash-line is 2D survey for experimental purpose.

8.2 Data acquisition

The 3D multi-component seismic data were acquired with digital MEMS (micro-electro-mechanical system) sensors over a mixed sand and shale sequence in the overburden. The use of digital MEMS sensors can substantially improved the quality of land PS-wave data (e.g. Roche et al., 2005; Mattocks et al., 2005; Calvert et al., 2005). The data consisted of four swaths. For each swath, there are twelve receiver lines with 300 receivers per line and 220m of line spacing. The receiver interval is 20m, giving an area coverage of about 15km^2 for each swath. The shots are located in the centre of the receiver patch and orthogonal to the receiver lines with 66 shots per shot line and 100m of shot line spacing (Figure 8.2.1). The geometry provides wide offset-azimuth coverage (Figure 8.2.2), which is essential in azimuthal anisotropy analysis and fluid detection. The fold for both the ACCP (Asymptotic common conversion point) gathers of

PS-waves and CMP (Common mid-point) gathers of P-waves is around 250 (Figure 8.2.3). Note that the periodic change of the fold number (Figure 8.2.3a) is caused by the asymmetric ray-paths of the down-going P-wave and up-going S-wave.

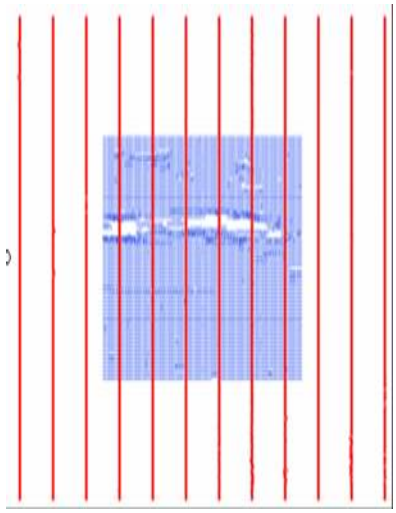

Figure 8.2.1: Field source and receiver layout in Ken 71 data acquisition. The receiver lines (red lines) were deployed in North-South direction; the blue area in the centre area is sources.

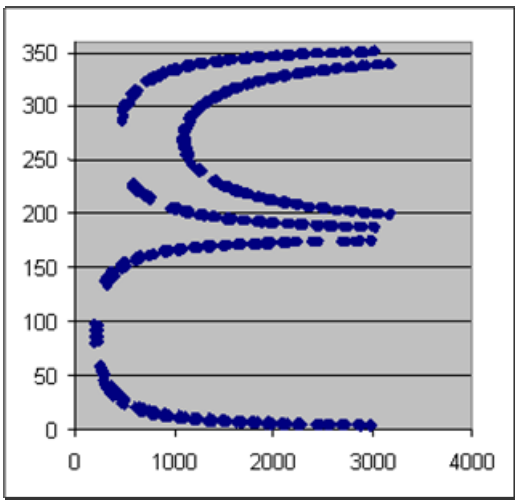

Figure 8.2.2: Offset-azimuth coverage of an ACCP gather. Vertical axis is azimuth in degrees; horizontal axis is offset in meters.

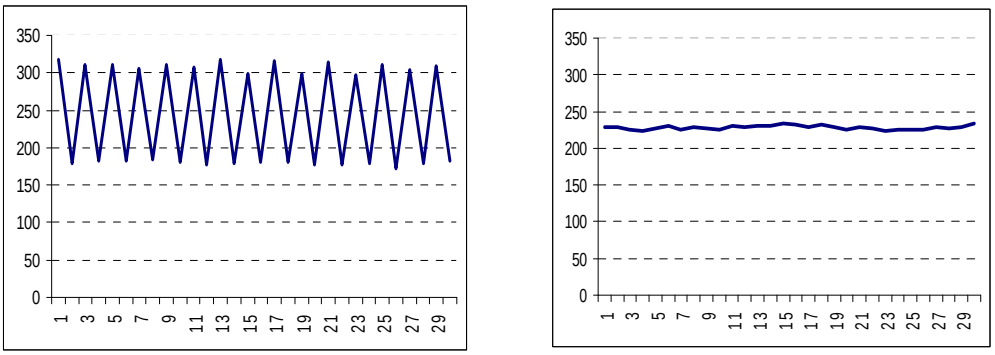

(a) (b)

Figure 8.2.3: Fold distribution of ACCP (a) and CMP (b) gathers.

The data are of medium quality with some random noise and strong ground roll (Figure 8.2.4), which means noise attenuation must be applied in the pre-processing, especially for the analysis based on amplitudes. The frequency of the PS-wave is usually lower than the P-wave (because S-wave are usually more attenuated). For the Ken 71 dataset, the

dominant frequency of the PS-wave is around 12Hz (Figure 8.2.5, F-K spectrum and amplitude spectrum).

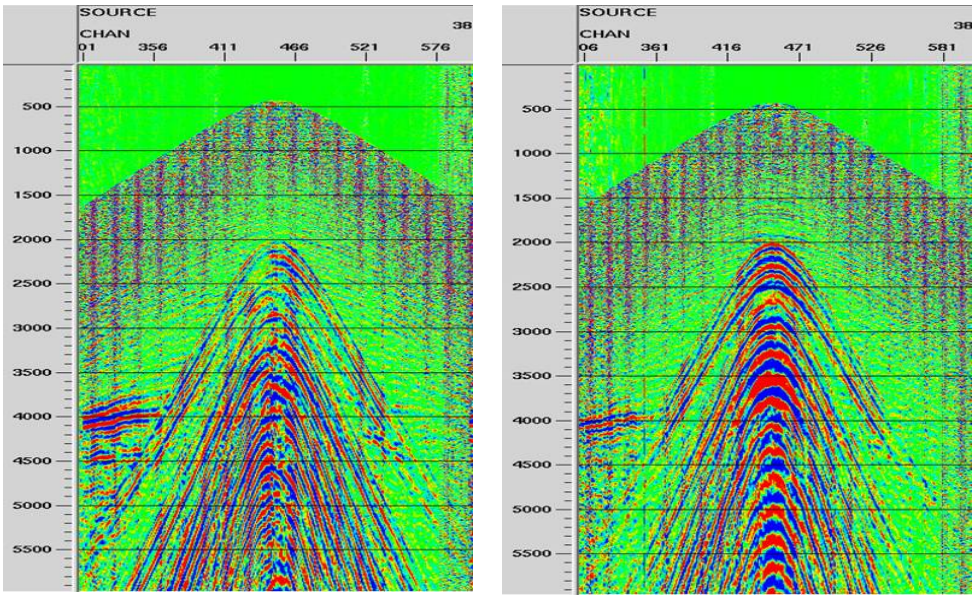

(a) X-component (b) Y-component

Figure 8.2.4: Raw data example in source gather.

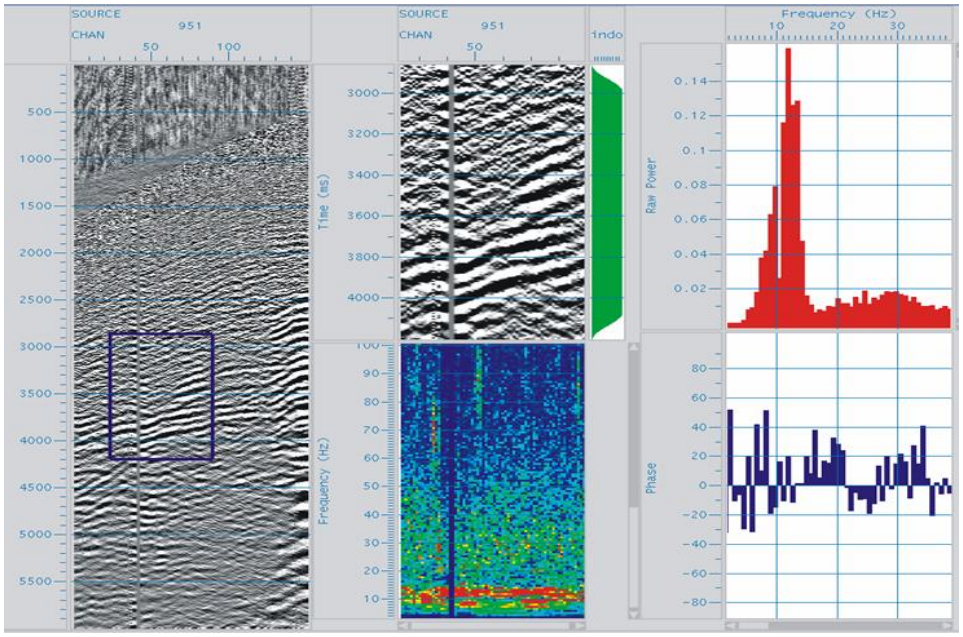

Figure 8.2.5: Frequency analysis on the original data of X-component, showing a dominant frequency of around 12Hz. Left: a data window from the original data; middle upper: data for F-K spectrum (middle lower); right upper: amplitude spectrum; right lower: phase spectrum.

8.3 Component rotation

8.3.1 Potential problems

Normally, component rotation is a routine procedure in 3D PS-wave data analysis, which seems to be so simple that few people doubt the rotation results because it is taken for granted that there should not be any technical problem in this step. However, in the component rotation of Ken 71 PS-wave data, I notice the results are beyond the normal case. Figure 8.3.1 shows the original X- and Y-components from a source gather (only one spread is displayed). The PS-wave reflections (e.g. 'A' indicated the zone on both sides in Figure 8.3.1a) can be perceived on the X-component data, while on the corresponding Y-component, it is hard to see any PS-wave reflections (Figure 8.3.1b). Normally, the presence of PS-waves on the T-component is regarded as an indicator for shear-wave splitting, the stronger the amplitudes, the larger the shear-wave splitting could be. Also, the amplitudes of reflections on the T-component are usually weaker than the corresponding part on the R-component. But on the Ken 71 data, the results are the contrary. After the implementation of component rotation, most energy of PS-wave is shifted to the T-component (Figure 8.3.1d), and very few PS-wave reflections can be observed on the R-component (Figure 8.3.1c). Do the results indicate extraordinary shear-wave splitting in the data or is something wrong when I perform the component rotation?

An error of component rotation in PS-wave data processing can bring serious problems in the fluid detection. If the data processing is for structural imaging, the error caused by wrong component rotation does not necessarily make a big problem, because the component rotation affects amplitudes much more than travel-time. Thus the reflection structures always remain nearly the same after rotation, but the amplitudes can be completely different.

Since the Ken 71 data is to be used for oil-water substitution analysis, which is completely amplitude dependent, incorrect component rotation can lead to completely wrong results. I decided to do a synthetic analysis first to ensure component rotation is correctly applied before any further analysis is carried out.

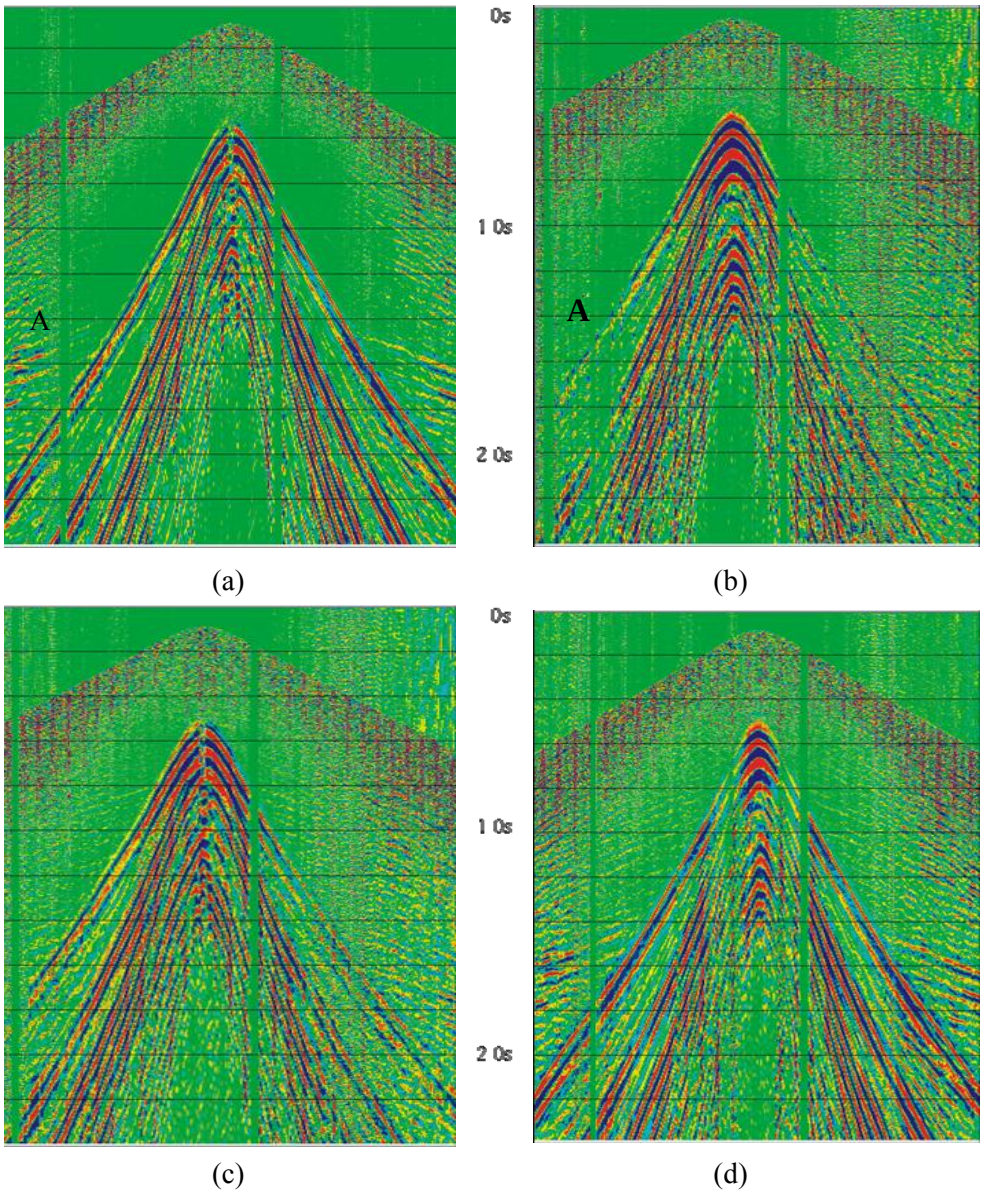

Figure 8.3.1: Component rotation experiment. (a) X-component, (b) Y-component, (c) R-component, (d) T-component. Note that converted shear-wave reflections can be observed on (a), as indicated by 'A'.

8.3.2 Synthetic analysis

Usually, the geodetic coordinate system is assigned to the data in seismic data processing, except in some special seismic processing software where a simplified coordinate system can be applied. For P-wave data processing, no matter what kind of coordinate definition is applied, the final results should be the same, as long as the relative relationship of space positions of sources and receivers is correctly defined. This means P-wave data

processing is independent from the coordinate system. But in the acquisition of multi-component seismic data, the receivers for horizontal component are azimuthally dependent.

In field multi-component seismic data acquisition, the receivers for the X-component are deployed along the inline direction which is usually in a near east-west direction, and the receivers for the Y-component are deployed along the cross-line direction which usually in a north-south direction. The data acquisition for Ken 71 is different, as the receivers for the X-component are deployed in a north-south cross-line direction instead of the in-line direction (Figure 8.2.1a). Since the component rotation is direction dependent, the unconventional deployment of horizontal receivers may make a difference in component rotation. In order to verify this, I create a synthetic dataset which has the same geometry and do the component rotation with the same parameters.

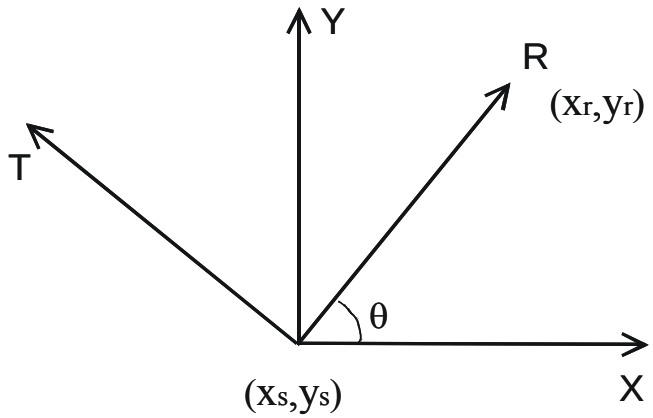

Figure 8.3.2: Component relationship, illustrating the relationship between X-Y coordinates and R-T coordinates. Receivers for X-component are usually deployed in the inline direction; receivers for Y-component are deployed in the cross-line direction. θ is the angle between X-Y and R-T coordinates.

Figure 8.3.2 illustrates the relationship of rotation between X-Y coordinate and R-T coordinate system. X and Y denote the directions in which horizontal receivers are deployed. R (radial) direction is the direction of rays travelling from sources to receivers, and T (transversal) direction is the direction normal to radial direction. θ is the angle between X-Y and R-T coordinate system, which θ can be calculated according to the X-Y coordinates of source and geophone by

$$\theta = \sin^{-1}((y_r - y_s)/\sqrt{(y_r - y_s)^2 + (x_r - x_s)^2}) \tag{8.3.1}$$

Figure 8.3.3 shows the X- and Y-component of a synthetic source gather generated with isotropic media, which only contains PS-waves. The conventional definition of a coordinate system is applied to the data. As we know, when shear-waves travel in isotropic media, shear-wave splitting will not happen, thus there will not be any reflections on the T-component.

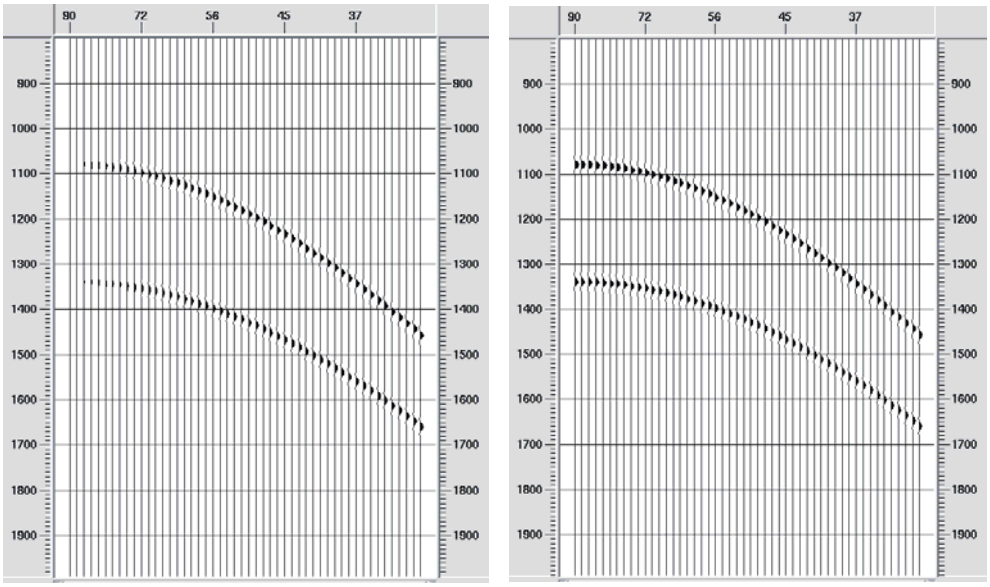

(a) (b)

Figure 8.3.3: The X- and Y-component from the synthetic source gather which only contains PS-wave reflections. Note that both components contain reflections. The horizontal axis is the angle of incidence.

Normally, the rotation of components from X- and Y-component to R- and T-component is carried out with equation (8.3.2)

$$\begin{vmatrix} R(t) \\ T(t) \end{vmatrix} = \begin{vmatrix} \cos\theta & \sin\theta \\ -\sin\theta & \cos\theta \end{vmatrix} \begin{vmatrix} X(t) \\ Y(t) \end{vmatrix} \tag{8.3.2}$$

Figure 8.3.4 displays the results after component rotation from X- and Y-components (Figure 8.3.3) to the R- and T-components, showing that all the reflections have been shifted to the R-component, which demonstrates the rotation applied is correct.

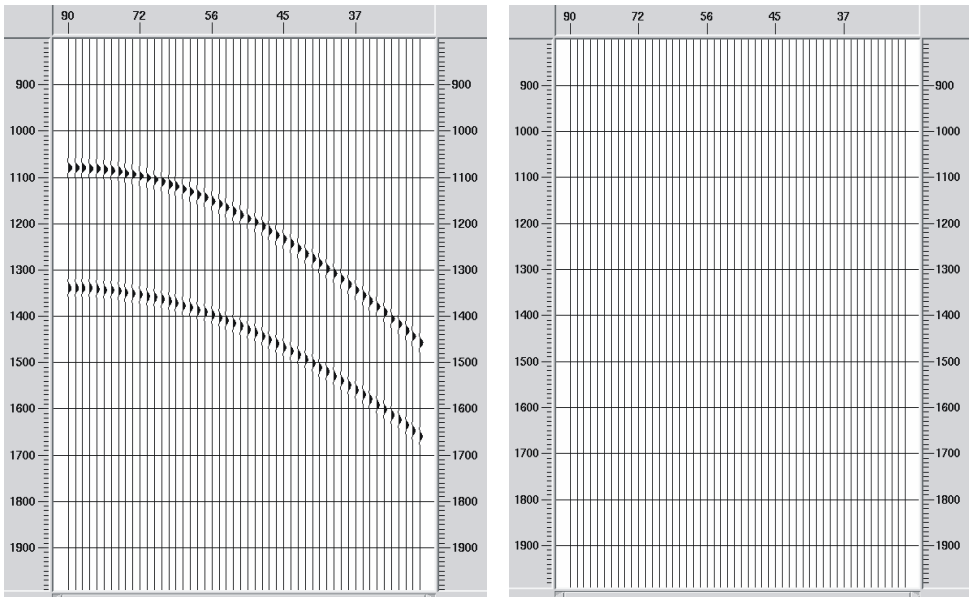

(a) (b)

Figure 8.3.4: Rotation of X- and Y-components into R- and T- components. (a) R-component; (b) T-component.

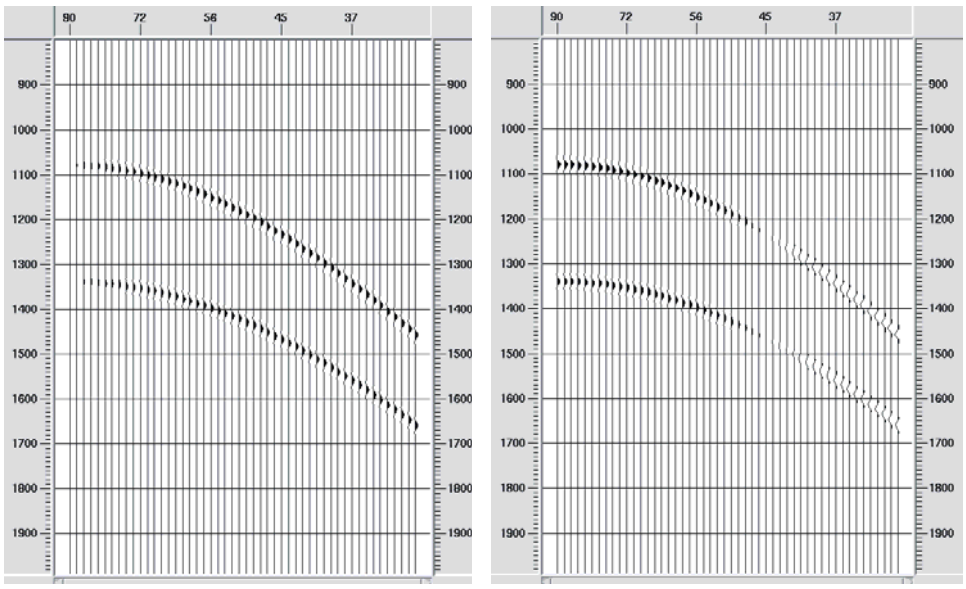

(a) (b)

Figure 8.3.5: Rotation of X- and Y-component data into R- and T- component data, where only coordinate system is changed. (a) R-component; (b) T-component calculated with equation (8.3.2).

To investigate whether there is anything wrong with the component rotation of Ken 71 data, I change the coordinate system of the synthetic data to the same as Ken 71, and performed the same rotation calculation with the results displayed in Figure 8.3.5, which

are completely different from Figure 8.3.4. This means the component rotation has not been correctly applied. Note that when the angle of incidence is less than 45^o, the phase of reflections becomes reversed on the T-component.

It is not difficult to find that, if we exchange the coordinate system to comply with Ken 71, the rotation angle should be calculated with equation (8.3.3), other than with equation (8.1.1).

$$\theta = \sin^{-1}((x_r - x_s)/\sqrt{(y_r - y_s)^2 + (x_r - x_s)^2}) \tag{8.3.3}$$

It means that there is a rotation angle difference of (2θ-90^o) between the rotations with different coordinate system. This also means that when the rotation angle is less than 45^o, the rotation results will be the same. If the rotation angle is larger than 45^o, the component rotation should be performed with equation (8.3.4) other than equation (8.3.2),

$$\begin{vmatrix} R(t) \\ T(t) \end{vmatrix} = \begin{vmatrix} \sin\theta & \cos\theta \\ -\cos\theta & \sin\theta \end{vmatrix} \begin{vmatrix} X(t) \\ Y(t) \end{vmatrix} \tag{8.3.4}$$

Figure 8.3.6 shows the new rotation results from X- and Y-component (Figure 8.3.3) to R- and T-component with equation (8.3.4), which are exactly the same as that in Figure 8.3.4.

This result tells us that, in component rotation in PS-wave data processing, the specific geometry must be considered. The equation (8.3.2) is only suitable for the case when receiver lines are deployed in near east-west direction. When receiver lines are deployed in near north-south direction, the rotation calculation must be carried out with equation (8.3.4).

Since component rotation is a routine procedure in 3D multi-component seismic data analysis, if we ignore the direction of the receiver lines and always use equation (8.3.2) to do component rotation, the results can be completely wrong, especially in this shear-wave splitting analysis for oil-water distribution.

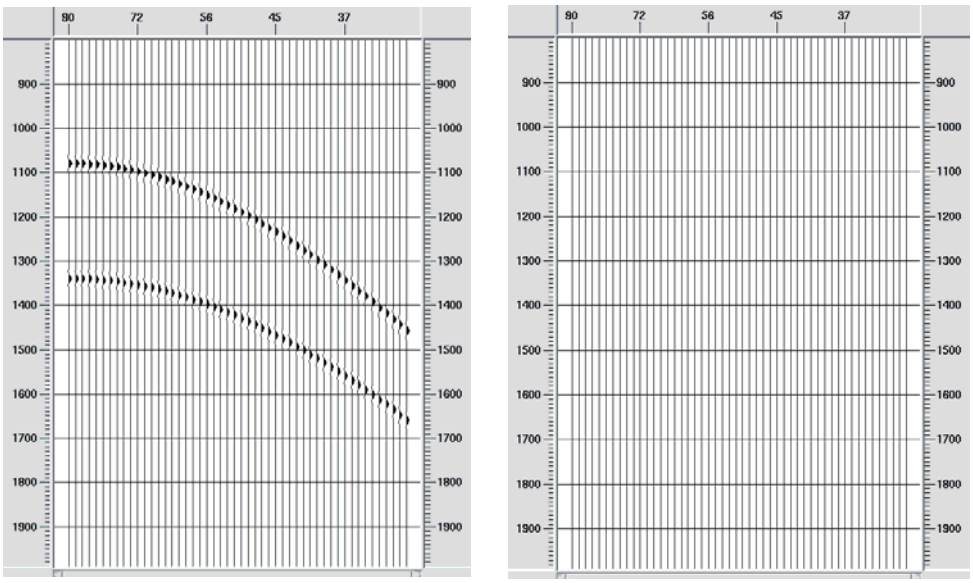

(a) (b)

Figure 8.3.6: Component rotation from Figure 8.3.3 with equation (8.3.4). (a) R-component (b) T- component.

8.3.3 Component rotation in Ken 71 data

The synthetic analysis in 8.3.2 reveals that different ways of deploying receiver lines in field operations require different algorithms to perform rotation. Since the receiver lines in Ken 71 data acquisition are deployed in the north-south direction (Figure 8.2.1), it is equation (8.3.4) rather than equation (8.3.2) that must be used to perform the component rotation. The results with equation (8.3.4) (Figure 8.3.7) are different from those calculated with equation (8.3.2) (Figure 8.3.1). Most of energy of the PS-wave reflections stays on the R-component (Figure 8.3.7a), while on T-component, only very weak reflections can be perceived, indicating weak shear-wave splitting, if any.

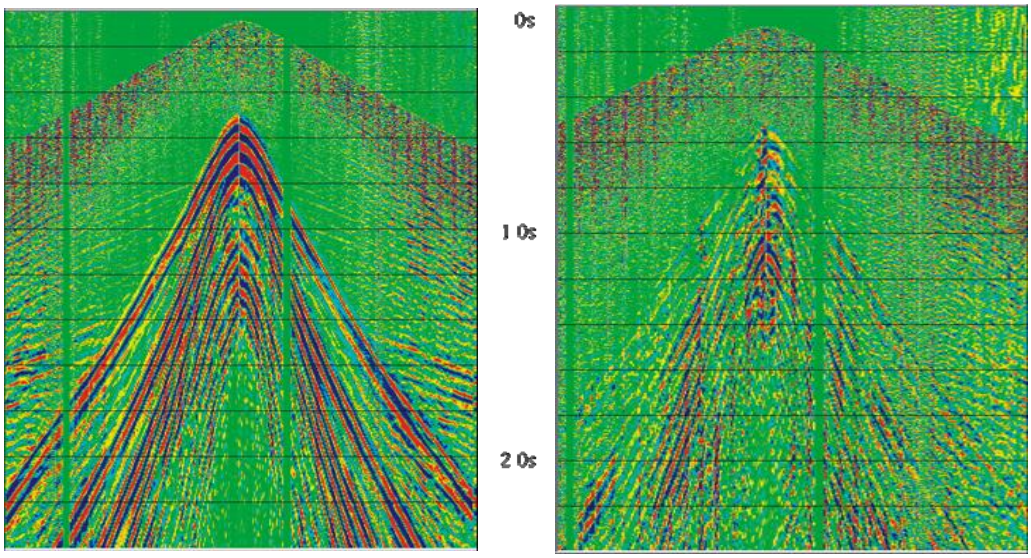

(a) (b)

Figure 8.3.7: Component rotation of the data in Figure 8.3.1 with equation (8.3.4). (a) R-component; (b) T-component.

8.4 Noise attenuation

8.4.1 Noises on PS-wave data

Noise attenuation is an important procedure in data processing with low signal to noise ratio. But how to reduce noise and improve the data quality is not an easy thing to do in seismic data processing. Furthermore, the noise issue can be more problematic for PS-wave processing than P-wave processing due to the PS-wave's greater sensitivity to noise and field data acquisition geometries. There are many kinds of noise that may appear on PS-wave data, but for the Ken 71 data, it mainly includes strong ground roll and guided waves which show coherent features on source gathers (Figure 8.3.7). The 3D physical modelling data analysis in Chapter 4 reveals that the results of fracture characterisation are more sensitive to the presence of noise than routine seismic processing. High signal to noise ratio of data is a basic requirement to obtain reliable fracture characterisation, especially for analysis based on amplitudes. Furthermore, as the final aim of the data analysis is to do viscosity analysis which is completely dependent on amplitude attributes, the presence of noise on the data will seriously distort the results. Thus, noise attenuation is an essential procedure before the data is suitable for fracture and fluid substitution analysis.

The 3D PS-wave data from the Ken 71 survey is heavily contaminated with noise (Figure 8.3.7). For P-wave data, when there is a big gap between the dominant frequencies of noise and reflection signals, the noise can be removed by frequency filtering. However, for PS-wave data, this method is not necessarily suitable, because the dominant frequencies of PS-wave reflections and noise are very close (e.g. Figure 8.4.1). If we try to remove the low frequency noise through frequency filtering, we will also lose PS-wave signals. Although there are many other ways to suppress noise (Kanasewich, 1990), it is difficult to obtain satisfactory results in dealing with the noise presented in the 3D PS-wave data.

For coherent noise in seismic data, F-K filtering is often used to remove the noise. However, when we try to remove the noise on Ken 71 data with F-K filtering, the noise on near-offset traces still remains due to the limits of the method (Figure 8.4.2b). Especially, when strong coherent noise is predominant in pre-stack 3D PS-wave data, it is usually hard to obtain satisfactory results. In order to improve the reliability of fracture characterization of Ken 71, an effective method to eliminate strong coherent noise on the ken 71 3D PS-wave data needs to be found.

Here, I develop a new and robust method to attenuate the noise on 3D PS-wave data, which is based on the scheme of adaptively recognizing and removing noises while keeps true amplitudes of PS-wave reflections.

8.4.2 New method for noise attenuation

Careful examination shows that it is the 3D geometry that causes the hyperbolic distribution of the strong noises in 3D seismic data (Figure 8.4.2a). However, the spatial nature of strong noise does not change in a pre-stack source gather. If the acquisition geometry is taken into account and 2D data is regarded as a specific case of 3D data, the hyperbolic events in pre-stack 3D seismic data can be considered as the noises with linear features. Then we can recognize and eliminate the coherent noise in the 3D source gather with respect to linear features.

At a point (i_0,j_0) in pre-stack seismic records, the scanning stack energy can be defined as

$$E_{j_0}(k)=\sum_{j=j_0-\frac{M}{2}}^{j=j_0+\frac{M}{2}}\sum_{i=i_0-\frac{L}{2}}^{i_0+\frac{L}{2}}A(i,j,k) \qquad k\in[k1,k2] \tag{8.4.1}$$

where, $A(i,j,k)$ is the amplitude; $[k1, k2]$ defines the dip range scanned; i represents the ith time sample; j is the trace number within the searching radius. A series of scanning amplitude $E(k)$ with respect to different dips can be obtained. We take

$$E_{\max}=\max\{E(k)\} \qquad k\in[k1,k2] \tag{8.4.2}$$

the value of k corresponding to E_{max} represents the dip of the coherent events at point (i_0, j_0). If the dip range of coherent noise is given as $[a1, a2]$, let

$$P=\begin{cases}1 & K_{\max}\in[a1,a2]\\ 0 & K_{\max}\notin[a1,a2]\end{cases} \tag{8.4.3}$$

where, $P=1$ means that the event detected at point (i_0, j_0) is coherent noise, while $P=0$ means no coherent noise exists. If the value of k represents the dip of coherent noise at point (i_0, j_0), median or prediction filtering can be applied to remove the noise. Taking the median along the dip of the coherent noise, we have the following expression:

$$V_m=MED\left\{A\left(i_0,j-\frac{k}{2},\cdots\cdots,j+\frac{k}{2}\right)\right\} \tag{8.4.4}$$

and the result after noise elimination with median filtering is given by

$$A'(i_0,j_0)=\begin{cases}A(i_0,j_0) & p=0\\ A(i_0,j_0)-V_m & p=1\end{cases} \tag{8.4.5}$$

Figure 8.4.1a displays a spread of a source gather of 3D converted shear-wave where strong coherent noise can be observed. Figure 8.4.1b is the results after noise attenuation with the method. From the comparison we can see that the strong noise has been effectively eliminated from the data.

The method presented here adapts to arbitrary variation of apparent velocity of the coherent noise by using an automatic recognition approach to distinguish strong coherent noise and subtract it point by point in pre-stack 3D seismic data. The method is effective

in eliminating coherent noise in 3D PS-wave data with little disturbance to reflection events.

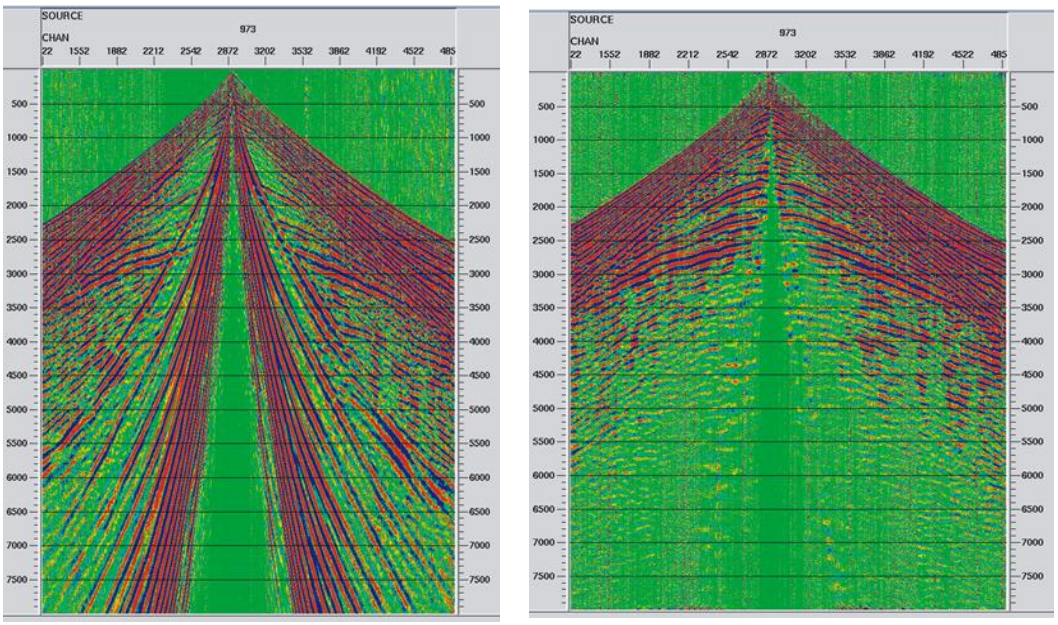

(a) (b)

Figure 8.4.1: Noise removal on R-component data. (a) original data; (b) after noise attenuation.

8.4.3 Application on the Ken 71 PS-wave data

The main target of the Ken 71 data processing is to obtain high-resolution shear-wave data with maximum preservation of shear-wave splitting information. Thus noise reduction in the data is a necessary step. I first do experimental noise attenuation on the Ken 71 data with the new method and the conventional F-K filtering. Figure 8.4.2 shows the comparison of the results for the source gather of Ken 71 converted-wave data. Figure 8.4.2b is the results from F-K filtering: though the noise in far offset traces has been reduced, there is still strong noise left in the near offset traces. Figure 8.4.2c is the result of processing with the new method: the strong coherent noise with hyperbolic forms has been substantially removed from the data. The comparison reveals that the new method is obviously much better than F-K filtering in attenuating the strong coherent noise in 3D PS-wave data.

After performing noise attenuation on the whole dataset, I do preliminary stacking to examine the effects of the noise attenuation. Figure 8.4.3 displays the comparison of the

R-component stack before and after noise attenuation, which shows that, after noise attenuation, the quality of the stack section has been significantly improved in terms of signal to noise ratio. Figure 8.4.4 is the corresponding comparison for the T-component, the PS-wave reflection events can be well observed at the target zone (around 3000ms in time in figure 8.4.3).

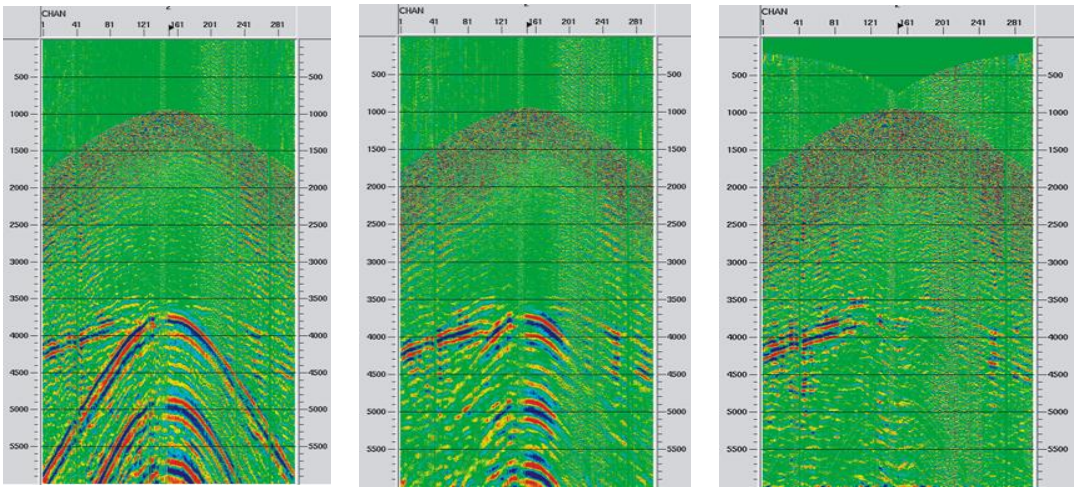

(a) (b) (c)

Figure 8.4.2: Comparison of the results using different methods. (a) original 3D PS-wave source gather; (b) after F-K filtering; (c) after applying the new method.

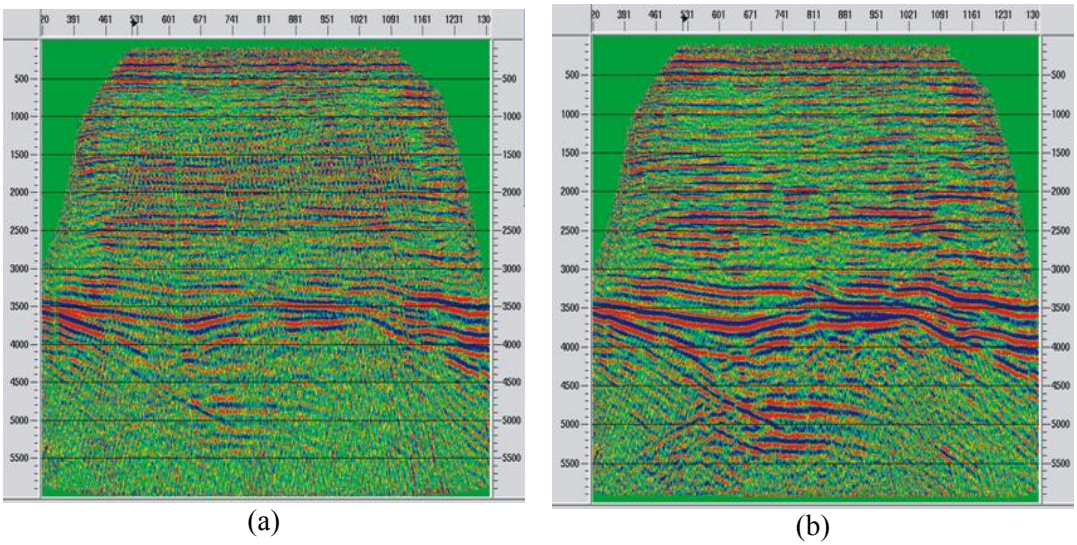

(a) (b)

Figure 8.4.3: Comparison of the stacking results of R-component. (a) stack section with original data; (b) stack section with data after noise attenuation.

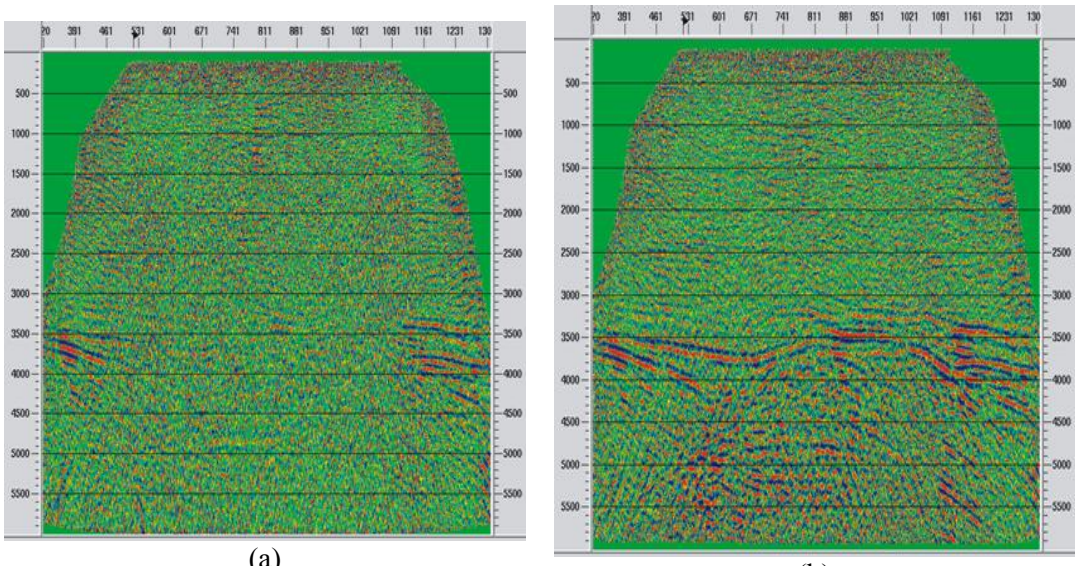

(a) (b)

Figure 8.4.4: Comparison of the stacking results of T-component. (a) stack section with original data; (b) stack section with data after noise attenuation.

8.5 Anisotropic processing

Processing land multi-component seismic data in the presence of anisotropy is a challenging task. As we know, sedimentary layers such as shales and thin bedding sequences in the overburden can give rise to vertical transverse isotropy (VTI, or polar anisotropy). To account for the non-hyperbolic effects, I use the four-parameter theory (Li and Yuan, 2003) to estimate and compensate for the VTI effects. Besides asymmetric ray-paths, there are also complicated HTI anisotropic effects on the move-out signatures of the Ken 71 PS-wave data. Since the conventional PS-wave velocity analysis based on isotropic media cannot remove the move-out effects related to HTI anisotropy on traces at big offsets, a key issue is how to account for HTI anisotropic effects whilst preserving shear-wave splitting to the maximum. To solve this problem, I divide the data into two orthogonal azimuthal sub-gathers (45 degrees and 135 degrees) according to the azimuth distribution, and process each azimuthal sector separately using a processing flow incorporating both the effects of VTI and the asymmetric ray-path.

8.5.1 Stack processing

As has been discussed in Chapter 6, the stack processing scheme for PS-wave data normally includes ACCP binning, NMO, DMO and post-stack migration, which involves

inherent problems such as asymmetric ray-paths and conversion-point binning and is sensitive to anisotropy. I use the anisotropic processing flow in Figure 6.5.1 (Chapter 6) in Ken 71 data processing. Since the move-out signature of PS-waves is not sensitive to γ_0 (Li and Yuan 2003), γ_0 cannot be determined from the move-out signature analysis. I estimate γ_0 through a coarse correlation of the P- and PS-wave stack sections which are generated by processing the P- and PS-wave data using hyperbolic methods (when the offset is small, the move-out signature of PS-wave can be assumed as hyperbolic, as discussed in Chapter 6). Figure 8.5.1 illustrates the event calibration for determining γ_0 (the middle curve in Figure 8.5.1). If γ_0 is appropriate, the sections of P- and PS-wave match very well when the PS-wave section is compressed into the P-wave time (Figure 8.5.2). Note γ_0 is variable in space.

Having determined γ_0 for all analysis points, I estimate V_{C2}, γ_{eff}, χ_{eff} of the velocity model according to the PS-wave move-out signatures which are offset-dependent (Dai, 2003). Figure 8.5.3 shows a velocity spectrum for the parameters of velocity. I pick up the PS-wave stack velocity V_{C2} on the move-out signatures on traces of near offset (when offset-depth ratio is less than 1.0), where move-out signatures are not sensitive to asymmetric ray-paths and anisotropy; I determine the effective velocity ratio γ_{eff} on the traces with offset-depth ratio larger than 1.0 and less than 1.5, which control the non-hyperbolic move-out signatures caused by asymmetric ray-paths; within this offset range, the move-out signatures are not sensitive to anisotropy either (Dai, 2003). Finally, I estimate the effective anisotropic parameter χ_{eff} through move-out segments on the traces of offsets larger than 1.5 and less than 2.0. All three parameters are determined by judging whether the corresponding event segments have been flattened (Figure 8.5.3d).

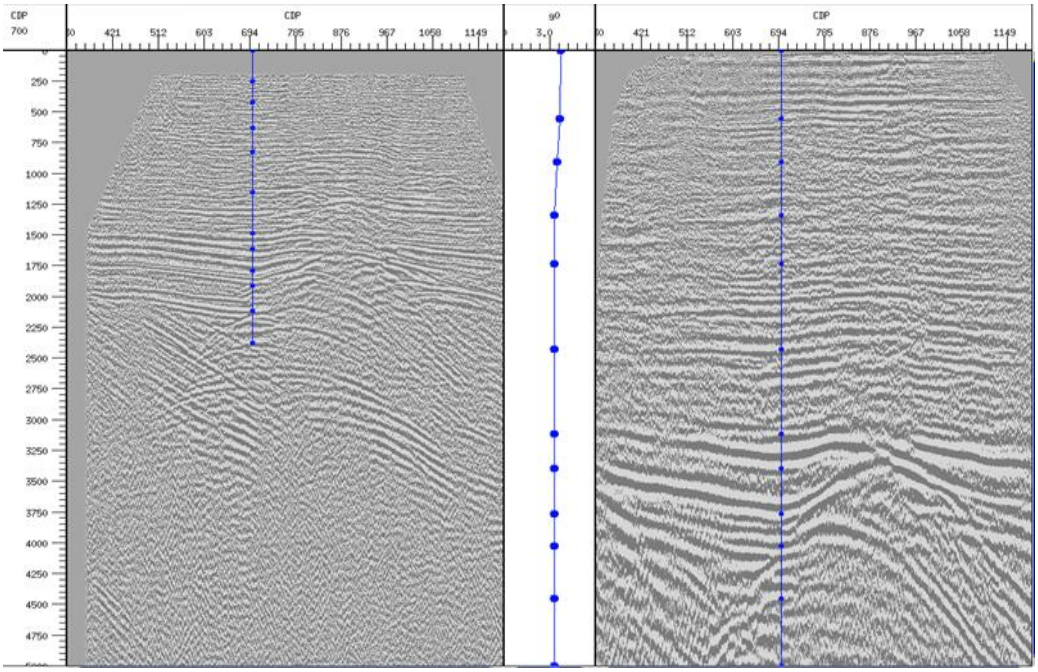

(a) (b) (c)

Figure 8.5.1: Event calibration on (a) P-wave and (c) R-component sections for estimating (b) γ_0 at an analysis point. Note γ_0 varies in space.

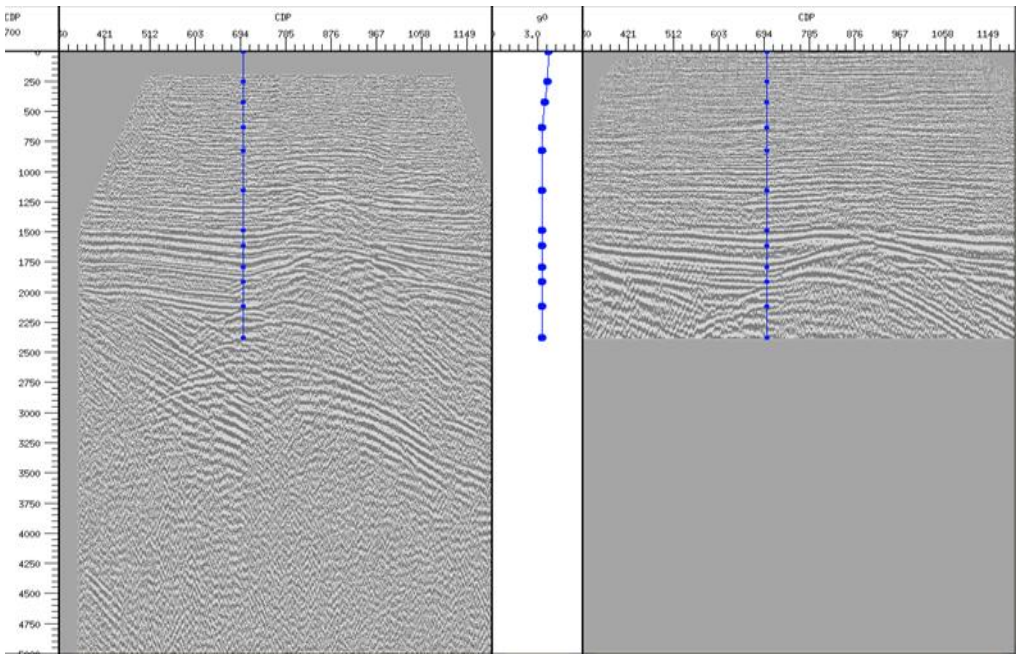

(a) (b) (c)

Figure 8.5.2: Conversion of PS-wave time to P-wave time. (a) P-wave section; (b) γ_0 ; (c) PS-wave section after time conversion.

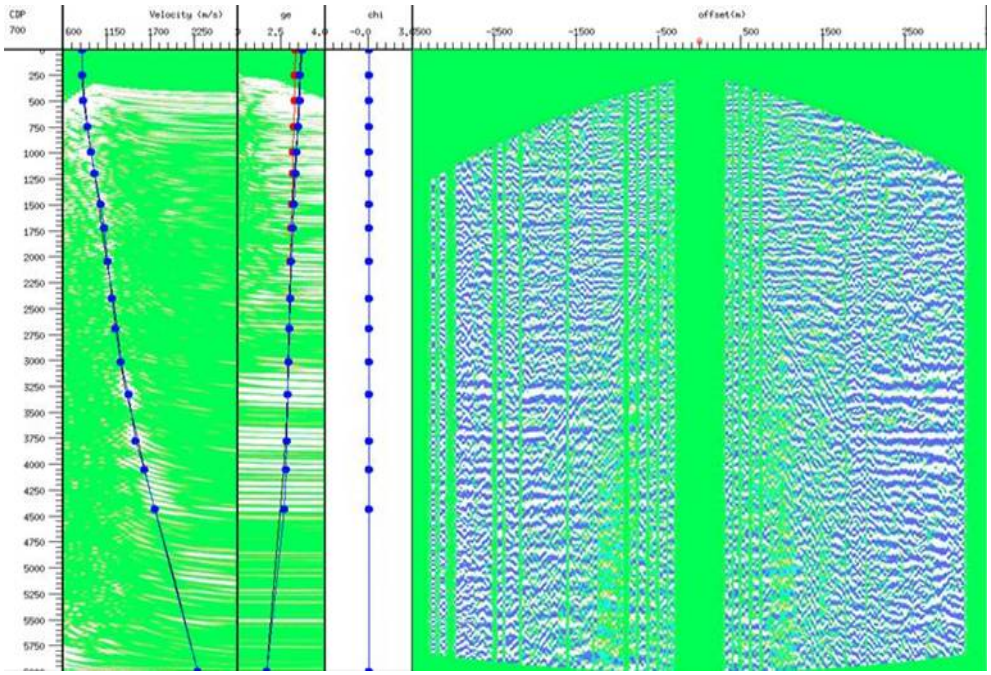

(a) (b) (c) (d)

Figure 8.5.3: Interactive analysis for determining V_{C2}, γ_0, γ_{eff}, χ_{eff} and the input data are asymptotic conversion point (ACCP) gathers. (a) V_{C2}; (b) γ_0/γ_{eff}; (c) χ_{eff}; (d) ACCP gather.

The final stack section P- and PS-wave are shown in Figure 8.5.4 and Figure 8.5.5, the overall quality of the PS-wave stack is excellent compared with that of the P-wave stack. The events can be mapped from both the P- and PS-wave sections, giving rise to a very high degree of correlation (Figure 8.5.6). The stacks demonstrate that all the processing procedures and parameters applied in PS-wave pre-processing so far, such as geometry definition, amplitude gain recovery, receiver statics correction (for PS-wave), wavelet de-convolution, pre-stack noise attenuation, PS-wave velocity analysis and NMO, etc., is correct and the data can be used in the next stage analyses (such as pre-stack time migration, pre-stack attribute analyses for viscosity information, etc.).

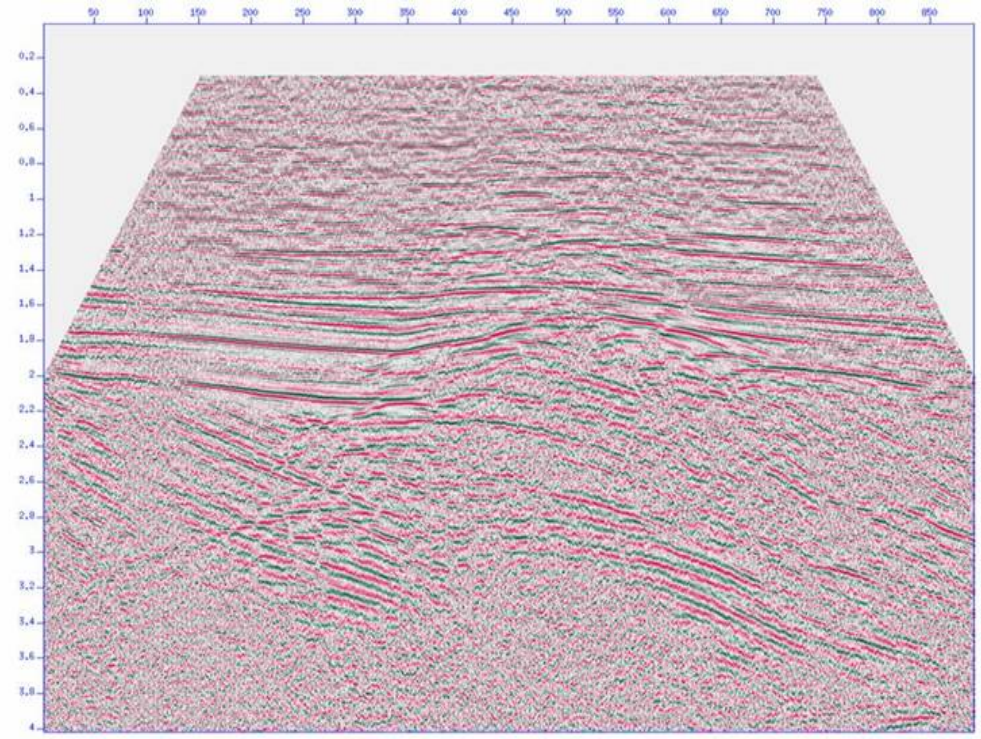

(a) P-wave section from the stack volume.

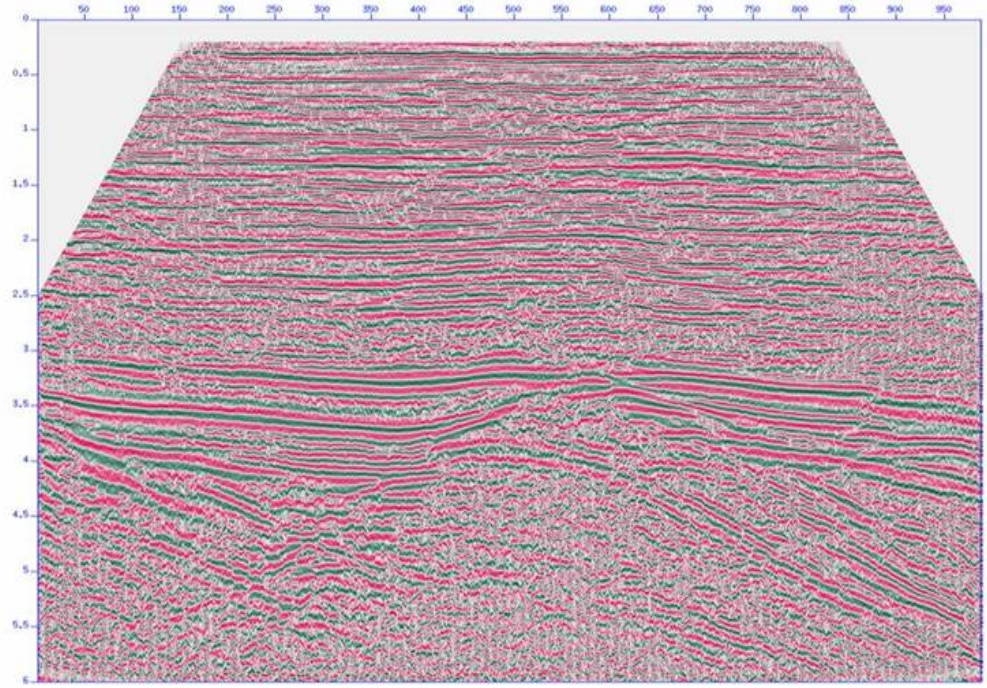

(b) R-component section from the PS-wave stack volume.

Figure 8.5.4: P-wave and PS-wave stack sections (in-line).

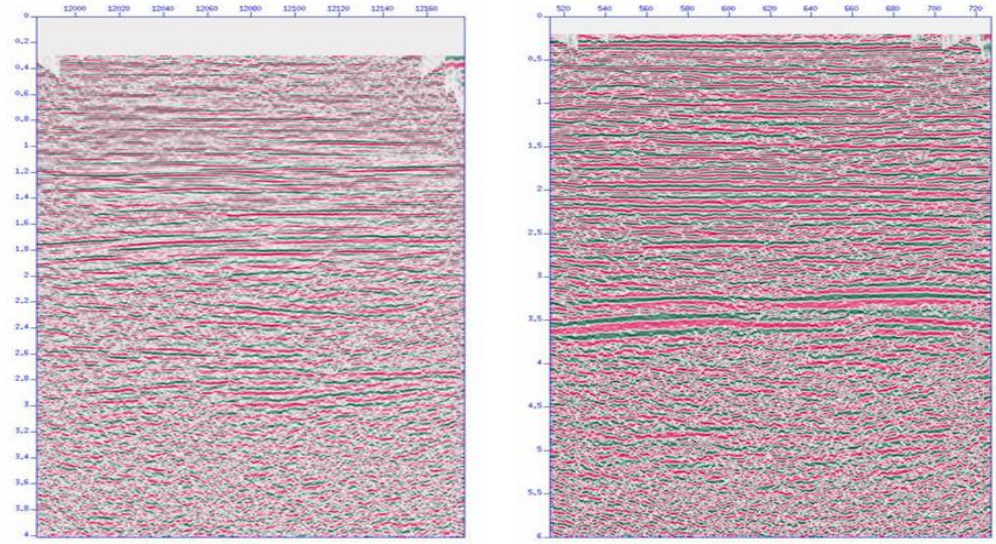

(a) (b)

Figure 8.5.5: P-wave and PS-wave stack sections (cross-line). (a) P-wave; (b) PS-waves (R-component).

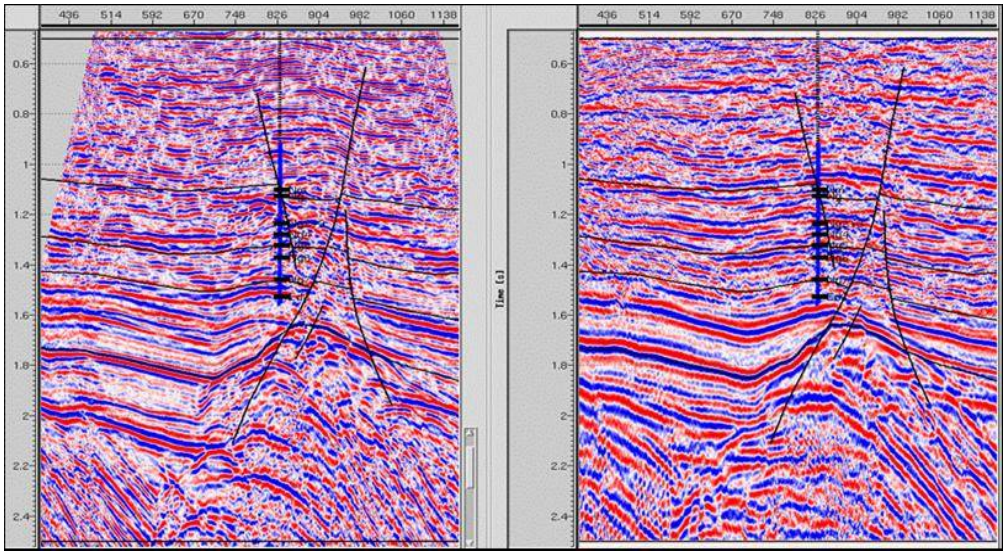

(a) (b)

Figure 8.5.6: Event calibration on P-wave (a) and PS-wave (b) stack section (the time of PS-wave has been converted to P-wave time).

8.5.2 Pre-stack time migration

To carry out PS-wave pre-stack time migration (PSTM), the first step is to build a PS-wave stack velocity model, because the initial migration velocity model is calculated

from the stack velocity model. That is why conventional stack processing is a necessary part of the PSTM workflow. Since I have obtained the stack velocity model in section 8.5.1, here I just convert the stack velocity model into the initial migration velocity model and perform pre-stack time migration to generate CIP (common image point) gathers which the pre-stack time migration velocity analysis is based on. Figure 8.5.7 shows the migration velocity analysis, and the criterion for picking the right parameters is to flatten the events on the CIP gather as in stack velocity analysis. Then I use the CIP gathers to update the migration velocity model by analyzing the residual move-out in the CIP gathers, and after several iterations and overall examinations of the migration sections, I establish the final velocity model for pre-stack time migration.

Figure 8.5.8 displays a section from the final migration of the PS-wave data of Ken 71, compared with the corresponding stack section. There are substantial improvements to the reservoir structure in the migration section. But towards the shallow part of the section, the stack results appear to be better than the PSTM imaging. This is due to the fact that the near-offset field in the shallow section has a better signal than the wave field in the intermediate offsets, and a larger mute for the shallow events shall improve the results. More significantly, the improvements over the target interval agree with the well data as shown in Figure 8.5.8.

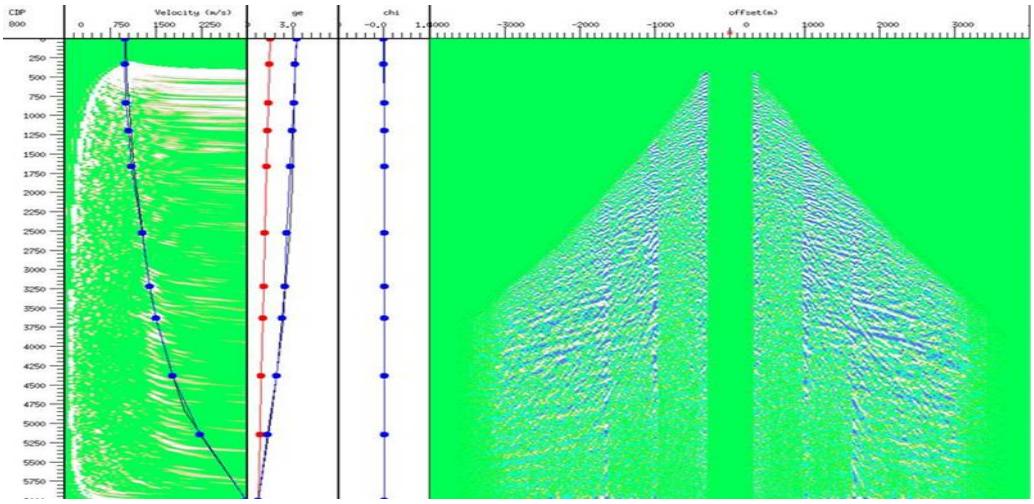

Figure 8.5.7: PSTM velocity analysis. (a) migration velocity spectrum where V_{Cmig} is picked. (b) vertical and effective velocity ratio of P- and PS-wave: γ_0: red curve; γ_{eff}: blue curve; (c) PS-wave anisotropic parameter χ_{eff}; (d) updated CIP gather.

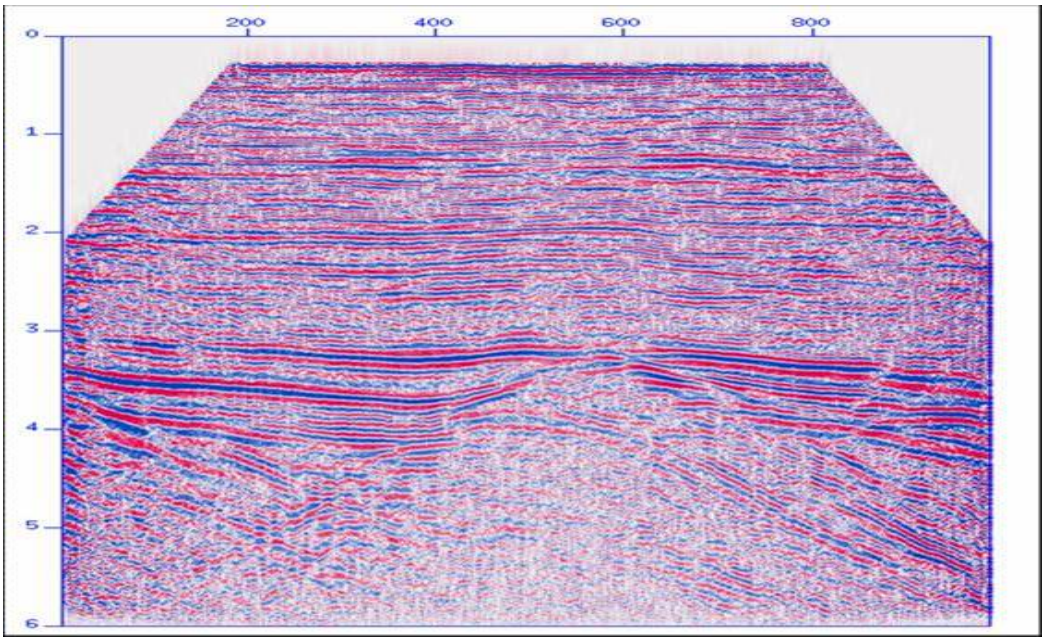

(a)

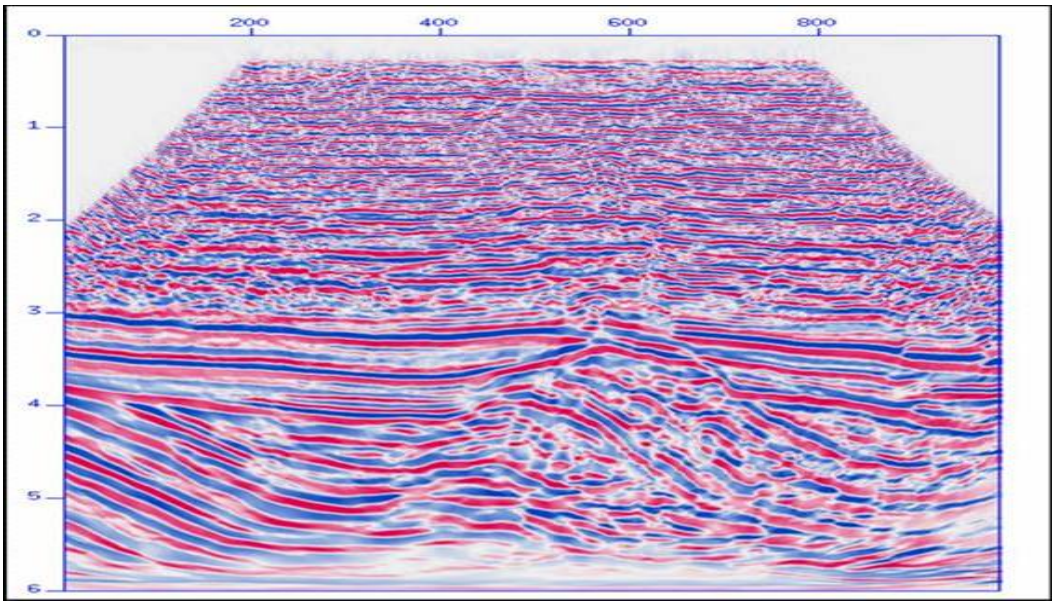

(b)

Figure 8.5.8: Comparison between stack (a) and PSTM (b) section of the R-component data.

8.6 Anisotropy analysis for fluid viscosity

In the numerical analysis in Chapter 7, I theoretically demonstrated that seismic measurements of the properties of the slow shear-wave can potentially give access to

information on fluid saturation in fractured rock, even in circumstances where the P-wave response is rather insensitive to fluids. This is possible because for angles of incidence between 0 and 45 degrees the slow shear-wave is strongly attenuated and dispersed, in contrast to the P-wave and fast shear-wave which suffer little fracture-related attenuation in these directions. For the slow shear-wave propagating near-vertically, the main effect of fluid-substitution comes through the change in fluid viscosity. The synthetic study (Chapter 7) reveals that, since the viscosity of fluids saturating a fractured medium can affect the medium elastic properties, it is theoretically possible to use seismic data, especially multi-component seismic data to infer fluid viscosity information and monitor fluid substitutions in producing reservoirs.

In this section, I use the Ken 71 3D3C dataset to infer and monitor the oil-water distribution in the reservoir. It has undergone water flooding and water and oil saturated zones have been roughly located from the analysis of logging data. The multi-component data provides a good experimental dataset to study oil-water distribution by analyzing the seismic anisotropy caused by viscosity, and to examine the application potential of using viscosity for oil-water discrimination.

8.6.1 Azimuthal anisotropy and Shear-wave splitting

The use of multi-component seismic data for oil-water substitution analysis is based on the assumption of HTI anisotropy, because there are links between fluid-saturated HTI media and seismic anisotropy (e.g. Chapman, 2003). Thus, in using of multi-component seismic data for viscosity analysis, the first thing to be done is to analyze the magnitude of HTI anisotropy in the data. If no evidence of HTI anisotropy can be found in the data, it is not likely that anisotropic methods can be used on the data to obtain fracture information as well as azimuth related viscosity . Figure 8.6.1 shows an azimuthally sorted gather from the data which shows strong azimuthal anisotropy with azimuthally varying travel time on the R-component (as indicated by yellow lines in Figure 8.6.1a), revealing the potential of the data for HTI anisotropy analysis of the reservoir.

When a shear-wave enters an anisotropic distribution of stress-oriented cracks (which is usually a HTI medium), it splits into two quasi-shear waves, with one polarizing in maximum stress direction (fast shear-wave) and another in minimum stress direction

(slow shear-wave) (Crampin and Peacock, 2005). The shear-wave splitting is known to be sensitive to the fracture properties and fluid bulk modulus and it has long been hoped that analysis of shear-wave splitting in multi-component data would be able to improve our ability to detect fluid substitution in fractured reservoirs.

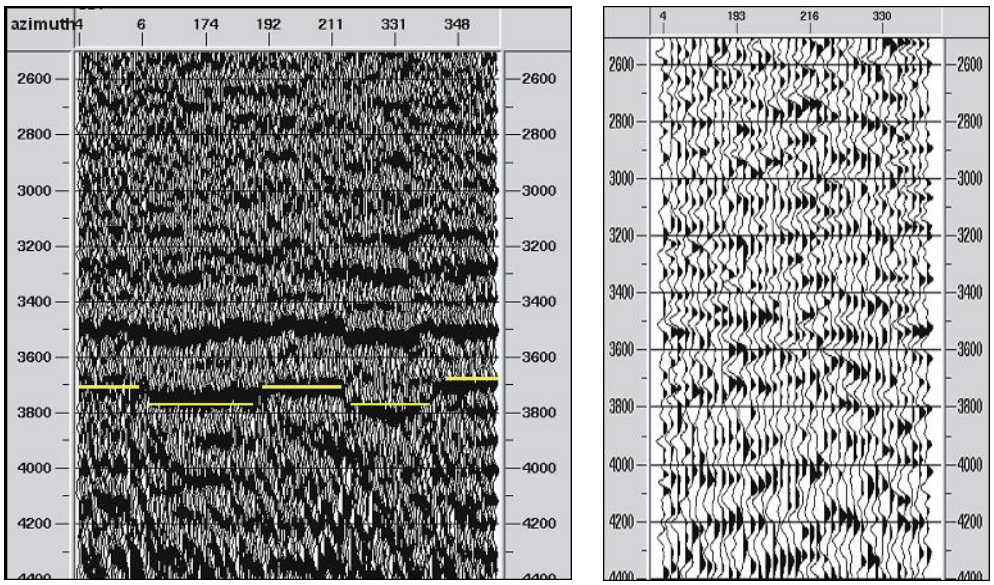

(a) (b)

Figure 8.6.1: Travel-time variation with azimuth on PS-wave data. (a) R-component; (b) T-component.

A common offset gather example from the Ken 71 3D PS-wave data indicates azimuthal anisotropy of the PS-waves (Figure 8.6.1). Preliminary stack results for the fast and slow shear-wave also show the phenomena of shear-wave splitting (Figures 8.6.2 and 8.6.3). The fast component is obtained by rotating the data into the azimuth of 330^{o}. Figures 8.6.4 are the sections of the fast and slow shear waves from the preliminary stack processing. The reflection events at around 3s and 4s on the section of the slow shear wave can be observed. It confirms the shear wave splitting at the reservoirs. Based on the preliminary stack data, I study the shear-wave splitting through the computation of time delay gradient sections before studying the azimuthal variation of the PS wave amplitude and find that water-saturated zones tend to have higher values of shear-wave splitting, whereas zones where the original oil is in place tend to exhibit low values of shear-wave splitting. The difference is quite large, with approximately an extra 5% shear-wave anisotropy in the water saturated zones.

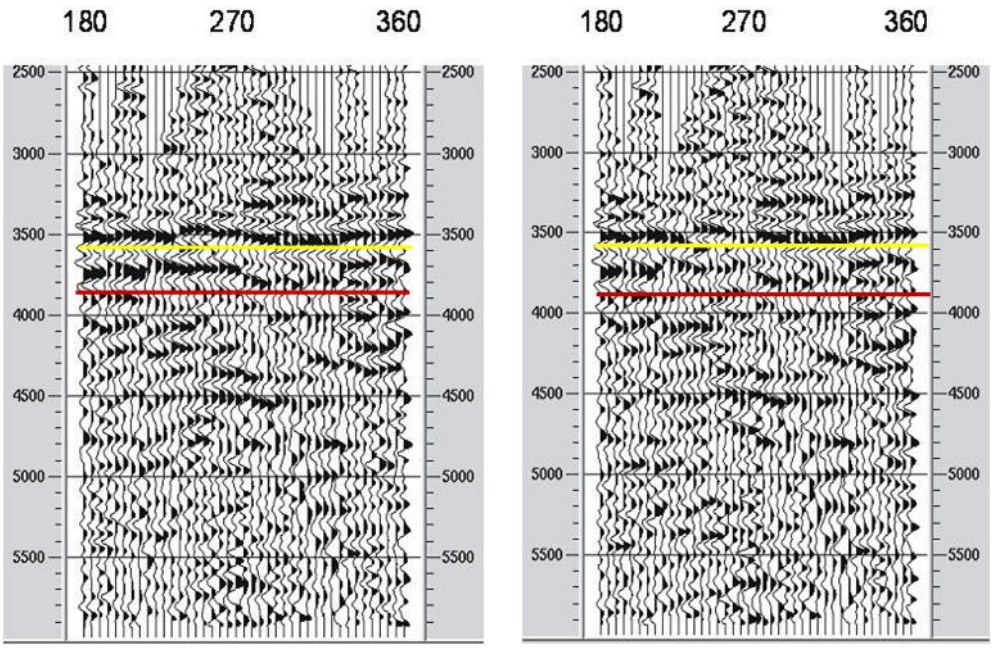

(a) (b)

Figure 8.6.2: Comparison of azimuthally sorted common offset gather between R-component and Fast-component (b).

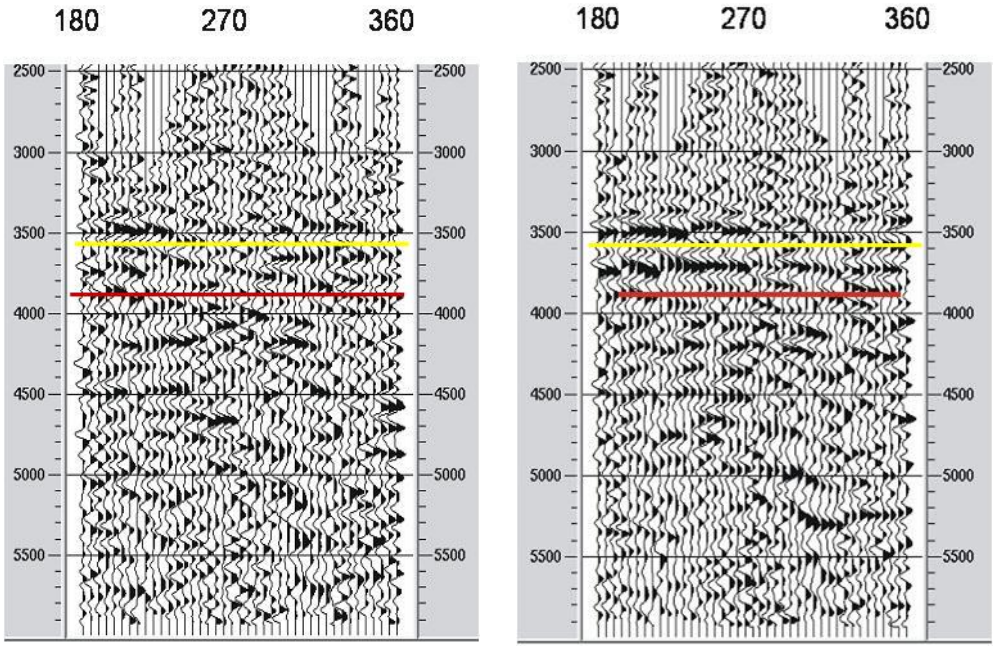

(a) (b)

Figure 8.6.3: Comparison of azimuthally sorted common offset gather between the T-component and the Slow component (b).

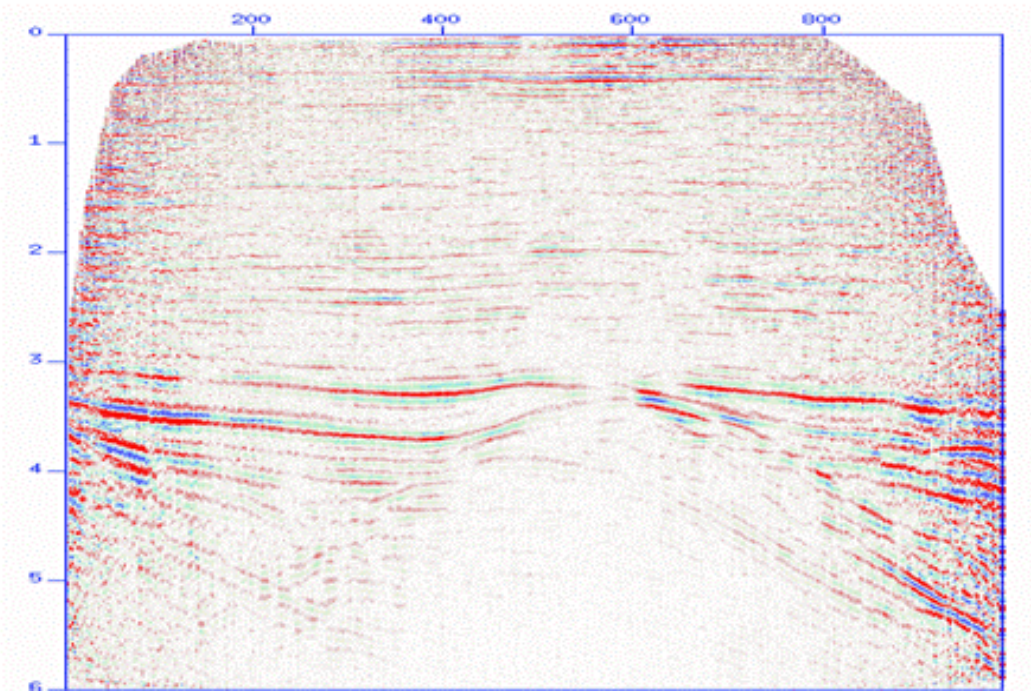

(a)

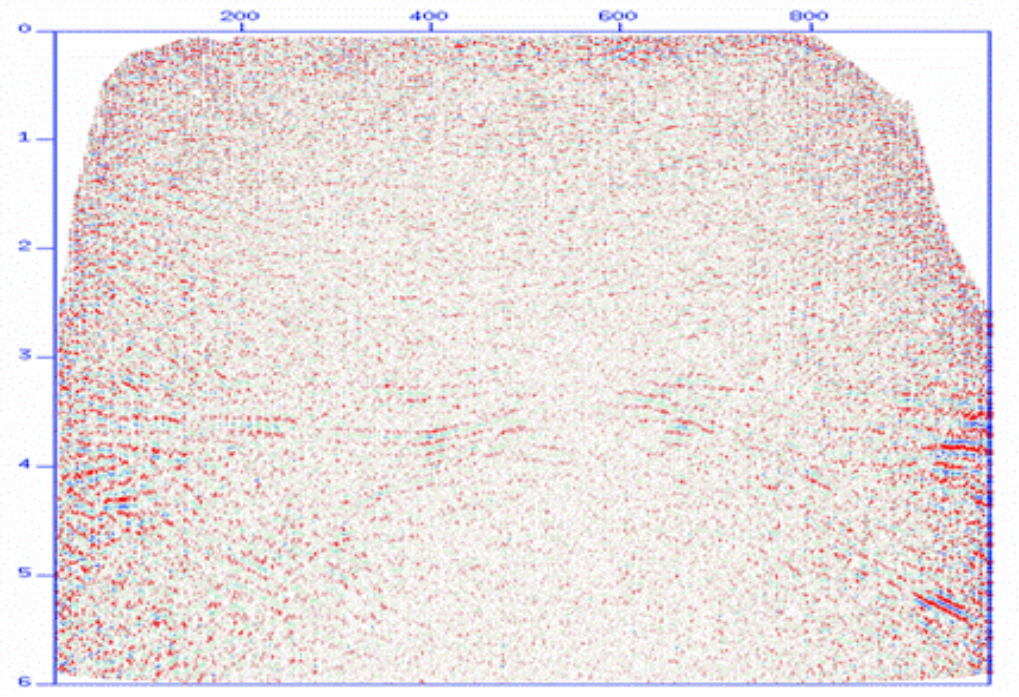

(b)

Figure 8.6.4: An inline section of final stack volumes. (a) Fast wave; (b) Slow wave.

8.6.2 Analysis for fluid distribution

Figure 8.6.5 shows the comparison between P-wave and PS-wave stack sections for the fast and slow directions, revealing amplitude anomalies for the slow PS-wave section which appears to correlate with fluid saturation. The P-wave sections from the two directions (one is along high-stress direction, another is along low-stress direction) show little differences. I now consider in detail the differences between PS-wave data from two well locations, one known to be in an oil saturated zone and the other from a water saturated zone. Figure 8.6.5a and 8.6.5b show that for the water saturated zone we have dim amplitudes, with little difference between the fast and slow directions. The oil saturated zone corresponds to higher amplitude, but there is a significant difference between the fast and slow azimuth.

Undoubtedly some uncertainties remain, principally related to the effect of pore-fluid pressure which presumably differs significantly between the water flooded and oil saturated zones. Nevertheless, we are encouraged by the correspondence between the shear-wave data and the fluid saturation information, and believe that the use of multi-component data to discriminate oil and water saturation in fractured reservoirs will be a fruitful direction in the future.

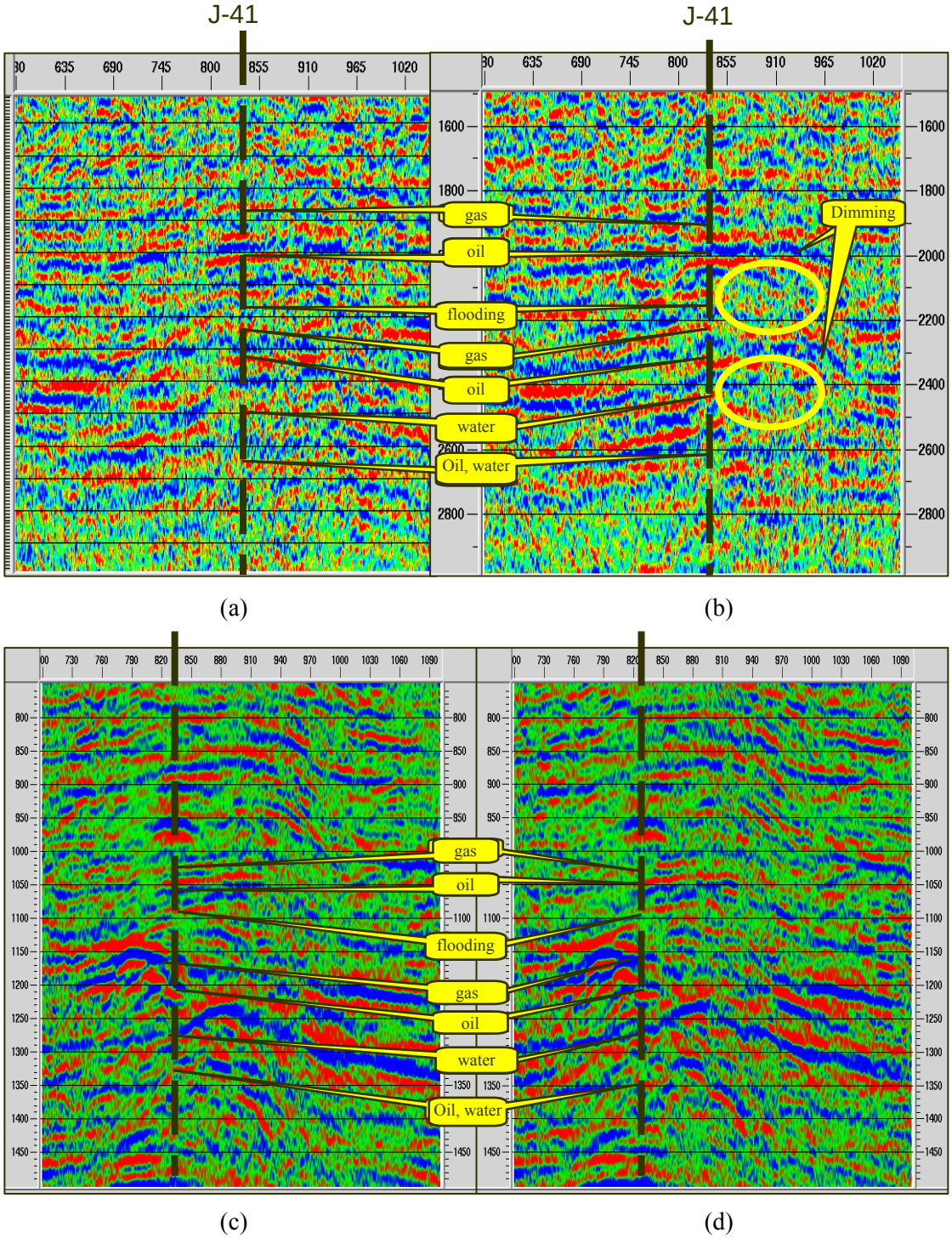

Figure 8.6.5: Stack sections of P-wave (c, d) and PS-waves (a, b). Note the similarity between the P-wave sections; while on (b), it appears to show fluid-related amplitude effects. (a) fast shear-wave, (b) slow shear-wave, (c) P-wave in fast shear-wave direction, (d) P-wave in slow shear-wave direction.

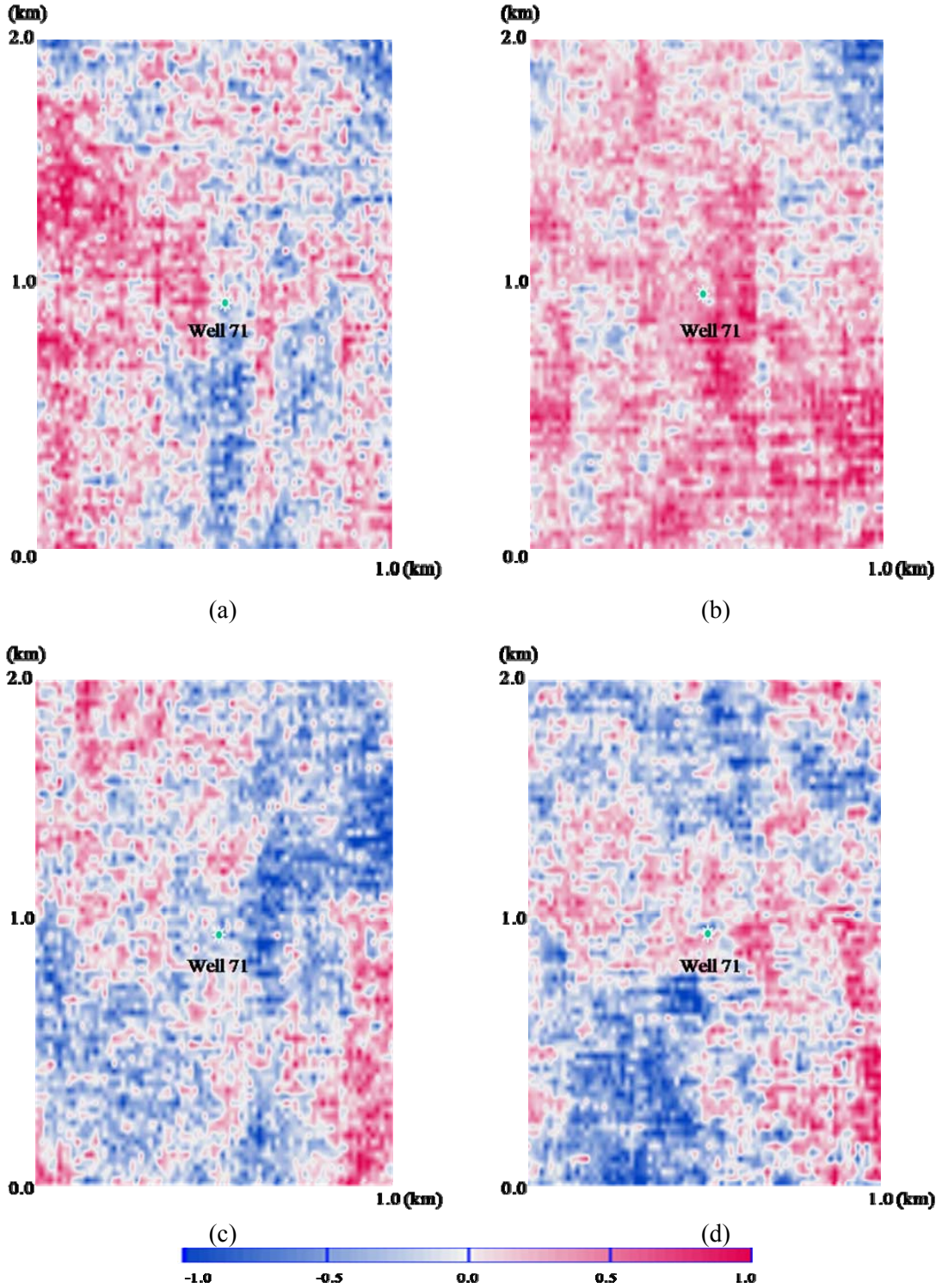

Figure 8.6.6: Horizontal amplitude slice from PS-wave volumes around wells in water saturated zone (top) and oil saturated zone (bottom). (a) Water bearing layer fast S-wave slice, (b) Water bearing layer slow S-wave slice. (c) Oil bearing layer fast S-wave slice, (d) Oil bearing layer slow S-wave slice,

8.7 Conclusions

In this Chapter, my main aim is to use the multi-component data of Ken 71 to understand fluid pore-pressure and saturation substitution in the reservoir. The analysis reveals it is hard to use the P-wave to discriminate oil-water substitution in Ken 71. There is little difference between the P-waves travelling along the high-stress and low-stress directions. However, analysis of the shear-wave splitting due to pore pressure and viscosity changes reveals the potential for discriminating oil and water distribution. The split shear-wave shows consistent changes in amplitude dimming, time delay anomalies, which indicate pore-pressure change due to water-flooding, meaning shear-wave splitting is sensitive to oil-water saturation change.

Noise attenuation in PS-waves is more important in fluid viscosity analysis than conventional processing, because the viscosity analysis is very sensitive to amplitude changes. The original data of Ken 71 is heavily contaminated with noise which can not be effectively reduced with conventional methods. I have developed a method which can automatically recognize and eliminate the strong noise point by point with little interference to useful signals, and thus adapts to the features of the strong noise on Ken 71 PS-wave data. After the application of the method, the signal to noise ratio of the data is significantly improved, which makes it possible to use the data for fracture and fluid substitution analysis.

In 3D multi-component seismic analysis, component rotation is a routine procedure. However, if we do not pay attention to the direction of the receiver lines in carrying out this step, it may be hard to perceive the difference in real data analysis, and the rotation results may lead to wrong results in amplitude-dependent analysis, especially in shear-wave splitting analysis for oil-water discrimination.

The amplitude and travel-time anomalies in Ken 71 data can be correlated with well information on fluid saturation. Water saturated zones tend to be associated with higher values of shear-wave splitting than oil saturated zones, and their amplitudes are dimmer. I note that this is the exact opposite of what would be expected from an anisotropic fluid-substitution calculation using the change in bulk modulus alone without a viscosity component. In the oil-saturated zones we see a strong change in PS-wave amplitude

between the fast and slow direction, while in water saturated zones there is no azimuthal change. This behaviour is consistent with our theoretical modelling in Chapter 7.

Chapter 9

Findings and future work

This Chapter summarizes the finding I have obtained from my PhD project. Since seismic anisotropy is a big topic, there is still a lot of worthwhile work to be done for further insights in the area, which will be very helpful to the oil industry. From my study in the last few years, I have a few suggestions for future work on the subject.

9.1 Findings

In this thesis I have systematically analyzed seismic anisotropy with forward modelling data, 3D physical modelling data, 3D OBC seismic data and 3D land multi-component seismic data. With these datasets, I have studied how seismic anisotropy can be observed in multi-component seismic data and how it can be used to characterize subsurface fracture systems, improve imaging quality, and monitor fluid substitution in a producing fractured reservoir. The results have demonstrated the limits and new areas, challenges and opportunities of using 3D multi-component seismic reflection data for seismic anisotropy study. The observation and analyses of anisotropic phenomena in the seismic data and the conclusions will be very useful in characterising and monitoring a producing fractured reservoir.

Seismic anisotropy analysis: numerical modelling

Though P-waves azimuthal attributes (i.e. amplitude, travel-time), etc., are commonly believed to be able to be used to infer fracture information by elliptical fitting with the major axis of the ellipse denoting the fracture strike, the numerical modelling in Chapter 3 reveals that this is not always true. When the offset is small (i.e. offset-depth ratio is less than 0.2), the amplitudes of the P-wave from the top interface of the fractured layer are insensitive to fractures and thus do not show observable elliptical variation with azimuth.

When the offset is large enough, (i.e. offset-depth ratio is less than 1.5), the amplitudes of the P-wave change with azimuth dramatically, but not in an elliptical shape and therefore not suitable for elliptical fitting either. The modelling results reveal that the amplitudes which are ideal for elliptical analysis are those with an offset-depth ratio between 0.3 and 1.0. Only within this offset range do the amplitudes of P-wave data show elliptical distribution with azimuth in the presence of HTI anisotropy. This result means that, when performing elliptical anisotropy analysis with P-wave amplitudes for fracture characterisation, we should choose the data with the appropriate offset range according to the depth of the fractured layer to obtain robust results.

Besides providing useful information on P-wave amplitudes, the modelling results in Chapter 3 also proved the fact that the interval travel-time of the P-wave in a HTI layer can be used to infer fracture information in the same way as for amplitude analysis. It also has similar offset limits. The azimuthal interval travel-time analysis should only be carried out on data with sufficiently large offset (i.e. offset-depth ratios is larger than 1.0), because the azimuthal variations can only be observable in the data with sufficiently large offset. When the offset is small (i.e. offset-depth ratio is less than 1.0), no azimuthal variation can be discerned in the travel-time data, which means no seismic anisotropy information can be obtained from the data. Thus we should only use the data with large offset with respect to the depth of the target layer when using interval travel-time for seismic anisotropy analysis in real data analysis.

The numerical modelling proved that, for a fixed offset, the ratio of the major axis to minor axis of the ellipse fitted with P-wave amplitudes or travel-time may be used to infer fracture density. However, the value of the ratio may vary with offset and need to be calibrated when a wide range of offsets are applied in fracture density estimation.

The numerical modelling proved that fracture properties can be obtained by studying rock stress distributions through shear-wave splitting analysis. Both the amplitudes and interval travel-time of the radial component of PS-waves can be used to infer fracture information through elliptical anisotropy analysis in a similar way in P-wave azimuthal attribute analysis. The azimuthal amplitudes of radial component of the PS-wave at the top of the fractured layer display an elliptical distribution with azimuth, which is similar to the behaviour of the P-wave amplitudes. For the same offset, the amplitudes of the PS-wave

radial component vary more dramatically with azimuth than those of the P-wave. The data suitable for ellipse fitting are those with offset-depth ratio ranging from 0.1 to 2.0, which means more offsets of radial component data can be included for elliptical anisotropy analysis compared with the P-wave data. In contrast to P-wave analysis where the major axis of the fitted ellipse indicates the direction of fracture strike, the major axis of the ellipse from radial component analysis indicates the direction of fracture normal. The amplitudes of transverse component of the PS-wave reveal zero-crossings and polarity reversals with azimuth, which can also be used to infer fracture information.

The numerical analysis reveals that the interval travel-time of the radial component within the fracture layer displays an elliptical distribution with azimuth where the major axis of the ellipse indicates the direction of fracture normal, which is consistent with that from the P-wave analysis. It also requires propagation at sufficiently large offset to allow azimuthal variations of interval travel-time to develop significantly enough to be observed. The PS-wave modelling also reveals that, at a fixed offset, the major to minor axis ratio of the ellipse fitted with amplitudes or interval travel-time can be used to infer fracture density.

Seismic anisotropy analysis: physical modelling and real data analysis

Compared with numerical modelling, physical modelling provides a way to verify the physical basis of using azimuthal attributes for seismic anisotropy analysis and can be used to study the merits and limitations for different kinds of attributes and methods, so as to obtain guidelines for real data application. The analyses of two 3D physical modelling datasets in Chapter 4 confirm the numerical modelling results based on the equivalent medium theory. It reveals that the amplitude is the most sensitive attribute in azimuthal anisotropy analysis, even when the offset-depth ratio to a target is very small (i.e., offset-depth with respect to the top interface of the target layer is less than 0.6), the fracture information can still be determined quite accurately. However, the amplitude analysis is very sensitive to the presence of noise, even a small amount of noise can significantly distort the fracture information. Thus, when amplitude is used for the analysis, it is very important to reduce the noise level in the data and preserve true reflection amplitudes.

The physical modelling also proved that travel-time is more dependent on the offset-depth ratio because it needs large offset to allow variations to develop sufficiently.

If the offset coverage is not large enough (i.e., the offset to depth ratio is less than 1.0), the results can be heavily influenced by structural imprints and acquisition footprints. Thus, if travel-time is used for seismic anisotropy analysis, sufficient offset coverage is necessary. A robust estimation from travel-time analysis required an offset-depth ratio of 1.0 or more. When the magnitude of azimuthal variation due to anisotropy exceeds that due to structural variations, the structural imprint can be significantly reduced.

The physical modelling showed that narrow-azimuth stacking methods (i.e. AVO, NMO velocity) appear to be easily influenced by the acquisition footprint and noise, while full-azimuth and full-offset surface fitting methods agree with the physical parameters. The offset-depth ratio to the target layer is a key parameter for the successful application of the P-wave techniques. It affects the choices of attributes and choice of processing methods. Small offset-depth coverage may only be applicable to amplitude attributes with high quality data, whilst large offset coverage makes it possible to use travel-time attributes.

The real data analysis with Clair 3D-4C OBC data show that, though the data has wide offset-azimuth coverage, the offset range designed for field data acquisition does not guarantee a sufficient offset coverage for the target interval, and the effective offset range for the target interval analysis should be taken into account. The azimuthal P-wave stack velocities and stack panels can be used to help characterise fracture information when necessary. The fracture information derived from the interval travel times appears more reasonable than that from other seismic attributes.

Seismic anisotropy for image improvement

PS-wave processing involves some inherent problems, such as asymmetric ray-paths and common-conversion-point binning, increased sensitivity to anisotropy, etc., which is different to P-wave processing. Normally, PS-wave PSTM is a better approach than a conventional PS-wave processing scheme comprising CCP binning, NMO, DMO and post-stack migration.

Though seismic anisotropy may affect the image quality, its magnitude of influence depends on the type of the data and the depth of the target. The real data analysis of Clair OBC data reveals that the seismic anisotropy of both the P-wave and converted S-wave

decrease with time, but the converted S-wave data are affected more by anisotropy than the P-wave data. From the results of the anisotropic parameter analysis, the P-wave anisotropy is relatively small while S-wave anisotropy is around eight times the P-wave anisotropy and should not be neglected in PS-wave processing. As a matter of fact, the PS-wave PSTM result based on the anisotropic velocity model is better than that based on the isotropic velocity model. However, the improvements are mainly located in the upper part of the seismic section due to the presence of VTI.

Noise attenuation in multi-component data

In analysis for seismic anisotropy, the noise in seismic data can seriously reduce the reliability of results from fracture characterisation, anisotropic seismic processing and fluid detection, etc., which are sensitive to amplitude values. No field seismic data, especially converted wave seismic data, is really free from noise contamination. Thus, effective removal of noise in converted wave seismic data is a very urgent and important issue in seismic anisotropy analysis. In order to remove the strong noise contamination in the 3D land data for seismic anisotropy analysis, I developed a new noise reduction technique for improving the signal to noise ratio in 3D PS-wave data, and tested the effectiveness of the method with the synthetic and field data. The method can automatically recognize and eliminate strong noise point by point from 3D PS- wave seismic data with little interference to useful signals and thus it adapts to the features of the strong noise. Data quality can be significantly improved in terms of signal to noise ratio after the application of the method, and thus it will help to improve the reliability of assessment of seismic anisotropy in the target formations.

Component rotation

In 3D multi-component seismic analysis, component rotation is a routine procedure. However, I found that incorrect rotations may arise due to changes in acquisition geometry. These could easily be ignored, which would lead to completely wrong results in amplitude dependent analysis, especially in shear-wave splitting analysis for oil-water discrimination. I investigated the effects of component rotation on the data quality using synthetics and developed a QC procedure to ensure the correct application of the procedure.

Seismic anisotropy for fluid detection

Rock physics theories have demonstrated how the fluid viscosity in a saturated HTI medium influences elastic properties. The Chapman squirt-flow model and the poroelastic equivalent medium theory indicate the fluid viscosity in a saturated HTI medium can influence medium elastic properties and thus the Thomsen anisotropic parameters. The synthetic study in Chapter 7 proved the theoretical possibility of using seismic properties to infer the fluid viscosity and monitor fluid substitution in producing reservoirs. The numerical modelling in Chapter 7 shows that effects of fluid viscosity can be revealed in anisotropic parameters and certain P- and PS-wave seismic measurements. The PS-wave amplitude in the direction of the fracture normal can be very sensitive to the fluid, even when P-wave attributes are insensitive to fluids, and thus has more potential to provide us with fluid information for fractured reservoirs.

The numerical modelling in Chapter 7 also reveals that, besides fluid viscosity, seismic frequency, angle of incidence and fracture density also have influence on the seismic anisotropy possessed by fluid saturated HTI media. Seismic frequency and fluid viscosity have equivalent influence on elastic properties, and within the seismic frequency band, the changes of Thomsen parameter (i.e. ε and δ) with fracture density are more detectable than changes with viscosity. To observe viscosity change, the required angle of incidence should be larger than 20^{o} and the fracture density should be larger than 4% for the model. There is a minimum angle of incidence requirement for the fluid influence to be detectable.

Real data analyses for oil-water discrimination were performed with Shengli 3D land multi-component seismic data. They revealed that it is hard to use the P-wave to discriminate oil-water substitution because there is very little difference between the P-waves travelling along the high-stress and low-stress directions. However, analyses on the variation of shear-wave splitting due to pore pressure changes have revealed the potential of discriminating oil and water distributions. The split shear-wave showed consistent changes in amplitude dimming, time delay anomalies, indicating that shear-wave splitting is sensitive to oil-water substitution. The final results revealed that the amplitude and travel-time anomalies can be correlated with well information on saturating fluid type. Water saturated zones tend to be associated with higher values of

shear-wave splitting than oil saturated zones, and the PS-wave amplitudes are dimmer which is the opposite of what would be expected from an anisotropic fluid-substitution calculation using the change in bulk modulus alone without a viscosity component. In the oil saturated zones a strong change in PS-wave amplitude between the fast and slow direction can be observed, while in water saturated zones there is no azimuthal change.

9.2 Future work

Since seismic anisotropy is a big topic, there is still a lot of worthwhile work to be done for further insights in the area, which will be very helpful to the oil industry. From my study in the last few years, I have a few suggestions for future work on the subject.

Due to many practical issues and limitations in seismic data, integrated analysis for fracture characterisation still needs development to improve the reliability of natural fractures information from seismic anisotropy analysis. This work will at least include the following aspects:

- Processing methods to handle converted shear-wave splitting in 3D seismic data, including how to estimate shear-wave splitting and how to compensate for the splitting effects to improve imaging.
- Statistical correlation methods for comparing the results from different seismic attributes, e.g. P-wave AVD analysis and converted shear-wave analysis, in order to improve the reliability of the results.
- Statistical decomposition methods for removing structural imprint and overburden effects, aided by borehole and outcrop data.

Synthetic study and real data analysis have shown the potential of using fluid viscosity for oil-water discrimination. However, the study is still in a preliminary stage, and undoubtedly some uncertainties remain. These are principally related to the effect of pore-fluid pressure which presumably differs significantly between the water flooded and oil saturated zones. To make the approach of using multi-component data to discriminate oil and water saturation in fractured reservoirs really practical in the future, at least the following work needs to be carried out:

- Physical modelling to understand better the physical basis of seismic responses from oil-water saturations, especially comparison analysis of the results between numerical modelling and physical modelling.
- Analysis of frequency response of shear-wave splitting in 3D3C data.
- Time-lapse 3D seismic analysis to study seismic anisotropy changes with respect to oil-water substitution.
- More field case studies to assess the application potential of the method.

All these work will be very helpful in using seismic anisotropy for the characterisation of fractured reservoirs and reducing the uncertainty of the final results.

References

Aki, K. and Richards, P. G., 2002. *Quantitative Seismology*. University Science Books, 2nd edition.

Alford, R., 1986. Shear data in the presence of azimuthal anisotropy. *56th Ann. Internat. Mtg., Expanded Abstracts*, Soc. of Expl. Geophys., S9.6.

Alkhalifah, T.A. and Tsvankin, I., 1995. Velocity analysis for transversely isotropic media. *Geophysics*, **60**, 1550-1566.

Angerer E., Crampin S., Li X.-Y. and Davis T.L. 2002. Processing, modelling and predicting time-lapse effects of overpressured fluid-injection in a fractured reservoir. *Geophysical Journal International*, **149**, 267–280.

Backus, M., 1962. Long-wave elastic anisotropy produced by horizontal layering. Journal of *Geophysical Research*, **67**, 4427-4440.

Bakulin, A., Grechka, V. and Tsvankin, I., 2000a. Estimation of fracture parameters from reflection seismic data – Part I. *Geophysics*, **65**, 1788-1802.

Bakulin, A., Grechka, V. and Tsvankin, I., 2000b. Estimation of fracture parameters from reflection seismic data – Part II. *Geophysics*, **65**, 1803-1817.

Bakulin, A., Grechka, V. and Tsvankin, I., 2000c. Estimation of fracture parameters from reflection seismic data – Part III. *Geophysics*, **65**, 1818-1830.

Batzle, M., Han, D.-H. and Hofmann, R., 2006. Fluid mobility and frequency-dependent seismic velocity – direct measurements. *Geophysics*, **71**, N1-N9.

Berryman, J.G., 1979. Long-wave elastic anisotropy in transversely isotropic media. *Geophysics*, **44**, 896-917.

Berryman, J.G., 1980. Long-wavelength propagation in composite elastic media. *Journal of the Acoustical Society of America*, **68**, 1809-1831.

Booth, D.C. and Crampin, S., 1983. The anisotropic reflectivity technique. Theory. *Geophys. J. R. Astron. Soc.* **72**, pp. 755–766

Brown, R.J., Lawton, D.C. and Cheadle, S.P., 1991. Scaled physical modelling of anisotropic wave propagation: Multioffset profiles over an orthorhombic medium. *Geophys. J. Int.*, **107**, 693-702.

Bush, I. and Crampin, S., 1991. Paris Basin VSPs: Case history establishing combinations of fine-layer (or lithologic) anisotropy and crack anisotropy from modelling shear wavefields near point singularities. *Geophysical Journal International*, **107**, 433-447.

Calvert, A.S., Novak, J.M., Maher, J., Burch, D.N., Bird, D., Larson, R., 2005. A tale of two surveys: experiences processing two similar but different land 3D-3C MEMS surveys. *75th Ann. Internat. Mtg., Expanded Abstracts*, Soc. of Expl. Geophys, 975-978.

Chapman, M., 2003 Frequency dependent anisotropy due to meso-scale fractures in the presence of equant porosity. *Geophysical prospecting*, **51**, 369-379.

Chapman M., Maultzsch S., Liu E. and Li X.-Y. 2003. The effect of fluid saturation in an anisotropic multi-scale equant porosity model. *Journal of Applied Geophysics*, **54**, 191–202.

Cheadle, S. P., Brown, R. J. and Lawton, D. C., 1991. Orthorhombic anisotropy: A physical seismic modelling study. *Geophysics*, **56**, 1603-1613.

Cheret, T., Bale, R. and Leaney, S., 2000. Parameterization of polar anisotropic moveout for converted waves. *70th Ann. Internat. Mtg., Expanded Abstracts*, Soc. of Expl. Geophys, 1181-1184.

Coney, D., Fyfe, T. B., Retail, P., and Smith, P. J., 1993. Clair appraisal: The benefits of a co-operative approach, in Parker, J. R., Ed., Petroleum Geology of Northwest Europe. *Geol. Soc. London*, 1409–1420.

Crampin, S., 1966. Higher modes of seismic surface waves: propagation in Eurasia. *Bulletin of the Seismological Society of America*, **56**, 1227-1239.

Crampin, S., 1981. A review of wave motion in snisotropic and cracked elastic media. *Wave Motion*, **3**, 343-391.

Crampin, S. and Radovich, 1982. Interpretation of synthetic common-depth-point gathers for a single anisotropic layer. *Geophysics*, **47**, 323-335.

Crampin, S., 1985. Evaluation of anisotropy by shear wave splitting, *Geophysics*, **50**, 142-152.

Crampin, S., Bush, I., Naville, C. & Taylor, D.B., 1986. Estimating the internal structure of reservoirs with shear-wave VSPs. *The Leading Edge*, **5**, 11, 35-39.

Crampin, S., 1987. Geological and industrial applications of extensive dilatancy anisotropy. *Nature*, **328**, 491-496.

Crampin, S., 1989. Suggestions for a consistent terminology for seismic anisotropy. *Geophysical Prosp.*, **37**, 753-770.

Crampin, S. and Peacock, S., 2005. A review of Shear-wave splitting in the compliant crack-critical anisotropic Earth. *Wave motion*, **41**, 59-77.

Dai, H. and Li, X.-Y., 2001. Anisotropic migration and model building for 4-C seismic data: A case from Alba. *71st Ann. Internat. Mtg., Expanded Abstracts*, Soc. of Expl. Geophys, 795-798.

Dai, H. and Li, X.-Y., 2002. Sensitivity analysis of migration velocities for P-S converted wave imaging. *64th Annual Conference, Expanded Abstracts*, European Association of Geoscientists and Engineers.

Dai, H., 2003. Integrative analysis of anisotropy parameter and velocities for PS converted waves. *73rd Ann. Internat. Mtg., Expanded Abstracts*, Soc. of Expl. Geophys, 1577-1580.

Dai, H. and Li, X.-Y., 2006. The effects of migration velocity errors on traveltime accuracy in prestack Kirchhoff time migration and the image of PS converted waves. *Geophysics*, **71**, S73–S83.

Dai, H. and Li, X.-Y., 2007a. Velocity model updating in prestack Kirchhoff time migration for PS converted waves: Part I – Theory. *Geophysical Prospecting*, **55**, 525–547.

Dai, H. and Li, X.-Y., 2007b. Velocity model updating in prestack Kirchhoff time migration for PS converted waves: Part II – Application. *Geophysical Prospecting*, **55**, 549–559.

Dai, H. and Li, X.-Y., 2008. Effect of errors in the migration velocity model of PS-converted waves on traveltime accuracy in prestack Kirchhoff time migration in weak anisotropic media. *Geophysics*, **73**, S195–S205.

Esheby, J.D., 1957. The determination of the elastic field of an ellipsoidal inclusion, and related problem. *Proceedings of the Loyal Society of London*, **A241**, 376-396.

Esheby, J.D., 1959. The Elastic Field Outside an Ellipsoidal Inclusion. *Proceedings of the Royal Society of London*, **A 252**, 561-569.

Gaiser, J. and Probert, T., 2006. Recent developments in converted PS-wave analysis processing of shear S-wave splitting and prestack migration. CSEG recorder, Special Edition.

Gardner, G.H.F., Wyllie, M.R.J. and Droschak, D.M., 1964. Effects of pressure and fluid saturation on the attenuation of elastic waves in sands. *Journal of petroleum Technology*, **16**, 189-198.

Gray, D. and Head, K., 2000. Fracture detection in Manderson field: A 3-D AVAZ case history. *The leading Edge*, **19**, 1214-1221.

Grechka, V. and Tsvankin, I., 1997. Inversion of nonhyperbolic moveout in transversely isotropic media. 1685-1688. *67st Ann. Internat. Mtg., Expanded Abstracts*, Soc. of Expl. Geophys, 1685-1688.

Grechka, V. and Tsvankin, I., 1998. 3-D description of normal moveout in anisotropic inhomogeneous media. *Geophysics*, **63**, 1079-1092.

Hall, S., Barkved, O., Mueller, M.C. and Kendall, J-M, 2000. An approach for P-wave AVOA in 3D-OBC data. *62nd Ann. Internat. Mtg., Expanded Abstracts*, Soc. of Expl. Geophys, 1, C-09.

Hall, S.A. and Kendall, J.M., 2003. Fracture characterization at Valhall: Application of P-wave amplitude variation with offset and azimuth AVOA analysis to a 3D ocean-bottom data set. *Geophysics*, **68**, 1150-1160.

Harrison, M., 1992. Processing of P-SV surface-seismic data: Anisotropy analysis, dip moveout, and migration. Ph.D. thesis, The University of Calgary

Helbig, K., 1994. Foundations of elastic anisotropy in exploration seismics. *Handbook of Geophysical Exploration*, Seismic exploration, Pergamon Press.

Herraiz, M. and A.F. Espinosa, 1987. Codawaves: A review. *Pure and Applied Geophysics*, **125**, 499–577.

Hess, H., 1964. Seismic anisotropy of the uppermost mantle under oceans. *Nature*, **203**, 629-631.

Horne, S. and MacBeth, C., 1997. AVA observations in walkaround VSPs. *67th Ann. Internat. Mtg., Expanded Abstracts*, Soc. of Expl. Geophys, 290-293.

Horne, S., McGarrity, J.P., Sayers, C.M., Smith, R.L. and Wijnands, F.M., 1998. Fractured reservoir characterisation using multi-azimuthal walkaway VSPs. *68th Ann. Internat. Mtg., Expanded Abstracts*, Soc. of Expl. Geophys, 1640-1643.

Hudson, J. A., 1980. The excitation and propagation of elastic waves. Cambridge University Press.

Hudson, J.A., 1981. Wave speeds and attenuation of elastic waves in material containing cracks. *Geophysical Journal Royal Astronaut Society*, **64**, 133-150.

Hudson, J. A. 1990. Overall elastic properties of isotropic materials with arbitrary distribution of circular cracks. *Geophys. J. Int.*, **102**, 465–469.

Hudson, J.A. and Crampin, S., 2003. Comment on: 'The 3D shear experiment over the Natih field in Oman: The effect of fracture-filling fluids on shear propagation by C.M. van der Kolk, W.S. Guest and J.H.H.M. Potters. *Geophysical prospecting*, **51**, 365-368.

Hudson, J.A., Liu, E. and Crampin, S., 1996. The mechanical properties of materials with interconnected cracks and pores. *Geophysical Journal International*, **124**, 105-112.

Ikelle, L.T., 1997. Parameterization of AVAZ (Amplitude variation with Azimuth) inversion. *Journal of Seismic Exploration*, **6**, 19-34.

Johnston, D.H. and Toksöz, M.N., 1980. Ultrasonic P and S wave attenuation in dry and saturated rocks under pressure. *Journal of Geophysical Research*, **85**, 925-936.

Johnston, D.H., 1981. Attenuation: A state of the art summary. *Seismic Wave Attenuation*, SEG geophysical reprint series, 123-135.

Johnston, D. H., McKenny, R. S., Verbeek, J., and Almond, J., 1998. Time-lapse seismic analysis of Fulmar Field. *The Leading Edge*, **17**, 1422–1428.

Kanasewich, R.E., 1990. *Seismic noise attenuation*. Pergamon Press.

Kolk, C.M., Guest, W.S. and Potters, J.H.H.M., 2001. The 3D shear experiment over the Natih field in Oman: The effect of fracture-filling fluids on shear propagation. *Geophysical Prospecting*, **49**, 179-197.

Korneev, V.A., Goloshubin, G.M., Daley, T.M. and Silin, D.B., 2004. Seismic low frequency effects in monitoring fluid-saturated reservoirs. *Geophysics*, **69**, 522-532.

Landro, M. and Stronen, L.K., 2003. 4D study of fluid effects on seismic data in the Gullfaks Field, North Sea. *Geofluids*, **3**, 233-244.

Lefeuvre, F., 1994. Fracture related anisotropy detection and analysis: "and if the P-waves were enough". *64th Ann. Internat. Mtg., Expanded Abstracts*, Soc. of Expl. Geophys, 942-945.

Li, X.-Y., 1997. Viability of azimuthal variation in P-wave moveout for fracture detection. *67th Ann. Internat. Mtg., Expanded Abstracts II*, Soc. of Expl. Geophys, II, 1555-1558.

Li, X.-Y., 1998a. Fracture detection using P-P and P-S wave in multicomponent sea floor data. *68th Ann. Internat. Mtg., Expanded Abstracts*, Soc. of Expl. Geophys, 2056-2059.

Li X.-Y. 1998b. Processing PP and PS waves in multicomponent sea-floor data for azimuthal anisotropy: theory and overview. *Proceedings of the Eighth International Workshop on seismic Anisotropy* (Revue De L'institut francia du petrole), **53**, 607-620.

Li X.-Y. 1999. Fracture detection using azimuthal variation of P-wave moveout from orthogonal seismic survey lines. *Geophysics*, **64**, 1193-1201.

Li, X.-Y., Dai, H. and Mancini, F., 2007. Converted-wave imaging in anisotropic media: theory and case studies. *Geophysical Prospecting,* **55**, 345–363

Li, X.-Y. and Druzhinin, A., 2000. A practical approach to P-SV prestack time migration and velocity analysis for transverse isotropy. *70th Ann. Internat. Mtg., Expanded Abstracts I*, Soc. of Expl. Geophys, 1142-1145.

Li, X.-Y. and Yuan, J., 2001. Converted-wave imaging in inhomogeneous, anisotropic media: Part I – Parameter estimation. *63rd Annual Conference, Expanded Abstracts*, European Association of Geoscientists and Engineers, P1-9.

Li, X.-Y. and Yuan, J., 2003. Converted-wave moveout and conversion-point equation in layered VTI media: Theory and application. *Journal of applied Geophysics*, **54**, 297-318.

Li, X.-Y., Wei, X., Maultzsch, S., Liu, E., Chapman, M. and Fowler, S. 2004. An integrated study of Clair 4C and VSP data for fracture detection. *EAP Research Reports*, A1-30.

Liu, E., Crampin, S., Queen, J.H. and Rizer, W.D., 1993. Velocity and attenuation anisotropy caused by microcracks and microfractures in a multiazimuth reverse VSP. *Canadian Journal of Exploration Geophysics*, **29**, 177-188.

Liu, E., Hudson, J.A. and Pointer, T., 2000. Equivalent medium representation of fractured rock. *Journal of Geophysical Research*, **105**, 2981-3000.

Liu, E., Li, X.-Y. and Queen J. H., 2000. Discrimination of porefluids from P and converted shear-wave AVO analysis. *Anisotropy 2000: Fracture, converted waves and case studies*, Soc. of Expl. Geophys.

Liu, E., Maultzsch, S., Chapman, M., Li, X.-Y., Queen, J.H. and Zhang, Z., 2003. Frequency-dependent seismic anisotropy and its implication for estimating fracture size in low porosity reservoirs. *The leading Edge*, **22**, 663-665.

Liu, Y.J., 2003. Analysis of P-wave Seismic Reflection Data for Azimuthal Anisotropy. *PhD thesis*, University of Edinburgh.

Lorenz, J.C. Warpinski, N.R. and Teufel, L.W., 1996. Natural fracture characteristics and effects. *The Leading Edge*, **15**, 909-911.

Lucet, N. and Zinszner, B., 1992. Effects of heterogeneities and anisotropy on sonic and ultrasonic attenuation in rocks. *Geophysics*, **57**, 1018-1026.

Lumley, D., Nur, A., Strandenes, S., Dvorkin, J., and Packwood, J., 1994. Seismic monitoring of oil production: A feasibility study. *64th Ann. Internat. Mtg., Expanded Abstracts*, Soc. Of Expl. Geophys., 319–322.

Luo, M. and Evans, B.J., 2004. An amplitude-based multiazimuth approach to mapping fractures using P-wave 3D seismic data. *Geophysics*, **69**, 690-698.

Lynn, H.B. and Thomsen, L.A., 1986. Reflection shear-wave data along the principal axes of azimuthal anisotropy. *56th Ann. Internat. Mtg., Expanded Abstracts*, Soc. of Expl. Geophys., 473-476.

Lynn, H.B., Simon, K.M. and Bates, C.R., 1996. Correlation between P-wave AVOA and S-wave traveltime anisotropy in a naturally fractured gas reservoir. *The Leading Edge*, **15**, 931-936.

Lynn, H.B., Beckham, W.E., Simon, K.M., Bates, C.R., Layman, M. and Jones, M., 1999. P-wave and S-wave azimuthal anisotropy at a naturally fractured gas reservoir, Bluebell-Altamont field, Utah. *Geophysics*, **64**, 1312-1328.

Mavko, G. and Jizba, D., 1991. Estimating grain-scale fluid effects on velocity dispersion in rocks. *Geophysics*, **56**, 1940-1949.

Markov, G.., Mukerji, T. and Dvorkin, J., 1998. *The rock physics handbook*, Cambridge university press.

Mattocks, B., Li, J. and Roche, S.L., 2005. Converted-wave azimuthal anisotropy in a carbonate foreland basin. *75th Ann. Internat. Mtg., Expanded Abstracts*, Soc. of Expl. Geophys, 897-890.

Maultzsch, S., Chapman, M., Liu, E. and Li, X.-Y., 2003. Modelling frequency-dependent seismic anisotropy in fluid-saturated rock with aligned fractures: implication of fracture size estimation from anisotropic measurements. *Geophysical Prospecting*, **51**, 381-392.

Maultzsch, S., Horne, S., Archer, S. and Burkhardt, H., 2003. Effects of an anisotropic overburden on azimuthal amplitude analysis in horizontal transverse isotropic media. *Geophysical Prospecting*, **51**, 61-72.

Mukerji, T. and Mavko, G., 1994. Pore fluid effects on seismic velocity in anisotropic rocks. *Geophysics*, **59**, 233-244.

Murphy, W.F., 1985. Sonic and ultrasonic velocities: Theory versus experiment. *Geophhysical Research Letters*, **12**, 85-88.

Nishizawa, O. 1982. Seismic velocity anisotropy in a medium containing oriented cracks-transversely isotropic case. *Journal Physical Earth*, **30**, 331-347.

Nur, A. and Winkler, K., 1980. The role of friction and fluid flow in wave attenuation in rocks. *Geophysics*, **45**, 591-592.

O'Connell, R.J. and Budiansky, B., 1974. Seismic velocities in dry and saturated cracked solids. *Journal of Geophysical Research*, **79**, 5412-5426.

Pointer, T., Liu, E. and Hudson, J.A., 2000. Seismic wave propagation in cracked porous media. *Geophysical Journal International*, **142**, 199-231.

Queen, J. H., and Rizer W. D., 1990. An integrated study of seismic anisotropy and the natural fracture systems at the Conoco Borehole Test Facility. *Journal of Geophysical Research*, **95**, 11255-11273.

Queen, J. H., Rizer W. D. and DeMartini D., 1992. Geophysical methods of fracture detection and estimation. *The Leading Edge*, **11**, 19-21.

Rathore, J. S., Fjaer, E., Holt, R. M. and Renlie, L., 1995. P- and S-wave anisotropy of a synthetic sandstone with controlled crack geometry. *Geophysical Prospecting*, **43**, 711-728.

Roche, S.L., Wagaman, M., and Watt, H.J., 2005. Analysis of P-wave and Converted-wave 3D seismic data, Anadarko Basin, Oklahoma, USA. *75th Ann. Internat. Mtg., Expanded Abstracts*, Soc. of Expl. Geophys, 979-982.

Rommel B. E. 1996. Dip move out processing (DMO) for converted waves in transversely isotropic media. *58th Annual Conference, Expanded Abstracts*, European Association of Geoscientists and Engineers, P136.

Rüger, A., and Tsvankin, I., 1997. Using AVO for fracture detection: Analytical basis and practical solutions. *The Leading Edge*, **16**, 1429-1434.

Rüger, A., 1998. Variations of P-wave reflectivity with offset and azimuth in anisotropic media. *Geophysics*, **63**, 935-947.

Sams, M.S., Neep, J.P., Worthington, M.H. and King, M.S., 1997. The measurement of velocity dispersion and frequency-dependent intrinsic attenuation in sedimentary rocks. *Geophysics*, **62**, 1456-1464.

Sayers, C.M., and Ebrom, D. A., 1997, Seismic traveltime analysis for azimuthally anisotropic media: Theory and experiment: *Geophysics*, **36**, 1570–1582.

Sayers, C.M. and Kachanov, M., 1991. A simple technique for finding effective elastic constants of cracked solids for arbitrary crack orientation statistics. *International Journal of Solids and Structures*, **27**, 671-680.

Sayers, C.M. and Kachanov, M., 1995. Microcrack-induces elastic wave anisotropy of brittle rocks. *Journal of Geophysical research*, **100**, 4149-4156.

Sayers, C.M., 2002. Fluid-dependent shear-wave splitting in fractured media. *Geophysical Prospecting*, **50**, 393-401.

Schoenberg, M., 1980. Elastic wave behaviour across linear slip interfaces. *Journal of the Acoustical Society of America*, **68**, 1516-1521.

Schoenberg, M., 1994. Transversely isotropic media equivalent to thin isotropic layers. *Geophysical Prospecting*, **42**, 885-915.

Schoenberg, M., 1998. Acoustic characterization of un-derground fractures. *68th Ann. Internat. Mtg., Expanded Abstracts*, Soc. of Expl. Geophys, 1624-1627.

Schoenberg, M. and Douma, J., 1988. Elastic wave propagation in media with parallel fractures and aligned cracks. *Geophysical Prospecting*, **36**, 571-590.

Schenoberg, M. and Helbig, K., 1997. Orthorhombic media: Modelling elastic wave behavior in a vertically fractured earth. *Geophysics*, **62**, 1954-1974.

Schoenberg, M. and Sayers, C., 1995. Seismic anisotropy of fractured rock. *Geophysics*, **60**, 204-211.

Sena, A.G., 1991. Seismic travel time equations for azimuthally anisotropic and isotropic media. Estimation of interval elastic properties. *Geophysics*, **56**, 2090-2101.

Sheriff, R. and Geldart, L., 1995. *Exploration seismology*, Cambridge University Press, 2nd edition.

Slack, R., D., Ebrom, D., McDonald, J. A. and Tatham, R. H., 1991. Thin Layers and shear-wave splitting. *61th Ann. Internat. Mtg., Expanded Abstracts*, Soc. of Expl. Geophys, 1549-1552.

Smith, R.L. and McGarrity, J.P., 2001. Cracking the fractures from seismic anisotropy in an offshore reservoir. *The Leading Edge*, **20**, 19-26.

Sothcott, J., McCann, C. and O'Hara, S., 2000. The influence of two pore fluids on the acoustic properties of reservoir sandstones at sonic and ultrasonic frequencies. *70th Ann. Internat. Mtg., Expanded Abstracts*, Soc. of Expl. Geophys, 1883-1886.

Spencer, J.W., 1981. Stress relaxation at low frequencies in fluid-saturated rocks: Attenuation and modulus dispersion. *Journal of Geophysical Research*, 86, 1803-1812.

Stewart, R.R., Gaiser, J.E., Brown, R.J. and Lawton, D.C., 2002. Converted-wave seismic exploration: Methods. *Geophysics*, **67**, 1345-1363.

Tessmer, G. and Behle, A., 1988. Common-conversion point stacking technique for converted wave. *Geophysical Prospecting*, **36**, 671-688.

Thomsen, L. 1986. Weak elastic anisotropy. *Geophysics*, **51**, 1954-1966

Thomsen, L., 1995. Elastic anisotropy due to aligned cracks in porous rock. *Geophysical prospecting*, **43**, 805-829.

Thomsen, L., 1999. Converted-wave reflection seismology over inhomogeneous, anisotropic media. *Geophysics*, **64**, 678-690.

Thomsen, L., 2002. Understanding seismic anisotropy in exploration and exploitation. *SEG distinguished instructor series, No.5*, Soc. of Expl. Geophys, 290-293.

Tod, S. R., 2001. The effects on seismic waves of interconnected nearly aligned cracks. *Geophys. J. Int*., **146**, 249-263.

Toksöz, M.N., Johnson, D.H. and Timur, A., 1979. Attenuation of seismic waves in dry and saturated rocks: I. Laboratory measurements. *Geophysics*, **44**, 681-690.

Tsvankin, I. and Thomsen, L., 1994. Nonhyperbolic reflection moveout in anisotropic media. *Geophysics*, **59**, 1290-1304.

Tsvankin I. and Grechka V. 2000. Dip moveout of converted waves and parameter estimation in transversely isotropic media. *Geophysical Prospecting*, **48**, 257-292.

Tsvankin, I., 2005. Seismic signature and analysis of reflection data in anisotropic media. *Handbook of geophysical exploration*, seismic exploration, Volume 29, Elsevier Ltd.

Varela, O.J., Verdín, C. T., Sen, M. K. and Roy, I. G., 2006. Using time-lapse seismic amplitude data to detect variations of pore pressure and fluid saturation due to oil displacement by water: a numerical study based on one-dimensional prestack inversion. *J. Geophys. Eng.* **3**, 177-193

Wang, S. and Li, X.-Y., 2006. Layer stripping of azimuthal anisotropy from P-wave reflection moveout in orthogonal survey lines. *J. Geophys. Eng.*, **3**, 1-11.

Wang, Z., 2002. Seismic anisotropy in sedimentary rocks, part 2. Laboratory data, *Geophysics*, **67**, 1423-1440.

White, J.E., Nicoletis, L. and Monash, C., 1983. Measured anisotropy in Pierre Shale. *Geophysical Prospecting*, **31**, 709-725.

White, J.E. and Sengbush, R. L., 1953. Velocity measurements in near-surface formations. *Geophysics*, **18**, 54-69.

Wild, P. and Crampin, S., 1991. The range of effects of azimuthal isotropy and EDA anisotropy in sedimentary basins. *Geophysical Journal International*, **107**, 513-529.

Winkler, K.W., 1986. Estimates of velocity dispersion between seismic and ultrasonic frequencies. *Geophysics*, **51**, 183-189.

Winterstein, D.F., 1990. Velocity anisotropy terminology for geophysicists. *Geophysics*, **55**, 1070-1088.

Yuan, J., 2001. Analysis of four-component seafloor seismic data for seismic anisotropy. *PhD thesis*, The University of Edinburgh.

Yuan, J. and Li, X.-Y., 2001. PS-wave conversion point equations for layered anisotropic media. *63rd Annual conference, Expanded Abstracts*, European Association of Geoscientists and Engineers, P112.

Zhang, Y., 1992. Stacking P-SV converted wave data with Raypath velocity. *62nd Ann. Internat. Mtg., Expanded Abstracts*, Soc. of Expl. Geophys, 1214-1217.

Zhang, Y., 1996. No-hyperbolic converted wave velocity analysis and normal moveout, *66th Ann. Internat. Mtg., Expanded Abstracts*, Soc. of Expl. Geophys, 1555-1558.

Zatsepin S.V. and Crampin S. 1997. Modelling the compliance of crustal rock—I. Response of shear-wave splitting to differential stress. *Geophysical Journal International*, **129**, 477–494.

Appendix Publications

Qian, Z., Chapman, M. and Li, X.-Y., 2008. Seismic measurements of fluid viscosity in HTI media: a numerical modelling analysis. *70th Annual Conference, Expanded Abstracts*, European Association of Geoscientists and Engineers, P112.

Qian, Z., Li, X.-Y. and Chapman, M., 2008. Fracture characterization with azimuthal attribute analysis of PS-wave data: modelling and application. *70th Annual Conference, Expanded Abstracts*, European Association of Geoscientists and Engineers, P354.

Qian, Z., Chapman, M., Li, X.-Y., Dai, H., Liu, E., Zhang, Y. and Wang, Y., 2007. Use of multicomponent seismic data for oil-water discrimination in fractured reservoirs. *The Leading Edge*, **26**, 1176-1184.

Qian, Z., Li, X.-Y. and Chapman, M., 2007. Effects of Fluid Saturation on Shear-wave Splitting in Multicomponent Seismic Data. *EAGE/SEG Research Workshop*, Perugia, Italy.

Qian, Z., Li, X.-Y., Chapman, M., 2007. Azimuthal variations of PP- and PS-wave attributes: a synthetic study. *77th Ann. Internat. Mtg., Expanded Abstracts*, Soc. of Expl. Geophys., 184-188.

Qian, Z., Li, X.-Y., Chapman, M., and Wang, Y., 2007. Effects of oil-water saturation on shear-wave splitting in multi-component seismic data. *77th Ann. Internat. Mtg., Expanded Abstracts*, Soc. of Expl. Geophys., 1019-1023.

Qian, Z. and Li, X.-Y., 2007. Sensitivity analysis of anisotropic parameters for C-wave pre-stack time migration in the Clair 3D OBC data. *69th Annual Conference, Expanded Abstracts*, European Association of Geoscientists and Engineers, P196.

Qian, Z. Li, X.-Y. and Chapman, M., 2007. Effects of Fluid Saturation on Shear-wave Splitting in Multicomponent Seismic Data. *EAGE/SEG Research Workshop*, Perugia, Italy.

Qian, Z., Li, X.-Y., Meng, X. and Bi, L., 2007. Converted-wave velocity analysis in the presence of anisotropy: a case study from Shengli oilfield, China. *69th Annual Conference, Expanded Abstracts*, European Association of Geoscientists and Engineers, P304.

Qian, Z., Li, X.-Y., Liu, E., and Wang, S., 2006. Fracture detection using 3D P-wave seismic data: an integrated study from southwest China. *76th Ann. Internat. Mtg., Expanded Abstracts*, Soc. of Expl. Geophys., 209-213.

Qian, Z., Li, X.-Y. and Liu, E., 2006. AVD analysis of the Clair 3D P-wave data with conclusions of 3D physical modelling. *68th Annual Conference, Expanded Abstracts*, European Association of Geoscientists and Engineers, E044.

Qian, Z., Li, X.-Y. and Wang, S., 2006. Comparison of two physical modelling studies of 3D P-wave fracture detection. *68th Annual Conference, Expanded Abstracts*, European Association of Geoscientists and Engineers, P296.

ROME 2008
LEVERAGING TECHNOLOGY

P112

Seismic Measurements of Fluid Viscosity in HTI Media - A Numerical Modeling Analysis

Z. Qian* (British Geological Survey), M. Chapman (British Geological Survey) & X. Li (British Geological Survey)

SUMMARY

We study the effects of fluids saturated HTI medium on elastic properties and seismic measurements and the possibility of discriminating oil-water saturations with them though numerical modeling. The results based on rock physics modelling demonstrate Thomsen anisotropy parameters and the seismic measurements for P- and PS-wave data are sensitive to fluid viscosity and can be used to monitor fluid substitutions in producing reservoirs.

Introduction

How to effectively monitor fluid saturations is an important issue in reservoir production, especially in cases where water injection is involved to drive remaining oil towards producing well to improve productivity. The similar bulk moduli of oil and water have impeded the use of seismic data to discriminate them. However, vertically fractured reservoirs, which can be simplified as HTI media introduce seismic anisotropy and many studies have revealed the links between the fluids in HTI media and seismic anisotropy.

The communication of fluids between fractures and equant porosity occurring as seismic wave passing by influences media elastic properties (Thomsen, 1995). Liu, et al. (2000) shows that the normal to shear compliance ratio is directly related to isolated pore or fracture fluids and it is possible to estimate fluid saturation with seismic data. Chapman (2003) introduces the squirt-flow model to study frequency dependent anisotropy and establishes the poro-elastic equivalent medium theory with considering the factors that influence elastic properties, such as fluid viscosity, fracture and crack density and porosity, etc.. Batzle et al. (2006) proposes the concept of fluid mobility as the ratio of permeability to viscosity to study frequency-dependent seismic velocities in the laboratory, which reveals that larger fracture size and density can increase fluid permeability, while viscosity influences fluid communication speed. Seismic frequency, fracture properties and fluid viscosity influence the time for fluid stress to equilibrate during seismic propagation. Among fluid properties, water and oil have markedly different viscosities. The ability to detect viscosity effects with seismic measurements can improve the chance of discriminating oil-water saturation in fractured reservoirs.

In this paper, we study the effects of fluid viscosity on seismic data and the possibility of using seismic measurements to characterize oil-water saturations with numerical modeling. The study also aims to gain more insights in using multi-component surface seismic data to detect oil-water saturations in fractured reservoirs (Qian, et al., 2007).

Seismic measurements for fluid viscosity

Though fluid saturations influence medium elastic properties and the effects are contained on certain seismic properties, it is ambitious to detect fluid viscosity direct from seismic reflection amplitudes because so many factors may have influenced the seismic reflection amplitudes and fluid viscosity is not the major one. Furthermore, what we really concern about in oil exploration is fluid distributions in space, not fluid viscosities. If we are able to obtain the distribution of fluid viscosity with seismic measurements, we may reach the purpose of monitoring fluid saturations in producing reservoirs. Thus, what matters in the detection of fluid saturations is to find a seismic measurement to detect the variations of fluid viscosity in space.

Here, we use the method proposed by Li (1998), with which we can characterize fluid viscosities though Thomsen anisotropy parameters for HTI medium. To apply the method, we first need to know the preferred direction of fracture strikes, which can be estimated with seismic methods (e.g. Thomsen, 2002). Instead of calculating absolute reflection coefficients, we just need to calculate the differences of the P- and PS-wave reflection coefficients between fracture parallel and fracture normal directions,

$$\Delta R_{pp} = \frac{1}{2}\left(\delta - 2\varepsilon + \frac{8\beta_0^2}{\alpha_0^2}\gamma\right)\sin^2 i$$

$$\Delta R_{PS} = \frac{\sin i}{2\cos j}\left[\frac{\alpha_0^2}{\alpha_0^2-\beta_0^2}(\delta-2\varepsilon)+\frac{4\beta_0}{\alpha_0}\gamma\cos i\cos j\right.$$
$$-\frac{\alpha_0\beta_0}{\alpha_0^2-\beta_0^2}(\delta-2\varepsilon)\cos i\cos j-\frac{4\beta_0^2}{\alpha_0^2}\gamma\sin^2 i$$
$$\left.+(\delta-2\varepsilon)\sin^2 i-\frac{\alpha_0^2}{\alpha_0^2-\beta_0^2}(3\delta-4\varepsilon)\sin^2 i\right]$$

where, ΔR_{pp} and ΔR_{ps} have included the effects of fluid properties and can be used as a seismic measurement to infer the variations of the fluid viscosity in space; δ, ε and γ are Thomsen anisotropy parameters for HTI medium, containing the effects of fracture properties, fluid properties and supposed seismic frequency; α_0 and β_0 are the average P- and S-wave velocities of the upper (isotropic) medium and lower (HTI) medium; *i* and *j* are the average propagation angles of the upper and lower medium for P- and S-wave, respectively.

Numerical modeling analysis

The numerical model is constructed with a porous, cracked, fluid saturated HTI layer under an isotropic layer to simulate fractured reservoirs under a shale layer. The elastic constants of the model are calculated with the method proposed by Chapman (2003), which carries the effects of fluid viscosity. The Thomsen anisotropy parameters for HTI medium are then calculated with the elastic constants.

Figure 1 displays the Thomsen anisotropy parameters and seismic measurements for P- and PS-wave with viscosity. The relative viscosity of water is supposed to be 1.0. The fracture density is 8% and the angle of incidence is 27° for the modeling. Figure 1a shows both ε and δ decrease with viscosity, while γ remains constant. Figure 1b reveals the seismic measurements for P- and PS-wave increase with viscosity, but the variation magnitude of the measurement for PS-wave is larger than that for P-wave, means P-wave is less sensitive to fluid saturations than PS-wave. It verifies the fact that, at seismic angle of incidence ranging from 0° to 45°, slow shear wave is strongly attenuated and dispersed in fracture normal direction, while P-wave and fast shear wave suffer little fracture related attenuation in fracture strike direction.

Figure 2 shows the Thomsen anisotropy parameters and PS-wave measurement on the plane of viscosity and frequency. Figure 2a shows ε changes with frequency and viscosity. Within seismic PS-wave frequency band ($10^{0.5}$ – $10^{1.5}$), the variation of ε can be observed from viscosities start from 5.0 (relative to the viscosity of water), then with the increase of viscosity, the frequency band suitable for ε variation analysis shifts towards lower frequency zone. Figure 2b shows γ does not change with viscosity or frequency. Figure 2c displays that δ's behavior is similar to that of ε. Figure 2d shows the seismic measurements for PS-wave on viscosity and frequency plane, revealing that, within seismic frequency band, the seismic measurement is directly related to the viscosity and can be used to describe the viscosity.

Figure 3 is Thomsen anisotropy parameters and the seismic measurements for PS-wave on the plane of viscosity and fracture density. It reveals that if fracture density is lower than 2%, ε does not change with viscosity. When fracture density is around 8%, ε gets most changes as viscosity is lower than 30.0. Figure 3b and 3c show that γ changes with fracture density but does not change with viscosity, while δ increases with viscosity. If fracture density is lower than 2%, the seismic measurement for PS-wave does not change with viscosity (Figure 3d).

The results on figure 2d and 3d reveal that, for fixed fracture density and seismic frequency, the seismic measurements for PS-wave can be used to characterize viscosity variations in space.

Discussion and conclusions

Rock physics theories have demonstrated how the fluid viscosity in saturated HTI medium influence elastic properties, which make it theoretically possible to use seismic measurements to detect fluid saturations and underlie the basis of using seismic anisotropy to monitor fluid substitution in producing reservoirs.

The numerical modeling results prove that the variations of fluid viscosity can be revealed on two Thomsen anisotropy parameters (ε and δ) and the seismic measurements for P- and PS-wave (ΔR_{pp} and ΔR_{ps}). Seismic frequency and fluid viscosity have similar effects on elastic properties, but within seismic frequency band, the changes of ε and δ are more detectable with frequency than with viscosity. To observe fluid substitution with the seismic measurement, the required fracture density should to be larger than 5%.

Acknowledgements

This work is supported by the SinoPec international collaboration programme and Shengli Oilfield Ltd. through the Edinburgh Anisotropy Project (EAP) of the British Geological Survey (BGS), and is published with the approval of all project partners and the Executive Director of BGS.

References

Batzle, M., Han, D.-H. and Hofmann, R., 2006. Fluid mobility and frequency-dependent seismic velocity – direct measurements. Geophysics. 71, N1-N9.
Chapman, M., 2003. Frequency-dependent anisotropy due to meso-scale fractures in the presence of equant porosity. Geophysical Prospecting. 51, 369-379.
Li, X.-Y., 1998. Processing P- and PS waves in multicomponent sea-floor data for azimuthal anisotropy: theory and review. Processing 8th International workshop on seismic Anisotropy, Revue le L'Institut Francais du Petrole. 53, 607-610.
Liu, E., Li, X.-Y. and Queen J. H., 2000. Discrimination of porefluids from P and converted shear-wave AVO analysis. SEG, Anisotropy 2000: Fracture, converted waves and case studies.
Qian, Z., Chapman, M., Li, X.-Y., Dai, H. Liu, E., 2007. Use of multicomponent seismic data for oil-water discrimination in fractured reservoirs. The Leading Edge. 26, 1176-1184.
Thomsen, L., 1995. Elastic anisotropy due to aligned cracks in porous rock. Geophysical Prospecting. 43, 805-829.
Thomsen, L., 2002. Understanding seismic anisotropy in exploration and exploitation. SEG distinguished instructor series, No.5.

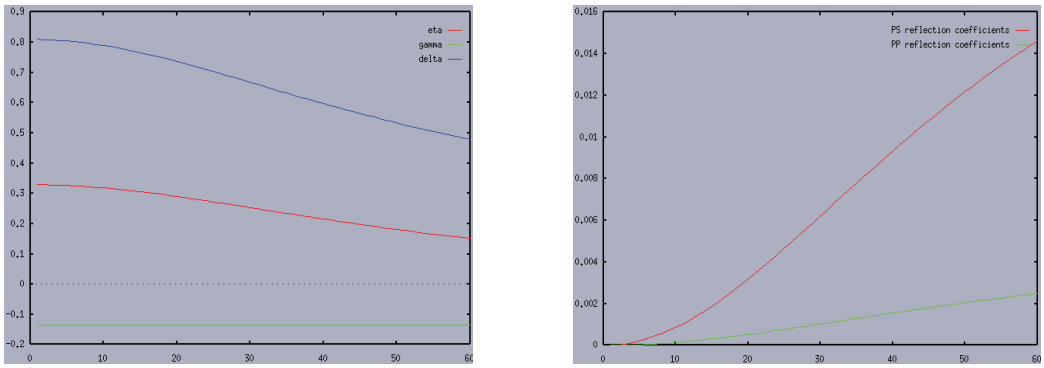

(a) (b)

Figure 1 Viscosity effects on Thomsen anisotropy parameters and reflection coefficients: (a) ε, γ and δ with viscosity; (b) seismic measurements for P- and PS-wave with viscosity. Fracture density: 8%; angle of incidence: 27°.

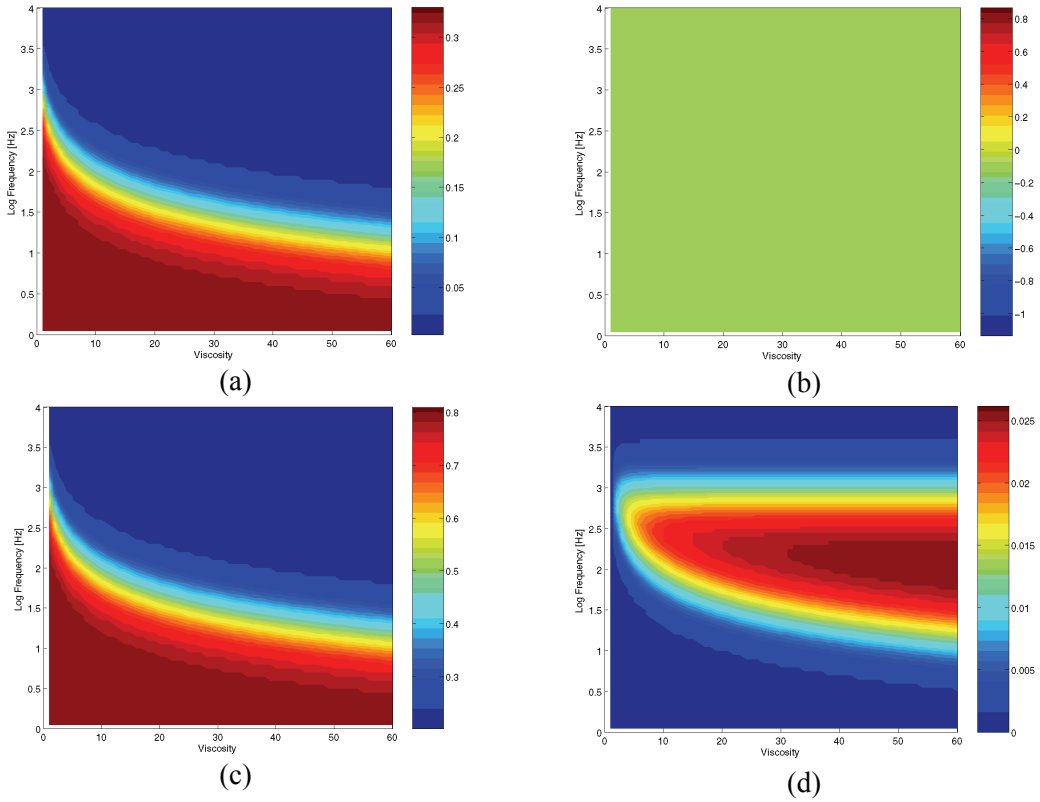

Figure 2 Thomsen parameters ε (a) , γ (b) δ (c) and PS-wave measurement (d) with viscosity and frequency. Fracture density: 8%; angle of incidence: 27°.

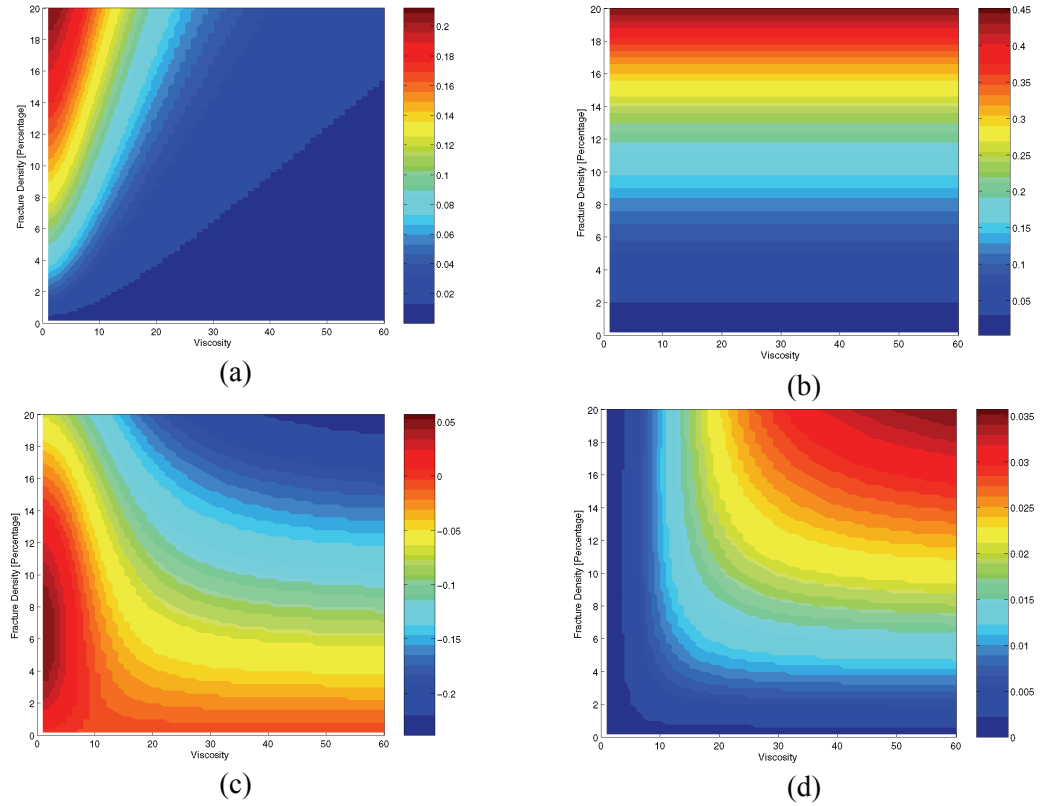

Figure 3 Thomsen anisotropy parameters ε (a) , γ (b) δ (c) and PS-wave measurement (d) with viscosity and fracture density. Frequency: 15Hz; angle of incidence: 27°.

ROME 2008
LEVERAGING TECHNOLOGY

P354

Fracture Characterization with Azimuthal Attribute Analysis of PS-wave Data - Modelling and Application

Z. Qian* (British Geological Survey), X. Li (British Geological Survey) & M. Chapman (British Geological Survey)

SUMMARY

We carry out azimuthal seismic anisotropy analysis of P- and PS-wave for fracture characterization with numerical modelling and a 3D3C dataset. Numerical results reveal that both the amplitudes and interval travel-time of the R-component of PS-wave can be used to infer fracture properties through ellipse fitting as that in azimuthal P-wave attribute analysis. In the real 3D3C data analysis, the fracture properties obtained from the azimuthal R-component analysis of the PS-wave data agrees with that inferred from the geological and logging information.

Introduction

Fractured reservoirs are common worldwide and fracture characterization plays an important part in reservoir development. The use of seismic anisotropy to characterize fractured reservoirs started in the 1980's and has been gradually gaining the acceptance of the hydrocarbon industry. The underline physics for this technology comes from the equivalent medium theory for seismic wave propagation in fractured media, which has been intensively studied by a range of authors (e.g. Hudson, 1981; Liu et al, 2000; Chapman, 2003; amongst others.). According to these theories, a medium containing vertically aligned fractures with scale length much less than the wavelength can be modeled by an equivalent azimuthally anisotropic medium for seismic wave propagation. Numerical modelling based on the equivalent medium theories reveals shear-wave splitting and azimuthal P-wave amplitude and travel-time variations as diagnostic features for fractured media. A 3D physical modelling example of azimuthal P-wave analysis also reveals different seismic attributes may have different requirements to obtain optimal results (Wang et al, 2007).

With the development of data acquisition techniques and the interest of use PS-wave to characterize fracture properties in fractured reservoirs, more and more 3D multi-component seismic data with wide azimuth-offset coverage have become available, which provide not only wide azimuth P-wave data, but also wide azimuth PS-wave data. If the azimuthal attributes of PS-waves also show similar azimuthal anisotropy features like that of P-wave, we may use the similar techniques applied on P-wave data to infer fracture properties with PS-wave data. Then with a combined analysis of the fracture information obtained from azimuthal P-wave and PS-waves analysis, the overall reliability of fracture characterization results can be improved.

In this paper, we first carry out azimuthal anisotropy analysis for azimuthal PS-wave based on HTI medium for fracture characterization through numerical modelling, then apply the method on a wide-azimuth 3D3C dataset acquired on a fractured reservoir.

Numerical modelling

The model and parameters are displayed in Figure 1a, the middle layer is a HTI medium. The modelling azimuth ranges from 0^o to 360^o and the azimuth sampling interval is 10^o. The colour of the curves in figure 1 represents the results come from different fracture densities: the red represents the fracture density of 18%, while the blue represents the fracture density of 10%. The offset is set as 500m for amplitude modelling and 1000m for interval travel-time modeling so that the depth to offset ratio at the reflection point is always 1.0. Since seismic ray paths are not straight lines, it is difficult to know the angle of incidence at analysis points. Thus it is more convenient to use the depth to offset ratio than use the angle of incidence.

We first carry out numerical modelling for azimuthal P-wave anisotropy analysis for comparison. Figure 1b shows the azimuthal amplitude distribution at the top interface of the HTI layer and figure 1c shows the azimuthal interval travel-time distribution within HTI layer. It reveals that both the amplitudes and the interval travel-time are in elliptical distribution with azimuth, the long axis of the ellipse is in fracture strike direction for amplitude attribute and in fracture normal direction for interval travel-time attribute, and the long to short axis ratio is related with fracture density. However, the modelling results also reveal that not all data are suitable for elliptical fitting to obtain fracture information, the azimuthal attributes of data with very small offset and very large offset do not appear in elliptical distributions. Thus the usable offsets are limited for elliptical fitting.

Figure 1d displays the azimuthal amplitudes of R-component of PS-wave at the top of the fractured layer. It also shows the azimuthal amplitudes appears in elliptical distribution, which is similar to the behaviour of azimuthal P-wave amplitudes, except that the long axis of the ellipse is in fracture normal direction for PS-wave and in fracture strike direction for P-wave. The azimuthal amplitudes of the T-component of the PS-wave data are displayed in figure 1e

and the azimuthal variations reveal zero-crossings and polarity reversals, which can also be used to infer fracture information. Figure 1f shows the interval travel-time of R-component of the PS-wave data within the fracture layer is in elliptical distribution with azimuth and the long axis of the ellipse indicates fracture normal, which is consistent with that in azimuthal P-wave analysis.

Figure 1d and 1f reveal that both the amplitudes and interval travel-time of R-component can be used to infer relative fracture density in the similar way in P-wave analysis. It also reveals that not all the R-component data of PS-wave are suitable for elliptical fitting, there are usable offset range limits just like that in azimuthal P-wave attribute analysis.

Real data analysis

The 3D3C land seismic data were acquired on a fractured reservoir in Shengli Oilfield with wide azimuth-offset coverage (Figure 2, where red lines are the receiver locations and the blue spots are the source locations), which aims to obtain water-oil distributions at the target layers through shear wave splitting analysis. The preliminary analysis of the PS-wave data shows good shear wave splitting information due to the well developed vertically aligned fractures in the area. Reliable fracture characterizations are extremely important for successful separation of fast and slow shear wave, which is essential for the subsequent oil-water characterization. Thus, how to obtain reliable fracture properties, especially fracture direction, is an important work that has to be done first in this oil-water discrimination attempt.

For this, we focus our effects on the use of azimuthal PS-wave data, mainly the R-component data, for the fracture characterization, then carry out combined analysis with other prior information to improve the reliability of fracture characterization results. In fact, the azimuthal anisotropy is so obvious on the PS-wave data that just a simple CCP super-gather of R-component sorted in azimuth sequence has shown significant azimuthal travel-time variations at the target reflections (Figure 3, where yellow lines indicate), revealing the good potential of using azimuthal PS-wave analysis for the fracture characterization.

In the azimuthal analysis with the R-component of PS-wave data, we use the amplitudes and interval travel-time as the main seismic attributes and apply exactly the same strategy in numerical modelling. Besides fitting azimuthal amplitudes and azimuthal interval travel-time with ellipse, we also perform independent azimuthal velocities analysis for quality control on six sub-supergathers obtained by dividing a CCP super-gather into six parts according to equally divided azimuth sections. The fracture strike direction of the final characterization results was identified as N45^{o}E, which is in agreement with the structural alignment of the area.

After fracture characterization, we perform component rotation to transform R- and T-component data to fast shear wave (in fracture strike direction) and slow shear wave (in fracture normal direction) and figure 4 shows good fast and slow shear wave separation (in CCP gather). Figure 5 displays the corresponding fast and slow shear wave stacks (target zone) for subsequent shear wave splitting and oil-water saturations analysis (Qian, et al.,2007).

Discussion and Conclusions

We carry out the azimuthal seismic anisotropy analysis with PS-wave data with numerical modelling and a real 3D3C dataset. Numerical results reveal that, through the amplitudes and interval travel-time of P-wave can be used to infer fracture information through ellipse fitting, there are limits on usable offset ranges. The R-component of PS-wave can also be used for fracture characterization through elliptical fitting. The only difference is that the long axis of ellipse fitted with the amplitudes of P-wave is in fracture strike direction while the long axis of ellipse from R-component of PS-wave indicates fracture normal direction. The modelling results also show that there are limits for usable offset ranges on azimuthal PS wave data attributes analysis (e.g. for amplitude attribute, the offset-depth ratio should be within 0.6-1.0).

The fracture characterization results from the 3D3C dataset acquired on a fractured reservoir agree with that from geological and logging analysis, demonstrate the applicability of using azimuthal PS-wave data analysis for fracture characterization.

Acknowledgements

We thank Shengli Oilfield for permission to show the real data. This work is supported by the SinoPec international collaboration programme and Shengli Oilfield Ltd. through the Edinburgh Anisotropy Project (EAP) of the British Geological Survey (BGS), and is published with the approval of all project partners and the Executive Director of BGS.

References

Chapman, M., 2003. Frequency-dependent anisotropy due to meso-scale fractures in the presence of equant porosity. Geophysical Prospecting, 51, 369-379.
Hudson, J.A., 1981. Wave speeds and attenuation of elastic waves in material containing cracks. Geophysical Journal of the Royal Astronomical Society, 64, 133-150.
Liu, E., Hudson, J. A. and Pointer, T., 2000, Equivalent medium representation of fractured rock, J. Geophys. Res., 105, No.B2, 2981-3000.
Qian, Z., Li, X.-Y. and Chapman, M., 2007. Effects of oil-water saturation on shear-wave splitting in multicomponent seismic data, 77th Ann. Internat. Mtg.: Soc. Of Expl. Geophys.
Wang, Li, X.-Y., Qian, Z., Di, B. and Wei, J. 2007. Physical modeling studies of 3-D P-wave seismic for fracture detection. Geophys. J. Int., 168, 745-756.

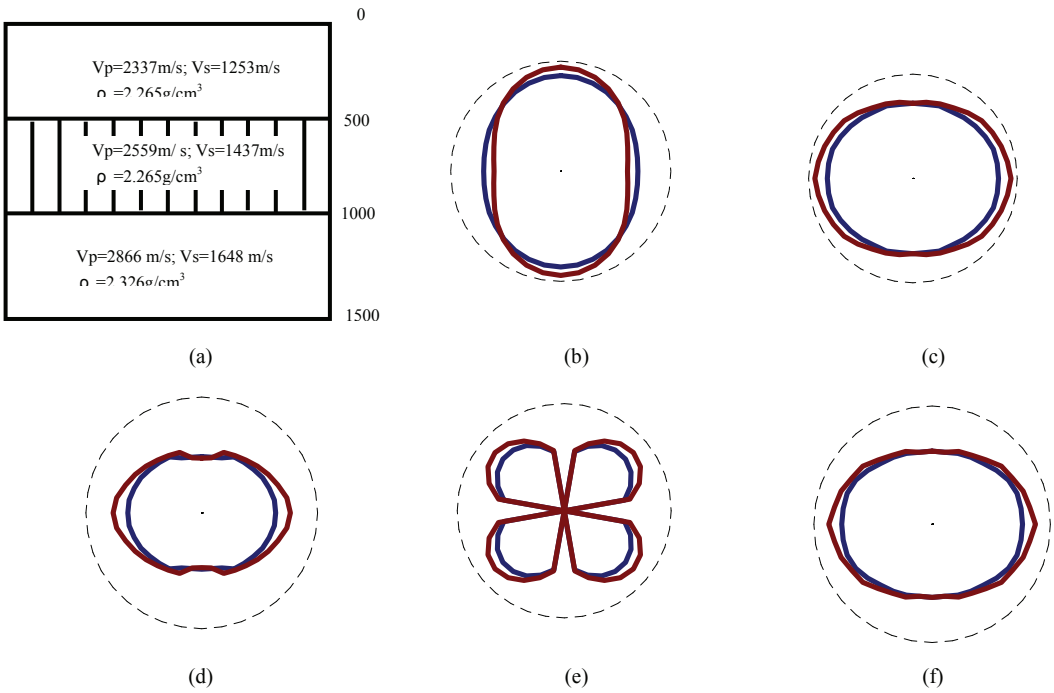

Figure 1 Numerical modelling for azimuthal P- and PS-waves.
(a) numerical model; (b) azimuthal P-wave amplitudes; (c) azimuthal P-wave interval travel-time; (d) azimuthal R-component amplitudes; (e) azimuthal T-components amplitudes; (f) azimuthal R-component interval travel-time. The Colours represent different fracture densities: the blue curve denotes fracture density of 10% and the red curve denotes the fracture density of 18%.

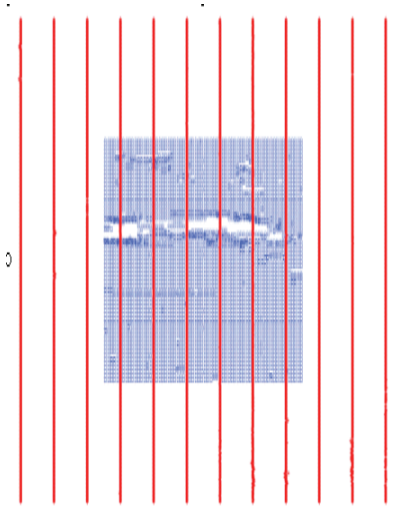

Figure 2 3D3C acquisition deployment.

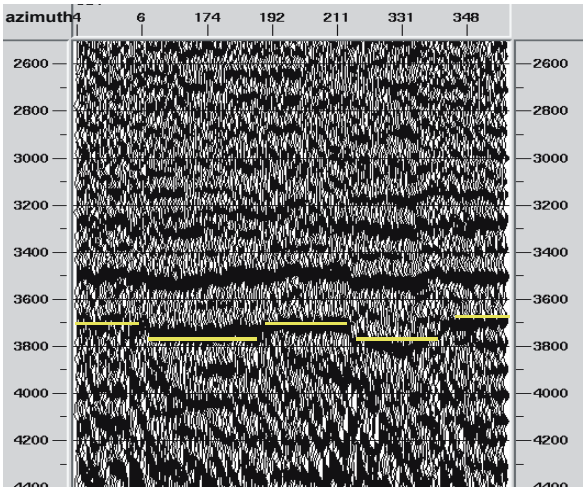

Figure 3 A CCP supergather in azimuth sequence.

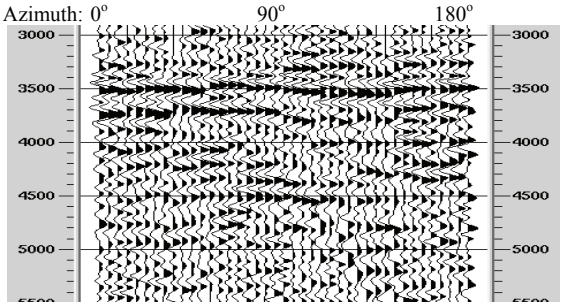

(a) R-component

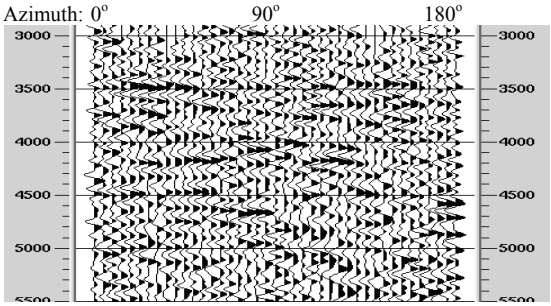

(b) T-component

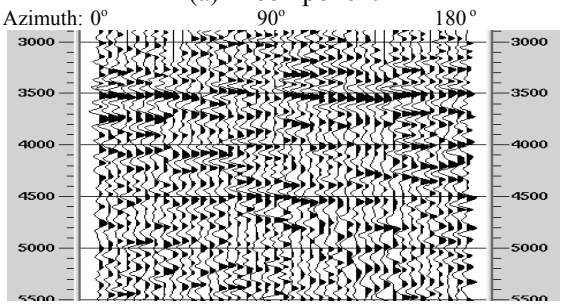

(c) Fast shear wave

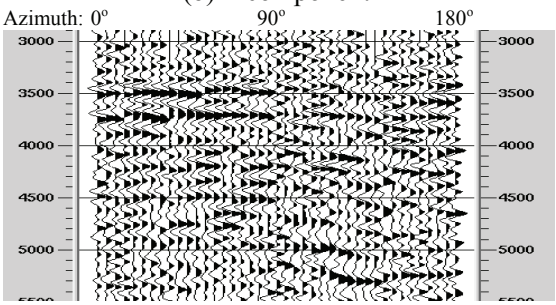

(d) Slow shear wave

Figure 4 Rotation of R- and T-component to fast and slow shear wave (CCP gather).

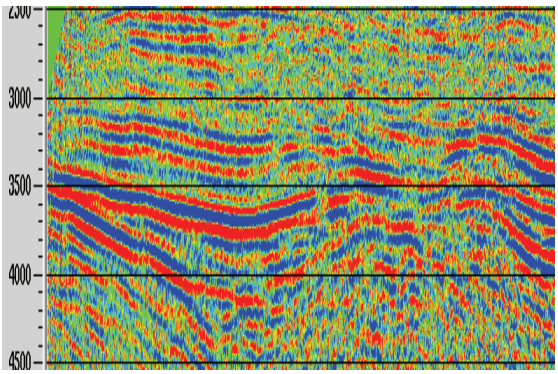

(a) Fast PS-wave

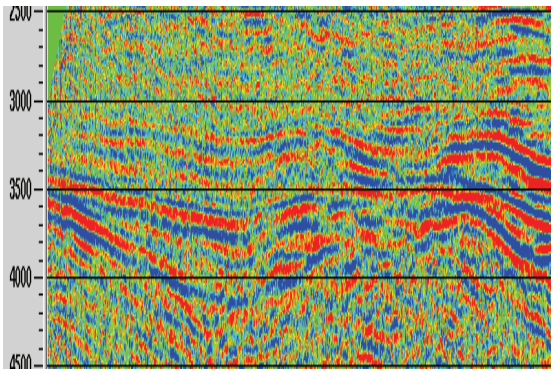

(b) Slow PS-wave

Figure 5 Stacks (target zone) of fast and slow shear wave.

Azimuthal variations of PP- and PS-wave attributes: a synthetic study

Zhongping Qian, Xiang-Yang Li and Mark Chapman, Edinburgh Anisotropy Project, British Geological Survey*

Summary

We present an azimuthal anisotropy analysis with synthetic wide azimuth multi-component data in the presence of vertically aligned fractures. The analysis of azimuthal P-wave amplitudes reveals that, though the data of near offset are suitable for elliptical anisotropy analysis, the data of very small offset do not show significant azimuthal variations, and the optimal data suitable for ellipse fitting may be limited to the those with offset-depth ratios of between 0.3 and 1.0. Azimuthal interval travel-time analysis is more suitable for data with large offset, because big azimuthal interval travel-time variations can only develop in data with large offset. Both amplitudes and interval travel-time of radial component of PS-wave may also be used to obtain fracture information through elliptical anisotropy analysis. The azimuthal amplitude variations of radial component of PS-wave show clearer elliptical distribution than that of P-wave, and the long axis of fitted ellipse indicates fracture normal. The overall offset range of PS-wave data suitable for azimuthal amplitude analysis is wider than that of P-wave. The azimuthal interval travel-time of radial component displays more obvious elliptical distribution than that of P-wave.

Introduction

The use of seismic anisotropy to characterize natural fractured reservoirs started in the 1980's, and the underlying physics for this technology comes from the equivalent medium theory for seismic wave propagation in fractured media, which has been intensively studied by many authors (e.g. Hudson, 1981; Liu et al, 2000) According to these theories, a medium containing vertically aligned fractures with scale length much less than the wavelength can be modelled by an equivalent azimuthally anisotropic medium for seismic wave propagation. Numerical modelling based on the equivalent medium theories reveals that azimuthal variations in P-wave amplitudes and travel-time can be used to characterise fractured medium and this has become standard practice. It is widely believed that in this practice a good azimuth-offset distribution is essential. A 3D physical modelling example of azimuthal P-wave analysis reveals that different data attributes may require different offset distribution to obtain optimal results (Wang et al, 2007).

Shear-wave splitting can be an effective way to obtain fracture information (Li, 1997). Yet, with the development of data acquisition techniques, more and more 3D multi-component data with wide azimuth-offset distribution have become available, which provide not only wide azimuth P-wave data, but also wide azimuth PS-wave data. Do the attributes of PS-waves also show elliptical distribution with azimuth just like that we have seen in azimuthal P-wave analysis and can be used to infer fracture information? If so, it will provide additional opportunities to obtain fracture information and the reliability of final fracture characterisation results will be improved when we do a combined azimuthal analysis with azimuthal P-wave and PS-wave data.

Model and synthetic data

The model we used to generate synthetic multi-component data is shown in Figure 1a, which is a simple three-layer model so that we can get the answers more directly. The top layer of the model is isotropic, and the middle layer is a

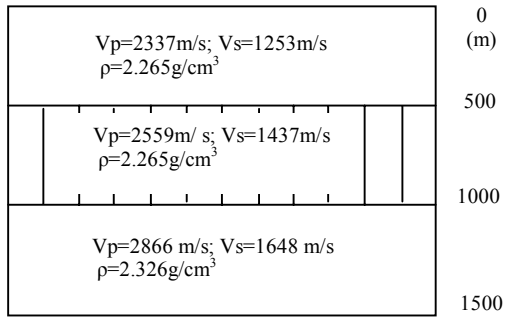

(a)

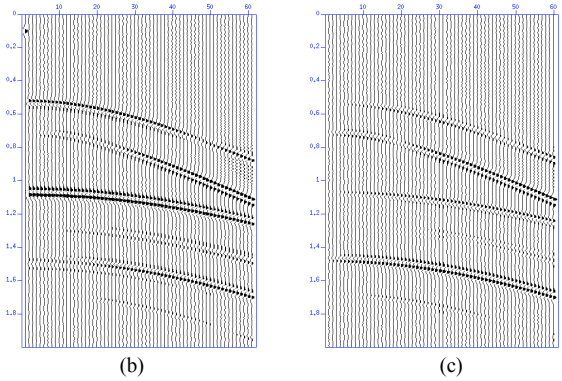

(b) (c)

Figure 1: Model and synthetic data in source gather.
(a) model; (b) P-wave; (c) Radial component of PS-waves.

simulated HTI media with vertical aligned fractures in an isotropic medium. The fractures are simulated with aligned cracks of penny shape in planar distribution (Liu et al, 2000), and the aspect ratio and radius are 0.01 and 0.1, respectively. In order to study the efforts of fracture density in azimuthal seismic response, the fracture density is assigned with 0.1 and 0.18 separately. The azimuth of fracture strike in the layer is 0^o. The material in cracks is assumed to be fluid with P-wave velocity of 1200m/s and density of $0.95g/cm^3$. The bottom layer is an isotropic medium.

Figure 1b and 1c show a synthetic data example based on the model. Notice the first trace in Figure 1b denotes the source wavelet. The offsets of the data range from 25m to 1500m, indicating the straight ray-path incident angles ranging from 0^o to 37^o for the reflections at the bottom of the fracture layer. Since the ray-paths normally are not straight in practice, it will be easier for us to use offset-depth ratio to represent incident angle. The azimuth of the synthetic data ranges from 0^o to 360^o and the azimuth sampling interval is 10^o.

Effects of offset coverage on P-wave

Though the P-wave amplitudes of near offset may be used for elliptical anisotropy analysis, how to choose appropriate offset still remains not so clear. Figure 2a shows the azimuthal variations of P-wave amplitudes at the top of the fracture layer with different offsets. It is obvious that only the amplitudes with offset-depth ratio less than 1.0 are suitable for ellipse fitting. When offset-depth ratio is bigger than 1.0, the fitted ellipses may give contradictory information. However, it also shows that the ellipse fitted with amplitudes of very small offset (e.g., offset-depth ratio is 0.2) is quite close to a circle, which means the azimuthal amplitude variations at small offsets are very small. In real data analysis, where noise problem is often involved, the azimuthal amplitude variations at very small offset will become even more ambiguous. In this case, the optimal offset-depth ratio for ellipse fitting with amplitudes is between 0.6 and 1.0. The long axes of fitted ellipses indicate fracture strike.

When interval travel-time is used for ellipse fitting, the effect of offset coverage is the opposite. Azimuthal variations of interval travel-time can only be observed in data with sufficiently large offset. If the offset-depth ratio is less than 1.0 in this model (Figure 3a), the azimuthal variations of travel-time are almost ignorable.

Figure 4 and Figure 5 show that, for a fixed offset, the ratio of long axis to short axis of the ellipse fitted with P-wave amplitudes (Figure 4d, 4e, 4f) or travel-time (Figure 5d, 5e, 5f) may be used to infer fracture density. However, the value of axis ratio may vary with offset (Figure 2, Figure 3) and need to be calibrated when a wide range of offsets are applied to estimate fracture density.

Elliptical analysis of PS-waves

Figure 2b shows that azimuthal amplitudes of radial component of PS-wave at the top of the fractured layer also display elliptical distribution with azimuth, which is similar to the behaviors of azimuthal P-wave amplitudes. For the same offset, the amplitudes of radial component vary more dramatically with azimuth than those of the P-wave, and the data suitable for ellipse fitting are those with offset-depth ratio ranging from 0.1 to 2.0, which means more offsets of radial component data can be included for elliptical anisotropy analysis compared to the P-wave data. In contrast to the results from P-wave data where the long axes of ellipses fitted with azimuthal amplitudes indicate fracture strike for this model, the long axes of the ellipses fitted with the amplitudes of radial component indicate fracture normal.

Figure 2c shows the azimuthal amplitude variations of the transverse component of the PS-wave data and the variations reveal zero-crossings and polarity reversals, which can also be used to infer fracture information (Li, 1998).

Figure 3b reveals that the interval travel-time of radial component of the PS-wave data within the fracture layer displays elliptical distribution with azimuth and the long axis of the ellipse indicates fracture normal, which is consistent with that from azimuthal P-wave analysis. It also requires sufficiently large offset to allow azimuthal variations of interval travel-time to develop significantly.

At a fixed offset, the ratio of long axis to short axis of the ellipse fitted with amplitudes (Figure 4a, 4b, 4c) or interval travel-time (Figure 5a, 5b, 5c) may increase with fracture density, which means the value of the axis ratio may be used to infer fracture density.

Discussion and Conclusions

We have carried out an azimuthal anisotropy analysis with the synthetic multi-component data. The azimuthal amplitude analysis of P-wave data reveals that the data suitable for elliptical anisotropy analysis are limited to those with offset-depth ratio of between 0.3 and 1.0. Thus, when we apply P-wave amplitudes for elliptical anisotropy analysis, we should focus on the data within this offset range. Since significant azimuthal interval travel-time variations only develop in the data with offset-depth ratio larger than 1.0, we may need to pay more attention to the

far-offset data when we use interval travel-time for elliptical anisotropy analysis.

The analysis of azimuthal PS-wave data reveals that both the amplitudes and interval travel-time of radial component can be used to infer fracture information through ellipse fitting. The azimuthal amplitudes of the radial component of PS-waves at the top of fracture layer display clearer elliptical variations than that of the P-wave and the offset range suitable for azimuthal amplitude analysis is also larger. The long axis of ellipse fitted with the amplitudes of radial component indicates fracture normal for this model. The azimuthal interval travel-time of radial component of PS-waves also displays elliptical distribution and may be used to infer fracture information through elliptical anisotropy analysis.

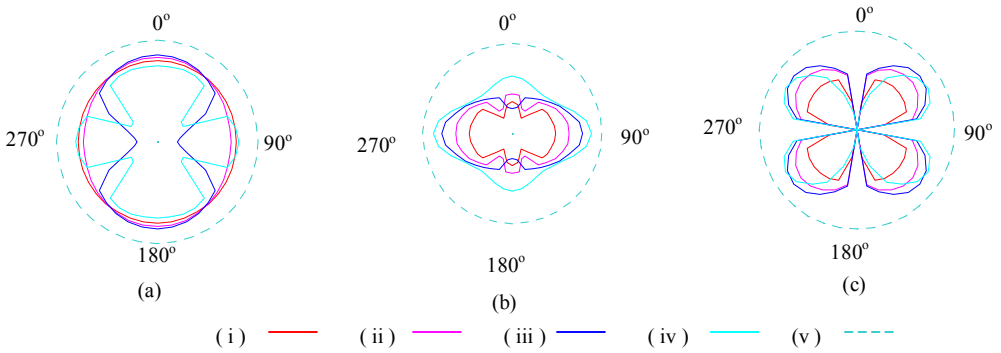

Figure 2: Azimuthal amplitude variations at the top of the fractured layer.
(a) P-wave; (b) R-component (PS-waves); (c) T-component (PS waves). The color curves (i) to (iv) represent offset-depth ratios of 0.2, 0.6, 1.0, 2.0, respectively. The curve (v) represents reference circle.

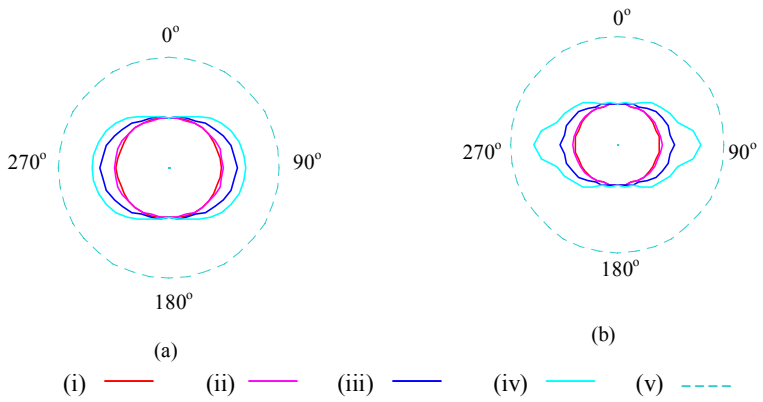

Figure 3: Azimuthal travel-time variations at the bottom of the fractured layer.
(a) P-wave; (b) R-component (PS-waves). The color curves (i) to (iv) represent the offset-depth ratios of 0.3, 0.5, 1.0, 1.5, respectively. The color curve (v) represents reference circle.

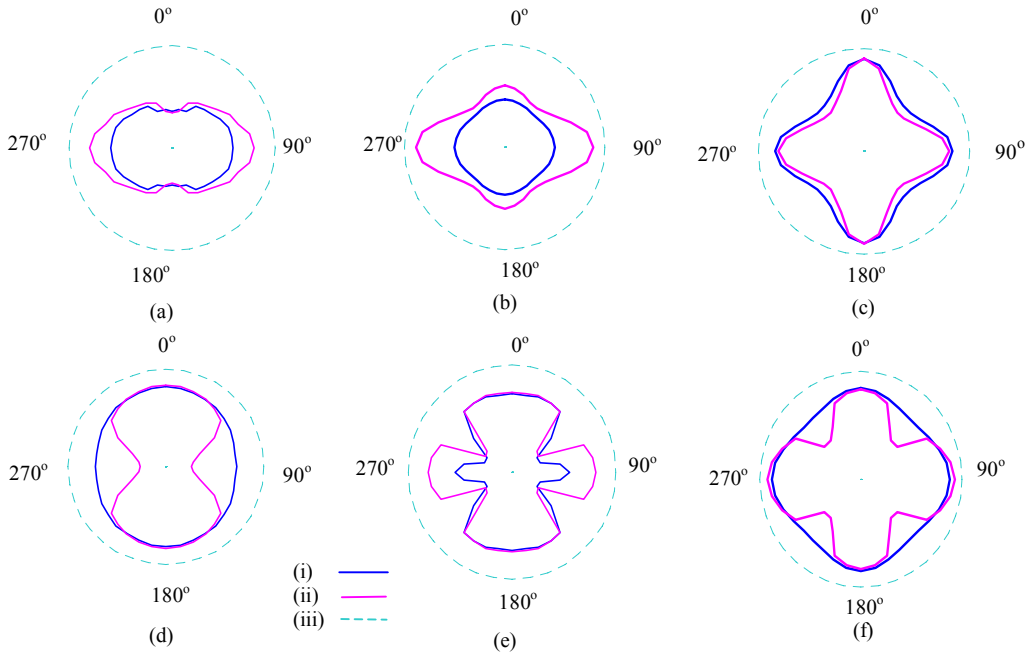

Figure 4: Azimuthal variations of amplitudes at the top of the fractured layer, with different fracture densities. (a), (b) and (c) are from PS-waves (R-compnent), with the offset to depth ratios of 1.0, 2.0 and 3.0, respectively; (d), (e) and (f) are from P-wave. (i) and (ii) represent fracture densities of 0.1 and 0.18, and (iii) represents reference circle.

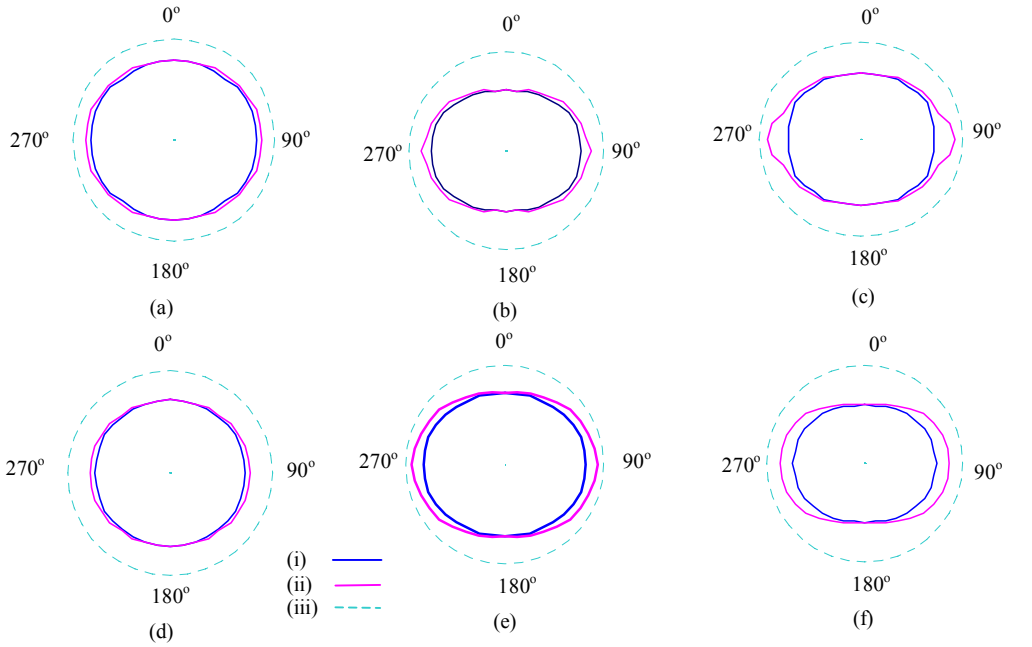

Figure 5: Azimuthal variations of travel-time at the bottom of the fractured layer, with different fracture densities. (a), (b) and (c) are from PS-waves (R-compnent), with offset to depth ratios of 0.5, 1.0 and 1.5, respectively; (d), (e) and (f) are from P-wave. (i) and (ii) represent fracture densities of 0.1 and 0.18, and (iii) represents reference circle.

EDITED REFERENCES

Note: This reference list is a copy-edited version of the reference list submitted by the author. Reference lists for the 2007 SEG Technical Program Expanded Abstracts have been copy edited so that references provided with the online metadata for each paper will achieve a high degree of linking to cited sources that appear on the Web.

REFERENCES

Hudson, J. A., 1981, Wave speeds and attenuation of elastic waves in material containing cracks: Geophysical Journal of the Royal Astronomical Society, 64, 133–150.

Li, X.-Y., 1997, Fractural reservoir delineating using multicomponent seismic data: Geophysical Prospecting, 54, 39–64.

———, 1998, Processing PP and PS waves in multicomponent sea-floor data for azimuthal anisotropy: theory and overview, Procedding of the Eighth International Workshop on seismic Anisotropy (Revue De L'institut francia du petrole), 53, 607-620.

Liu, E., J. A. Hudson, and T. Pointer, 2000, Equivalent medium representation of fractured rock: Journal of Geophysical Research, 105, 2981–3000.

Wang, S., X-Y. Li, Z. Qian, B. Di, and J. Wei, 2007, Physical modeling studies of 3-D P-wave seismic for fracture detection: Geophysical Journal International, 168, 745–756.

Effects of oil-water saturation on shear-wave splitting in multicomponent seismic data

Zhongping Qian, Xiang-Yang Li and Mark Chapman, British Geological Survey; Yonggang Zhang and Yanguang Wang, SinoPec Corporation*

Summary

Understanding saturation changes is important in mature reservoirs. Here we analyze shear-wave splitting in a 3D3C onshore survey from Shengli Oilfield, China, where the thin sand-reservoir has been undergone production through water-flooding which altered the fluid composition and the pore-fluid pressure. Dividing the data into orthogonal azimuthal sectors and processing each sector separately reveals significant shear-wave splitting. The amount of shear-wave splitting can be correlated with the degree of water saturation. Furthermore, the slow shear-wave component shows amplitude dimming in water-flooded areas, whereas the zone of original oil in place shows only weak shear-wave splitting. Rock physics modeling based on the evolution of microcracked rocks and anisotropic fluid substitution incorporating both saturation and pressure changes confirm the observations. The saturation changes have little effect on the P and the fast shear-wave as confirmed by core analysis in the laboratory. However, the substitution of water for oil changes the fluid viscosity that has a strong effect on the slow (quasi) shear-wave. These observations reveal the potential of using shear-wave splitting for oil-water discrimination.

Introduction

Discriminating oil from water is one of the most challenging problems in exploration geophysics. This is because the effects of oil and water saturation on pure P- and shear-wave are very similar, and the impedance variation is very small. As a result, traditional seismic methods based on wave propagation in isotropic media have not been very successful. In this paper we present an example of using shear-wave splitting for such a purpose in a 3D3C onshore survey from the Ken 71 area in the Shengli Oilfield, China.

The Ken-71 reservoir consists of mainly thin sands buried in a sand-shale sequence at depths from 1 to 2 km. The average sand thickness is only about 5-8m and average porosity is between 20-30%. The reservoir has been undergone production through water-flooding, which altered the fluid composition and the pore-fluid pressure. According to Chapman et al. (2003), if the reservoir contains fluid-filled micro-cracks and meso-scale heterogeneities, anisotropic fluid substitution predicts a strong effect on the slow shear-wave between water and oil saturation due to the change in fluid viscosity. Furthermore, the change in pore-fluid pressure will also cause the compliant cracks to open and close dynamically and hence modify the effective elastic constants of the fluid-filled rock, further enhancing shear-wave splitting (Zatsepin and Crampin, 1997). Consequently, we may use shear-wave splitting to monitor changes in the reservoir due to changes in the fluid saturation and stress field induced by the production process.

The Ken-71 study area

The Ken 71 area is only about 20 km^2 and located at the Yellow River delta besides the Bohai Sea. The area is relatively flat, and the reservoir is a gentle anticline with heavy faulting (Figure 1). Average oil column is 26m with area coverage of 4 km^2, and the estimated total oil reserve is about 13 million tons. The reservoir was discovered in 1978 and oil production started in 1981 with water flooding followed in 1988. Up to July 2005, cumulative oil production reached 49.2 million tons and cumulative water production 43.7 million tons. Overall water content reached as high as 95%. Since the average recovery rate is about 40% in this area, 60% residual oil will still be left in place. In 2005, an integrated programme of reservoir geophysics was implemented, aiming to characterize the by-passed oil in the area, including the acquisition of high resolution 3D3C seismic data, together with cores, logs, 3D VSPs, and crosswell seismic (Figure 1).

Digital MEMS (micro-electro-mechanical system) sensors were used to improve data quality for the acquisition of the 3D3C data, and more details can be found in Qian et al. (2007).

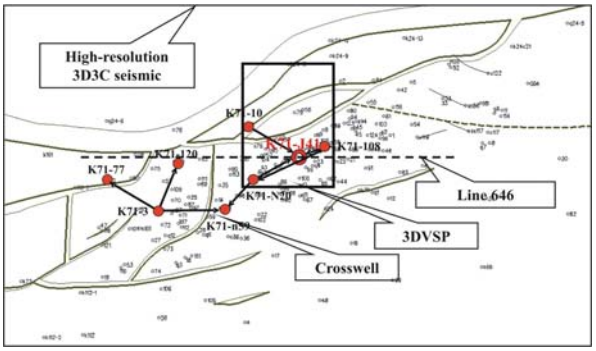

Figure 1. The Ken-71 study area and various datasets including 3D VSPs, crosswell seismic and core data at well J-41.

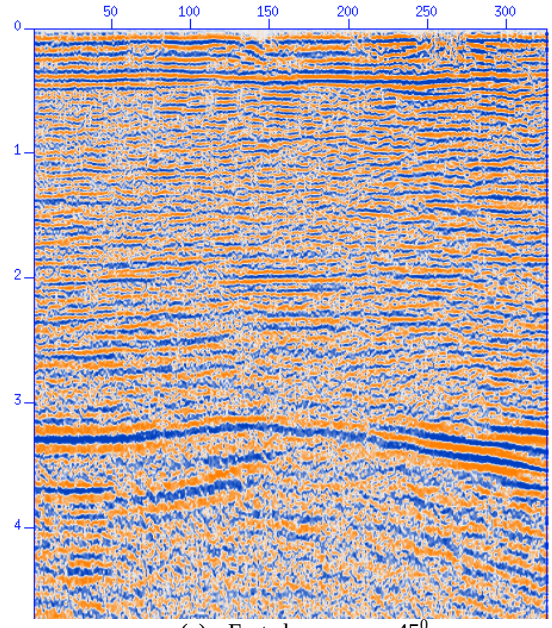

(a) Fast shear-wave: 45^0

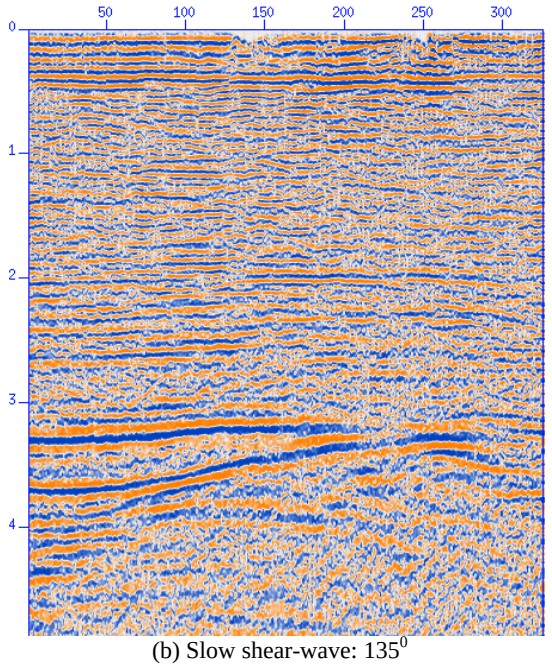

(b) Slow shear-wave: 135^0

Figure 2. The fast and slow shear-wave along Line 646 in Figure 1 extracted from the 3D volume. (a) The fast section is from azimuthal sector N45°E, and (b) the slow section from sector N135°E.

Data processing

The main challenge is to create high-resolution shear-wave data with maximum preservation of shear-wave splitting. The added complication in this case is the asymmetric raypath of the converted-wave as well as the presence of vertical transverse isotropy (VTI) in the background sand-shale sequence, which gives rise to strong non-hyperbolic moveout in the prestack data. Therefore, successful anisotropic processing not only needs to preserve shear-wave splitting, but also account for the non-hyperbolic effects. In order to do this, we design the following two-stage work flow.

The first stage aims to determine the principal coordinate system, or the directions of the fast and slow split shear-wave. The main steps in this stage include coordinate rotation, noise reduction, statics and azimuthal analysis of the transverse component data. At the very beginning, the data are rotated into the Radial and Transverse components from the field coordinate system. After noise and statics, azimuthal analysis of the transverse component may then be used to determine the principal coordinate system based on polarity reversal (Li, 1998). 2D lines of radial and transverse component data may also be extracted from the 3D volume to perform shear-wave splitting analysis. At this stage, the VTI effects are ignored. For this data, the fast direction is identified as N40°E, which is in agreement with the main structural alignment of the area (Figure 1).

The second stage aims to account for the VTI effects and asymmetric raypath whilst also preserving shear-wave splitting. This is usually achieved by dividing the 3D data into different azimuthal sectors and then processing each azimuthal sector separately using a processing flow incorporating both the effects of VTI and the asymmetric raypath (Li and Yuan 2003). Here, the data are divided into two orthogonal azimuthal sectors (45 degrees and 135 degrees). The details of the processing flow in the presence of VTI can be found in Qian et al. (2007). High quality fast and slow shear-wave volumes are obtained (Figure 2).

Data analysis and results

We first analyze the time delay between the fast and slow shear-waves. A short time-window correlation method is used to create time-delay spectra (Figure 3), from which the time-delay attribute can be obtained. Figure 4 shows a time-delay gradient section (Line 646) intersecting well J-41. The variation of shear-wave splitting is about 5%, and it can be correlated with the degree of water saturation at the well position (Figure 4). Furthermore, the slow shear-wave component shows amplitude dimming in the water-flooded

areas, whereas the zone of original oil in place appears to show weak shear-wave splitting (Figure 5). In contrast, the P-wave sections at the corresponding azimuthal sectors show little changes (Figure 6). Horizontal amplitude slices of the slow shear-wave at the corresponding oil and water formations show clear amplitude anomalies associated with oil and water saturation (Figure 7).

The above observed correlation of shear-wave splitting with saturation can be modeled using anisotropic fluid substitution as proposed by Chapman et al. (2003) incorporating the pore pressure effects based on the evolution of microcracked rocks in Zatsepin and Crampin (1997). The effects of saturation on the P and the fast shear-wave velocity is very small (less than 1%), as revealed by the modeling (Figure 8a) and confirmed by core analysis in the laboratory. However, the substitution of water for oil changes the fluid viscosity which induces a change in the slow (quasi) shear-wave velocity as high as 4% (Figure 8b), hence leading to a significant increase in shear-wave splitting for the water saturation case, as compared with the oil case (Figure 8c). Moreover, the fluid substitution due to water flooding also changes the pore-fluid pressures, thus modifying the crack aspect ratios and further enhancing shear-wave splitting. The driving mechanism for the model is fluid migration by flow or dispersion along pressure gradients between cracks at different scale lengths.

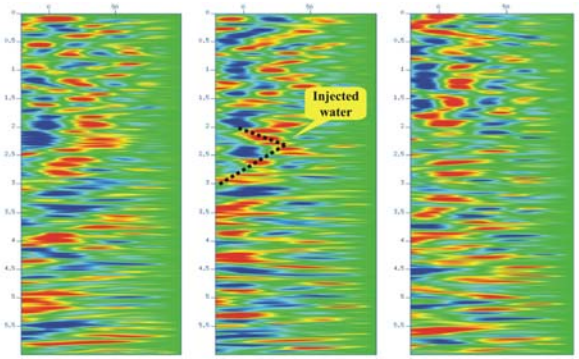

(a) CDP 820 (b) CDP 832 (c) CDP 850

Figure 3. Time-delay spectra of selected CDPs in Figure 3, Line 646. CDP 832 is at well J-41.

Discussion and conclusions

Understanding pore-pressure and saturation changes is important in mature reservoirs. It has been observed that shear-wave splitting is very sensitive to pore-pressure change and is the principal seismic diagnostic for the detection of pressure effects (Angerer *et al.* 2002). In this paper, we have shown that shear-wave splitting is also sensitive to oil-water saturation change. We analyzed shear-wave splitting in a 3D3C onshore survey from Shengli Oilfield, China, and we observed strong correlation between shear-wave splitting and water saturation, and this confirms the potential of using shear-wave splitting for oil-water discrimination.

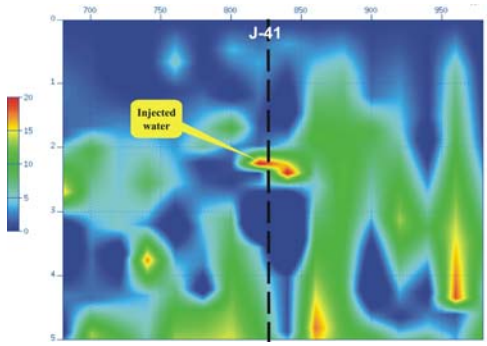

Figure 4. Time-delay gradient section of Line 646 picked from Figure 3.

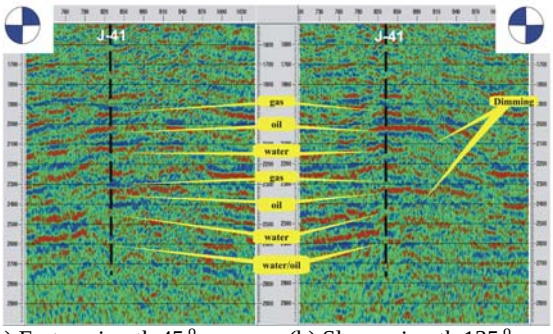

(a) Fast –azimuth 45 ^{o} (b) Slow-azimuth 135 ^{o}

Figure 5. Comparison of the fast and slow-wave amplitudes at well J-41, noting the dimming spots at the slow section corresponding to the water layers.

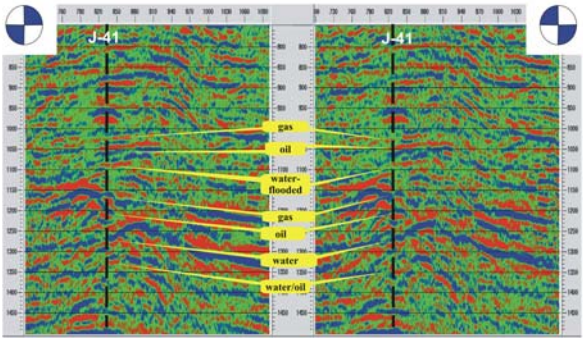

(a) Fast –azimuth 45 ^{o} (b) Slow-azimuth 135 ^{o}

Figure 6. Comparison of the P-waves from the two azimuthal sectors at well J-41, and there is no significant difference between the two sections.

Acknowledgements

We thank SinoPec Shengli Oilfield for permission to show the data. The Shengli data are processed by Zhongping Qian and Haizheng Zhao of EAP, and Lifei Bi and Jianxin Shi of SinoPec. This work is supported by the SinoPec international collaboration programme and SinoPec Shengli Oilfield Ltd. through the Edinburgh Anisotropy Project (EAP) of the British Geological Survey (BGS), and is published with the approval of all project partners and the Executive Director of BGS.

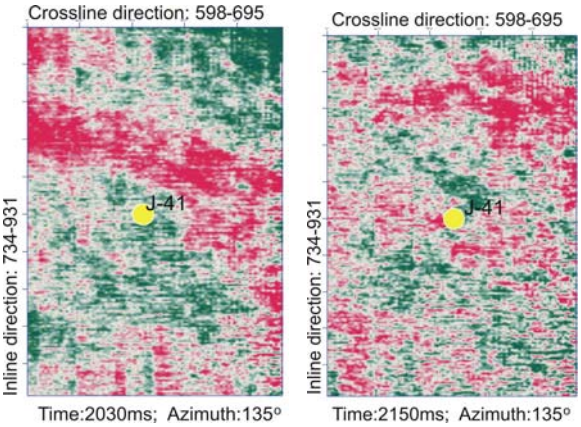

Figure 7. Horizontal amplitude slices of the slow wave at azimuth 135 ^{o} for (a) the oil layer at 2.03s and (b) the water-flooded layer at 2.15s. Green indicates oil and red indicates water.

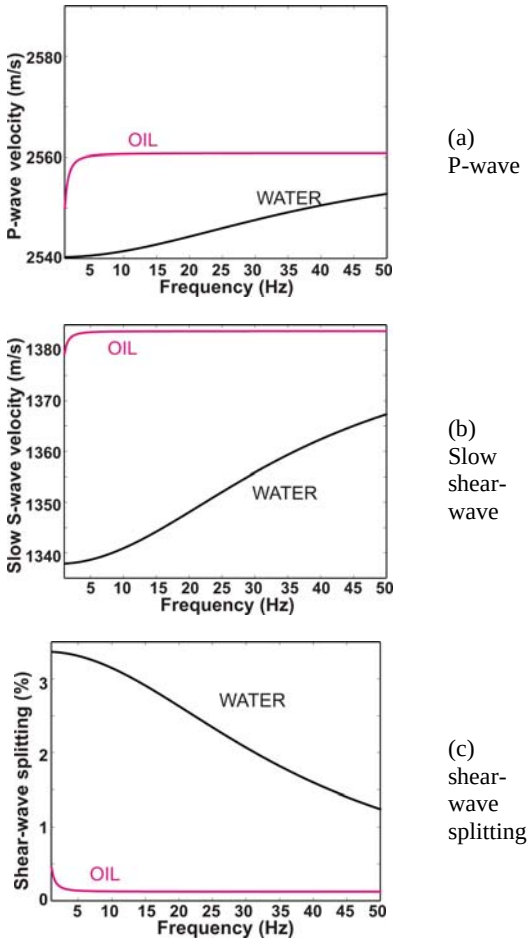

Figure 8. Effects of oil-water saturation for the thin sand at depth 1.5km in the study area, calculated using Chapman et al. (2003).

EDITED REFERENCES

Note: This reference list is a copy-edited version of the reference list submitted by the author. Reference lists for the 2007 SEG Technical Program Expanded Abstracts have been copy edited so that references provided with the online metadata for each paper will achieve a high degree of linking to cited sources that appear on the Web.

REFERENCES

Angerer, E., S. Crampin, X-Y. Li, and T. L. Davis, 2002, Processing, modelling and predicting time-lapse effects of overpressured fluid-injection in a fractured reservoir: Geophysical Journal International, 149, 267–280.

Chapman, M., S. Maultzsch, E. Liu, and X-Y. Li, 2003, The effect of fluid saturation in an anisotropic multi-scale equant porosity model: Journal of Applied Geophysics, 54, 191–202.

Li, X.-Y., 1998, Processing PP and PS waves in multicomponent sea-floor data for azimuthal anisotropy: Theory and overview: Proceedings of the Eighth International Workshop on seismic Anisotropy (Revue De L'institut francia du petrole), 53, 607–620.

Li, X.-Y., and J. Yuan, 2003, Converted-wave moveout and conversion-point equations in layered VTI media: Theory and application: Journal of Applied Geophysics, 54, 297–318.

Qian Z., X-Y. Li, X. Meng, and L. Bi, 2007, Converted-wave velocity analysis in the presence of anisotropy: A case study from Shengli oilfield, China: 77th Annual International Meeting, SEG, Expanded Abstracts, this issue.

Zatsepin, S. V., and S. Crampin, 1997, Modelling the compliance of crustal rock — I. Response of shear-wave splitting to differential stress: Geophysical Journal International, 129, 477–494.

Use of multicomponent seismic data for oil-water discrimination in fractured reservoirs

Zhongping Qian, Mark Chapman, Xiang-Yang Li, Heng-Chang Dai, and Enru Liu, British Geological Survey, Edinburgh, U.K.
Yonggang Zhang and Yanguang Wang, Sinopec, Dongying, China

Geophysicists have devoted great efforts to the problem of determining fluid saturation from seismic measurements, with some notable successes. It is commonly believed that fluid information is to be found in the P-wave data, with shear waves being insensitive to fluid, and indeed almost all successful fluid-detection methodologies have been based on analysis of the P-wave.

Nevertheless, when we deal with fractured reservoirs, we are faced with the phenomenon of seismic anisotropy, and the rock physics relationships relevant to fractured, anisotropic rock are more subtle than those for the more familiar isotropic case. In particular, shear-wave splitting occurs, and this is known to be sensitive to the fracture properties and fluid bulk modulus. It has long been hoped that analysis of shear-wave splitting in multicomponent data would be able to improve our ability to detect fluids.

More recent theoretical advances in the area of frequency-dependent anisotropy have offered a new approach to this problem. These theories allow anisotropic dispersion and attenuation to be related to rock and fluid properties, typically through a fluid mobility parameter, defined as the ratio of permeability to fluid viscosity.

The ability to detect a viscosity effect is of great potential relevance to the problem of oil-water discrimination. Oil and water have similar bulk moduli, and this fact has impeded efforts to tell the two apart from analysis of seismic data. The two fluids have markedly different viscosities, however; so if we can find a robust seismic signature of fluid viscosity, we would greatly improve our chances to discriminate the two fluid saturations.

In this paper, we offer a theoretical analysis of wave propagation in vertically fractured rock which exhibits frequency-dependent anisotropy. For angles of incidence typical of seismic reflection data, we show that the slow shear wave suffers most attenuation and that its properties are most sensitive to fluid viscosity. Further to this, we demonstrate that the converted-wave amplitude in the fracture normal direction can be very sensitive to the fluid, even when the P-wave attributes are insensitive to fluid.

Based on our analysis, we devise a processing strategy which is applied to 3D/3-C data from Shengli oil field in China, which has undergone water flooding. We find amplitude and traveltime anomalies which correlate with known water- and oil-saturated zones, and which are consistent with the effects predicted by our theoretical modeling. We conclude that proper processing and interpretation of multicomponent data can help us to discriminate oil and water saturation in fractured reservoirs.

Theoretical background. We consider fracture distributions in porous rock which are approximately aligned and vertical. Traditional techniques for modeling the elastic properties of such systems use static-equivalent medium theories in the long-wavelength limit. Such theories have many features in common, and the simplest can be shown to be consistent with the notation of Schoenberg and Sayers (1995), in which the "excess compliance" associated with the fracture network can be written in terms of two parameters, Z_N and Z_T, which are the normal and shear compliances, respectively, of the fractures.

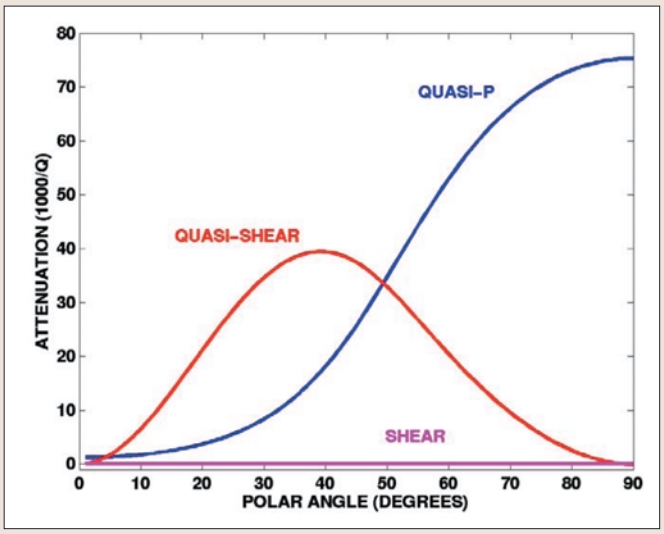

Figure 1. Calculated attenuation for the three wave modes as a function of polar angle (0° is vertical, 90° horizontal) for propagation perpendicular to the fractures.

A typical assumption is that Z_T would be insensitive to fluid whereas Z_N would decrease with increasing fluid-bulk modulus. Theories which assume the cracks are penny-shaped allow explicit computation of Z_N in terms of the fluid properties, either assuming the cracks are fluid-isolated (based on Hudson's theory) or allowing fluid communication with the surrounding rock (following Thomsen's model).

Such theories demonstrate that for near-vertical propagation, shear-wave splitting can vary markedly with fluid saturation. The predicted change in shear-wave splitting arising from a given change in fluid properties varies markedly between the different theories, but the models do predict a consistent trend. Fluids with lower bulk moduli give rise to increased Z_N values, and this tends to lead to an increase in measured shear-wave splitting, for near-vertical propagation. It is the slower quasi-shear wave whose velocity changes with the fluid; the faster wave is a pure shear wave whose velocity is insensitive to fluid bulk modulus in accordance with Gassmann's relation.

More complex theories attempt to predict the anisotropic dispersion and attenuation which is generated by fluid-saturated fracture systems. In these theories a central role is played by the fluid mobility parameter (Batzle et al., 2006):

$$M = \frac{k}{\eta}$$

in which k is the permeability and η is the fluid viscosity. The fluid mobility appears in a "characteristic frequency," which divides the frequency range into broadly three bands: a low-frequency range, a transition band, and a high-frequency range. The low- and high-frequency ranges correspond to the static cases in which we assume fluid-

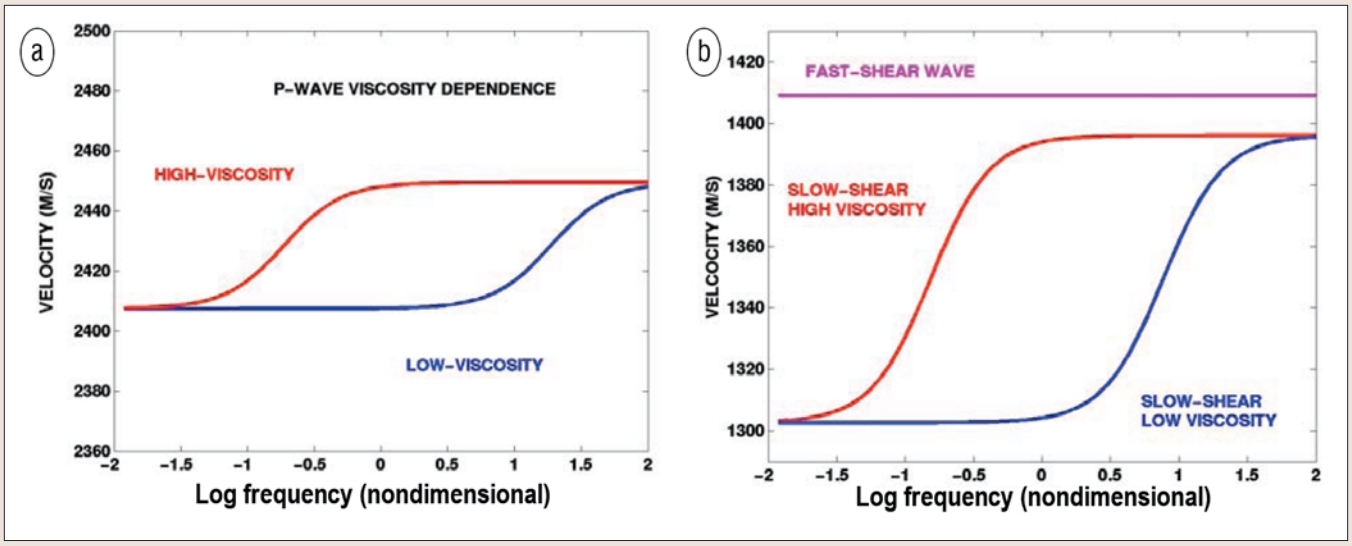

Figure 2. *Velocity as a function of nondimensional frequency for (a) P-wave and (b) fast and slow shear waves, for two different viscosities. Propagation is perpendicular to the fractures, with a polar angle of 30°.*

communicating or fluid-isolated cracks respectively. The behavior in the transition band is rather different, since in this case the velocities change rapidly with frequency and attenuation occurs.

In the case in which we have a single vertical fracture set, theoretical models predict the attenuation should be strongly anisotropic. Waves propagating in the plane of the fractures are predicted to suffer very little attenuation, but in the plane perpendicular to the fractures strong attenuation can take place.

Figure 1 demonstrates typical behavior, assuming propagation perpendicular to the fractures, for all three wave modes as a function of polar angle (see Chapman, 2003, for details of the theory). We set the convention that for a vertical fracture set, a polar angle of 0° corresponds to vertical propagation while 90° is horizontal. The pure shear wave should suffer no fluid-related attenuation, but both the P-wave and quasi-shear wave can be strongly attenuated.

This behavior comes about because the attenuation is assumed to occur because of the relaxation of fluid-pressure gradients between the fractures and the surrounding pore space. The pure shear wave does not compress either the fractures or the pore space and so can create no such attenuation. Both the P-wave and quasi-shear do compress the fractures relative to the pore space and create attenuation. The effect is most pronounced for the P-wave, which suffers the highest absolute attenuation of any of the waves when it propagates at 90°. Nevertheless, the polarizations of the P- and quasi-shear are at right angles to one another, and this means the angle of maximum attenuation differs for the two modes. In particular, while the P-wave has maximum attenuation for horizontal propagation, the maximum quasi-shear attenuation occurs for propagation around 45°.

In reflection seismology, we are typically concerned with angles of incidence between 0 and 45°. A striking conclusion to be drawn from Figure 1 is that for such angles of incidence, the greatest effect of the fracture-related attenuation should be on the quasi-shear wave. Furthermore, for these angles of incidence, the quasi-shear mode is typically the slow shear wave.

The strong attenuation of the slow shear wave has many implications, but in this study we focus on the implications for fluid substitution. For each wave mode and for each

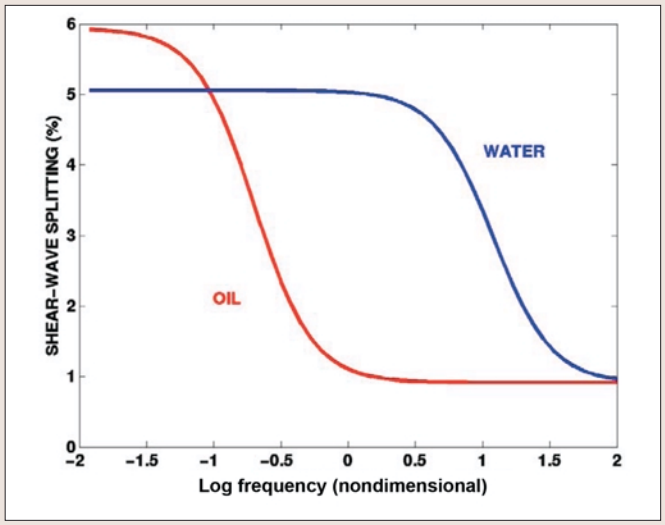

Figure 3. *Predicted values of shear-wave splitting as a function of frequency for oil and water saturation.*

direction of propagation, the behavior is predicted to resemble that of a standard linear solid. In particular, the wave propagation exhibits the Kramers-Kronig relationship between attenuation and dispersion.

Figure 2 shows the predicted velocities as a function of nondimensional frequency corresponding to the model discussed above for all wave modes propagating at 30° from vertical and for two different viscosities. Figure 2a demonstrates the predicted P-wave behavior. The velocities increase with frequency, but the change is modest since there is little attenuation for this direction. When the viscosity is increased, the dispersion curve shifts to lower frequencies, creating a frequency band in which the velocity is sensitive to viscosity. Figure 2b shows the corresponding shear-wave behavior. The faster shear wave is not attenuated, and so its velocity does not depend on viscosity. The slow shear wave suffers more attenuation than the P-wave and this corresponds to a greater frequency dependence of the velocities. This leads to a frequency band in which the slow shear wave is very sensitive to the viscosity.

Substituting one fluid for another involves changing at least the fluid bulk modulus, viscosity, and density. In the

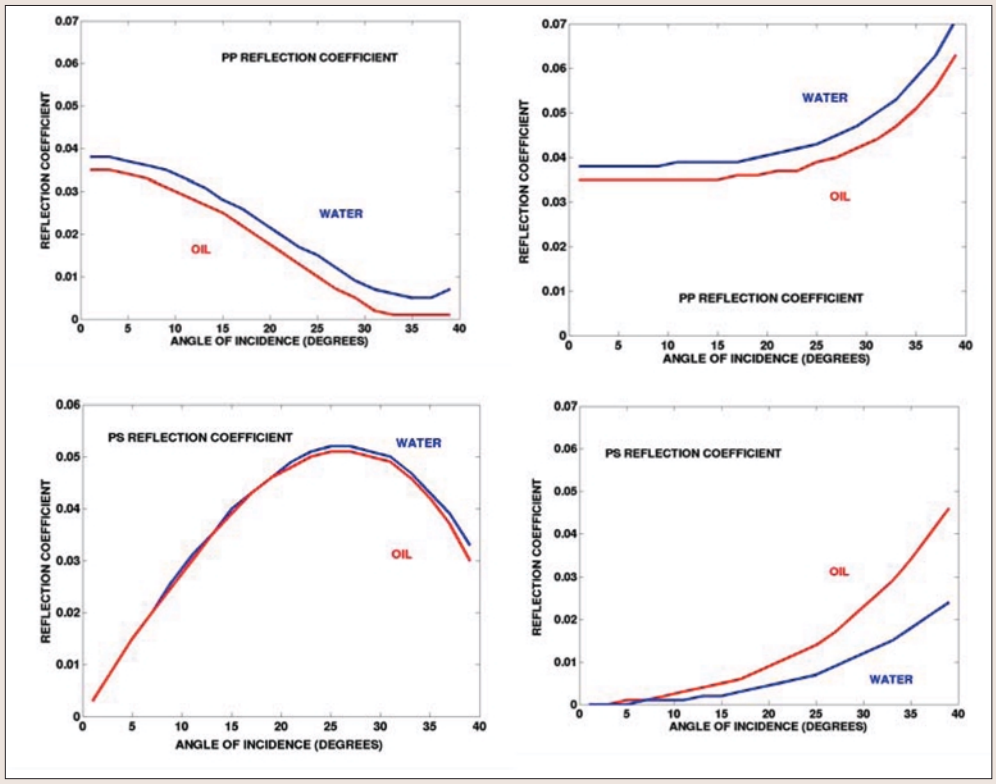

Figure 4. Computed values for the reflection coefficient. Top diagrams are for PP, bottom for PS. Left diagrams are parallel to the fractures, right are perpendicular.

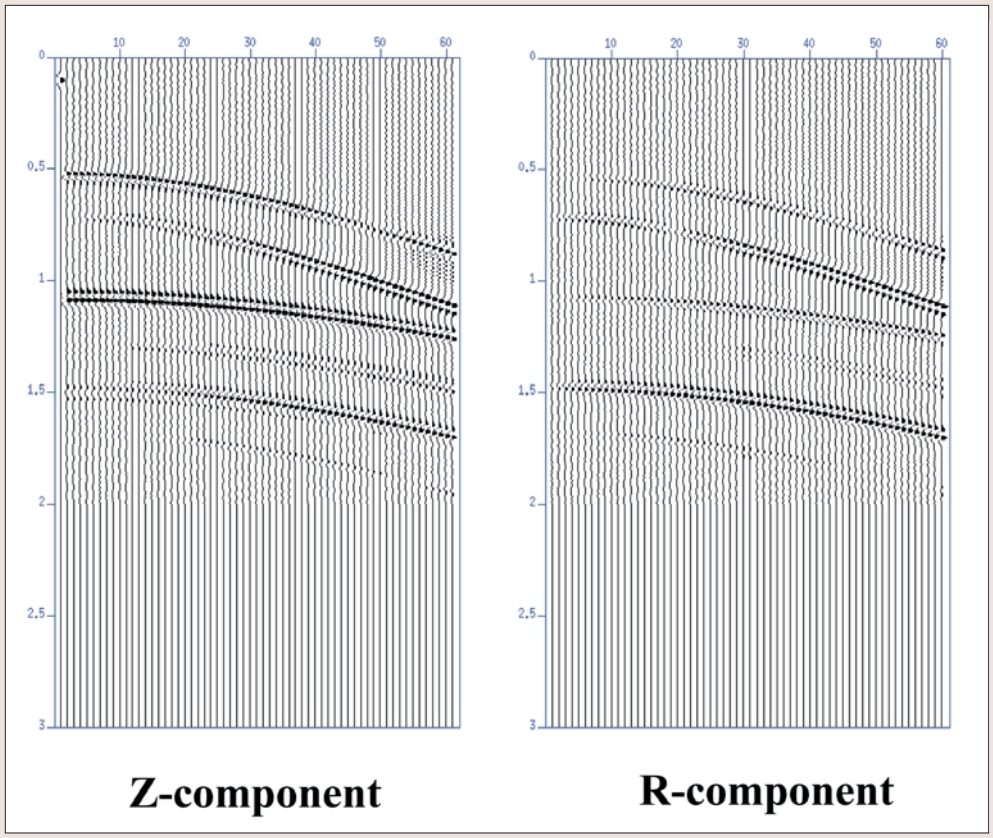

Figure 5. Sample synthetic seismograms, vertical and radial components, for our model of a fractured layer; propagation is parallel to the fractures.

water-to-oil case, the oil typically has a slightly lower bulk modulus and density than the water, but a much larger viscosity. Fluid-substitution theories which ignore the viscosity typically suggest that oil-water discrimination is practically impossible. Since we expect theoretically that the slow shear-wave should be dependent on viscosity in fractured media, it is worth considering whether this effect can be used for oil-water discrimination in fractured reservoirs.

Certainly, shear-wave splitting is sensitive to oil-water substitution in the modeling framework we describe. Figure 3 shows shear-wave splitting as function of frequency for oil and water saturation. In the low-frequency limit, oil saturation gives rise to higher values of shear-wave splitting, since the lower oil bulk modulus makes the fractures more compliant than the water-saturated case. In the high-frequency limit, there is little effect of the fluid for thin cracks, although oil will give higher values of shear-wave splitting if we assume much fatter cracks. Between these cases, we have again a transition zone corresponding to the frequency dependence of the slow shear velocity as shown in Figure 2. We note that within the transition zone, the sensitivity to fluid is greater than, and the direction of the change opposite to, that predicted in either the low- or high-frequency limit.

This behavior has implications for converted-wave reflectivity. We demonstrate this effect with a numerical example, in which the parameters have been taken from velocity logs from Shengli oilfield (the relevant seismic data is discussed below). The model which we consider consists of a high-to-low interface which has an isotropic layer overlying a vertically fractured target. In the general case, an incident P-wave will generate three reflections corresponding to the PP, PS1, and PS2 modes. If we confine ourselves to propagation in the symmetry planes, however (parallel and perpendicular to the fracture strike), only two reflections, PP and PS, will be generated.

Figure 4 shows the PP and PS reflection coefficients for waves propagating parallel and perpendicular to the frac-

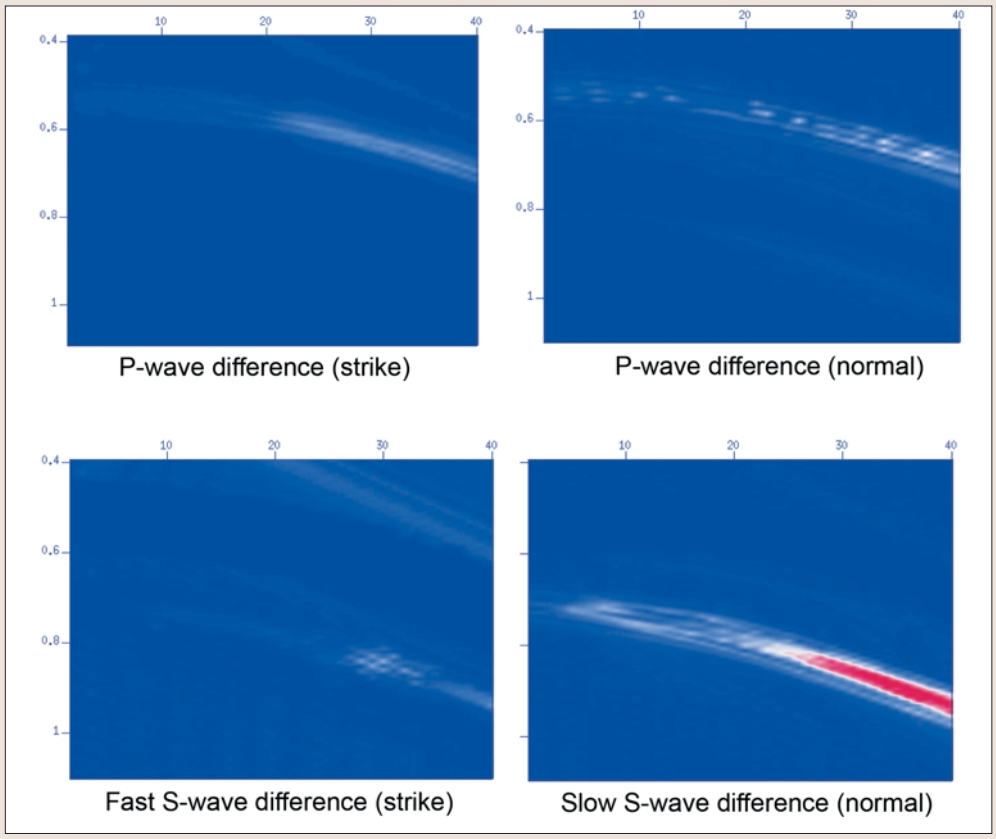

Figure 6. Results of differencing the synthetics calculated for oil saturation from those calculated for water saturation. Top is P-wave; bottom is converted wave. Left diagrams are for propagation in the fracture strike direction; right are in the fracture normal direction. Only the converted wave propagating normal to the fractures shows sensitivity to fluid.

tures, for water and oil saturation. As expected for the PP reflection, there is very little sensitivity to the fluid in either direction. This is because of the low contrast in bulk modulus between oil and water and little viscosity dependence for these angles of incidence; indeed, the bulk modulus and viscosity effects even tend to cancel each other out. Likewise, when we assume propagation parallel to the fracture strike, the PS amplitude is predicted to be insensitive to the saturating fluid. This is not the case for propagation perpendicular to the fracture strike, however. In that case, the PS reflection is sensitive to the saturating fluid. This is because of the effect of the fluid viscosity for shear-wave propagation in that direction.

To further demonstrate the behavior, we calculate synthetic seismograms for a simple single-layer model, with an isotropic layer overlying a fractured layer with horizontal transverse isotropy, where the angle of incidence is taken to be up to 45°. Sample synthetic seismograms are shown in Figure 5.

We find that the converted-wave amplitude is indeed sensitive to the saturating fluid. Figure 6 shows the difference plots for PP and PS reflections parallel and perpendicular to the fractures. A strong anomaly is present for the converted wave traveling perpendicular to the fractures. No anomaly is present for the P-wave in either direction, or for the converted wave parallel to the fractures. To make this effect clear, we pick the amplitudes of the reflections for the different modes and directions (Figure 7). Only for the converted wave traveling perpendicular to the fractures is there fluid dependence of the amplitudes, with water saturation acting to dim the converted-wave amplitude in that case.

Recent observations of frequency-dependent shear-wave splitting in VSP and microseismic data suggest that such effects may be important at seismic frequencies, as is theoretically predicted when we have "meso- scale" fractures, but it remains an open question to demonstrate whether viscosity effects can be detected in seismic data. In the remainder of this paper, we consider a multicomponent data set from Shengli oilfield in China, and argue that such effects can indeed be detected in the data.

Field background and seismic data processing. In this paper, we consider 3D/3-C data from the Ken 71 area of the Shengli oilfield. This zone of 20 km^2 is in the Yellow River delta beside the Bohai Sea. The area is relatively flat, and the reservoir is a gentle anticline with heavy faulting. The reservoir has undergone production through waterflooding, which has altered the fluid composition and pressure.

In 2005, an integrated program of reservoir geophysics was implemented to characterize the bypassed oil in the area. This included the acquisition of high-resolution 3D/3-C data, cores, logs, 3D VSPs, and crosswell seismic. Digital MEMS sensors were used to improve data quality for the acquisition of the 3D/3-C data.

Processing the converted-wave data involved two main challenges: the asymmetric raypath of the converted-wave and the effect of vertical transverse isotropy (VTI) in the background sand-shale sequence, which gives rise to strong nonhyperbolic moveout in the prestack data. To address these problems we designed a two-stage work flow.

In the first stage, we determine the principal coordinate system, or the polarization directions of the fast and slow shear wave. The main steps are coordinate rotation, noise reduction, and statics, followed by azimuthal analysis of the transverse component data. This azimuthal analysis identifies the principal directions by identifying polarity reversals. In this data set, the fast direction was identified as N45E, which was in agreement with the structural alignment of the area.

In the second stage, we account for the VTI effects and asymmetric raypath whilst preserving shear-wave splitting. We achieve this by dividing the data into different azimuthal sectors and then processing each azimuth separately. Using a three-parameter theory which accounts for both the VTI and asymmetric raypath effects (see Li and Yuan, 2003, for details). In this case, the data are divided into two orthogonal sectors (45 and 135°), and high-quality fast and slow shear-wave volumes are obtained.

Data analysis and interpretation. Our analysis of the data has two components. We begin by considering shear-wave splitting through the computation of time-delay gradient sections, before studying the azimuthal variation of the con-

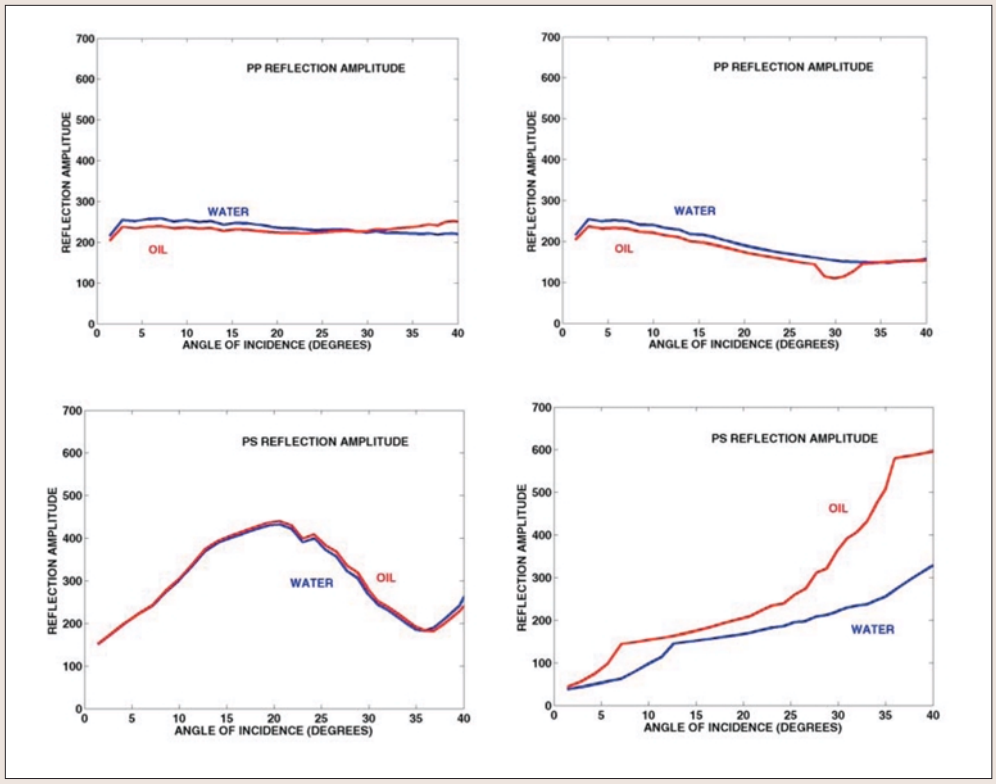

Figure 7. *Picked amplitudes from the synthetic seismograms under oil and water saturation. Top diagrams are P; bottom PS. Left diagrams are for propagation parallel to the fractures; right for propagation in the fracture normal direction.*

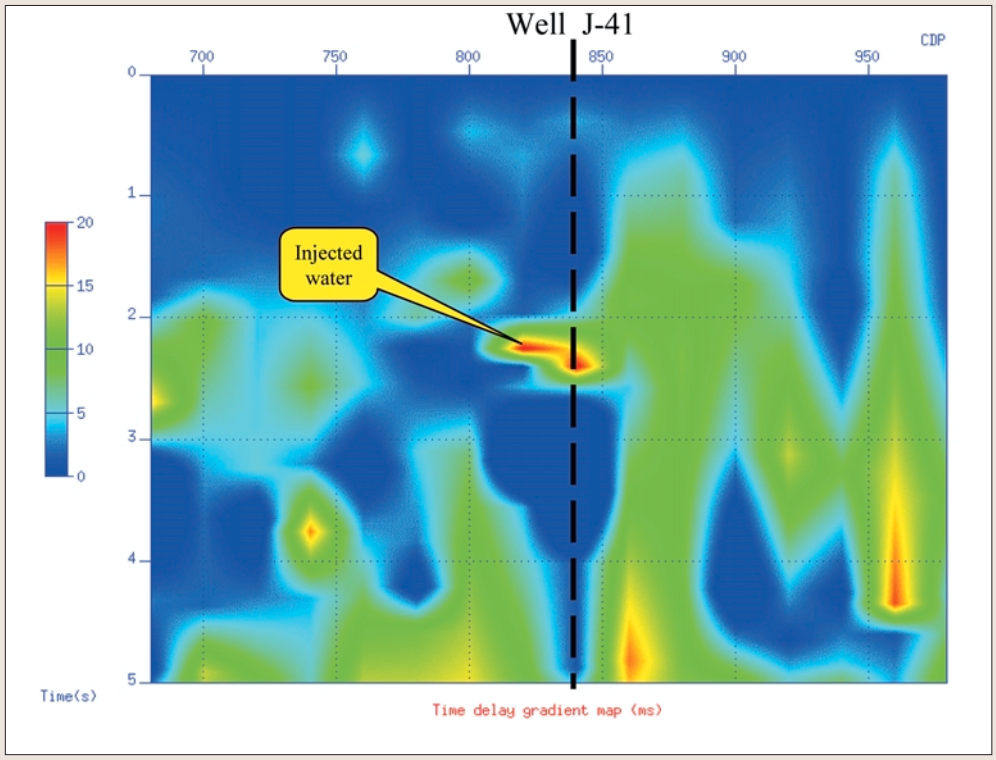

Figure 8. *Time-delay gradient section. The indicated anomaly is the zone at which water injection has taken place.*

verted-wave amplitude.

We used a short time-window correlation method to create time-delay spectra, which can then be differenced to create a time-delay gradient section (Figure 8). A time-delay anomaly is clearly visible around well J-41, where water injection has taken place. In general, we find that water-saturated zones tend to have higher values of shear-wave splitting, whereas zones where the original oil is in place tend to exhibit low values of shear-wave splitting. The difference is rather large, with around an extra 5% shear-wave anisotropy in the water-saturated zones.

Comparison of the PP and PS sections for the fast and slow directions reveals amplitude anomalies for the slow PS section which appear to correlate with fluid saturation. Figure 9 reveals that the P-wave sections from the two directions show little differences, but the amplitude of the slow PS section appears to be dimmer in the water-saturated zones.

We now consider in detail the differences between converted-wave data from two well locations, one known to be in an oil-saturated zone and the other from a water-saturated zone. Figure 10 shows that, for the water-saturated zone, we have a dim amplitude, with little difference between the fast and slow directions. The oil-saturated well corresponds to higher amplitude, but this time there is a significant difference between the fast and slow azimuth. The slow azimuth has a much stronger amplitude than the fast azimuth. This is entirely consistent with our theoretical modeling.

Conclusions. In this paper, we have demonstrated theoretically that seismic measurements of the properties of the slow shear wave can potentially give access to fluid-saturation information in fractured rock, even in circumstances in which the P-wave response is rather insensitive to fluid. This is possible because, for angles of incidence between 0 and 45°, the slow shear wave is strongly attenuated and dispersed, in contrast to the P-wave and fast shear wave which suffer little fracture-related attenuation in these directions. For the slow shear wave propagating near vertically, the

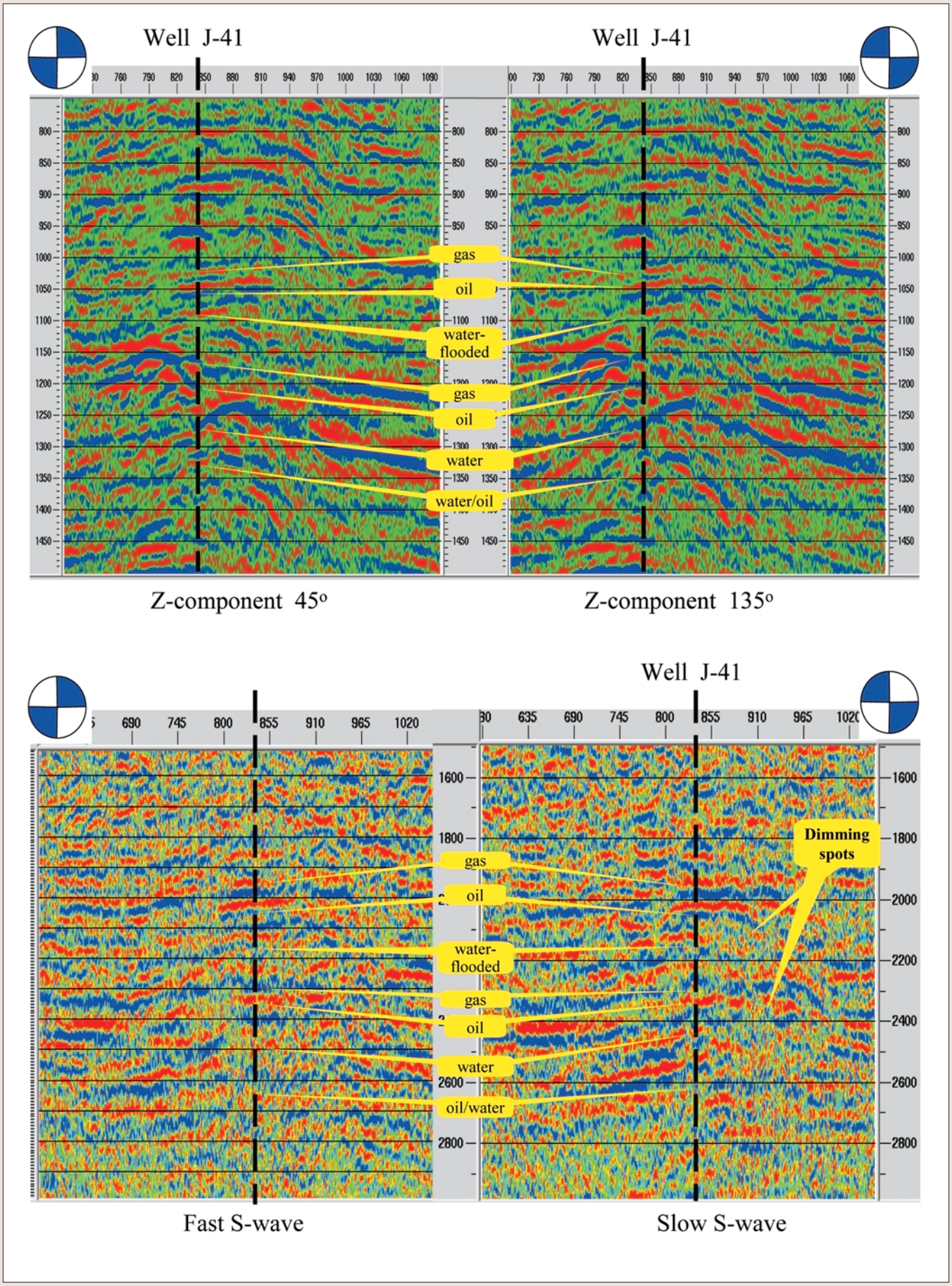

Figure 9. *Stacked sections for PP (top) and PS (bottom) created from data sectored from the fast (left) and slow (right) directions. Notice the similarity between the PP sections, while the slow PS section appears to show fluid-related amplitude effects.*

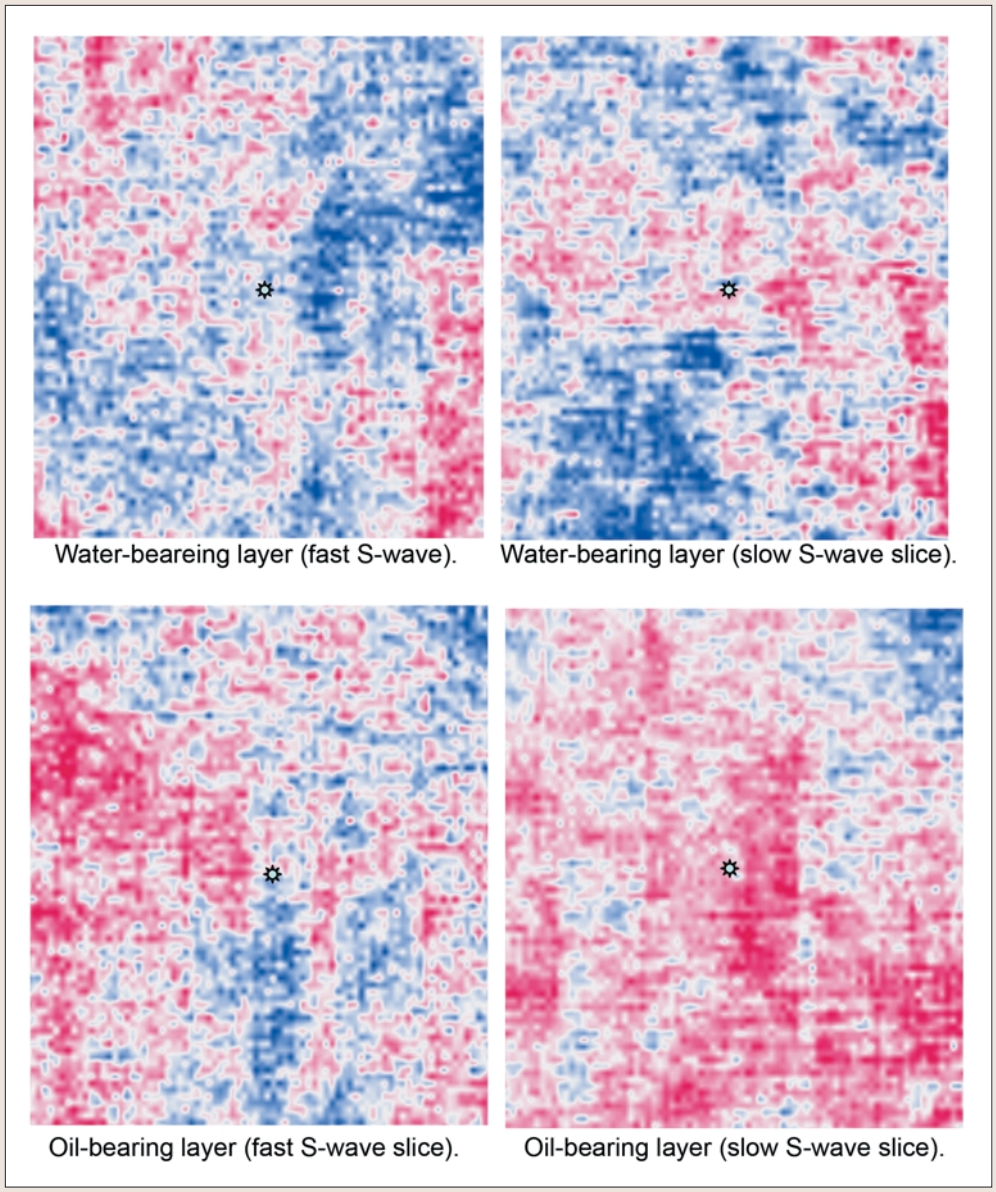

Figure 10. *Horizontal amplitude slice from converted-wave sections around wells in water-saturated zone (top) and oil-saturated zone (bottom). Left is the fast direction; right is the slow direction. Note the difference in amplitude between the fast- and slow-direction amplitude in the oil-saturated case, compared to the similarity between the two directions in the water-saturated case.*

main effect of fluid substitution comes through the change in fluid viscosity.

We analyze 3D/3-C data from Shengli oil field and detect amplitude and traveltime anomalies which are consistent with our theoretical modeling and which can be correlated with well information on the fluid saturation. Water-saturated zones tend to be associated with higher values of shear-wave splitting than oil-saturated zones, and their amplitudes are dimmer. We note that this is the exact opposite of what would be expected from an anisotropic fluid-substitution calculation using the change in bulk modulus alone without a viscosity component. In the oil-saturated zones, we see a strong change in converted-wave amplitude between the fast and slow directions, while in water saturated zones there is no azimuthal change. This behavior is predicted by our theoretical modeling.

Undoubtedly some uncertainties remain, principally related to the effect of pore-fluid pressure which presumably differs significantly between the water-flooded and oil-saturated zones. Nevertheless, we are encouraged by the correspondence between the shear-wave data and the fluid saturation information, and believe that the use of multicomponent data to discriminate oil and water saturation in fractured reservoirs will be a fruitful direction in the future.

Suggested reading. "Wave speeds and attenuation of elastic waves in material containing cracks" by Hudson (*Geophysical Journal of the Royal Astronomical Society*, 1981). "Seismic anisotropy of fractured rock" by Schoenberg and Sayers (GEOPHYSICS, 1995). "Elastic anisotropy due to aligned cracks in porous rock" by Thomsen (*Geophysical Prospecting*, 1995). "The 3D shear experiment over the Natih Field in Oman: The effect of fracture-filling fluids on shear propagation" by van der Kolk et al. (*Geophysical Prospecting*, 2001). "Frequency-dependent anisotropy due to meso-scale fractures in the presence of equant porosity" by Chapman (*Geophysical Prospecting*, 2003). "Processing, modeling, and predicting time-lapse effect of overpressured fluid-injection in a fractured reservoir" by Angerer et al. (*Geophysical Journal International*, 2002). "Converted-wave move-out and conversion-point equations in layered VTI media: Theory and application" by Li and Juan (*Journal of Applied Geophysics*, 2003). "Fluid mobility and frequency-dependent seismic velocity—direct measurements" by Batzle et al. (GEOPHYSICS, 2006). "Fluid-dependent shear-wave splitting in a poroelastic medium with conjugate fracture sets" by Galvin et al. (*Geophysical Prospecting*, 2007). TLE

Acknowledgments: We thank SinoPec Shengli oil field for permission to show the data. We thank Lifeng Wang for help with the data analysis and in particular for preparing Figure 8. This work is supported by the SinoPec international collaboration program and SinoPec Shengli Oilfield Ltd through the Edinburgh Anisotropy Project of the British Geological Survey, and is published with the approval of all project partners and the executive director of the BGS.

Corresponding author: mhch@bgs.ac.uk

A40

Effects of Fluid Saturation on Shear-wave Splitting in Multicomponent Seismic Data

Z. Qian* (British Geological Survey), X.Y. Li (British Geological Survey) & M. Chapman (British Geological Survey)

SUMMARY

Understanding pore-pressure and saturation changes is important in mature reservoirs. Here we analyze shear-wave splitting in a 3D3C onshore survey from Shengli Oilfield, China, where the thin sand-reservoir has been undergone production through water-flooding which altered the fluid composition and the pore-fluid pressure. Dividing the data into orthogonal azimuthal sectors and processing each sector separately reveals significant shear-wave splitting. The amount of shear-wave splitting can be correlated with the degree of water saturation. Furthermore, the slow shear-wave component shows amplitude dimming in water-flooded areas, whereas the zone of original oil in place shows only weak shear-wave splitting. Rock physics modeling based on the evolution of microcracked rocks and anisotropic fluid substitution incorporating both saturation and pressure changes confirm the observations. The saturation changes have little effect on the P and the fast shear-wave as confirmed by core analysis in the laboratory. However, the substitution of water for oil changes the fluid viscosity that has a strong effect on the slow (quasi) shear-wave. Moreover, the fluid substitution due to water flooding also changes the pore-fluid pressure that modifies the crack aspect ratios, further enhancing shear-wave splitting. These observations reveal the potential of using shear-wave splitting for oil-water discrimination.

Introduction

Discriminating oil from water is one of the most challenging problems in exploration geophysics. This is because the effects of oil and water saturation on pure P- and shear-wave are very similar, and the impedance variation is very small. As a result, traditional seismic methods based on wave propagation in isotropic media have not been very successful. In this paper we present an example of using shear-wave splitting for such a purpose in a 3D3C onshore survey from the Ken 71 area in the Shengli Oilfield, China.

The Ken-71 reservoir consists of mainly thin sands buried in a sand-shale sequence at depths from 1 to 2 km. The average sand thickness is only about 5-8m and average porosity is between 20-30%. The reservoir has been undergone production through water-flooding, which altered the fluid composition and the pore-fluid pressure. According to Chapman et al. (2003), if the reservoir contains fluid-filled micro-cracks and meso-scale heterogeneities, anisotropic fluid substitution predicts a strong effect on the slow shear-wave between water and oil saturation due to the change in fluid viscosity (Figure 1). Furthermore, the change in pore-fluid pressure will also cause the compliant cracks to open and close dynamically and hence modify the effective elastic constants of the fluid-filled rock, further enhancing shear-wave splitting (Zatsepin and Crampin, 1997). Consequently, we may use shear-wave splitting to monitor changes in the reservoir due to changes in the fluid saturation and stress field induced by the production process.

The Ken-71 study area

The Ken 71 area is only about 20 km^2 and located at the Yellow River delta besides the Bohai Sea. The area is relatively flat, and the reservoir is a gentle anticline with heavy faulting (Figure 2). Average oil column is 26m with area coverage of 4 km^2, and the estimated total oil reserve is about 13 million tons. The reservoir was discovered in 1978 and oil production started in 1981 with water flooding followed in 1988. Up to July 2005, cumulative oil production reached 49.2 million tons and cumulative water production 43.7 million tons. Overall water content reached as high as 95%. Since the average recovery rate is about 40% in this area, 60% residual oil will still be left in place. In 2005, an integrated programme of reservoir geophysics was implemented, aiming to characterize the by-passed oil in the area, including the acquisition of high resolution 3D3C seismic data, together with cores, logs, 3D VSPs, and crosswell seismic (Figure 2). Digital MEMS (micro-electro-mechanical system) sensors were used to improve data quality for the acquisition of the 3D3C data, and more details can be found in Qian et al. (2007, this conference).

Data processing

The main challenge is to create high-resolution shear-wave data with maximum preservation of shear-wave splitting. The added complication in this case is the asymmetric raypath of the converted-wave as well as the presence of vertical transverse isotropy (VTI) in the background sand-shale sequence, which gives rise to strong non-hyperbolic moveout in the prestack data. Therefore, successful anisotropic processing not only needs to preserve shear-wave splitting, but also account for the non-hyperbolic effects. In order to do this, we design the following two-stage work flow.

The first stage aims to determine the principal coordinate system, or the directions of the fast and slow split shear-wave. The main steps in this stage include coordinate rotation, noise reduction, statics and azimuthal analysis of the transverse component data. At the very beginning, the data are rotated into the Radial and Transverse components from the field coordinate system. After noise and statics, azimuthal analysis of the transverse component may then be used to determine the principal coordinate system based on polarity reversal (Li, 1998). 2D lines of radial and transverse component data may also be extracted from the 3D volume to perform shear-wave splitting analysis. At this stage, the VTI effects are ignored.

For this data, the fast direction is identified as N40^{o}E, which is in agreement with the main structural alignment of the area (Figure 2).

The second stage aims to account for the VTI effects and asymmetric raypath whilst also preserving shear-wave splitting. This is usually achieved by dividing the 3D data into different azimuthal sectors and then processing each azimuthal sector separately using a processing flow incorporating both the effects of VTI and the asymmetric raypath. Here, the data are divided into two orthogonal azimuthal sectors (45 degrees and 135 degrees). The details of the processing flow in the presence of VTI can be found in Qian et al. (2007, this conference). High quality fast and slow shear-wave volumes are obtained (Figure 3).

Data analysis and results

We first analyze the time delay between the fast and slow shear-waves. A short time-window correlation method is used to create time-delay spectra (Figure 4), from which the time-delay attribute can be obtained. Figure 5 shows a time-delay gradient section (Line 646) intersecting well J-41. The variation of shear-wave splitting is about 5%, and it can be correlated with the degree of water saturation at the well position (Figure 5). Furthermore, the slow shear-wave component shows amplitude dimming in the water-flooded areas, whereas the zone of original oil in place appears to show weak shear-wave splitting (Figure 6). In contrast, the P-wave sections at the corresponding azimuthal sectors show little changes (Figure 7). Horizontal amplitude slices of the slow shear-wave at the corresponding oil and water formations show clear amplitude anomalies associated with oil and water saturation (Figure 8).

The above observed correlation of shear-wave splitting with saturation can be modeled using anisotropic fluid substitution as proposed by Chapman et al. (2003) incorporating the pore pressure effects based on the evolution of microcracked rocks in Zatsepin and Crampin (1997). The effects of saturation on the P and the fast shear-wave velocity is very small (less than 1%), as revealed by the modeling (Figure 1a) and confirmed by core analysis in the laboratory. However, the substitution of water for oil changes the fluid viscosity which induces a change in the slow (quasi) shear-wave velocity as high as 4% (Figure 1b), hence leading to a significant increase in shear-wave splitting for the water saturation case, as compared with the oil case (Figure 1c). Moreover, the fluid substitution due to water flooding also changes the pore-fluid pressures, thus modifying the crack aspect ratios and further enhancing shear-wave splitting. The driving mechanism for the model is fluid migration by flow or dispersion along pressure gradients between cracks at different scale lengths.

Discussion and conclusions

Understanding pore-pressure and saturation changes is important in mature reservoirs. It has been observed that shear-wave splitting is very sensitive to pore-pressure change and is the principal seismic diagnostic for the detection of pressure effects (Angerer *et al.* 2002). In this paper, we have shown that shear-wave splitting is also sensitive to oil-water saturation change. We analyzed shear-wave splitting in a 3D3C onshore survey from Shengli Oilfield, China, and we observed strong correlation between shear-wave splitting and water saturation, and this confirms the potential of using shear-wave splitting for oil-water discrimination.

Acknowledgements

We thank SinoPec Shengli Oilfield for permission to show the data. The Shengli data are processed by Zhongping Qian and Haizheng Zhao of EAP, and Lifei Bi and Jianxin Shi of SinoPec. This work is supported by the SinoPec international collaboration programme and SinoPec Shengli Oilfield Ltd. through the Edinburgh Anisotropy Project (EAP) of the British Geological Survey (BGS), and is published with the approval of all project partners and the Executive Director of BGS.

References

Angerer E., Crampin S., Li X.-Y. and Davis T.L. 2002. Processing, modelling and predicting time-lapse effects of overpressured fluid-injection in a fractured reservoir. Geophysical Journal International, **149**, 267–280.

Chapman M., Maultzsch S., Liu E. and Li X.-Y. 2003. The effect of fluid saturation in an anisotropic multi-scale equant porosity model. Journal of Applied Geophysics, **54**, 191–202.

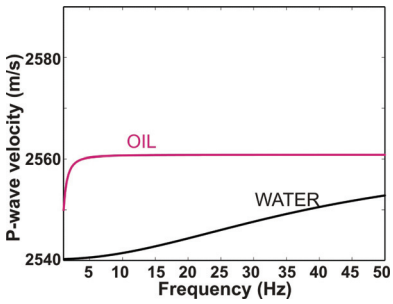

(a) P-wave

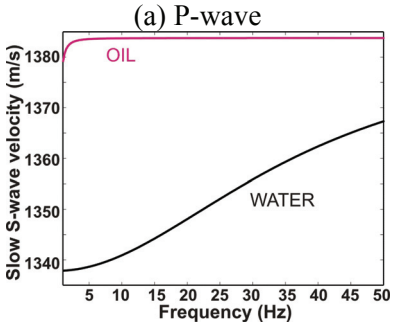

(b) Slow shear-wave

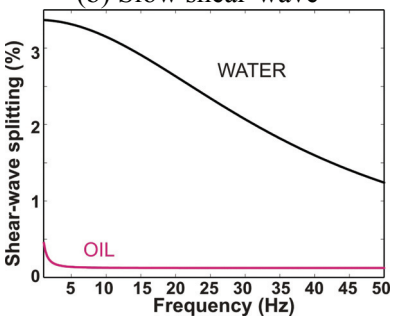

(c) Shear-wave splitting

Figure 1. Effects of oil-water saturation for the thin sand at depth 1.5km in the study area, calculated using Chapman et al. (2003).

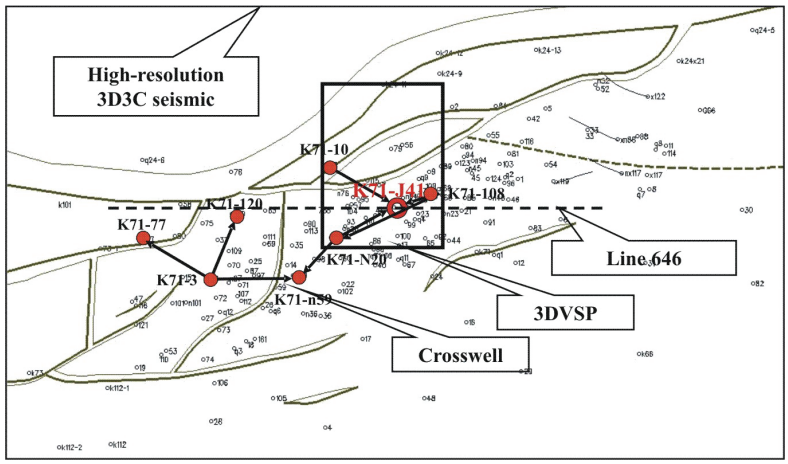

Figure 2. The Ken-71 study area and various datasets including 3D VSPs, crosswell seismic and core data at well J-41.

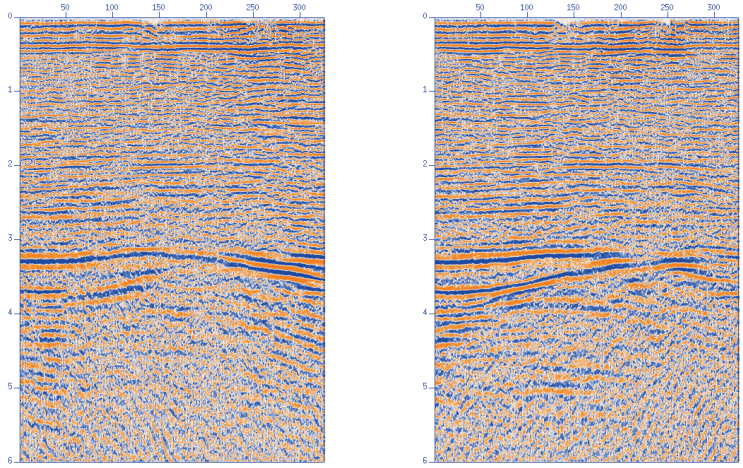

(a) Fast -45 ^{o} (b) Slow -135 ^{o}

Figure 3. The fast and slow shear-wave along Line 646 in Figure 2 extracted from the 3D volume: The fast section is from azimuthal sector N45^{o}E, and the slow section from sector N135^{o}E.

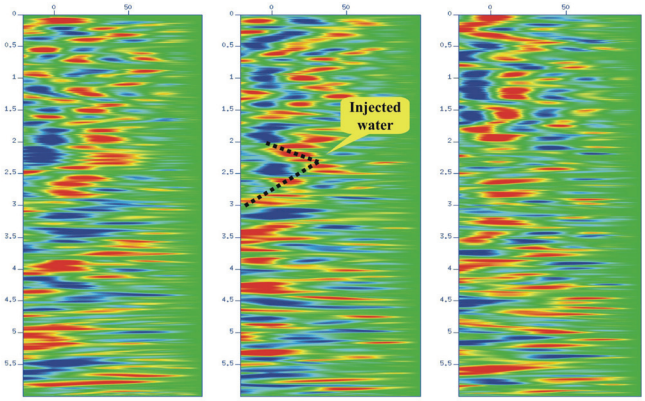

(a) CDP 820 (b) CDP 832 (c) 850

Figure 4. Time-delay spectra of selected CDPs in Figure 3, Line 646. CDP 832 is at well J-41.

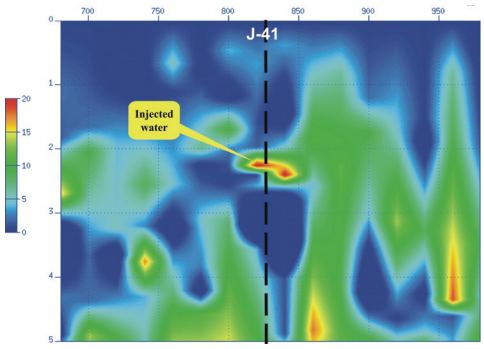

Figure 5. Time-delay gradient section of Line 646 picked from Figure 4.

Li X.-Y. 1998. Processing PP and PS waves in multicomponent sea-floor data for azimuthal anisotropy: theory and overview. Procedding of the Eighth International Workshop on seismic Anisotropy (Revue De L'institut francia du petrole), **53**, 607-620.

Qian Z., Li X.-Y., Meng, X and Bi, L. 2007. Converted-wave velocity analysis in the presence of anisotropy: a case study from Shengli oilfield, China. This conference.

Zatsepin S.V. and Crampin S. 1997. Modelling the compliance of crustal rock—I. Response of shear-wave splitting to differential stress. Geophysical Journal International, **129**, 477–494.

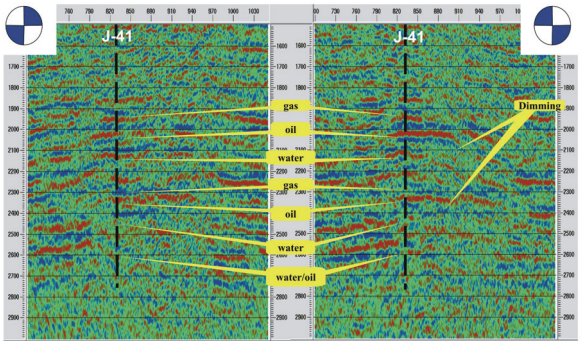

(a) Fast –azimuth 45 ^{o} (b) Slow-azimuth 135 ^{o}

Figure 6. Comparison of the fast and slow-wave amplitudes at well J-41, noting the dimming spots at the slow section corresponding to the water layers.

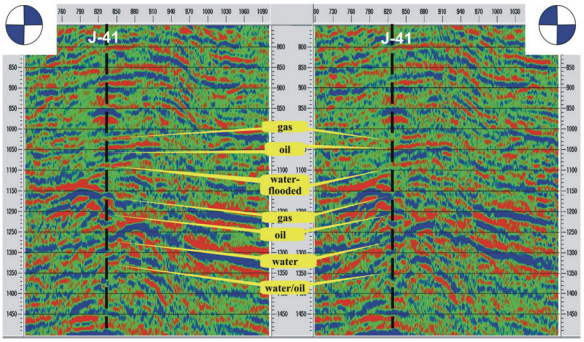

(a) Azimuth 45 ^{o} (b) Azimuth 135 ^{o}

Figure 7. Comparison of the P-waves from the two azimuthal sectors at well J-41, and there is no significant difference between the two sections.

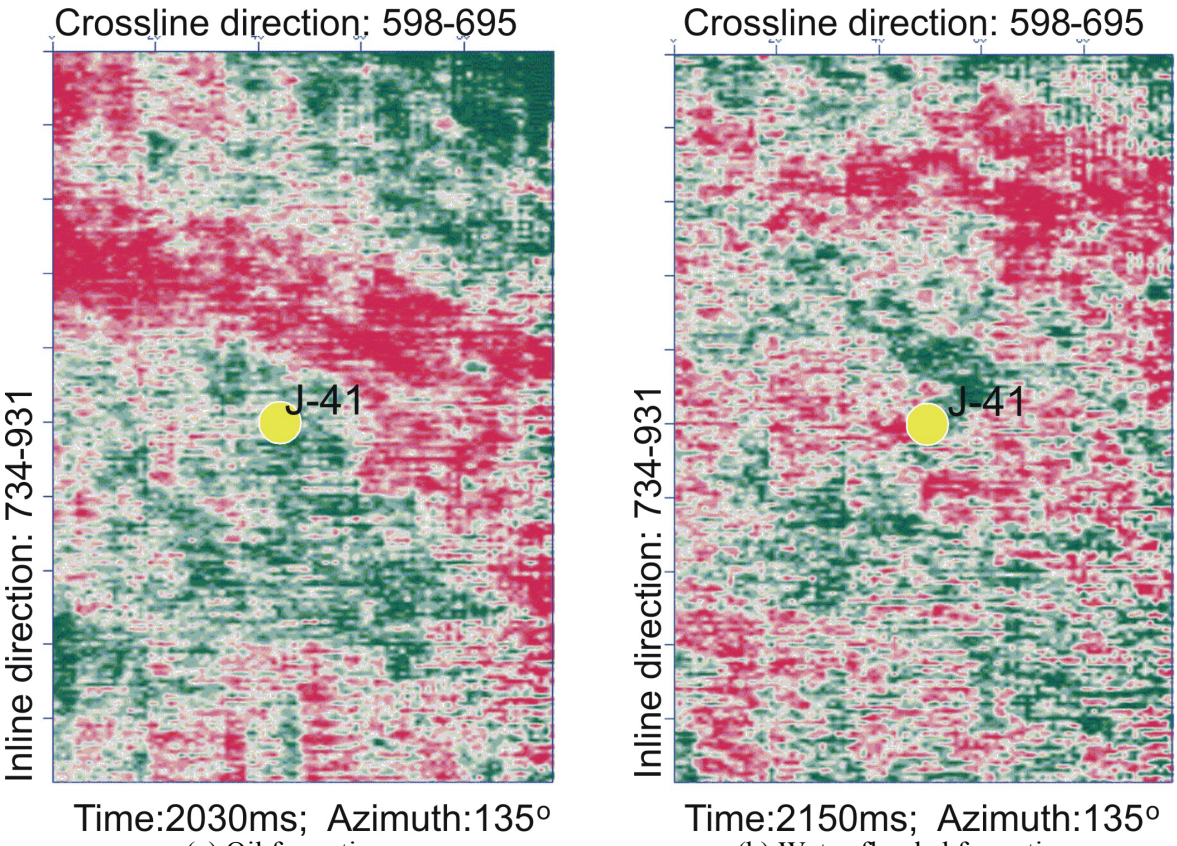

(a) Oil formation (b) Water-flooded formation

Figure 8. Horizontal amplitude slices of the slow wave at azimuth 135 ^{o} for (a) the oil layer at 2.03s and (b) the water-flooded layer at 2.15s. Green indicates oil and red indicates water.

04

Converted- ave elocity Analysis in the resence of Anisotropy A Case Study from Shengli ilfield, China

Z. Qian* (British Geological Survey), X. Li (British Geological Survey), X. Meng (Sino ec Shengli ilfield) & L. Bi (Sino ec Shengli ilfield)

SUMMARY

The Shengli en- multi-component seismic data were acquired with digital M MS (micro-electro-mechanical system) sensors over a mi ed sand and shale sequence in the overburden. This gives rise to serious non-hyperbolic moveout effects in the converted-wave data due to both the asymmetry raypath and the anisotropic effects. Conventional velocity analysis based isotropic methods cannot flatten the moveout. Here, we use a four-parameter theory developed for vertical transverse isotropy (T) to evaluate these effects and process the data. These four parameters include the PS converted wave stacking velocity, the vertical velocity ratio, the effective velocity ratio, and the anisotropy parameter. The method utilizes the moveout information at different offsets to estimate the different parameters, and ensures that the events are properly aligned for stacking. s a result, this four-parameter theory leads to an improvement in image quality and correlation between the P-waves and converted-waves.

Introduction

Processing land multi-component seismic data in the presence of anisotropy is often a challenging problem. In this paper, we present such an example from the Shengli Oilfield in east China. The Shengli multi-component seismic data were acquired with digital MEMS (micro-electro-mechanical system) sensors over a mixed sand and shale sequence in the overburden. The data consisted of four swaths. For each swath, there are twelve receiver lines with 300 receivers per line and 220m of line spacing. Receiver interval is 20m, giving area coverage about 15km^2 for each swath. The shots are located in the centre of the receiver patch and orthogonal to the receiver lines with 66 shots per shot line and 100m of shot line spacing. The data are of good quality with some random noise and ground roll (Figure 1).

As we know, sedimentary layers such as shales and thin bedding sequences in the overburden often give rise to vertical transverse isotropy (VTI, or polar anisotropy). This leads to serious non-hyperbolic moveout effects in the converted-wave data due to both the asymmetric raypath and the anisotropic effects. Conventional velocity analysis based isotropic methods cannot flatten the moveout. One of the key issues during processing multi-component seismic data is how to account for these VTI effects. Here, we use a four-parameter theory developed by Li and Yuan (2003) to evaluate these effects and process the Shengli data.

The basic four-parameter theory for VTI

According to Li and Yuan (2003), the *C*-wave moveout signature in horizontally layered VTI media can be expressed as,

$$t_C^2 = t_{C0}^2 + \frac{x^2}{V_{C2}^2} + \frac{A_4 x^4}{1 + A_5 x^2}, \tag{1}$$

where

$$A_4 = -\frac{(\gamma_0\gamma_{eff} - 1)^2 + 8(1+\gamma_0)\chi_{eff}}{4t_{C0}^2 V_{C2}^4 \gamma_0 (1+\gamma_{eff})^2}, \text{ and } A_5 = \frac{A_4 V_{C2}^2 (1+\gamma_0)\gamma_{eff}\left[(\gamma_0 - 1)\gamma_{eff}^2 + 2\chi_{eff}\right]}{(\gamma_0 - 1)\gamma_{eff}^2(1 - \gamma_0\gamma_{eff}) - 2(1+\gamma_0)\gamma_{eff}\chi_{eff}}. \tag{2}$$

V_{C2} is the *C*-wave stacking velocity, γ_0 and γ_{eff} are the vertical and effective velocity ratio, and χ_{eff} is the *C*-wave anisotropic coefficient. Equations (1) and (2) are accurate for offset-depth ratio up to 2.0 ($x/z \leq 2.0$) (Li and Yuan, 2003). Equation (1) controls the stacking process, and these four parameters are referred to as the *C*-wave stacking velocity model.

The *C*-wave diffraction curve from a point scatter in VTI media can be derived as (Dai and Li, 2001),

$$t_C = \sqrt{\left(\frac{t_{C0}}{1+\gamma_0}\right)^2 + \frac{(x+h)^2}{V_{P2}^2} - 2\eta_{eff}\Delta t_P^2} + \sqrt{\left(\frac{\gamma_0 t_{C0}}{1+\gamma_0}\right)^2 + \frac{(x-h)^2}{V_{S2}^2} + 2\zeta_{eff}\Delta t_S^2}, \tag{3}$$

where

$$\eta_{eff} = \frac{1}{8t_{P0}V_{P2}^4}\left[\sum_{i=1}^{n} V_{P2i}^4 \Delta t_{P0i}(1+8\eta_i) - t_{P0}V_{P2}^4\right], \text{ and } \zeta_{eff} = \frac{-1}{8t_{S0}V_{S2}^4}\left[\sum_{i=1}^{n} V_{S2i}^4 \Delta t_{S0i}(1-8\zeta_i) - t_{S0}V_{S2}^4\right]; \tag{4}$$

$$\Delta t_P^2 = \frac{(x+h)^4}{V_{P2}^2\left[t_{C0}^2 V_{P2}^2/(1+\gamma_0)^2 + (1+2\eta_{eff})(x+h)^2\right]}, \text{ and } \Delta t_S^2 = \frac{(x-h)^4}{V_{S2}^2\left[t_{C0}^2 V_{S2}^2 \gamma_0^2/(1+\gamma_0)^2 + (x-h)^2\right]}. \tag{5}$$

Subscript i denotes interval quantities. t_{C0} is the vertical two-way time, h is the half source-receiver offset, η is the well-known *P*-wave anisotropic parameter and ζ is the *S*-wave anisotropic parameter defined as $\zeta = \gamma_{eff}^2 \eta$. Equation (3) is accurate up to, at least, an offset-depth ratio of 2.5 (Yuan, 2001). The diffraction curve [Equation (3)] contains five parameters:

γ_0, V_{P2}, V_{S2}, η_{eff} and ζ_{eff}, controlling the process of *C*-wave prestack time migration (PSTM). Of these, the four parameters V_{P2}, V_{S2}, η_{eff} and ζ_{eff} are referred to as the *C*-wave PSTM velocity model. There is a one-to-one analytical link between the stacking and PSTM velocity models:

$$V_{P2}^2 = V_{C2}^2 \frac{\gamma_{eff}(1+\gamma_0)}{1+\gamma_{eff}}\ ,\ V_{S2}^2 = V_{C2}^2 \frac{(1+\gamma_0)}{\gamma_0(1+\gamma_{eff})}\ ,\eta_{eff} = \frac{\chi_{eff}}{(\gamma_0-1)\gamma_{eff}^2}, \text{and } \zeta_{eff} = \frac{\chi_{eff}}{(\gamma_0-1)}. \quad (6)$$

If the stacking velocity model (V_{C2}, γ_0, γ_{eff} and χ_{eff}) is known, equation (6) can be used to build the PSTM velocity model.

Work flow for anisotropic velocity analysis

The following workflow can be used to determine the stacking velocity model (V_{C2}, γ_0, γ_{eff} and χ_{eff}) using multi-component seismic data.

The first step is to estimate γ_0 through an initial processing sequence. The *C*-wave moveout is insensitive to the variation of γ_0 (Li and Yuan 2003). Thus, γ_0 cannot be determined from moveout analysis. A coarse correlation of the *P*- and *C*-wave stacked sections is required. This often involves processing the *P*- and *C*-wave data using hyperbolic methods to obtain two stacked sections. γ_0 is then obtained by correlating these two sections. Once γ_0 is determined, the second step is to estimate V_{C2}, γ_{eff} and χ_{eff} from the *C*-wave moveout signature by interactive analysis (Dai, 2003). This is because each of these parameters controls a particular data aperture of primary influence: V_{C2} controls the hyperbolic moveout at near offsets (x/z<1.0); γ_{eff} controls the non-hyperbolic moveout at intermediate offsets (x/z<1.5) due to the asymmetric raypath; χ_{eff} controls the anisotropic moveout at far offsets (x/z<2.0).

The third step is to determine the migration velocity. The initial model is calculated from the stacking velocity model using equation (6), and common imaging point (CIP) gathers can then be generated using the initial velocity model through PSTM. Model updating is achieved by analyzing the residual moveout in the CIP gathers. Updating is often restricted to V_{C2} and χ_{eff}. After updating, a final PSTM is applied to the data. This requires one NMO run and two PSTM runs.

Applications to the Shengli multi-component seismic data

The above processing scheme has been successfully applied to the Shengli multi-component seismic data. Figures 2 and 3 illustrate the correlation analysis for determining γ_0, where we have successfully matched up the P- and C-wave stacked sections through compressing the C-wave section into P-wave time. Figure 4 illustrates the process of stacking velocity analysis, where the far-right panel illustrates the input ACP (asymptotic conversion point) gather after moveout correction. The far-left panel displays the V_{C2} spectra for interactive picking. The second panel from the left displays the velocity ratio γ_{eff}. The third panel from the left displays the anisotropic coefficient χ_{eff}.. The flatness of an event over the intermediate and far offsets determines the values of γ_{eff} and χ_{eff}. This allows detailed analysis of the moveout and ensures that the proper moveout correction is applied to the data.

Figure 5 shows the results of migration velocity analysis, where a CIP gather generated by PSTM is input to the same interactive tool as in Figure 4 for updating the migration velocity model. Again, the criterion is to flatten the events in the CIP gather. This makes it possible to obtain an accurate migration velocity model for final migration.

The final stacked PP- and PS-sections are shown in Figure 6, where the regional events can all be mapped from both the PP- and PS-sections, giving rise to a very high degree of correlation. Figure 7 compares the migrated converted-wave section with the stacked section. We can see a clear improvement in the signal-to-noise ratio after migration, and the faults are generally better imaged.

Discussion and conclusions

We have evaluated the use of a four-parameter theory for processing the Shengli multi-component data. The four parameters are V_{C2}, γ_0, γ_{eff} and χ_{eff}, which can be determined from reflection moveout analysis and can then be used to build the anisotropic model for prestack time migration. This leads to an improvement in both image quality and event correlation between the PP and PS converted-waves in the Shengli multi-component seismic data.

Acknowledgements

We thank SinoPec Shengli Oilfield for permission to show the data. This work is supported by the SinoPec international collaboration programme and SinoPec Shengli Oilfield Ltd. through the Edinburgh Anisotropy Project (EAP) of the British Geological Survey (BGS), and is published with the approval of all project partners and the Executive Director of BGS.

References

Dai H. 2003. Integrative analysis of anisotropy parameter and velocities for PS converted waves. 73rd SEG meeting, Dallas, USA, Expanded Abstracts, 1577-1580.

Dai, H. and Li, X., 2001, Anisotropic migration and model building for 4-C seismic data: A case study from Alba, 71st Ann. Internat. Mtg: Soc. of Expl. Geophys., 795-798.

Li, X.-Y. and Yuan, J., 2003. Converted-wave moveout and conversion-point equations in layered VTI media: theory and application. Journal of Applied Geophysics, **54**, 297-318.

Yuan, J., 2001, Analysis of four-component sea-floor seismic data for seismic anisotropy: PhD Thesis, University of Edinburgh.

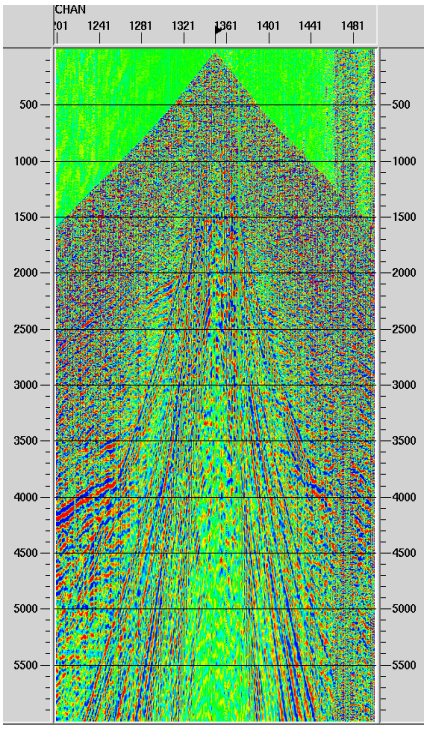

Figure 1. PS Converted-wave data from Shengli, X-component, Swath 3.

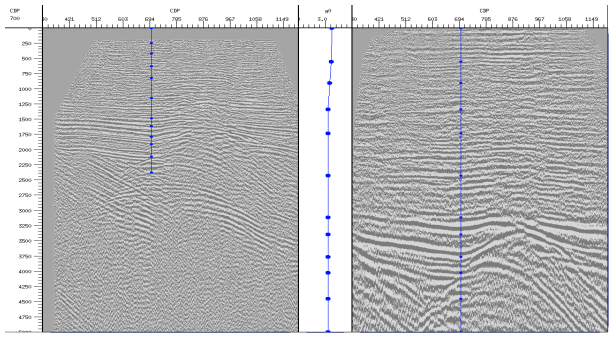

(a) PP (b) γ_0 (c) PS

Figure 2: Before compression: A coarse correlation of the (a) *P*- and (c) *C*-wave sections for estimating (b) γ_0.

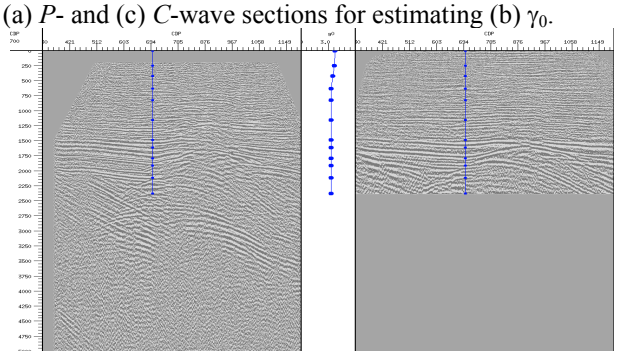

(a) PP (b) γ_0 (c) PS

Figure 3: After compression. As a result, the P- and C-wave sections are matched up successfully.

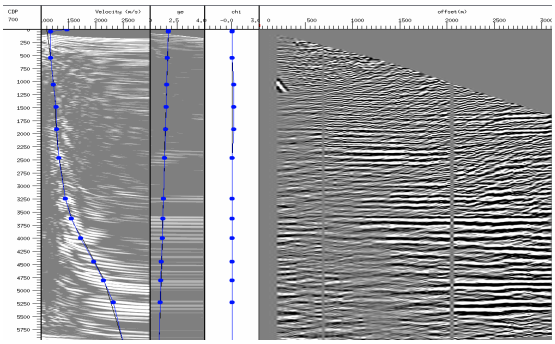

Figure 4: Interactive analysis for determining V_{C2}, γ_{eff} and χ_{eff}, and the input data are asymptotic conversion point (ACP) gathers.

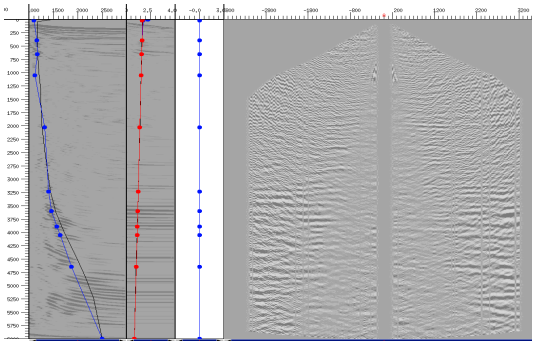

Figure 5: Migration velocity analysis, and the input data are common imaging point (CIP) gathers.

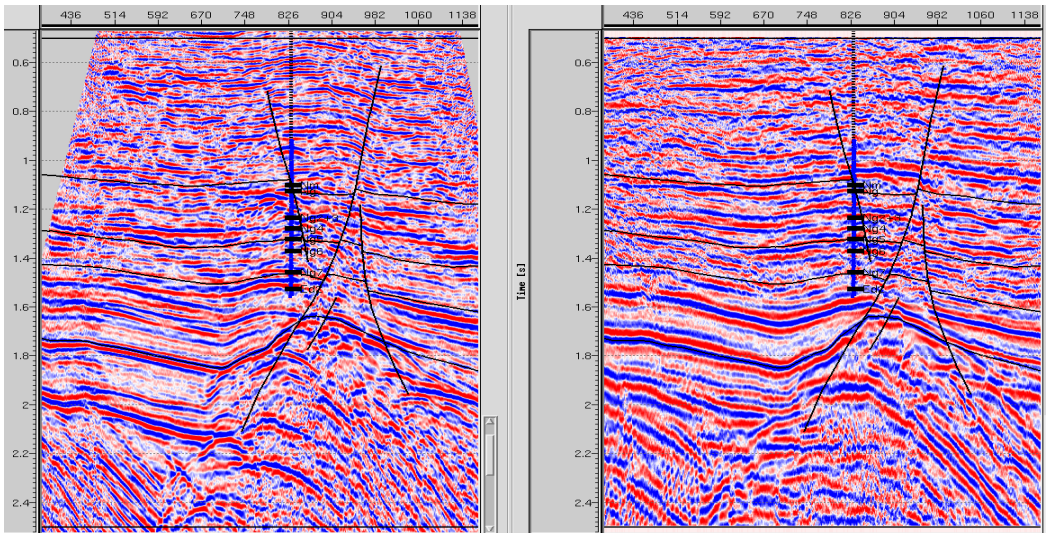

(a) PP (b) PS (compressed to PP time)

Figure 6. Comparison of final stacked sections: (a) PP-wave and (b) PS converted wave.

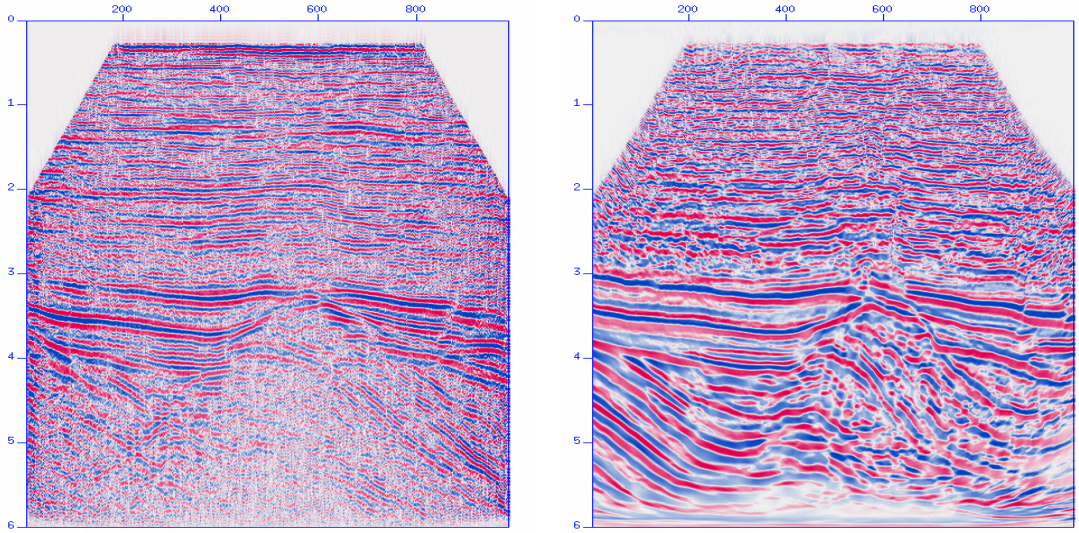

(a) stack (b) pre-stack time migration

Figure 7. Comparison of (a) final stacked with (b) migrated converted-wave sections.

LONDON2007

Sensitivity Analysis of Anisotropic arameters for C-wave re-stac ime Migration in the Clair D BC Data

Z. Qian* (British Geological Survey) & X. Li (British Geological Survey)

SUMMARY

e present a sensitivity analysis of the anisotropic parameters used for C-wave Pre-stack Time Migration (PSTM) applied to the Clair 3D O C data. Though the signal-noise ratio of the data often limits the image quality, anisotropy may also play a significant role. From the results of the anisotropic parameter analysis we find that both P-wave and converted S-wave anisotropy decrease with time, but the converted S-wave data are affected more by anisotropy than the P-wave data. The C-wave PSTM result based on the anisotropic velocity model is better than that based on the isotropic velocity model, and the improvements are mainly located in the upper part of the section.

Introduction

The Clair Oil Field is to the west of Shetland on the UK continental shelf, and the water depth is about 140m (Smith and McGarrity 2001). Several multi-component seismic data sets have been acquired to use seismic anisotropy to evaluate the reservoir. The 3D OBC data used in our analysis were acquired in 2002 with patch geometry to ensure a wide azimuth distribution for fracture analysis. Multiples are known to be a problem due to the hard seabed in the Clair field, and have been carefully removed by the contractor before anisotropic processing. One of main issues is how to compensate for the effects of vertical transverse isotropy (VTI) that is widely present in the marine sediments. The presence of VTI can cause mis-positioning both vertical and laterally, and thus affects image quality. In this study, we use anisotropic C-wave pre-stack time migration (PSTM) based on isotropic and anisotropic velocity models to study the effects of anisotropy on the Clair data.

C-wave processing strategy

Being different to P-wave processing, C-wave processing involves some inherent problems such as the asymmetric ray-path and conversion-point binning, more sensitivity to anisotropy, etc. C-wave PSTM is widely regarded as a better approach than the conventional C-wave processing scheme comprising CCP binning, NMO, DMO and post-stack migration. Normally, C-wave PSTM can be carried out in the following way (Dai and Li 2001, Li et al. 2004): (i) build a C-wave stacking velocity model from ACP (asymptotic conversion point) gathers; (ii) convert the stacking velocity model to an initial migration velocity model and carry out an initial PSTM to build CIP gathers for migration velocity analysis; (iii) use the CIP gathers to update the migration velocity model, and iterate until a satisfactory result is obtained; (iv) carry out the PSTM with the updated velocity model to obtain final imaging results. Based on these ideas, we establish a processing flow for the Clair C-wave data, as shown in Figure 1, in which both P-wave data and C-wave data are involved.

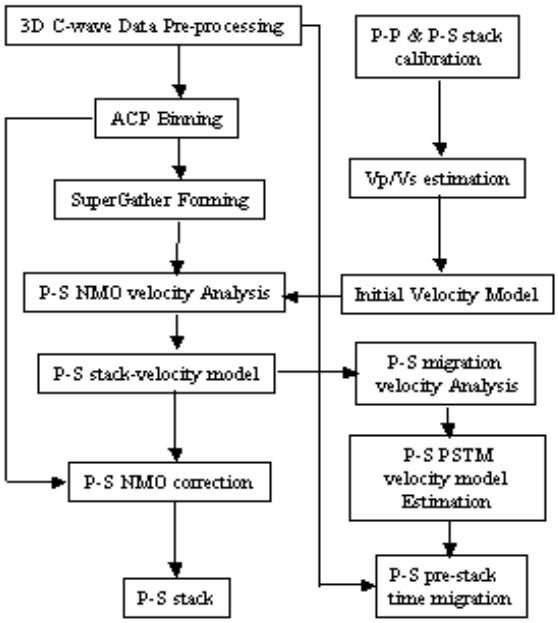

Figure 1: Anisotropic PSTM processing flow

Anisotropic PSTM velocity model

For anisotropic C-wave PSTM, the most important thing is to build a reasonable velocity model, and the first step is to build a C-wave stacking velocity model. The *C*-wave stacking velocity model in horizontally layered VTI media is specified by four parameters: V_{C2}, γ_0, γ_{eff} and χ_{eff}, which denote *C*-wave stacking velocity, vertical velocity ratio, effective velocity ratio and C-wave anisotropic parameter, respectively (Li and Yuan 2003). Except for γ_0, the parameters can be determined from the moveout signatures in the ACP gathers. A coarse correlation of the brute P- and C-wave stacking sections is needed to determine γ_0.The brute

stacking sections of P- and C-waves can be generated with near offset data. Because the Clair field exhibits horizontal transverse isotropy (HTI) due to vertical fractures, we need to divide the data into azimuthal sectors and then apply the VTI processing flow to each sector separately.

Figure 2 shows the C-wave PSTM velocity analysis, from which the three parameters V_{C2}, γ_{eff} and χ_{eff} can be picked. The flattened events in the CIP gather are used as criteria to guide the optimal parameter picking. We carry out several iterations before a reasonable PSTM velocity model is built. The *C*-wave PSTM velocity model is specified by five parameters: γ_0, V_{P2}, V_{S2}, η_{eff} and ζ_{eff}, which denote vertical velocity ratio, P-wave and S-wave stacking velocity, and P- and S-wave anisotropic parameters. There is a one-to-one analytical link between the stacking velocity model and the PSTM velocity model (Li et al. 2005; Dai, 2003). The parameters γ_0, V_{C2}, γ_{eff} and χ_{eff} can be directly transferred into V_{P2}, V_{S2}, η_{eff} and ζ_{eff}.

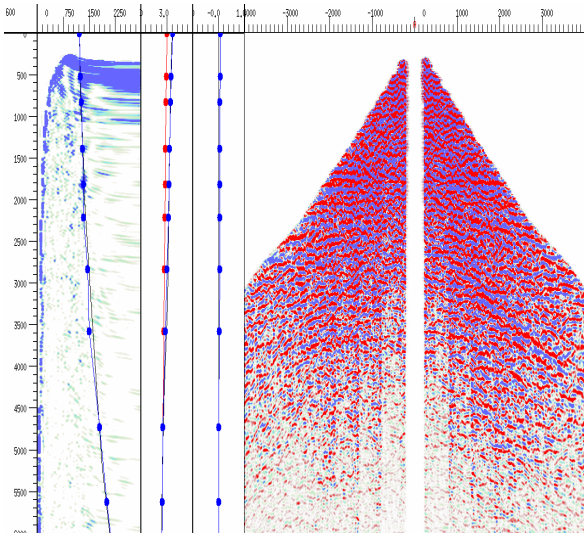

(a) (b) (c) (d)

Figure 2: PSTM velocity analysis. (a) V_{C2} spectrum, vertical axis denote time in ms, horizontal axis denotes velocity in m/s; (b) γ_{eff}; (c) χ_{eff}; (d) CIP gather.

The profiles of the four parameters based on the Clair C-wave data are shown in Figure 3. The P-wave velocities range from 2200 to 3109 (m/s), while the S-wave velocities range from 690 to 1138 (m/s). The overall trend of variation in the P-wave and S-wave velocities follow the structural trend. In the P-wave anisotropy profile (figure 3c), the anisotropic value varies from 0.1% to 0.5%, which is very small and can be ignored. However, in the S-wave anisotropy profile (figure 3d), the anisotropic value varies from 1% to 5% which is an order of magnitude higher than the P-wave anisotropy. This explains why we can ignore the VTI anisotropy for the P-wave data, but we cannot ignore the anisotropy effects for the converted wave data. Figures 3c and 3d also show that the anisotropy parameters decrease with depth.

PSTM results analysis

To analyze the anisotropic effects on the PSTM results using the C-wave data, we carry out the PSTM with two sets of velocity models: one is an anisotropic velocity model, which takes all four parameters into account; the other is an isotropic velocity model, which is obtained by omitting the two anisotropic parameters η_{eff} and ζ_{eff}. Figures 4a and 4b are the PSTM results based on the two different velocity models. In the PSTM section earlier than 2.5s, the PSTM result using the anisotropic velocity model is better than that the isotropic PSTM result in terms of both event continuity and focusing. However, in the deeper part, both sections are of similar quality, which means that the effect of anisotropy becomes weak. The results indicate that for shallow targets, we may have to pay more attention to anisotropic issues during C-wave processing.

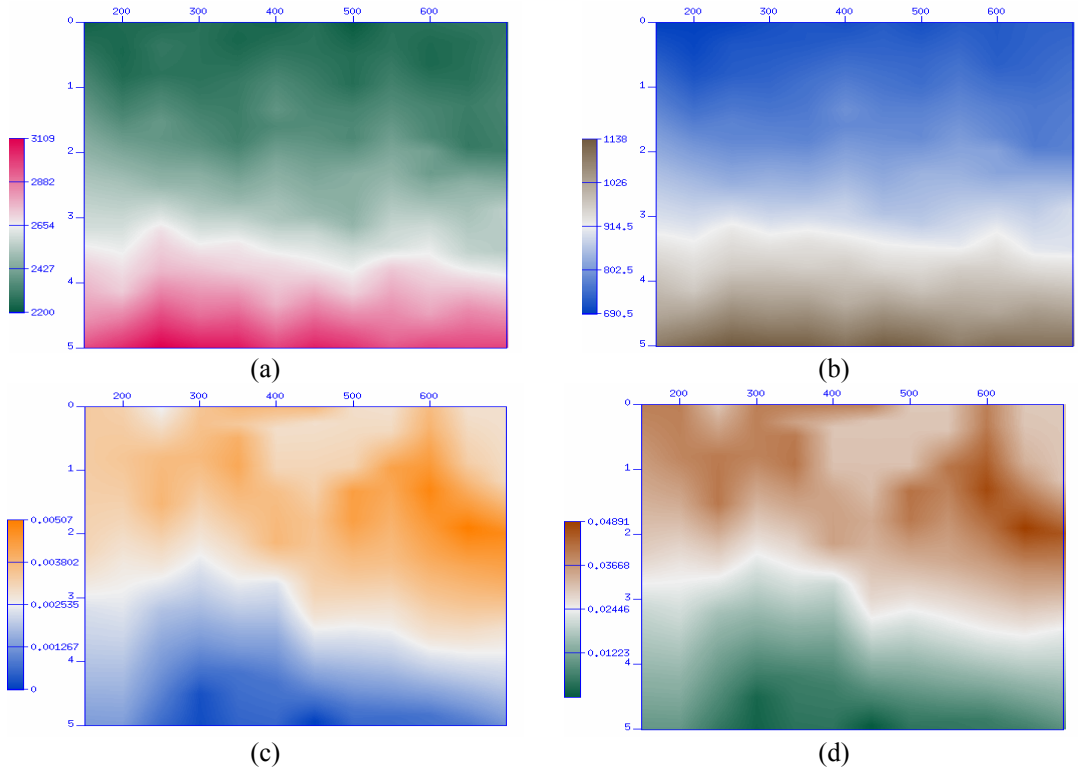

(a) (b)

(c) (d)

Figure 3: PSTM velocity model. (a) V_{P2}; (b) V_{S2} ; (c) η_{eff} ; (d) ζ_{eff} . The four parameters are transferred from V_{C2}, γ_{eff} and $\chi_{eff.}$, which are picked from the velocity spectrum, as shown in Figure 2. The vertical axis denotes time in second.

Discussion and conclusions

We have carried out a sensitivity analysis of the anisotropic parameters for C-wave PSTM in Clair 3D OBC data. Though signal-noise ratio of the data often limits the image quality, the anisotropy may also play a significant role. From the results of the anisotropic parameter analysis we find that the P-wave anisotropy is very small (less than 1%) and S-wave anisotropy varies from 1% to 5%, and cannot be neglected during C-wave processing. The C-wave PSTM result based on the anisotropic velocity model is better than that based on the isotropic velocity model, and the improvements are mainly located in the upper part of the section.

Acknowledgements

We thank the Clair license partners (BP, ConocoPhillips, Chevron, Shell and Hess) for providing and granting permission to show the Clair 4C data. We thank John McGarrity and Rodney Johnston of BP for useful discussions. This work is funded by the Edinburgh Anisotropy Project (EAP) of the British Geological Survey, and is presented with the approval of the Executive Director of British Geological Survey and the EAP sponsors.

References

Dai H. 2003. Integrative analysis of anisotropy parameter and velocities for PS converted waves. 73rd SEG meeting, Dallas, USA, Expanded Abstracts, 1577-1580.

Dai, H. and Li, X., 2001, Anisotropic migration and model building for 4-C seismic data: A case study from Alba, 71st Ann. Internat. Mtg: Soc. of Expl. Geophys., 795-798.

Li, X.-Y., Dai, H. and Mancini, F., 2004. Converted-wave imaging in anisotropic media: an overview, 74th Ann. Internat. Mtg.: Soc. of Expl. Geophys., 881-884.

Li, X.-Y. and Yuan , J., 2003, Converted-wave moveout and conversion-point equation in layered VTI media: theory and application, J. Appl. Geophys., **54**, 297-318.

Smith R.L. and McGarrity J.P. 2001. Cracking the fractures – seismic anisotropy in an offshore reservoir, The Leading Edge, **20**, no. 01, 18-24.

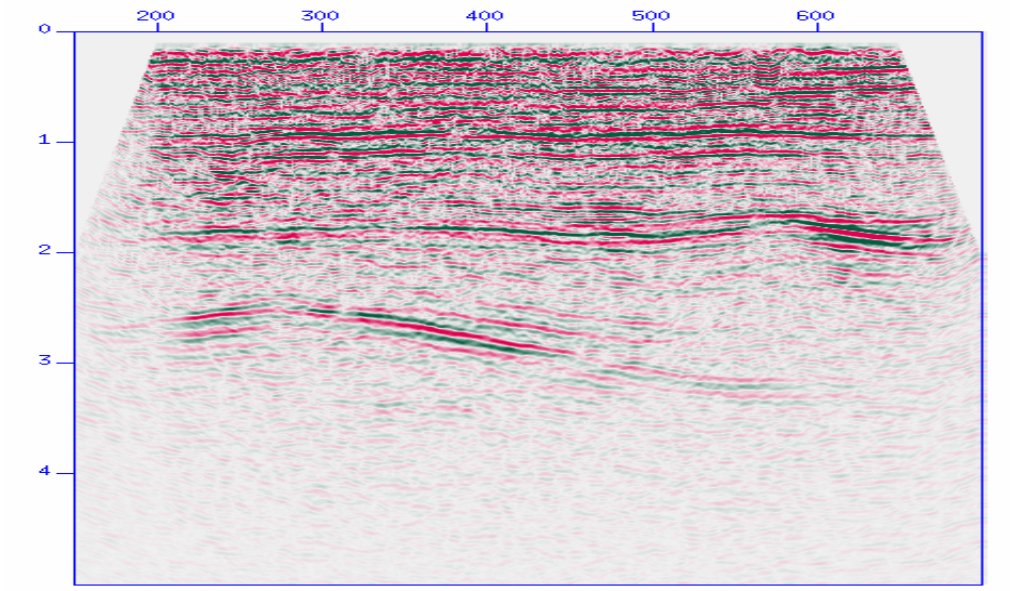

(a)

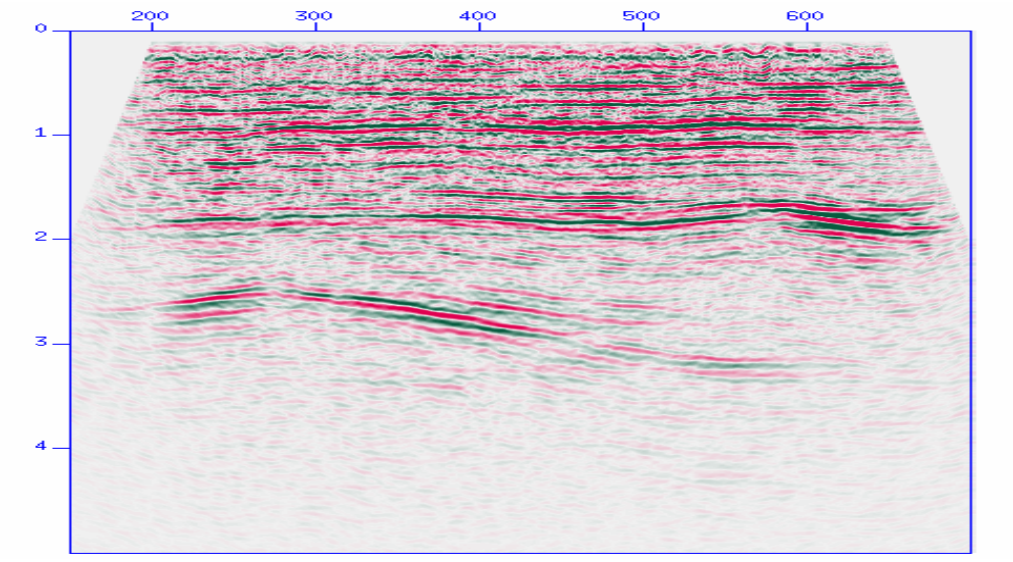

(b)

Figure 4: PSTM results (R-component). (a) Section based on the isotropic velocity model, omitting the anisotropic parameters shown in Figure 3c and 3d; (b) section based on the anisotropic velocity model in Figure 3.

Fracture detection using 3D P-wave seismic data: An integrated study from Southwest China

Zhongping Qian, Xiang-Yang Li and Enru Liu Edinburgh Anisotropy Project, British Geological Survey, Shangxu Wang and Shoudong Wang, CNPC Geophysical Key Lab, University of Petroleum, Beijing, China*

Summary

Here, we present a case study of fracture detection using 3D P-wave seismic data from the Sichuan Basin in Southwest China. A major aspect of this study is the integration of outcrop, core and wireline logs with seismic data for reducing the uncertainties in the seismic results. To guide seismic data analysis, a physical modeling study is also carried out to compare the use of different P-wave seismic attributes and different analysis techniques. The target is a gas reservoir buried at about 1700m depth, and the reservoir rocks are tight sandstones with an average porosity of only about 2%. Fractures are the main fluid pathways. Analysis of core and log data from 21 boreholes reveals that there are two major sets of fractures in the study area striking northeast and northwest, respectively, with an average linear fracture density of about one fracture every two meters. We have processed and analyzed 50km^2 of 3D P-wave seismic data in order to evaluate the fracture characteristics between the boreholes. The seismic data is of average quality. Nevertheless with carefully-calibrated processing, the final fracture orientation and intensity maps estimated from the amplitude attributes compare reasonably well with the regional pattern in the area, and the seismic results at the well locations are consistent with the borehole results. The physical modeling study provides a good benchmark for the selected seismic attributes.

Introduction

The use of seismic anisotropy in 3D P-wave seismic data for characterizing fractured reservoirs has gradually gained the acceptance of the hydrocarbon industry (Lynn 2004), and there has been a consistent increase in the number of studies reported in the literature (e.g. MacBeth and Li 1999, Gray et al. 2002, Li et. al. 2003, and amongst others). Fractures are often critical for ensuring economic oil and gas production in tight formations of otherwise low permeability.

Here, we present a case study of fracture detection using wide-azimuth 3D P-wave seismic data from the Sichuan Basin in Southwest China. The Sichuan Basin is one of the major gas-producing provinces in China. The target formation is naturally fractured Jurassic sandstone buried at depths from 1700m to 2420m. The thickness of the reservoir rock varies from 570m to 720m and it is distributed in an area of about 170km^2, forming an anticline (Figure 1). The purpose of the study is to identify zones of high fracture density with gas accumulation for future well planning.

A major aspect of this study is the integration of outcrop, core and log data with seismic data for reducing the uncertainties in the seismic method. The seismic data are of average quality compared with similar datasets from other areas, and borehole-calibrated data analysis is critical to obtain reliable results from the seismic data. Another aspect of this study is the use of physical modeling to guide seismic data analysis. We have acquired an equivalent of 20km^2 of 3D P-wave physical modeling data in order to compare the use of different P-wave seismic attributes and different analysis techniques for fracture detection.

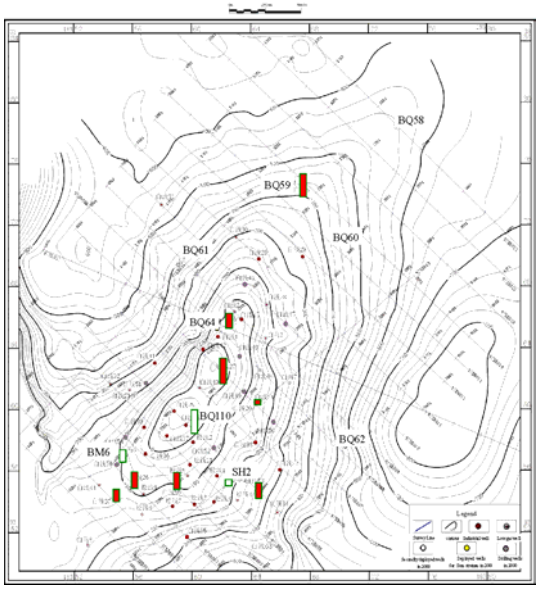

Figure 1. Target structure map and borehole locations. The bars indicated the relative fracture density and three un-shaded green bars (BM6, BQ110 and SH2) are within the seismic data area.

Outcrop study

A basic and direct way to investigate the fracture characteristics is through outcrop mapping. There exist several good sites of outcrop analogues to the Jurassic sandstone in the study area. We have carried out two

surveys of outcrop mapping in the area. There are two main types of fractures in the reservoirs as indicated from the outcrop analysis. One is structure-related and stress-induced fractures formed during structural movement, and the other is formed through deformation during physical diagenesis. The structure-related fractures are usually at the meter scale (Figure 2). These fractures are widespread and often regularly distributed in the Jurassic section. Their dominant trend is along the structural anticline.

Figure 2. Typical outcrop and core samples.

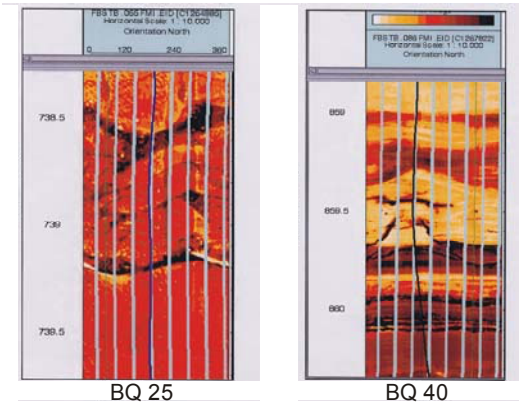

Figure 3. Sample image logs (FMI).

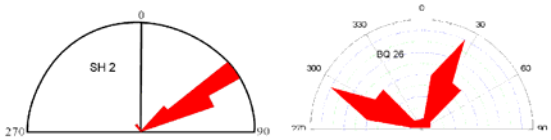

Figure 4. Fracture orientation from core and log data.

Core and log data analysis

We have analyzed cores from 21 boreholes and imaging logs (FMI) from nine boreholes in the study area, and the total length of cores is about 640m. Figures 2 and 3 show some typical core samples and image logs. Fractures can be clearly identified in both the cores and imaging logs. Table 1 lists the fracture parameters obtained from core and log data analysis from selected boreholes, and it is seen that there is a good correlation between the number of fractures and the gas production. Two sets of fractures can also be identified from cores and logs striking at about NE and NW respectively (Figure 4). Fractures with both low and high angle dips can be observed, and the high angle fractures (more than 70^0 dip) are distributed more regularly and with higher density than the low angle fractures.

Well #	Core length (m)	Fracture density (# / m)	Depth (m)	Gas prod. ($x10^4m^3/d$)
BM 6	52.39	0.67	1776-1847	1.01
BM 11	35.24	1.66	2405-2245	1.241
BQ 110	24.72	0.72	1827-1834	8.48
BM2	6.7	0.16	2251-2388	Dry
SH 2	82.1	0.18	2643-2583	Dry

Table 1. Core fracture density and gas production from selected boreholes.

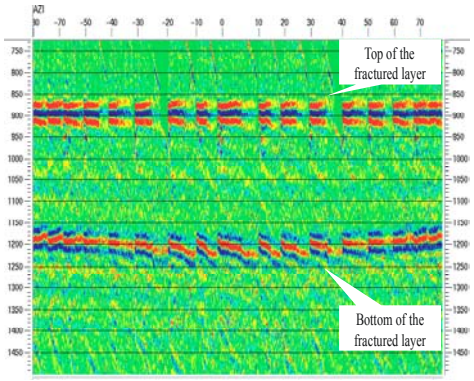

Figure 5. Physical modeling study showing variations of P-wave residual moveout with azimuth in azimuthally sorted supergathers. Note that the top event of the fractured layer is properly flattened, but the bottom event shows azimuthal variations of residual moveout.

Directional P-wave response

To guide our seismic data analysis, we first construct a physical model and acquire 3D seismic data in a laboratory experiment to verify and understand the effects of anisotropy on P-wave traveltime and amplitude. The base model consists of three horizontal layers. The first and third layers are constructed from the same material (epoxylite) and are believed to be isotropic. The second layer is constructed from a special industrial material and is believed to be azimuthally anisotropic with fracture density about 0.2. There are also two built-in geological features inside the fractured layer. One is a dome, and the other is a fault block, consisting of a normal and a vertical fault. On top of the base model, a water layer is added to speed up acquisition, and a 3D dataset equivalent to 20 km^2 was

acquired in a water tank. The physical modeling confirms that the P-wave seismic attributes, such as traveltime, velocity and reflected wave amplitude vary with azimuth, diagnostic of fracture-induced anisotropy (Figure 5).

Azimuthal attribute analysis (3A)

We utilize the concept of azimuthal attribute analysis (3A) for characterizing the fracture orientation and density from P-wave seismic data (Li et al. 2003, Hall and Kendall 2003). In practice, two methods are often employed to extract the fracture information: full-azimuth surface fitting and narrow-azimuth stacking. The first method fits an elliptical surface to data from all available azimuths and offsets by a least-square fitting technique. The second method divides the data into a number of narrow-azimuth volumes; here we choose nine 20^o (-10^o to 10^o) azimuthal bins over the 180^o range. Corresponding to these two methods, there are mainly four seismic attributes which may be used to extract the fracture information, including velocity, traveltime, amplitude, and AVO (amplitude versus offset) gradient. The surface fitting method is applicable to the amplitude and traveltime attributes, whilst the narrow-azimuth stacking method is applicable to the velocity and AVO gradient attributes (Li et al. 2003).

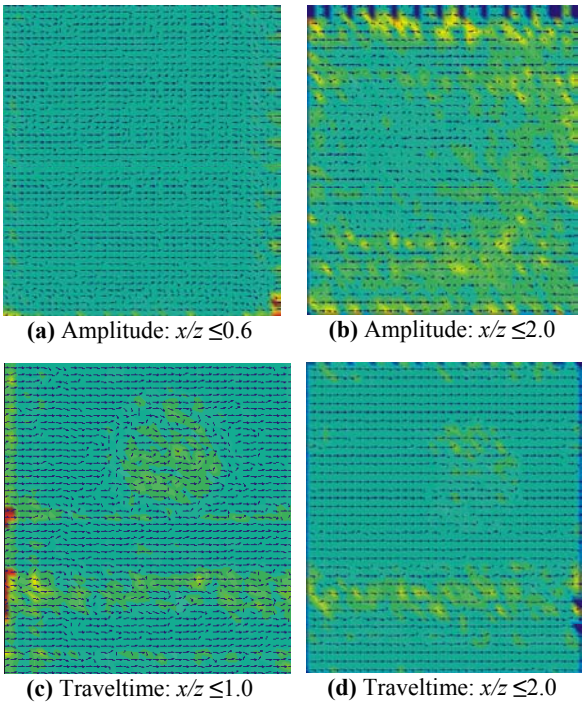

(a) Amplitude: $x/z \leq 0.6$ **(b)** Amplitude: $x/z \leq 2.0$

(c) Traveltime: $x/z \leq 1.0$ **(d)** Traveltime: $x/z \leq 2.0$

Figure 6. Comparison of results for the physical modeling data in Figure 3: (a) and (b) for top amplitudes and (c) and (d) for interval traveltime. x/z indicates the offset-depth ratio to the target.

Choices of attributes

Analysis of the physical modeling dataset reveals that full-azimuth surface fitting is preferred to the narrow-azimuth stacking method which appears to be influenced by the acquisition foot print and structural imprint. Among the four attributes, the amplitude is the most sensitive attribute. For even a small offset-depth ratio (offset/depth = 0.6), fracture parameters can still be determined quite accurately from the amplitude attributes (Figure 6a). However, the presence of a small amount of noise will significantly distort the results even with sufficient offset coverage (offset/depth = 2.0, Figure 6b). Therefore, to use the amplitude attribute, it is more important to reduce noise and preserve amplitude than to increase offset coverage.

The use of traveltime attributes requires sufficient offset coverage to allow the azimuthal variation to develop sufficiently. As shown in Figure 6d, for an offset-depth ratio of 2.0, the magnitude of azimuthal variation due to anisotropy exceeds that due to structural variations, so the structural imprint is significantly reduced. However, for insufficient offset coverage (offset/depth < 1.0), the results will be heavily influenced by the structural imprint (Figure 6c).

Field data analysis and results

We have selected $50km^2$ of 3D P-wave seismic data for characterizing the fractures between the boreholes. There are three wells within the seismic data areas: BM6, BQ110, and SH2, as marked in Figure 1 with unshaded green bars. The analysis is carried out in three stages: (1) data inspection and pre-processing including three key steps - surface-consistent static correction, surface-consistent amplitude corrections and noise attenuation, (2) test processing of part of the 3D dataset (about $10km^2$) using both narrow-azimuth stacking and full-azimuth surface fitting, and (3) full-field data analysis.

Figure 7 shows a stacked section passing through well BM6. The data quality is below average, although continuous horizons can be identified from the data. The target horizons are marked in the section. The stacked volume is used to produce a horizon file for aiding prestack picking. The analysis procedure for fracture detection includes two runs. The first run is for test purposes, and we select the four attributes (e.g. travel time and amplitude as well as the derived velocity and AVO gradient) for comparison. This requires automatically picking the travel times and amplitudes of the target events through the prestack volume. For this data, static correction is critical for aligning the events for horizon picking. After the test run, we find that the traveltime-related attributes as well as the AVO gradient are less reliable for this dataset. Instead,

the results from the analysis of the amplitude of the top target event are reasonable. This is partly due to the fact that the offset-depth ratio of the data is less than 1.0, as indicated in the physical modeling study in Figure 6. In the second run, we focus on the use of the amplitude attribute. The final results are shown in Figure 8, where the color contour shows the fracture density and short lines indicate the fracture orientation. The seismic results agree very well with the borehole results at the three well locations, and can also be correlated with the gas production (Table 1).

Conclusions

We have performed an integrated study of fracture characterization using P-wave seismic data. The work includes outcrop study, core and log analysis as well as processing and interpretation of 3D seismic data. The data are relative noisy, and the analysis is guided by physical modelling and borehole-calibrated processing. Analysis of the physical modeling reveals that a sufficiently large offset-depth ratio (at least 1.0) is required for the use of traveltime attributes; only the amplitude attribute may have sufficient sensitivity to resolve the fracture parameters for smaller offset-depth ratios around 0.6. The final fracture parameters predicted from the seismic data are consistent with the borehole and outcrop data, and can be correlated with the gas production in the study area. The focal point of this work is the integration of various studies for improving the reliability of the seismic method.

Acknowledgements

We thank CNPC and PetroChina Southwest Ltd. for permission to show the data. We thank Drs Liu Zhenwu and Fang Chaoliang for supporting the work. This work is funded by the CNPC international collaboration programme through its Geophysical Key Laboratory and the Edinburgh Anisotropy Project (EAP) of the British Geological Survey, and is published with the approval of all project partners and the Executive Director of British Geological Survey (NERC).

References

Gray, D., Roberts, G. and Head, K., 2002. Recent advances in determination of fracture strike and crack density from P-wave seismic data. The Leading Edge, **21**, 280-285.

Hall, S. A. and Kendall, J-M., 2003. Fracture characterization at Valhall: Application of P-wave amplitude variation with offset and amplitude (AVOA) analysis to a 3D ocean-bottom data set. Geophysics, **68**, 1150-1160.

Li, X. -Y., Liu, Y. -J., Liu, E., Shen, F., Qi, L. and Shouli, Q., 2003. Fracture detection using land 3D seismic data from the Yellow River Delta, China. The Leading Edge, **22**, 680-683.

MacBeth, C. and Li, X.-Y., 1999, AVD - An emerging new marine technology for reservoir characterization: Acquisition and application: Geophysics, **64**, 1153-1159.

Lynn, H. B., 2004. The winds of change: Anisotropic rocks--their preferred direction of fluid flow and their associated seismic signatures, Part 1. The Leading Edge, **23**, 1156-1162.

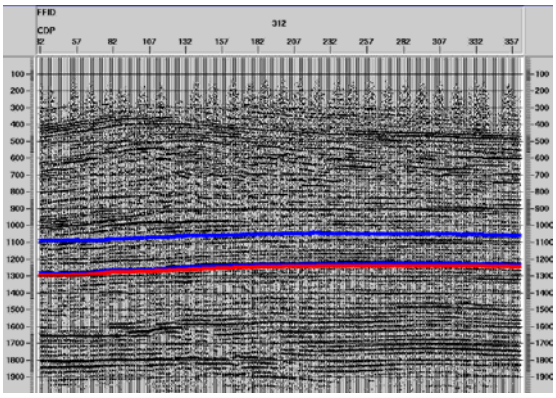

Figure 7. A stacked section passing through borehole BM6. The two lines mark the target.

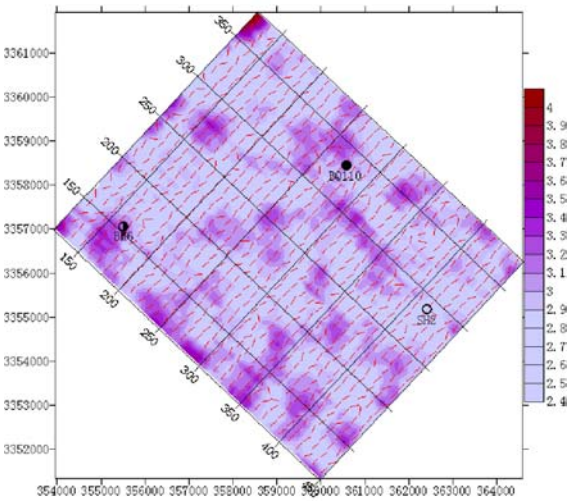

Figure 8. Fracture orientation and density from the 3D data in Figure 7.

EDITED REFERENCES

Note: This reference list is a copy-edited version of the reference list submitted by the author. Reference lists for the 2006 SEG Technical Program Expanded Abstracts have been copy edited so that references provided with the online metadata for each paper will achieve a high degree of linking to cited sources that appear on the Web.

REFERENCES

Gray, D., G. Roberts, and K. Head, 2002, Recent advances in determination of fracture strike and crack density from P-wave seismic data: The Leading Edge, **21**, 280–285.

Hall, S. A., and J.-M. Kendall, 2003, Fracture characterization at Valhall: Application of P-wave amplitude variation with offset and amplitude (AVOA) analysis to a 3D ocean-bottom data set: Geophysics, **68**, 1150–1160.

Li, X.-Y., Y.-J. Liu, E. Liu, F. Shen, L. Qi, and Q. Shouli, 2003, Fracture detection using land 3D seismic data from the Yellow River Delta, China: The Leading Edge, **22**, 680–683.

Lynn, H. B., 2004. The winds of change: Anisotropic rocks--their preferred direction of fluid flow and their associated seismic signatures, Part 1: The Leading Edge, **23**, 1156–1162.

MacBeth, C., and X.-Y. Li, 1999, AVD - An emerging new marine technology for reservoir characterization: Acquisition and application: Geophysics, **64**, 1153–1159.

vienna2006

E044

Fracture Characterization at Clair - Analysis of P-Wave Azimuthal Anisotropy in 2D & 3D Ocean-Bottom Data

Z. Qian* (School of Geosciences, The University of Edinburgh), X.Y. Li (British Geological Survey) & E. Liu (British Geological Survey)

SUMMARY

Over the past ten years, there has been a continuous increase in the use of 3D P-wave data for fracture characterization. In this study, we analyze P-wave azimuthal anisotropy in three 2D OBC (Ocean-Bottom-Cable) lines combined with a patch of 3D OBC data from the Clair Field, in the UK continental shelf (UKCS), in order to assess how seismic anisotropy can help improving fracture characterization in this field. The three 2D OBC lines are at 45-degree angle with each other, intersecting at a well position, and overlaps with the 3D survey. Analysis of the P-wave amplitude and velocity at the intersecting point shows significant azimuthal variation. P-wave interval velocities show about 10% variation in azimuth and the orientation is at N94oE, agreeing with previous studies. The 2D and 3D results are consistent at the intersecting point, and the joint analysis of 2D and 3D data increases the spatial coverage and improves the accuracy, further confirming the potential for using azimuthal variations of P-wave attributes for fracture detection.

Introduction

The Clair Field is located about 75km west of Shetland on the UK Continental Shelf (UKCS) with a water depth of 140 m. The field comprises of a Devonian/Carboniferous fractured reservoir beneath a Base Cretaceous unconformity (Coney et al. 1993) with an oil column about 600m. Studies on oriented core and field analogue data indicate that the Clair reservoir contains a complex variety of fracture types, orientations and scales. Successful production from the field is very much dependent on the ability to characterize the fracture system.

To achieve this goal, a series of seismic initiatives were taken to evaluate the use of seismic anisotropy for improving fracture characterization. The first initiative was the acquisition of a multi-azimuth walkaway VSP in October 1996 to investigate if the azimuthal variations of seismic P-wave attributes may aid in fracture analysis (Horne et al. 1998). This leads to a feasibility study of using crossed 2D and 3D surveys from repeated vintages to map fracture orientation and density (Smith and McGarrity 2001), and they successfully correlated the fracture density measured from velocity anisotropy to flow rates in appraisal wells. However, the intersecting points from these vintage surveys are very sparse. A 3D wide-azimuth OBC data set were then acquired in 2002 (Kommedal et al. 2005). Before that, three 2D OBC lines coinciding with the walkway VSP were acquired in May 2000, serving as a feasibility test for the 3D OBC survey. In this study, a patch of the Clair 3D OBC data is used for P-wave AVD (Attribute Versus Direction) analysis, and the results are analyzed jointly with the 2D results at the intersecting point.

Data acquisition and characteristics

The three lines of 2D OBC data were acquired in May 2000 using three Nessie-4C multi-component cables deployed on the seabed. The azimuths of the three 2D OBC lines are: North-South (Line A), N45^{o}E (Line B) and N135^{o}E (Line C), and intersecting at well 206/8-9Y (Figure 1a). The cables were 6 km long with receiver arrays every 25 m, giving 240 channels in total. Each array consisted of 7 hydrophones (P), and 21 orthogonal geophones (X, Y, & Z), hence a recorded channel group consisted of 7 receivers (P, X, Y, or Z). Shot spacing using a single array is 25 m for all lines, and CMP spacing for the 2D lines is 12.5 m with a nominal fold of 120.

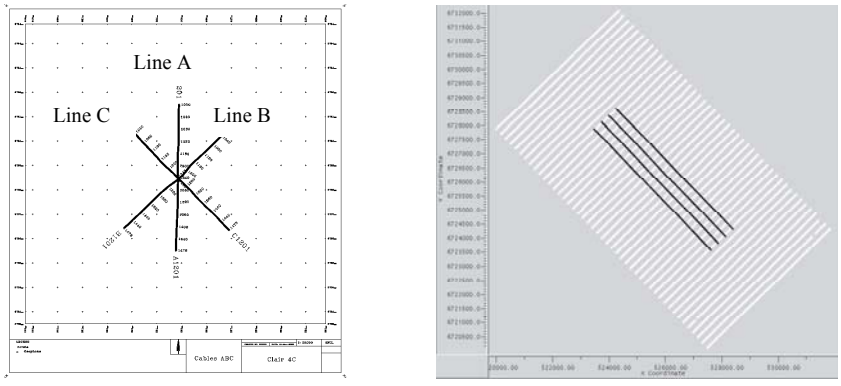

(a) (b)

Figure 1. Acquisition geometry of the Clair (a) 2D OBC lines, and (b) a single patch of the 3D OBC survey.

The 3D data were acquired by PGS in 2002 using the patch geometry where the sail lines are orthogonal to the receiver cables in order to obtain a wide azimuth coverage. Four cables are used with a cable separation of 355m, and sail line separation of 245m. A total of twenty patches were acquired and the patch we analyzed coincides with the 2D survey (Figure 1b). The patch shooting gives a good azimuthal coverage. Figure 2 shows the offset-azimuth

distribution of a CMP super gather from the 3D data. The horizontal axis denotes offset values, and the vertical axis denotes azimuth values. It shows that the data have a wide azimuth distribution that meets the requirement for fracture detection using P-wave data.

Figure 3 is a typical moveout-corrected supergather from the 3D data sorted in offset. The target horizon is below the base Cretaceous between 1400 and 1800ms. The maximum offset of the original data is around 3000m, but there is no useful information in the far offset traces at the target horizon due to interferences with the refracted arrivals. The effective offset for the target layer is less than 2000m, as indicated by the blue lines in Figure 3. This reduction in usable offset-range needs to be taken into account during acquisition design and data processing. Furthermore, there are significant multiple reflections present in the data raw due to the hard seabed. This will also compromise the result to some extent, especially for the target layer, where the primary reflections are relatively weak. Therefore, a careful processing procedure is required to attenuate the multiple and increase the signal to noise ratio in order to condition the data for azimuthal analysis. Further improvement in the data quality shall be very useful for successful fracture detection with the AVD method.

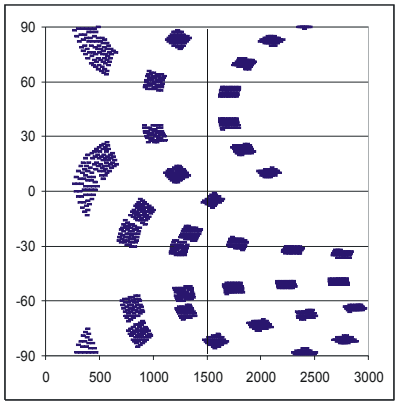

Figure 2. Offset-azimuth distribution of the super CMP gather in Figure 3.

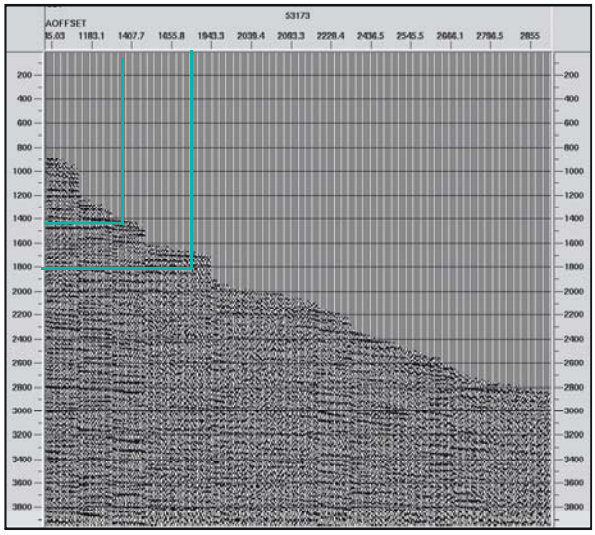

Figure 3. A super CMP gather from the 3D data

Azimuthal NMO velocity analysis

Azimuthal analysis is first carried out at the intersection point of the 2D OBC data. Amplitudes and traveltimes were picked for the event at 1.4s corresponding to the Base Cretaceous. The section down to the Base Cretaceous represents the overburden. The NMO velocity in the overburden shows weak azimuthal variation of 3-5%, which is within the error margins of conventional velocity analysis (Figure 4a), and there is no clear preferred direction; the interval velocity shows 10-15% variation with a clear fast direction at N94^{o}E (Figure 4b). We binned the 3D data into six narrow azimuths, and the corresponding velocity ellipse shows 5-10% variation at the east direction (N90^{o}E, Figure 4c). The 2D and 3D data agree with each other very well, and they are also in agreement with previous studies using streamer data (Smith and McGarrity 2001). However, the AVO gradient in the overburden shows abnormal variations of more than 100%, and the direction is along N45^{o}E, coinciding with the direction of Line B. This highlights the uncertainties associated with the amplitudes. More careful analysis is required for the amplitudes. Traveltime and velocity attributes may be more appropriate.

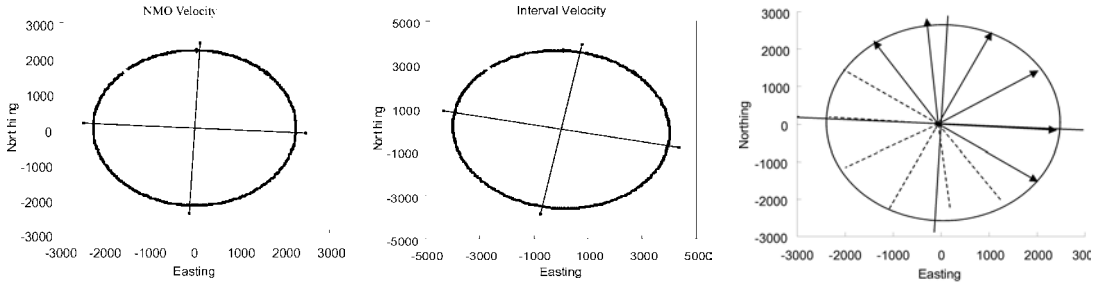

(a) 2D moveout velocity (b) 2D interval velocity (c) 3D interval velocity

Figure 4. Azimuthal variations of moveout velocities at the intersecting point from the 2D data: (a) 2D NMO stacking velocity for the overburden, and (b) 2D interval velocity of the target. (c) shows the variation of the interval velocity of the target from the super gather in Figure 3 with six narrow-azimuth bins.

Analysis of azimuthal stack panels in the 3D data

For a low to high impedance contrast, the reflection coefficient along the fracture strike should be larger than the reflection coefficients along any other direction, whilst the reflection coefficient along the fracture normal should be the smallest. Figure 5 displays the azimuthal stack panels in six azimuth directions in order to examine the variations of the stacked amplitudes. The stack section in the east direction (90^o) shows the strongest reflection event, and should denote a fracture strike along the east direction. In the north direction (0^o), the event is the weakest one, which denotes the fracture normal direction. This result agrees with the result obtained from azimuthal NMO velocity analysis. Both azimuthal NMO velocity and azimuthal stack display approximately a fracture strike in the east direction.

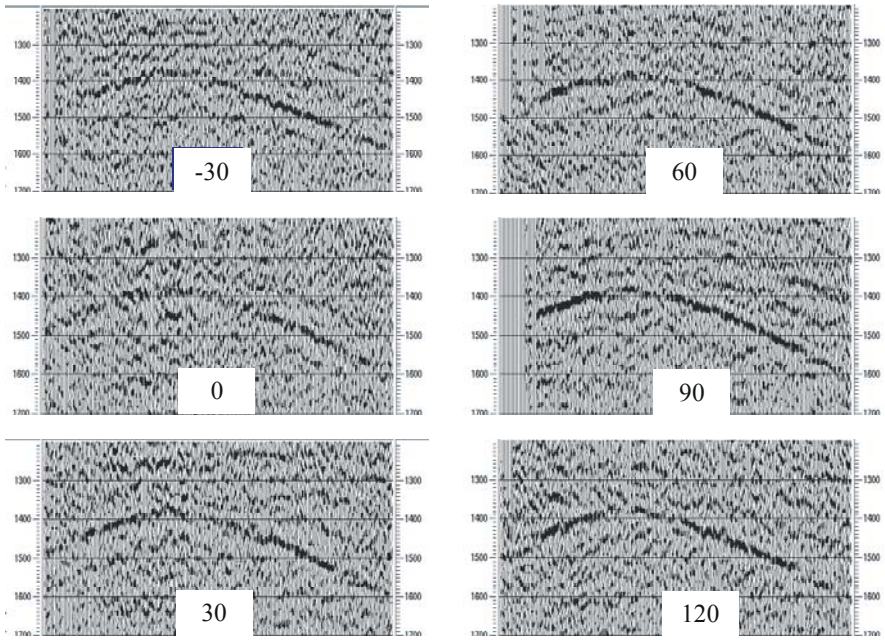

Figure 5. Azimuthal stack panels.

Estimated fracture distribution from the 3D data

Figure 6a shows the fracture distribution obtained from the analysis of the top reflection amplitude. The colour indicates the fracture density. From the analysis carried out at the intersecting point, we already know that the amplitude analysis is less reliable, and the results need to be interpreted more carefully. Figure 6b shows the fracture information derived by the AVO gradient. The distribution shows clear stripes parallel to the OBC lines, indicating the effects of the acquisition footprint. This is consistent with previous findings regarding the use

of the AVO gradient (Li et al. 2003). Figures 6c displays the results from the interval travel time, showing relatively stable fracture distribution trend. These results are consistent with the results at the intersecting point as shown in Figure 4.

Conclusions

The Clair 3D OBC data have a good offset-azimuth coverage, but refractions after the first arrival limit the effective offset range for azimuthal analysis. Only the data within the offset of 2000m can be reliably used for azimuthal attributes analysis. Thus, in OBC data acquisition, merely increasing the offsets is not good enough, and the effective offset range for the target horizon must be taken into account. The data also contain residual multiples, which have in turn reduced the reliability of the results obtained from the amplitude analysis. Both analyses of azimuthal stacking velocities and azimuthal stack panels reveal a fracture orientation striking at the east direction. This agrees with the results of VSP and 2D OBC data analysis in the area. Furthermore, the anisotropy in the overburden above the Base Cretaceous is weak. This represents a very favourable setup for the use of seismic anisotropy for characterizing fracture distribution in the Clair field.

Acknowledgements

We thank Rodney Johnston of BP for useful comments. We thank Sue Fowler and John McGarrity of BP for useful discussion. We thank the Clair Partners (BP, Chevron, ConocoPhillips, Shell and Amerada Hess) for permission to show the Clair 2D and 3D 4C data. This work is funded by the Edinburgh Anisotropy Project (EAP) of the British Geological Survey, and is presented with the approval of the Executive Director of British Geological Survey (NERC) and the EAP sponsors.

References

Coney, D., Fyfe, T. B., Retail, P., and Smith, P. J., [1993]. Clair appraisal: The benefits of a co-operative approach, in Parker, J. R., Ed., Petroleum Geology of Northwest Europe: Geol. Soc. London, 1409–1420.

Horne, S. A., McGarrity, J. P., Sayers, C. M., Smith, R. L. and Wijnands, F. M., [1998]. Fractured reservoir characterisation using multi-azimuthal walkaway VSPs. 68th SEG Meeting, New Orleans, USA, Expanded Abstrascts, 1640-1643.

Li, X. -Y., Liu, Y., Liu, E., Shen, F., Li, Q. and S. Qu, [2003]. Fracture detection using land 3D seismic data from the Yellow River Delta, China. The Leading Edge, **22**, 680-683.

Smith, R.L. and McGarrity, J.P., [2001]. Cracking the fractures from seismic anisotropy in an offshore reservoir. The Leading Edge, **20**, 19-26.

Kommedal, J. H. Fowler, S. McGarrity J., [2005]. Improved P-wave imaging with 3D OBS data from the Clair field. First Break, **23**, 51-54.

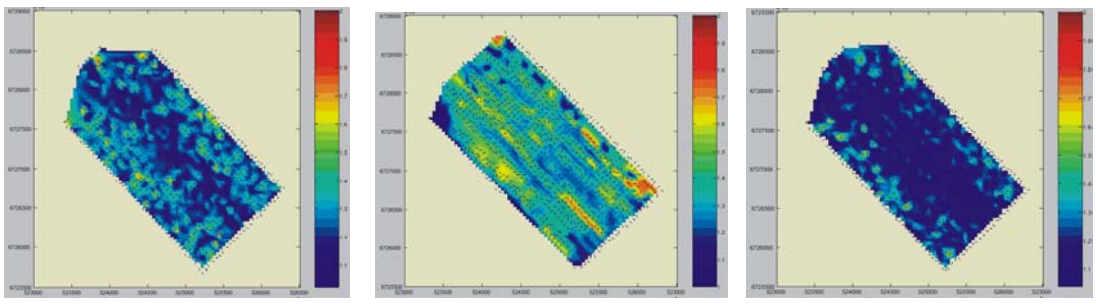

(a) (b) (c)

Figure 6. Fracture density and strike distribution from azimuthal attribute analysis: (a) amplitude; (b) AVO gradient; (c) interval traveltime.

vienna2006

P296

Comparison of Two Physical Modelling Studies of 3D P-Wave Fracture Detection

Z. Qian* (School of Geosciences, The University of Edinburgh), X.Y. Li (British Geological Survey) & S. Wang (CNPC Geophysical Keylab)

SUMMARY

Two 3D physical seismic data were acquired and analyzed to verify the physical basis of using P-wave attributes for fracture detection, to understand the usage of these attributes and their merits, and to investigate the effects of acquisition geometry and structural variations on these attributes. One model was designed to maximize the data quality, and another model was designed to increase the offset-depth ratio to the top of the fracture layer. The study of both datasets reveals that the P-wave attributes (traveltime, amplitude and velocity) exhibit azimuthal variations. For the data with high quality, the amplitude from the top of the fracture layer yields the best results that agree with the physical model parameters, but the results from other attributes (traveltime, velocity, AVO gradient) are either contaminated by the structural imprint, or by the acquisition footprint. For the data with larger offset-depth ratio, the traveltime attributes yield the best results, but the results from the amplitudes are affected by the noise and are less reliable.

Introduction

The underline physics of using seismic anisotropy to detect natural fractures comes from the equivalent medium theory for seismic wave propagation in fractured media, which has been intensively studied by many authors (e.g. Hudson, 1981; Schoenberg and Douma, 1988; Liu et al, 2000; Chapman, 2003; amongst others.). Numerical modelling based on the theory reveals that azimuthal variations in P-wave amplitude and traveltime are diagnostic features of the fractured medium. Over the past ten years, there has been a continual increase in the use of 3D P-wave data for fracture characterization. Both numerical modelling and case history of fracture detection using P-wave seismic has been the subject of intensive study (e.g. Lynn et al., 1996; Hall et al., 2001; Li et al., 2003; amongst others). In comparison, the number of corresponding physical-modelling studies is much less (Luo and Evans, 2004).

Here, we fill this gap by presenting physical modelling studies of fracture detection using large-scale 3D P-wave seismic data. In addition to an examination of the underlying physics, this study also investigated the effects of acquisition geometries and compared the use of different P-wave seismic attributes and different analysis techniques on fracture detection with the two physical modelling datasets.

The physical models and data acquisition

The base model consists of three horizontal layers. The first and third layers are constructed from the same material (epoxylite) and are believed to be isotropic. The second layer is constructed from a special industrial material and is believed to be azimuthally anisotropic with fracture density about 0.2. There are also two built-in geological features inside the fracture layer. One is a dome, and the other is a fault block, consisting of a normal and a vertical fault. The model is constructed with a scale of 1:10000 for spatial dimensions and time measurements with a corresponding velocity scaling of 1:1. Two models are derived from the base model for simulating different offset-depth ratios and acquisition geometries.

3D data acquisition is conducted in a water tank. The acquisition geometry is designed to ensure a wide-azimuth coverage. For each model, a 3D dataset equivalent to 20 km^2 was acquired. Figure 2 shows a comparison of sample shot gathers from the two models. The arrows mark the primary reflections from the base model in Figure 1. For Model 1, the data are of high quality. For Model 2, the primaries are contaminated with multiples and refracted arrivals, but the top and bottom reflection events of the fracture layer are still visible. Both datasets have a good coverage over azimuth, thus can be used for fracture analysis.

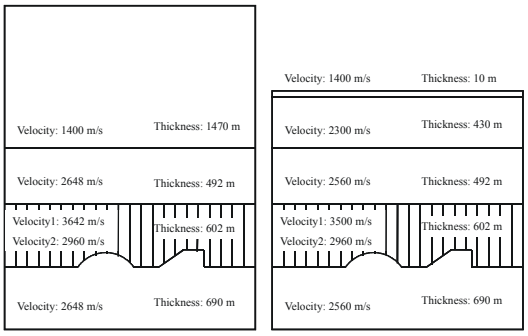

Figure 1. Section view of the two models: (a) Model 1, and (b) Model 2.

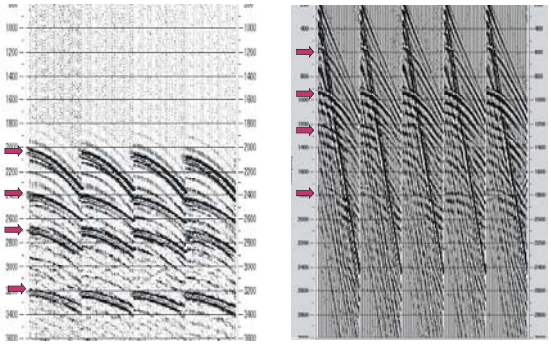

Figure 2. Sample shot gathers from (a) Model 1 and (b) Model 2.

Azimuthal variations of P-wave attributes

The physical model consists of only a single set of fractures. Numerical modelling of wave propagation in such a medium predicts that the P-wave seismic attributes, such as traveltime, velocity and reflected wave amplitude will vary with azimuth, diagnostic of fracture-induced

anisotropy (e.g. Hall et al., 2001). To verify this, we examine the azimuthal variations in P-wave attributes for both models.

Figure 3 shows the variations of P-wave residual moveout with azimuth. A super gather is binned into 18 azimuthal gathers with 10° azimuth bins and 100m offset bins. NMO correction has been applied to the azimuthal gathers using a single velocity function. The top event of the fracture layer is properly flattened, but the bottom event shows azimuthal variations of residual moveout. For the gathers of Model 2 at azimuths -50° and 40°, the bottom event is reasonably flattened. For the gather at azimuth 0°, the bottom event shows under-correction. However, for gather at azimuths -80° and 80°, as well as their adjacent gathers, the bottom event is over-corrected. This indicates that the fracture normal is at azimuth 0°, and the fracture strike is at azimuth 90°, since wave propagates slower along the fracture normal than along the fracture strike. At an intermediate azimuth, the wave propagates with a velocity faster than at the fracture normal but slower than at the fracture strike. When an intermediate velocity for an intermediate azimuth is used to correct the moveout, it will over-correct the events at the strike direction, but under-correct the event at the normal direction. However, due to the lack of offset coverage, this azimuthal residual normal moveout variation is not equally developed for the data of Model 1.

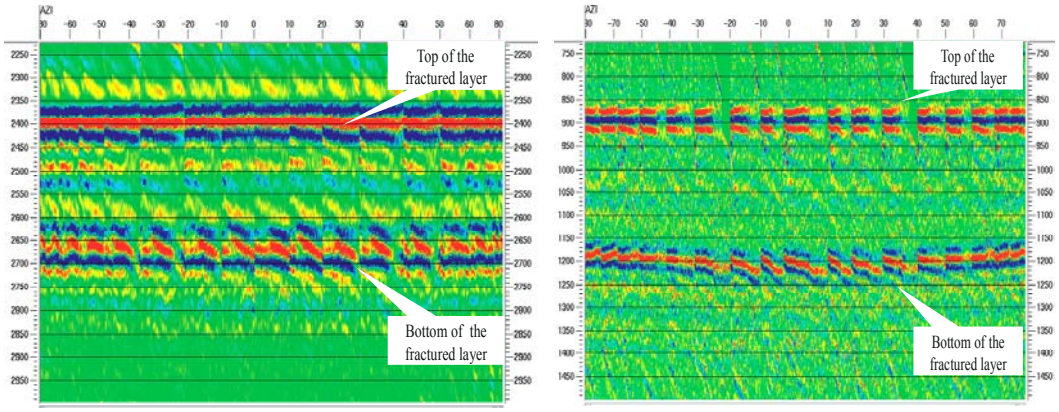

(a) (b)

Figure 3. Variations of P-wave residual moveout with azimuth. (a) azimuthally sorted supergathers for Model 1, and (b) azimuthally sorted supergathers for Model 2

Numerical modelling predicts that the azimuthal variations of P-wave attributes can be approximately described by an ellipse. For velocity variation, the long axis of the ellipse indicates the fracture strike, and the ratio of the short to long axis is proportional to the fracture density. This can clearly be observed in Figure 4b for Model 2. In comparison, the corresponding variation in Model 1 is much weak due to the lack of offset coverage.

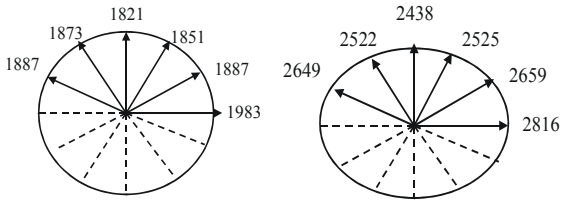

(a) (b)

Figure 4. Azimuthal NMO velocity variation fitted with an ellipse. (a) Model 1; (b) Model 2

Extracting fracture parameters

Two methods have been used to extract the fracture information from P-wave attributes: full-azimuth surface fitting and narrow-azimuth stacking. The first method fits an elliptical surface to data from all available azimuths and offsets by a least-square fitting technique. The second method divides the data into a number of narrow-azimuth volumes. Corresponding to these two methods, there are four principal seismic attributes: traveltime, amplitude, velocity and AVO gradient, which may be used to extract the fracture information. The surface fitting method is suitable for the traveltime and amplitude attributes. The narrow azimuth method is suitable for the velocity and AVO gradient attributes. Figure 5 shows the comparison of the results estimated from the top amplitudes of the two models. The color displays the fracture

intensity and the superimposed short lines indicate the fracture strike azimuth. Figure 6 shows the comparison of the results estimated from the interval velocity of the fracture layer.

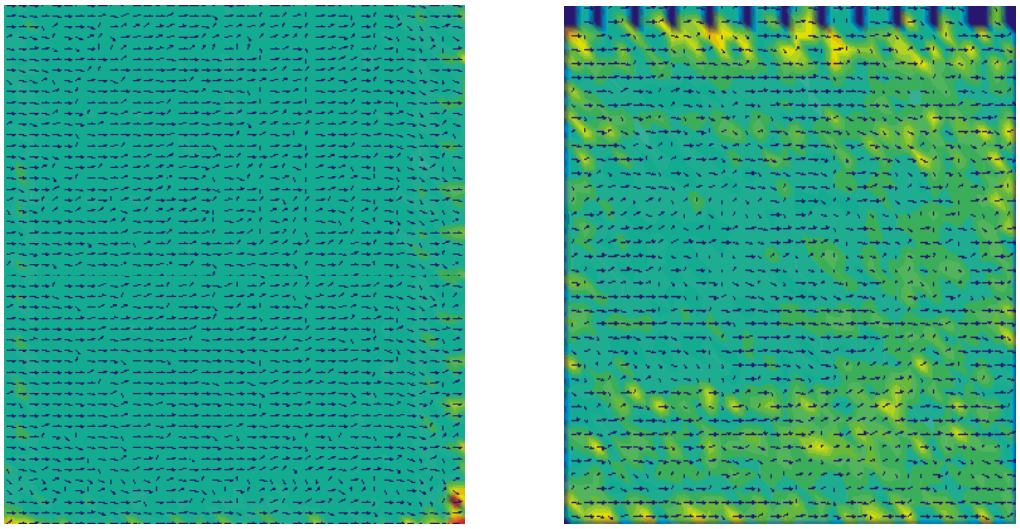

(a) (b)

Figure 5. Comparison of the results of the top amplitude: (a) Model 1 and (b) Model 2.

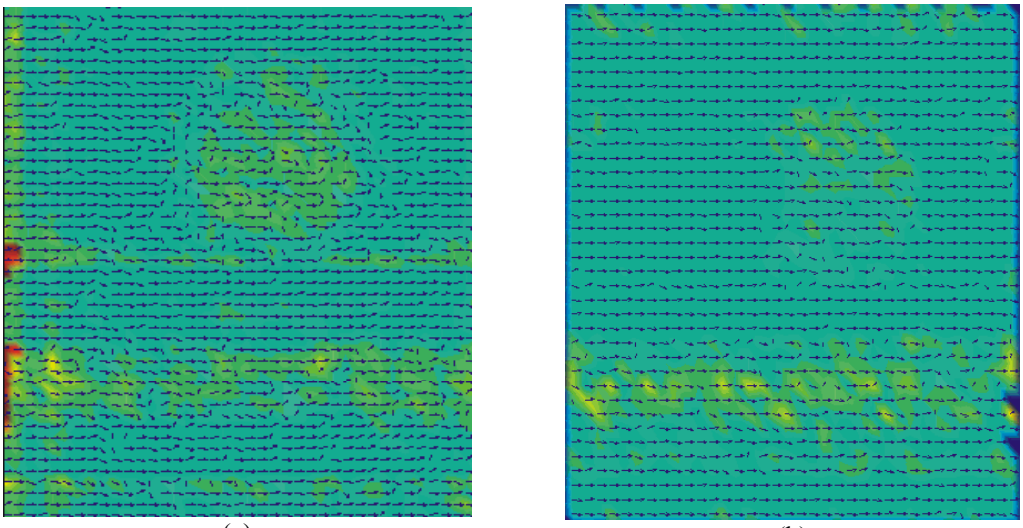

(a) (b)

Figure 6. Comparison of the results of interval velocity analysis: (a) Model 1 and (b) Model 2.

Analysis and findings

The amplitude is the most sensitive attribute. For the data of Model 1, even the offset-depth ratio to a target is quite small (offset/depth = 0.5), fracture parameters can still be determined quite accurately from the amplitude attributes. However, the presence of a small amount of noise will significantly distort the results even with sufficient offset coverage (offset/depth = 2.0). Therefore, for the use of amplitude attribute, it is more important to reduce noise and preserve amplitude than to increase offset coverage.

The use of traveltime attributes required sufficient offset coverage to allow the azimuthal variation sufficiently developed. For insufficient offset coverage (offset/depth < 1.0), the results will be heavily influenced by structural imprint. The offset and azimuthal coverage is critical for the success of using P-waves for fracture detection. The study reveals that the offset-depth ratio should be at least larger than 1.0. Only in a noise-free environment, may there be sufficient sensitivities from the amplitude attribute to resolve the fracture parameter for offset-dept ratio approaching 0.6. Large offset coverage makes it possible to use the

traveltime attributes. A reliable estimation from traveltime attributes required offset-depth ratio of 1.0 or more.

The structural variation will leave a significant imprint on the estimated results, particularly if the offset-depth ratio is not sufficiently large. However, these effects may be compensated for by increasing the offset coverage and by the use of traveltime attributes. When the magnitude of azimuthal variation due to anisotropy exceeds that due to structural variations, the structural imprint will be significant reduced.

Conclusions

We have carried out two physical experiments and performed a detailed analysis. Azimuthal variations of P-wave attributes are observed, confirming the numerical modelling results based on the equivalent medium theory. Two methods (full-azimuth/full-offset and narrow-azimuth/full-offset) have been used and four seismic attributes have been analyzed for fracture parameter estimation. The offset-depth ratio to the target is a key parameter for the success of the P-wave techniques, which affects the choices of attributes and the choice of processing methods. Smaller offset-depth coverage may only be applicable to amplitude attributes with high quality data; whilst large offset coverage makes it possible to use traveltime attributes, which is less sensitive to noise, reducing the effects of acquisition foot print as well as the structural imprint. A reliable estimation from traveltime attributes required offset-depth ratio of 1.0 or more.

Acknowledgements

The authors thank China National Petroleum Corporation (CNPC) for providing the funds to conduct the physical experiments. Wang Shoudong processed the data of Model 1. The work is supported under a collaboration agreement between the CNPC Geophysical Key Laboratory at the China University of Petroleum and the Edinburgh Anisotropy Project (EAP) at the British Geological Survey (BGS), and is published with the approval of all project partners and the permission of the Executive Director of the British Geological Survey (NERC).

References

Chapman, M., 2003. Frequency dependent anisotropy due to meso-scale fractures in the presence of equant porosity. Geophysical Prospecting, **51**, 369-379.

Hall, S., Barkved, O., Mueller, M.C. and Kendall, J-M, 2001, An approach for P-wave AVOA in 3D-OBC data: 62nd EAGE Meeting, Expanded Abstracts, **1**, C-09.

Hudson, J.A., 1981. Wave speeds and attenuation of elastic waves in material containing cracks. Geophysical Journal of the Royal Astronomical Society, **64**, 133-150.

Li, X.-Y., Liu, Y., Liu, E., Shen, F., Li, Q. and Qu, S., 2003, Fracture detection using land 3D seismic data from the Yellow River Delta, China: The Leading Edge, **22**, No. 7, 680-683.

Liu, E., Hudson, J. A. and Pointer, T., 2000, Equivalent medium representation of fractured rock, J. Geophysical Research, **105**, No.B2, 2981-3000.

Luo, M. and Evans, B.J., 2004, An amplitude-based multiazimuth approach to mapping fractures using P-wave 3D seismic data: GEOPHYSICS, Soc. of Expl. Geophys., **69,** 690-698.

Lynn, H. B., Simon, K. M. and Bates, C. R., 1996, Correlation between *P*-wave AVOA and *S*-wave traveltime anisotropy in a naturally fractured gas reservoir: The Leading Edge, **15**, 931-936.

Schoenberg, M. and Douma, J., 1988, Elastic-wave propagation in media with parallel fractures and aligned cracks: Geophysical Prospecting, Eur. Assn. Geosci. Eng., **36,** 571-590.